

# Spectral Analysis of Terrestrial Gamma-ray Flashes and Their Connection to Lightning Discharges

---

Anders Lindanger

Thesis for the degree of Philosophiae Doctor (PhD)  
University of Bergen, Norway  
2022

UNIVERSITY OF BERGEN



# **Spectral Analysis of Terrestrial Gamma-ray Flashes and Their Connection to Lightning Discharges**

Anders Lindanger



Thesis for the degree of Philosophiae Doctor (PhD)  
at the University of Bergen

Date of defense: 01.04.2022

© Copyright Anders Lindanger

The material in this publication is covered by the provisions of the Copyright Act.

Year: 2022

Title: Spectral Analysis of Terrestrial Gamma-ray Flashes and Their Connection to Lightning Discharges

Name: Anders Lindanger

Print: Skipnes Kommunikasjon / University of Bergen

# Acknowledgements

First and foremost, I want to thank my supervisor Martino Marisaldi for excellent guidance, inspiration and support. I have always found his office door open, both at the institute and online during the ongoing covid-19 pandemic. I would also like to thank co-advisor Nikolai Østgaard together with all the employees at Birkeland Centre for Space Science.

I would like to thank the AGILE team for giving me access to their database and excellent cooperation. I would also like to thank Torsten Neubert, Nikolai Østgaard, Victor Reglero and other partners of the ASIM mission for providing unprecedented measurements of Terrestrial Gamma-ray Flashes.

Furthermore, I would like to thank all my good friends and colleagues for coffee- and lunch breaks at the institute and online. This thesis would not have been possible without you. Thank you to Helene Flinstad for keeping my written English in shape. I would also like to give a special thanks to Villy Nielsen for the everyday morning greetings and for keeping the spirit of the institute at top level.

I wish to thank my family for all the support they have given me in my academic pursuits and elsewhere.

Finally, I would like to thank my fiancée Christina for always supporting and encouraging me. I am extremely grateful.

Bergen, January 2022  
Anders Lindanger



# Outline

This thesis consists of an introductory part and three scientific papers. The papers have been published in an international, peer-reviewed journal. Paper III was under review at the time of the defense and in the printed version of the thesis, but is updated to the published version in this PDF-file.

**Paper I** A. Lindanger, M. Marisaldi, C. Maiorana, D. Sarria, K. Albrechtsen, N. Østgaard, M. Galli, A. Ursi, C. Labanti, M. Tavani, C. Pittori, and F. Verrecchia, *The 3rd AGILE Terrestrial Gamma Ray Flash Catalog. Part I: Association to Lightning Sferics*, Journal of Geophysical Research: Atmospheres, **125**, doi:10.1029/2019JD031985, 2020

**Paper II** A. Lindanger, M. Marisaldi, D. Sarria, N. Østgaard, N. Lehtinen, C. A. Skeie, A. Mezentzev, P. Kochkin, K. Ullaland, S. Yang, G. Genov, B. E. Carlson, C. Köhn, J. Navarro-Gonzalez, P. Connell, V. Reglero, T. Neubert, *Spectral Analysis of Individual Terrestrial Gamma-ray Flashes Detected by ASIM*, Journal of Geophysical Research: Atmospheres, **126**, doi:10.1029/2021JD035347, 2021

**Paper III** A. Lindanger, C. A. Skeie, M. Marisaldi, I. Bjørge-Engeland, N. Østgaard, A. Mezentsev, D. Sarria, N. Lehtinen, V. Reglero, O. Chanrion, T. Neubert, *Production of Terrestrial Gamma-ray Flashes During the Early Stages of Lightning Flashes*, Journal of Geophysical Research: Atmospheres, **127**, doi:10.1029/2021JD036305, 2022

During my PhD I have also contributed to the following peer-reviewed papers. They are not a part of this thesis.

- A** M. Marisaldi, M. Galli, C. Labanti, N. Østgaard , D. Sarria, S. A. Cummer, F. Lyu, A. Lindanger, R. Campana, A. Ursi, M. Tavani, F. Fuschino, A. Argan, A. Trois, C. Pittori, and F. Verrecchia, *On the High-Energy Spectral Component and Fine Time Structure of Terrestrial Gamma Ray Flashes*, Journal of Geophysical Research: Atmospheres, **124**, doi:10.1029/2019JD030554, 2019
- B** C. Maiorana, M. Marisaldi, A. Lindanger, N. Østgaard, A. Ursi, D. Sarria, M. Galli, C. Labanti, M. Tavani, C. Pittori, and F. Verrecchia, *The 3rd AGILE Terrestrial Gamma-ray Flashes Catalog. Part II: Optimized Selection Criteria and Characteristics of the New Sample*, Journal of Geophysical Research: Atmospheres, **125**, doi:10.1029/2019JD031986, 2020
- C** D. Sarria, N. Østgaard, P. Kochkin, N. Lehtinen, A. Mezentsev, M. Marisaldi, A. Lindanger, C. Maiorana, B. E. Carlson, T. Neubert, V. Reglero, K. Ullaland, S. Yang, G. Genov, B. H. Qureshi, C. Budtz-Jørgensen, I. Kuvvetli, F. Christiansen, O. Chanrion, J. Navarro-González, P. Connell, C. Eyles, *Constraining Spectral Models of a Terrestrial Gamma-Ray Flash From a Terrestrial Electron Beam Observation by the Atmosphere-Space Interactions Monitor*, Geophysical Research Letters, **125**, doi:10.1029/2021GL093152, 2021
- D** A. J. Castro-Tirado, N. Østgaard, E. Göğüş, C. Sánchez-Gil, J. Pascual-Granado, V. Reglero, A. Mezentsev, M. Gabler, M. Marisaldi, T. Neubert, C. Budtz-Jørgensen, A. Lindanger, D. Sarria, I. Kuvvetli, P. Cerdá-Durán, J. Navarro-González, J. A. Font, B. B. Zhang, N. Lund, C. A. Oxborrow, S. Brandt, M. D. Caballero-García, I. M. Carrasco-García, A. Castellón, M. A. Castro Tirado, F. Christiansen, C. J. Eyles, E. Fernández-García, G. Genov, S. Guziy, Y. D. Hu, A. Nicuesa Guelbenzu, S. B. Pandey, Z. K. Peng, C. Pérez del Pulgar, A. J. Reina Terol, E. Rodríguez, R. Sánchez-Ramírez, T. Sun, K. Ullaland, and S. Yang, *Very-high-frequency oscillations in the main peak of a magnetar giant flare*, Nature, **600**, doi:10.1038/s41586-021-04101-1, 2021

# Contents

<b>Acknowledgements</b>	<b>i</b>
<b>Outline</b>	<b>iii</b>
<b>1 Introduction</b>	<b>1</b>
1.1 Objectives . . . . .	2
1.2 Outline . . . . .	2
<b>2 Atmospheric Electricity</b>	<b>3</b>
2.1 Thunderclouds and Electric Fields . . . . .	3
2.2 Lightning Discharges . . . . .	4
2.2.1 Electron Avalanche . . . . .	4
2.2.2 Streamers and Leaders . . . . .	5
2.3 High-Energy Phenomena and Transient Luminous Events . . . . .	6
<b>3 Lightning Detection by Radio Waves</b>	<b>9</b>
3.1 WWLLN . . . . .	10
3.2 GLD360 . . . . .	11
<b>4 Terrestrial Gamma-ray Flashes</b>	<b>13</b>
4.1 Observations of TGFs . . . . .	14
4.1.1 BATSE . . . . .	14
4.1.2 RHESSI . . . . .	15
4.1.3 Fermi . . . . .	15
4.1.4 AGILE . . . . .	16
4.1.5 ASIM . . . . .	18
4.1.6 Overview of the Main Space Missions Observing TGFs . . . . .	22
4.1.7 Terrestrial Electron Beams . . . . .	23
4.1.8 Other TGF detections from Space, Aircraft and Ground . . . . .	24
4.2 TGF Characteristics as Observed from Space . . . . .	24
4.3 Production Mechanisms of TGFs . . . . .	27
4.3.1 Runaway Electrons . . . . .	27
4.3.2 Relativistic Runaway Electron Avalanches . . . . .	28
4.3.3 Relativistic Feedback Mechanism . . . . .	28
4.3.4 Thermal Runaway Mechanism . . . . .	29
4.4 Lightning Discharges and TGFs . . . . .	29
4.5 Spectral Analysis of Terrestrial Gamma-ray Flashes . . . . .	31

---

<b>5 Summary of Papers</b>	<b>33</b>
5.1 Summary of Paper I . . . . .	33
5.2 Summary of Paper II . . . . .	34
5.3 Summary of Paper III . . . . .	35
<b>6 Conclusions and Future Prospects</b>	<b>37</b>
6.1 Conclusions . . . . .	37
6.2 Future Prospects . . . . .	38
<b>Bibliography</b>	<b>40</b>
<b>7 Scientific results</b>	<b>55</b>
<b>Paper I The 3rd AGILE Terrestrial Gamma Ray Flash Catalog. Part I: Association to Lightning Sferics</b>	<b>57</b>
<b>Paper II Spectral Analysis of Individual Terrestrial Gamma-ray Flashes Detected by ASIM</b>	<b>75</b>
<b>Paper III Production of Terrestrial Gamma-ray Flashes During the Early Stages of Lightning Flashes</b>	<b>119</b>
<b>List of abbreviations</b>	<b>139</b>

# Chapter 1

## Introduction

Terrestrial Gamma-ray Flashes (TGFs) were first detected in 1991 by the Burst and Transient Source Experiment (BATSE) onboard the Compton Gamma-ray Observatory [Fishman *et al.*, 1994]. TGFs are sub-millisecond bursts of intense gamma radiation with energies up to tens of MeV, making them a manifestation of the most energetic natural particle acceleration processes on Earth. TGFs have been continuously observed by the few space missions capable of detecting them: BATSE, Reuven-Ramaty High Energy Solar Spectroscopic Imager (RHESSI) [Smith *et al.*, 2005], Astrorivelatore Gamma a Immagini Leggero (AGILE) [Marisaldi *et al.*, 2010], Fermi [Briggs *et al.*, 2010], and the Atmosphere Space Interactions Monitor (ASIM) [Neubert *et al.*, 2019]. There have also been a few observations from other satellites [Ursi *et al.*, 2017; Bogomolov *et al.*, 2017], airplane [Smith *et al.*, 2011a,b; Bowers *et al.*, 2018], and from ground [e.g. Hare *et al.*, 2016; Enoto *et al.*, 2017; Belz *et al.*, 2020].

BATSE was launched to study celestial gamma-ray sources. Therefore, the detection of hard gamma radiation from the Earth was completely unexpected. Wilson [1925a] had predicted that energetic phenomena could occur in the atmosphere, but in the case of TGFs he had not predicted their intensity and energy range. The terrestrial origin of TGFs and their association with thunderstorms were recognized from the beginning. However, they were believed to be connected to electric phenomena in the upper atmosphere, and not in the lower atmosphere as we know today [Fishman *et al.*, 1994]. Connaughton *et al.* [2010] showed that TGFs are often simultaneous with detected lightning discharges within a few hundreds of microseconds. In particular, the TGFs are directly associated with the initial phase of a lightning discharge during the upward propagation of leaders [e.g. Cummer *et al.*, 2015].

Various models have been proposed to explain the production of TGFs. The key idea is the acceleration of electrons to relativistic energies in an electric field and that these electrons produce photons by bremsstrahlung in the atmosphere. This process is called the Relativistic Runaway Electron Avalanche (RREA) [Gurevich *et al.*, 1992]. There are two leading theories explaining how this could happen in thunderstorm electric fields: acceleration and multiplication of the electrons in a uniform ambient electric field through the Relativistic Feedback model [e.g. Dwyer, 2003], and acceleration of electrons in the non-uniform field in front of the lightning-streamer tip before further acceleration in the field in front of the lightning-leader [e.g. Celestin and Pasko, 2011]. One model does not exclude the other and the empirical evidence has been ambiguous supporting one model over the other.

Although almost thirty years of TGF detection has left us with a long list of observations, few questions have been answered. For example, much still remains to be uncovered about the occurrence rate of TGF production worldwide, the intrinsic duration, source luminosity, altitude and beaming geometries, and the exact relationship between TGFs and lightning discharges.

## 1.1 Objectives

The goal of this thesis is to further investigate the relationship between TGFs and lightning discharges, and source properties using spectral analysis. Paper I correlates gamma-ray data from AGILE with ground-based lightning data to identify TGFs. Together with the companion paper, *Maiorana et al. [2020]*, it constitutes a new, inclusive and consolidated TGF catalog from the AGILE mission. The study investigates geographical distribution, coast/ocean/land preferences, multi-pulse TGFs, and reports the first Terrestrial Electron Beam detected by AGILE.

Paper II performs spectral analysis of TGFs detected by ASIM taking into account all relevant processes from TGF source to satellite. A careful modeling of instrumental effects during the high TGF count rates is included. The study investigates the source properties of the individual TGFs and the intrinsic limitations of spectral analysis of TGFs detected from space.

Paper III revisits the connection between TGFs and lightning discharges using all the available TGF catalogs from RHESSI, Fermi, AGILE and ASIM, and correlates them with ground-based lightning data. The study does not focus on the simultaneity between TGF and individual lightning discharges like previous studies in the literature, but takes a step back and focuses on the TGF in the perspective of the full lightning flash consisting of several discharges over several hundreds of milliseconds. Optical measurements detected by ASIM with high temporal resolution, that originate from the TGF source locations, are also included in the study to give a more detailed temporal view of each flash as observed from space.

## 1.2 Outline

In chapter 2, the reader is given a brief introduction to the physics of atmospheric electricity: thunderclouds, lightning discharges, and high-energy phenomena occurring in the atmosphere. Chapter 3 gives an introduction to lightning detection by radio waves with focus on the WWLLN and GLD360 lightning detection networks. Chapter 4 explores the history and characteristics of TGF detections from space. TGF detection from ground is only briefly mentioned as it is not the focus of this thesis. A brief introduction to production mechanisms, the association to lightning discharges, and spectral analysis of TGFs is also given. Chapter 5 gives a summary of the papers included in this thesis, and chapter 6 summarizes and relates their conclusions to future studies. Finally, all papers are printed in chapter 7.

# Chapter 2

## Atmospheric Electricity

### 2.1 Thunderclouds and Electric Fields

The formation of fair-weather clouds starts with the Sun warming up the ground, and the ground warming up the air in contact with it. As an air parcel gets warmer, it expands and therefore has lower density than its surroundings. The air parcel will then start to rise. As the surrounding pressure decreases with altitude, the air parcel expands further. Due to the expansion of the air parcel, eventual moisture in the air parcel starts condensing, hence forming the microscopic water drops that a cloud consists of. For a thundercloud to form, the updraft of warm air needs to cool slower than the surrounding air. This happens when the updraft is sufficiently moist because the condensation will supply latent heat and therefore sustain a higher temperature. This column of rising moist air is the first stage of a thundercloud. As the temperature decreases with altitude up to the tropopause, and starts to increase after, the tropopause generally marks the upper limit for thunderclouds. The altitude of the tropopause varies from 8 km to 18 km, depending on latitude and season [Rakov and Uman, 2003, p. 68]. In the case of very strong updrafts, cloud-tops can reach altitudes up to 20 km; so-called overshooting tops.

As the temperature decreases with altitude, the water particles in the updraft go through different phases. Water particles start to freeze between 0°C and -40°C, while some remain supercooled up to -40°C. All water particles are frozen below -40°C. Some supercooled particles collide with ice crystals and freeze on impact. These particles are called graupels. When the graupels increase in size, the updraft can not sustain them anymore and they start to fall due to their increased mass.

The graupels are considered the most likely source of charge generation in thunderclouds due to the experiments by *Takahashi* [1978] and *Jayaratne et al.* [1983]. The experiments show that charge and polarity of the graupels are mainly dependent on water content and temperature.

The charge distribution in a thundercloud is often approximated with a simple tripole model as shown in Figure 2.1. The tripole model consists of an upper positive charge layer, a main negative charge layer, and a low positive charge layer. The upper positive and main negative have the same charge magnitude, and the lower positive has a much lower charge magnitude than the upper positive and main negative. Note that occasionally the charge structure can be inverted with the main negative over the main positive. In a real thundercloud the tripole structure is not static and the charge layers are mixed in a complicated manner due to strong winds and updrafts mixing the

particles in the cloud. Although a real thundercloud is much more complicated than the tripole model, the tripole model is generally accepted as a good approximation of the charge distribution in a thundercloud [Williams, 1989].

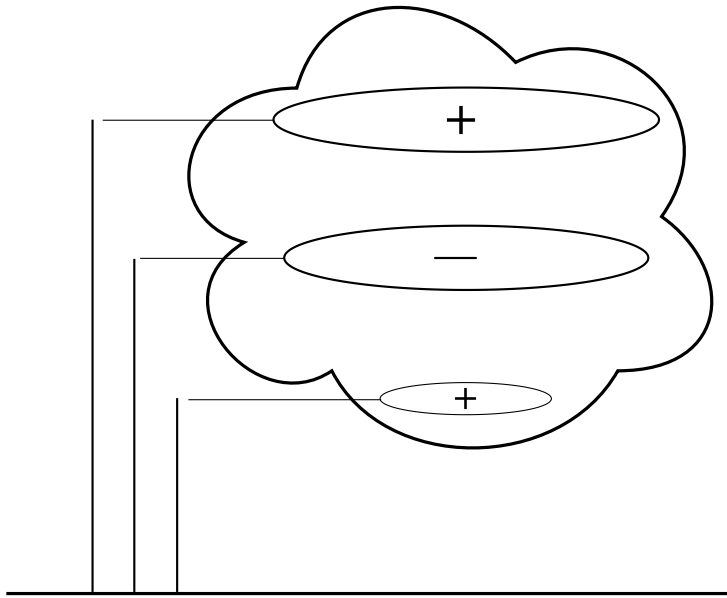


Figure 2.1: The idealized tripole structure of a thundercloud with typical altitudes. The altitudes are from *Rakov and Uman* [2003, p. 69].

## 2.2 Lightning Discharges

Lightning discharges can be divided into four groups: cloud-to-ground (CG), intra-cloud (IC), cloud-to-cloud (CC), and cloud-to-air (CA). Roughly 75% of Earth's lightning is IC lightning [Rakov and Uman, 2003, p. 4]. The remaining lightning discharges are mainly CG, while CC and CA are rare. Case studies of TGFs and lightning discharges have shown that +IC lightning is associated to TGFs detected from space [Stanley *et al.*, 2006; Lu *et al.*, 2010; Shao *et al.*, 2010; Østgaard *et al.*, 2013; Cummer *et al.*, 2015]. The +IC lightning discharge typically develops from the main negative charge layer towards the upper positive charger layer.

### 2.2.1 Electron Avalanche

Essential to understanding all discharges, is the electron avalanche. Imagine an electron in an electric field, where the electric field is strong enough to accelerate the electron to such energies that inelastic collisions between the electron and atoms may ionize the atoms. Then the new electrons also will be accelerated and ionize other atoms. If the number of ionization collisions is larger than the number of electron attachments, we have an electron avalanche. This can be described by

$$n = e^{(\alpha - \eta)z} \quad (2.1)$$

where  $n$  is the number of electrons,  $\alpha$  is the number of ionization collisions per unit length,  $\eta$  is the number of electron attachments per unit length, and  $z$  is the distance along the electric field. Both  $\alpha$  and  $\eta$  varies as a function of the electric field. When  $\alpha = \eta$ , this is called the conventional breakdown field and is typically  $E_k \approx 32 \times 10^5$  V/m at sea level for practical applications [Moss *et al.*, 2006; Cooray, 2015, p. 9]. For larger electric fields than this, the rate of ionization collisions is larger than the rate of electron attachments, leading to an electric breakdown.

We also know that with decreasing air density, a smaller electric field is needed for a breakdown. The electric field,  $E$ , necessary for an electrical breakdown with air density  $\rho$  is given by

$$E = E_0 \frac{\rho}{\rho_0} \quad (2.2)$$

where  $E_0$  is the critical electric field necessary for an electrical breakdown with  $\rho_0$ , which is the density of air at sea level. The density of the Earth's atmosphere can be approximated with

$$\rho = \rho_0 e^{-x/\xi} \quad (2.3)$$

where  $x$  is the altitude in meters,  $\rho_0 \approx 1.225 \text{ kg/m}^3$ , and  $\xi \approx 7.8 \cdot 10^3$  m. Combining equation 2.2 and 2.3 gives

$$E = E_0 e^{-x/\xi} \quad (2.4)$$

which describes how the critical electric field for electrical breakdown scales with altitude  $x$ .

Note that this is not the (relativistic) avalanche mechanism supposed to be at play in TGF production.

### 2.2.2 Streamers and Leaders

We see from equation 2.1 that the number of electrons in an electron avalanche grow with increasing distance if the ambient electric field is larger than  $E_k$ . When the number of electrons increases, at some point the *local* electric field of the electron avalanche will be greater than  $E_k$ . For the region where the local electric field is greater than  $E_k$  the electron avalanche will be self-sustained. The self-sustained electron avalanche is called a streamer. The number of electrons necessary for such an electric field is in the order of  $n \approx 10^8 - 10^9$  and is called the Raether-Meek criterion. If we approximate the streamer as a point charge, we can write the following equation

$$\frac{1}{4\pi\epsilon_0} \frac{ne}{z^2} = E_k \quad (2.5)$$

where  $e$  is the elementary charge,  $\epsilon_0$  is the permittivity of free space,  $n = 10^8$ ,  $E_k = 32 \times 10^5$  V/m, and  $z$  is the distance from the point charge. Solving for  $z$ , we get 200 μm. This distance is the boundary of the streamer's active region. Once initiated, the streamers have been observed to travel in ambient electric fields lower than  $E_k$ . This is due to the streamer propagation being supported by the local electric field of the streamer itself. It is likely that the propagation also is supported by photoionization of

UV photons that are absorbed within the active region of the streamer. If the ambient electric field increases, the number of active streamers increases.

When there is a sufficient number of streamers, this will form the start of the so-called leader channel. A leader is a highly ionized, and therefore highly conductive, channel. This happens when a sufficiently large number of streamer electrons transfer parts of their kinetic energy to the neutral atoms by impact ionization, leaving behind an ion track. In the tip of the leader, there is a strong electric field that will support the production of new streamers that in turn will form a new highly conductive channel. This enables leader self-propagation through air. It is a current flowing through a leader channel that makes the visible part of the lightning flash. The highly conducting leader channel enables charge transfer either between cloud and the ground (CG flash) or between different charge layers in the cloud (IC flash).

The polarity of leaders can be either positive or negative. In the case of a positive leader, the electrons produced ahead of the leader tip move towards the tip because they are attracted by the positive charge. In the case of a negative leader, electrons move ahead because they are repelled by the negative charge in the negative leader tip.

## 2.3 High-Energy Phenomena and Transient Luminous Events

In addition to regular lightning flashes, our atmosphere contains a zoo of other more exotic electric phenomena. The different phenomena, that have been discovered the last few decades, are illustrated in Figure 2.2.

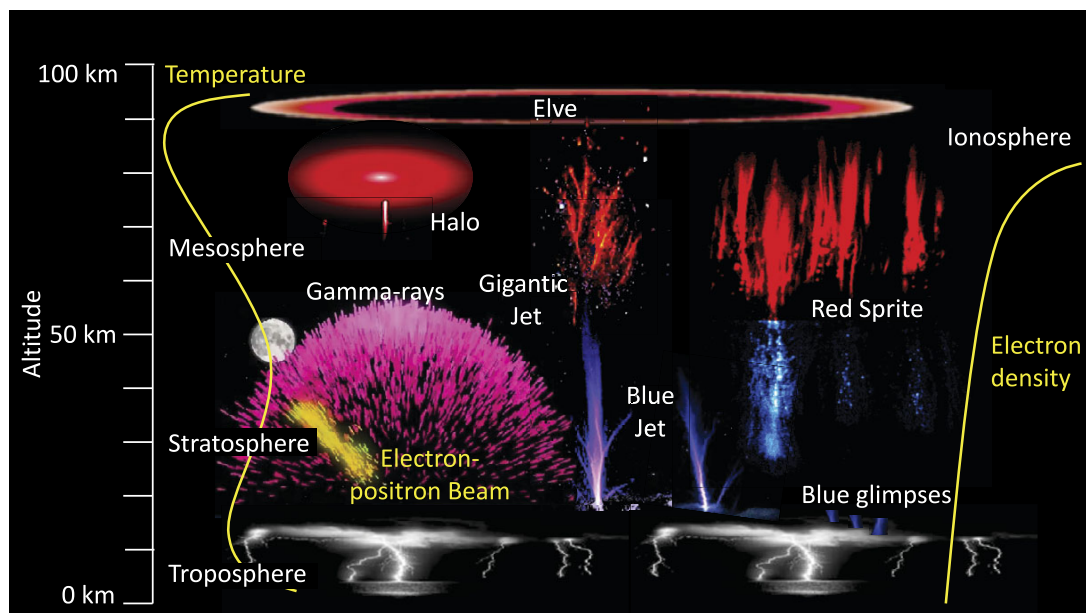


Figure 2.2: An overview over the zoo of atmospheric phenomena powered by thunderstorms. Taken from *Neubert et al.* [2019].

Lightning also emits X-rays, in addition to radio waves and optical light. This was not supported by clear evidence before it was reported by *Moore et al.* [2001]; *Dwyer et al.* [2003, 2004a,b]. Long lasting gamma-ray glows have also been observed in association with thunderstorms. The glows, sometimes called Thunderstorm Ground

Enhancements, can be measured from ground, balloons, and aircraft [McCarthy and Parks, 1985; Eack *et al.*, 1996; Chilingarian *et al.*, 2010; Østgaard *et al.*, 2019a]. TGFs and Terrestrial Electron Beams (TEBs) are also observed in association with lightning discharges. TGFs will be thoroughly discussed in chapter 4, as it is the main research topic of this thesis. TEBs will also be discussed in section 4.1.7.

Besides the high-energy phenomena, there exists another category of electric phenomena in the atmosphere called Transient Luminous Events (TLEs). They are optical emissions (elves, halos) or streamer discharges (sprites, blue jets, gigantic jets) occurring above the thunderclouds and in association with lightning discharges. The subject of TLEs are outside the scope of this thesis and are mentioned for completeness to give an overview over the zoo of atmospheric phenomena occurring above thunderstorms.



# Chapter 3

## Lightning Detection by Radio Waves

Lightning discharges emit electromagnetic waves in a wide range of frequencies. The radio waves emitted by lightning are often referred to as atmospherics, also called sferics. From distant sources, sferics have a frequency content in the VLF range (3 - 30 kHz), but can extend to the LF range (30 - 300 kHz), and above [Rakov and Uman, 2003, p. 432]. Sferics can be observed up to several thousands of kilometers from the lightning because the sferics travel in the Earth's Ionospheric Wave Guide (EIWG), meaning that the sferics are reflected between the Earth's surface and the ionosphere. The reflection of radio waves in the ionosphere is frequency dependent. Sferics that travel along the EIWG are called skywaves, while waves that travel along the surface of the Earth are called groundwaves. Figure 3.1 shows an illustration of the radio waves produced by lightning and their propagation.

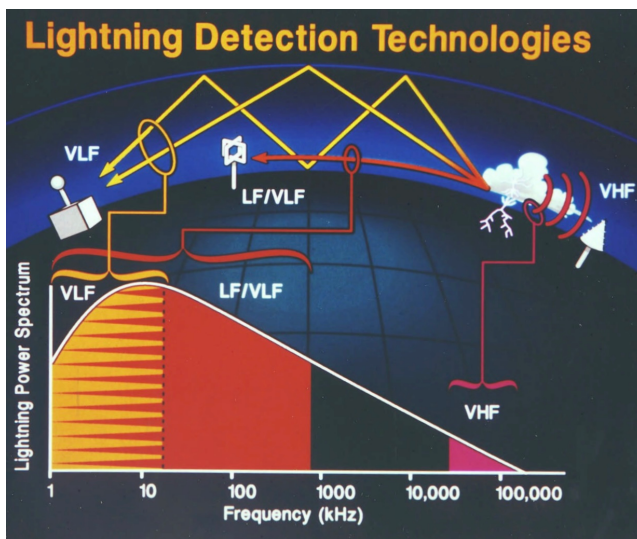


Figure 3.1: Illustration showing the radio waves produced by lightning and how the different radio bands propagate. Adapted from Cummins *et al.* [2000].

The location of the lightning producing sferics can be triangulated based on the difference in time of arrival (TOA) of the wave. Skywaves are dispersed by the propagation in the atmosphere and therefore the TOA of skywaves are very hard to accurately determine at large distances. Groundwaves do not travel long distances but have a sharp wave pulse that can be used to accurately determine the TOA of the wavetrain. A dense

network of ground stations separated by a few hundred kilometers at the most is needed for lightning location by ground waves [Dowden *et al.*, 2002].

As lightning is easily detected in the VLF band up to several thousand kilometers, it is ideal for a lightning location network to work in the VLF band [Dowden *et al.*, 2002]. Such a lightning location network can have a high lightning detection efficiency with much lower density of stations. The issue with triangulating sferics is that the initial sharp wave pulse of the lightning is dispersed in the EIWG. Therefore, the TOA of the wave pulse cannot be determined accurately leading to low timing and location accuracy. Dowden *et al.* [2002] describe a solution to this by using the whole dispersed wavetrain, and measure the rate of change of the phase with respect to frequency to find the time of group arrival (TOGA) down to a few microseconds accuracy.

An additional method to locate lightning discharges is the magnetic direction finding (MDF) method. This is often used together with the TO(G)A techniques described above. The MDF method can be used to locate a vertical current like a return stroke. A return stroke is a near vertical current that forms circular magnetic loops. At any given point the magnetic field is parallel to the circular loops, thus the lightning discharge is along the line perpendicular to the magnetic field and can be triangulated by several stations. Note also that the direction of the magnetic field contains information on the polarity of the lightning discharge. If at least three stations with magnetic field measurements measure a lightning discharge, one can triangulate the position of the discharge and give information about the polarity.

There are several lightning detection networks. In the following we focus on the two networks used for the studies presented in this thesis: WWLLN and GLD360.

### 3.1 WWLLN

The World Wide Lightning Location Network (WWLLN) is a global VLF lightning detection network that detects lightning sferics and locates the discharges producing the sferics. The network uses the TOGA technique described in Dowden *et al.* [2002] and expanded from 18 stations in 2004 to 70 stations in 2013 [Mallick *et al.*, 2014].

The WWLLN detection efficiency varies with the density of ground-stations, and the effect that orography and ionospheric conditions have on the EIWG. The dependency of ground-stations is shown clearly in Figure 3.2, which shows the relative detection efficiency of WWLLN for a particular date [Hutchins *et al.*, 2012]. The United States, with many ground-stations, has a good relative detection efficiency, while for example Africa has a very poor detection efficiency with a few ground-stations surrounding the entire continent. The detection efficiency of WWLLN also heavily depends on the peak current of the lightning discharge itself. By comparing WWLLN with the National Lightning Detection Network (NLDN) in the United States, Abarca *et al.* [2010] reported a detected efficiency for CG flashes from 3.88% in 2006-2007 to 10.30% in 2008-2009. Rudlosky and Shea [2013], comparing WWLLN with the Tropical Rainfall Measuring Mission Lightning Imaging Sensor (TRMM-LIS), reported steadily increasing detection efficiency in the United States from 6% in 2009 to 9.2% in 2012. Bürgesser [2017], comparing WWLLN with LIS, estimated a WWLLN detection efficiency between 1% and 10% for continental regions, and 20% for oceanic regions worldwide.

The mean global location accuracy of WWLLN is estimated to be below 5 km, but

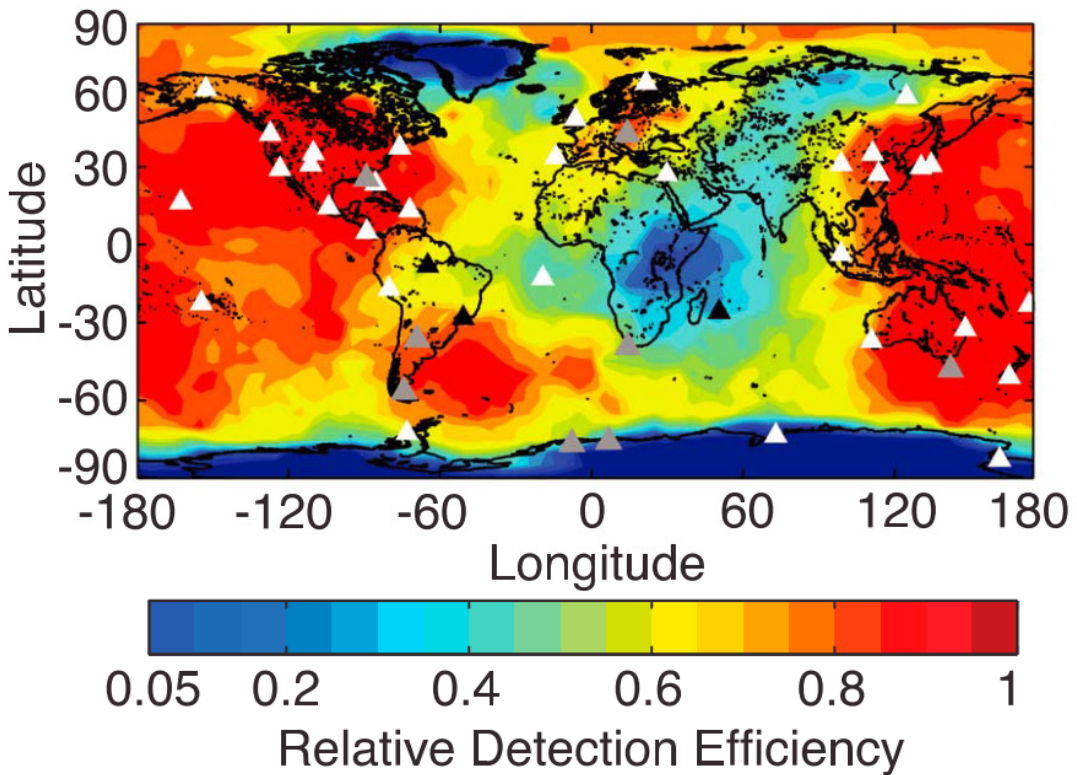


Figure 3.2: Relative detection efficiency for WWLLN on 16. June 2010. Operational WWLLN stations are shown as white triangles, non-operational stations are in black, and partly active stations in grey. The figure is from *Hutchins et al.* [2012], Fig. 12 a).

can be up to  $\sim 30$  km [*Rodger et al.*, 2005; *Abarca et al.*, 2010]. However, *Jacobson et al.* [2006] found a location accuracy of  $\sim 15$  km, and *Fan et al.* [2018] estimated a location accuracy of  $\sim 10$  km over the Tibetan Plateau. The timestamps of the WWLLN detections are given with microsecond resolution.

## 3.2 GLD360

The global lightning data set, GLD360, is operated by Vaisala and is sensitive between 500 Hz and 50 kHz, which is mainly in the VLF range. It is a long range lightning detection network that makes use of TOA and MDF techniques. After a software upgrade in 2015 the median location accuracy was  $\sim 2$  km, and the 90th percentile was  $\sim 6$  km for the United States. The detection efficiency of CG lightning strokes, relative to NLDN, is about 75%. The timestamps of the GLD360 detections are given with nanosecond resolution. GLD360 is well described in *Said et al.* [2010, 2013]; *Said and Murphy* [2016].



# Chapter 4

## Terrestrial Gamma-ray Flashes

In the early 1920s, Nobel laureate C. T. R. Wilson studied the electrical field of thunderclouds. In two papers, *Wilson* [1925a,b] described several keypoints relevant to the production of energetic electrons and gamma-rays in thunderstorms. From experiments with the cloud chamber, Wilson found that the friction force acting on electrons decreases with the kinetic energy of the electron. He noted that if a strong electric field was present and further accelerated the electron, the kinetic energy of the electron would further increase, leading to the friction force decreasing even more. Thus, the electric field could accelerate the electron close to the speed of light. This is the description of the runaway electron that is one of the cornerstones for understanding the production of TGFs. The runaway electron is further described in Section 4.3.1.

Wilson also pointed out that as the density of the atmosphere decreases with altitude, the electrical breakdown threshold will decrease. Therefore, there would be a point above the thundercloud where electrical breakdown can occur. This was a prediction for the phenomena we now call “red sprites” [*Williams*, 2010].

In *Wilson* [1925b], Wilson writes that at high altitudes the magnetic force becomes more important for electrons, and that the electrons will tend to travel mainly along the direction of the Earth’s magnetic field lines. This is the basic principle for Terrestrial Electron Beams (TEBs) that will be further discussed in Section 4.1.7.

The high energy runaway electron, discovered by Wilson, can collide with air molecules and produce other electrons that will be accelerated in the electric field to high energies, creating more electron avalanches. These electrons will also produce high-energy photons by bremsstrahlung when colliding with air molecules. Wilson wrote in *Wilson* [1925a]:

*“It would be of interest to test by direct experiment whether a thundercloud does emit any measurable amount of extremely penetrating radiation of  $\beta$ - or  $\gamma$ -ray type.”*

There were several attempts to measure energetic radiation from thunderclouds and the results were mixed [*Parks et al.*, 1981; *Suszczynsky et al.*, 1996; *Williams*, 2010]. It took almost 66 years from Wilson’s prediction to the discovery of TGFs.

## 4.1 Observations of TGFs

### 4.1.1 BATSE

In 1991, over half a century after Wilson took interest in radiation produced in thunderclouds, the Burst and Transient Source Experiment (BATSE), onboard the Compton Gamma Ray Observatory (CGRO), observed the first TGF [Fishman *et al.*, 1994]. Fishman *et al.* [1994] reported 12 “intense gamma-ray flashes of atmospheric origin” and made the connection between these gamma-ray flashes and thunderstorm systems below BATSE at the time of the detection. These 12 TGFs are shown in Figure 4.1.

BATSE was designed to detect celestial gamma-ray bursts (GRBs) but also detected a total of 78 TGFs in its lifetime between 1991 and 2000. It consisted of eight sets of scintillators, sensitive to photons with energies between 20 keV and 2 MeV, located at every corner of CGRO [Grefenstette *et al.*, 2008]. The relative intensity between the scintillators could be used to estimate the incoming direction of the photon beam. For the 12 TGFs in Fishman *et al.* [1994], this was used to conclude that the gamma-ray flashes observed had atmospheric origin. The trigger window of BATSE was 64 ms. We now know that TGFs have a median duration of less than 100  $\mu$ s, and therefore only the most intense TGFs were detected by BATSE due to the 64 ms trigger window. Fishman *et al.* [1994] pointed this out saying that it is likely that many weak events are not detected due to the relatively large trigger window.

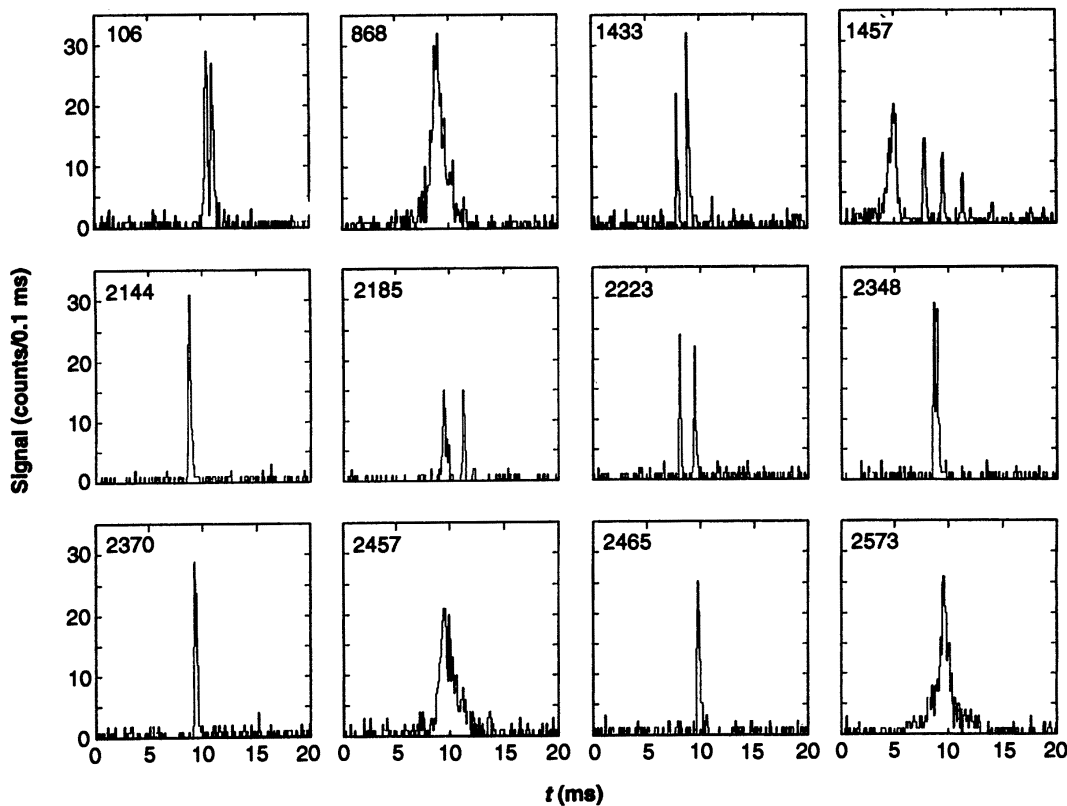


Figure 4.1: Example of 12 TGFs detected by BATSE. The bin size is 0.1 ms and the time is arbitrary. The figure is taken from Fishman *et al.* [1994].

### 4.1.2 RHESSI

The next instrument to detect TGFs was the Reuven Ramaty High Energy Solar Spectroscopic Imager (RHESSI) that detected over 3000 TGFs while in operation between 2002 and 2018 [Smith *et al.*, 2005, 2020]. Four TGFs detected by RHESSI are shown in Figure 4.2. RHESSI was originally dedicated to solar physics and consisted of an array of nine germanium detectors with an energy range between 3 keV and 17 MeV. Counts with energy larger than 17 MeV were measured in an overflow channel [Smith *et al.*, 2002]. Although RHESSI was designed to observe the Sun, it was much better suited for TGF detection than BATSE. This was due to a larger energy range and that RHESSI continuously collected data, while BATSE had a trigger system. This means that a trigger algorithm did not affect the TGF detection efficiency of RHESSI. The search for TGFs can be performed on ground on all available data [Grefenstette *et al.*, 2009; Gjesteland *et al.*, 2012; Albrechtsen *et al.*, 2019].

Dwyer and Smith [2005] confined the source altitude of TGFs to between 15 and 21 km based on comparisons of Monte Carlo simulations and the cumulative observed energy spectrum of RHESSI TGFs. This was an important result because TGFs were believed to be produced at much higher altitudes prior to this study.

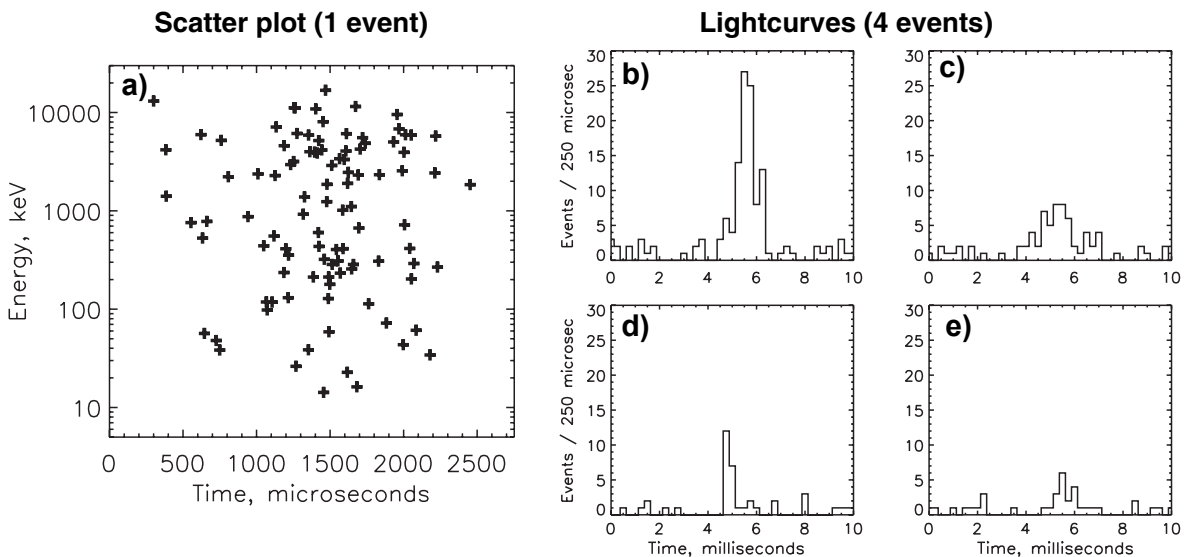


Figure 4.2: Example of RHESSI detected TGFs reported in Smith *et al.* [2005]. a) The energy versus time scatter plot for the brightest TGF. b) Lightcurve for the brightest TGF. c) Lightcurve for the longest TGF. d) Lightcurve for the shortest TGF. e) Lightcurve for the faintest TGF.

### 4.1.3 Fermi

The Fermi Gamma-ray Space Telescope (Fermi) is a NASA mission and was launched in 2008 and consists of the Large Area Telescope (LAT) and the Gamma-Ray Burst Monitor (GBM). The GBM has 12 thallium-doped sodium iodide (NaI:Tl) detectors with an energy range 8-1000 keV, and two Bismuth-Germanium Oxide (BGO) detectors with an energy range 0.2-40 MeV [Meegan *et al.*, 2009]. The two BGO detectors are the main instruments for TGF detection. The minimum trigger window of Fermi is 16 ms,

compared to the 64 ms of BATSE. Fermi-GBM is a good example on how the TGF detection rate is affected by the trigger algorithms for the spacecraft. This is shown in Figure 4.3, where the monthly TGF detection rate is shown as a function of time for different data acquisition modes. The initial trigger algorithm had a TGF detection rate of 10 TGFs per year. In November 2009, an updated trigger algorithm improved this to 95 TGFs per year. Between July 2010 and November 2012 continuous data, so-called time-tagged event (TTE), were downloaded when Fermi passed active thunderstorm regions. This increased the TGF detection rate, allowing for studying fainter TGFs. After November 2012, Fermi-GBM was operated in continuous data collection mode downloading all TTE data for each full orbit. The yellow color in Figure 4.3 shows the TGFs triggered by the onboard trigger algorithm. Only the brightest TGFs would have been downloaded if only triggered data were downloaded to ground. This would have biased the Fermi TGF sample to bright TGFs like those detected by BATSE. As a continuous data acquisition mode was implemented for Fermi, the TGF detection rate is only affected by the sensitivity of the GBM instrument itself and by the TGF identification method.

The first Fermi-GBM TGF catalog consists of 4144 TGFs detected between 2008 and 2016 [Roberts *et al.*, 2018]. Fermi is still operational at the time of writing.

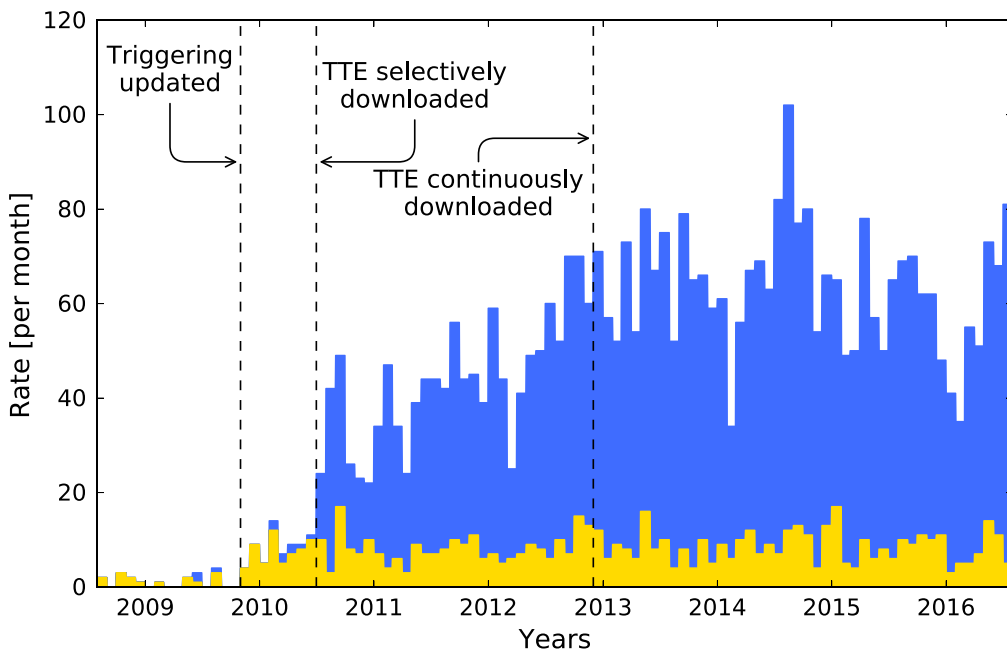


Figure 4.3: TGF detection rate for Fermi-GBM for different telemetry modes. The figure is taken from Roberts *et al.* [2018].

#### 4.1.4 AGILE

The Astrorivelatore Gamma a Immagini Leggero (AGILE) is a small satellite of the Italian Space Agency (ASI) launched in 2007 with the main purpose of observing celestial gamma-ray sources [Tavani *et al.*, 2009]. AGILE consists of several instruments, but the main TGF detecting instrument is the Mini-Calorimeter (MCAL), which is the main instrument used in Paper I. MCAL can be operated in two modes: the GRID

mode where MCAL is part of the other instrument onboard AGILE, and the BURST mode where MCAL operates as an independent instrument. Both modes are active at the same time, but it is the BURST mode that is relevant for TGF detection. MCAL consists of 30 CsI(Tl) scintillator bars placed on two orthogonal layers, where each bar acts as an independent detector. In BURST mode the dead time of each individual bar is  $\sim 20\ \mu\text{s}$ . The energy range of MCAL is 300 keV to 100 MeV and the absolute timing accuracy is  $\sim 2\ \mu\text{s}$  [Labanti *et al.*, 2009]. The trigger windows vary from 8 seconds down to 293  $\mu\text{s}$ , where the shorter trigger windows (293  $\mu\text{s}$ , 1 ms, and 16 ms) are those relevant for TGF detection [Marisaldi *et al.*, 2014]. In March 2015, the AGILE TGF detection rate increased one order of magnitude after the anti-coincidence shield acting on MCAL was disabled on purpose [Marisaldi *et al.*, 2015]. In June 2015, an issue with the onboard GPS caused a degradation of the AGILE microsecond timing performance, leading to a timing accuracy of several tens of milliseconds [Lindanger *et al.*, 2020]. In January 2018, the GPS issue was resolved, restoring the microsecond timing accuracy of AGILE. AGILE is still operational at the time of writing.

Figure 4.4 shows an example of four TGFs detected by MCAL where the second row shows a multi-pulse TGF.

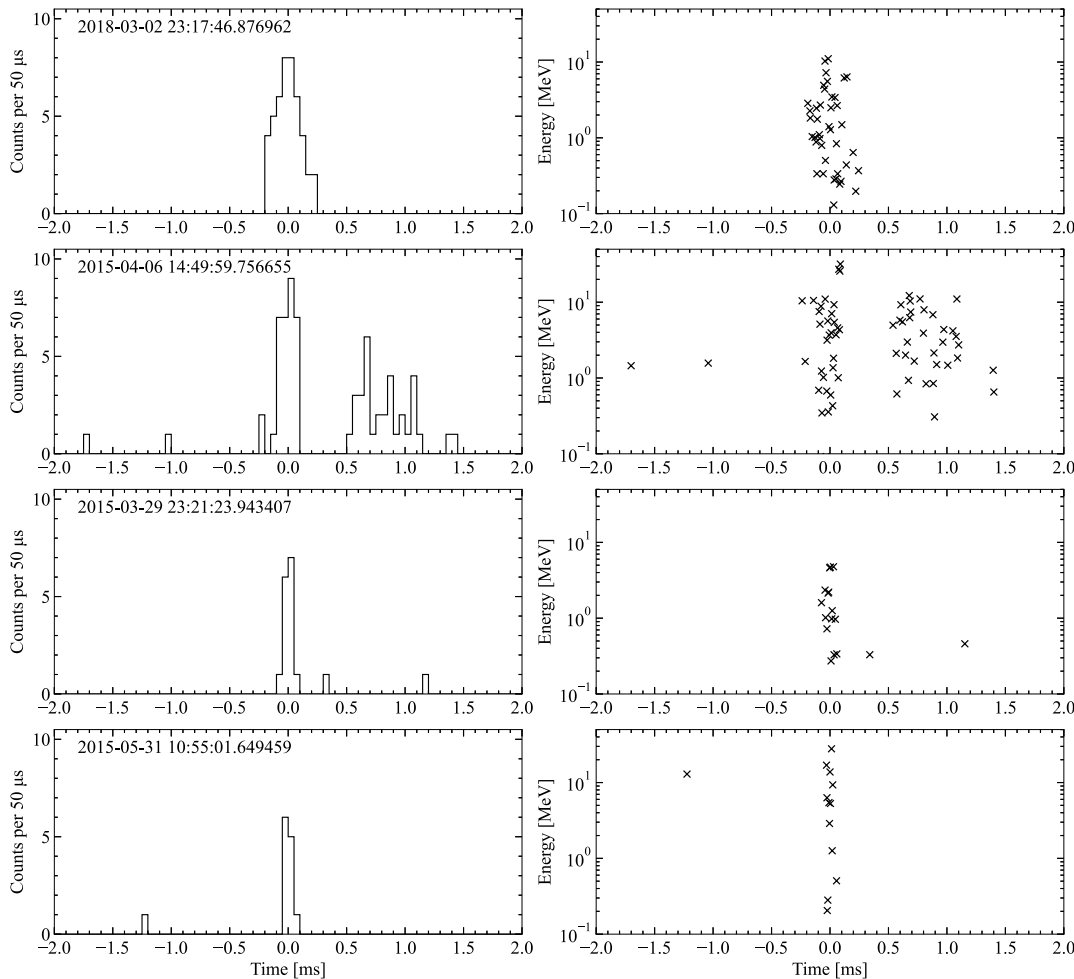


Figure 4.4: Light curves and energy versus time scatter plot for 4 TGFs detected by AGILE. The TGFs are published in the 3rd AGILE TGF catalog [Lindanger *et al.*, 2020; Maiorana *et al.*, 2020].

#### 4.1.5 ASIM

The Atmosphere-Space Interactions Monitor (ASIM) was launched in April 2018 and mounted on the Columbus Module aboard the International Space Station (ISS) [Neubert *et al.*, 2019]. ASIM is the first space mission specifically designed to observe Transient Luminous Events (TLEs) and TGFs. The payload consists of two scientific instruments: the Modular X- and Gamma-ray Sensor (MXGS) [Østgaard *et al.*, 2019b], and the Modular Multi-Spectral Imaging Array (MMIA) [Chanrion *et al.*, 2019]. This makes ASIM capable of observing both gamma and optical wavelengths. MXGS detects TGFs and MMIA detects optical signals associated with lightning and TLEs.

The MMIA instrument consists of two cameras and three photometers. The cameras are sensitive in the 337.0 nm (bandwidth of 5 nm) and 777.4 nm (bandwidth of 3 nm) bands, and provide 12 images per second. The photometers are sensitive in the 337.0 nm (bandwidth of 4 nm), 180-240 nm (UV), and 777.4 nm (bandwidth of 5 nm) bands. The photometers have a 100 kHz sampling rate. The 777 nm emission is weakly absorbed in the atmosphere and is due to the emission from atomic oxygen in hot lightning channels. The UV signal is strongly absorbed in the atmosphere and is therefore mostly detected in association with high altitude phenomena such as Elves and other TLEs. The 337 nm is more absorbed in the atmosphere than 777 nm, and is mostly detected in association to lightning but can also include some signal from TLEs, as it is close to the UV band. Further details on the MMIA instrument can be found in Chanrion *et al.* [2019].

MXGS consists of two detectors: the High Energy Detector (HED) and the Low Energy Detector (LED). HED is sensitive to photons with energies from  $\sim$ 300 keV to  $>30$  MeV and is made up of 12 BGO scintillators, each connected to a photomultiplier tube (PMT). The time resolution of HED is 27.8 ns and each BGO-PMT detector has a dead-time of  $\sim$ 550 ns. The energy resolution of HED is  $<20\%$  at 511 keV [Østgaard *et al.*, 2019b]. After high energy counts in HED, there is a voltage drop in the PMT dynode chain that can last up to  $\sim$ 30  $\mu$ s for counts above 30 MeV, and  $\sim$ 0  $\mu$ s for counts less than 400 keV meaning that there is no voltage drop. As the high voltage is not constant over the dynode chain, the gain varies, and therefore the channel to keV energy calibrations is not valid during the voltage drop because the pulse-heights of the following counts are measured incorrectly. Note that this is for counts following the previous energetic count that causes the voltage drop. The voltage drop has been extensively studied also with experimental activity because its proper handling is crucial for an accurate spectral analysis. The proposed approach to account for it is a crucial part of Paper II, Lindanger *et al.* [2021]. We account for the voltage drop by the implementation of an energy dependent “safety time” criterion that is the time the high voltage in the dynode chain needs for recovering to a level where the energy measurement is within 20% accuracy. Counts that do not meet this criterion cannot be used for spectral analysis because their measured energy is incorrect. These counts are still physical counts and can be used for fluence calculations and light curves. The safety time criterion are discussed in more detail in Appendix A in Lindanger *et al.* [2021].

LED is sensitive to photons with energies from 20 to 400 keV and consists of 16 384 pixels made of Cadmium-Zinc-Telluride (CZT). A coded mask is placed in front of the detector making LED capable of imaging the incident TGFs by means of the coded mask imaging technique, widely used in high-energy astrophysics for imaging

of celestial sources. The time resolution of LED is  $\sim 1 \mu\text{s}$ . The LED detection plane is divided into 16 independent readout chains, and each chain is served by 8 Application Specific Integrated Circuits (ASIC) with a dead-time of  $1.4 \mu\text{s}$ . If two hits occur in different ASICs in the same chain within  $1.4 \mu\text{s}$ , the energy of the two hits will be mixed but the hits will be distinguishable. The energy resolution of LED is  $< 10\%$  at 60 keV [Østgaard *et al.*, 2019b].

Due to a non-optimal timing interface between ASIM and ISS, the absolute timing accuracy of ASIM varies stochastically between  $\sim 0$  and  $\sim 30$  ms. This can be seen in Figure 4.5 where stacking analysis of the closest in time sferic relative to TGF time, shows that most sferic matches are within 0 and  $\sim 32$  ms with a peak at 17 ms. Note also the outliers at about  $-20$  and  $-7$  ms, and that the distribution has a tail extending to about 70 ms significant above 3 standard deviations above background level. The absolute timing of ASIM can be corrected down to a few milliseconds by aligning several MMIA-detected optical pulses with ground detected sferics [Heumesser *et al.*, 2021; Maiorana *et al.*, 2021; Østgaard *et al.*, 2021].

Figure 4.6 shows four TGF events detected by ASIM, where two of the events are multi-pulse TGFs. Because of its large effective area and fast electronics specifically tailored to high-flux events, ASIM detects more counts per TGF compared to RHESSI, Fermi-GRB and AGILE. Note the periodicity and striking similarity between TGF number 1457 detected by BATSE (Figure 4.1), and the TGF detected by ASIM at 22. October 2018 (Figure 4.6). As ASIM does not have instrumental effects on millisecond level, this ASIM detection shows experimentally that the periodicity in the TGF detection by BATSE cannot be due to instrumental effects, but a real feature.

A key finding with the ASIM instrument is the observation of an Elve associated with a TGF [Neubert *et al.*, 2020]. Elves are ultraviolet and optical emissions excited in the lower ionosphere by strong electromagnetic pulses.

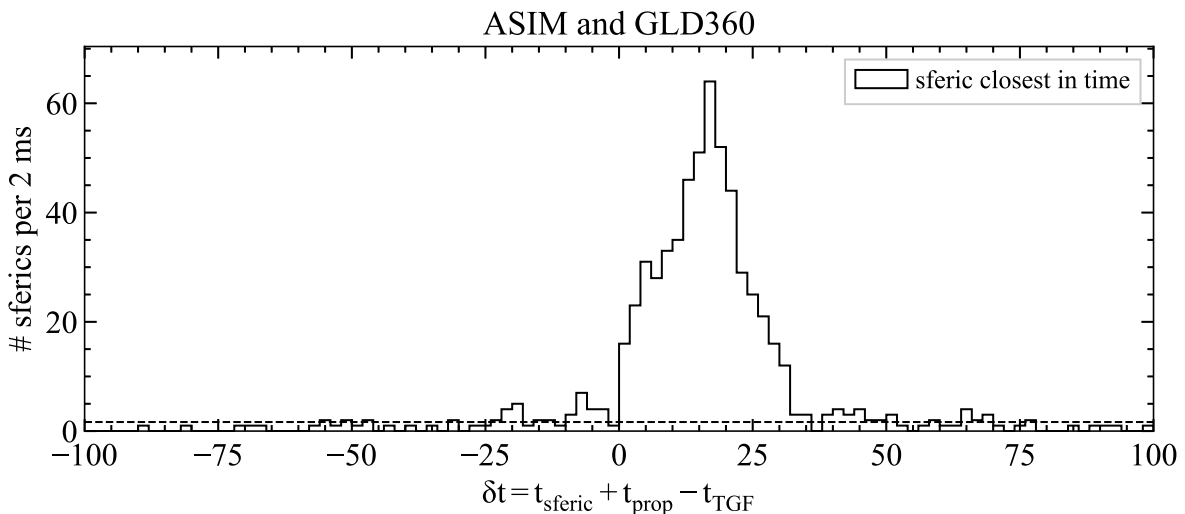


Figure 4.5: Stacking analysis of the sferic closest in time to TGFs detected by ASIM. The dashed line is  $3\sigma$  above background ( $-200, -50$  ms).

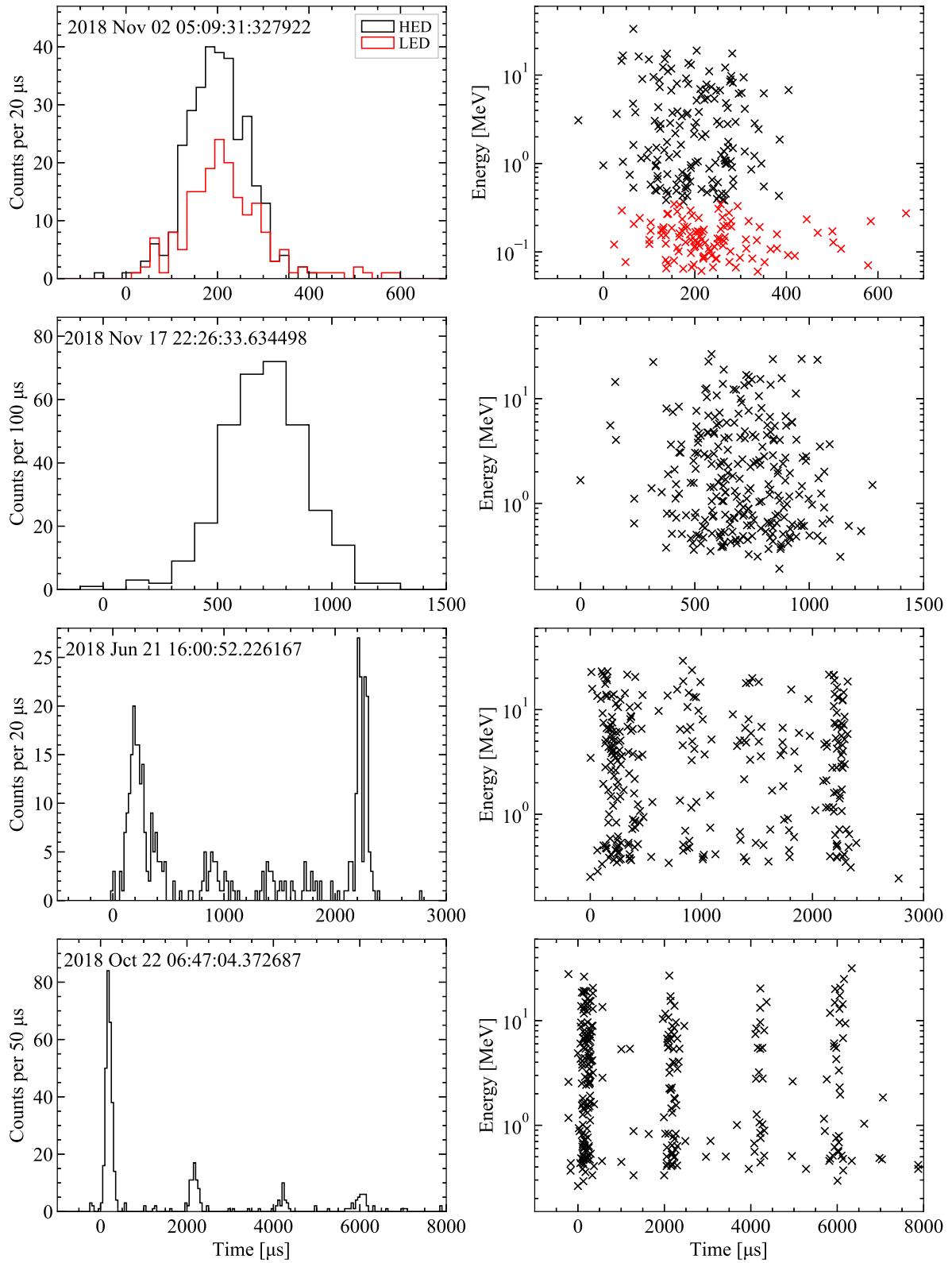


Figure 4.6: Example of two single-pulse TGFs, and two multi-pulse TGFs detected by ASIM. Counts from the High Energy Detector (HED) are shown in black color and counts from the Low Energy Detector (LED) are shown in red color.

### Cosmic Gamma-Ray Burst Detection with ASIM

The first detection of TGFs happened by chance. BATSE, originally designed to observe GRBs, was also able to detect bright and long duration TGFs. Conversely, ASIM, which is designed to detect very short duration and high intensity TGFs, is also able to trigger on GRBs but only triggers on short and relatively high flux GRBs. This is because the trigger algorithm of ASIM is designed to trigger on short bursts like TGFs. ASIM's fast electronics is designed to collect data from TGFs, which have in general much higher fluxes than GRBs. Hence, when ASIM first triggers on a GRB, the fast detectors and electronics will not be saturated (as other GRB-dedicated instruments) when detecting the longer duration and lower intensity of GRBs. That is, when ASIM is detecting GRBs the MXGS instrument suffers very little instrumental effects, making it an excellent GRB detector. On 15. April 2020, ASIM triggered on a short GRB named GRB 200415, which was detected by several spacecraft and resulted in several Nature publications [Castro-Tirado *et al.*, 2021; *The Fermi-LAT Collaboration*, 2021; Roberts *et al.*, 2021; Svinkin *et al.*, 2021]. What was initially thought to be a GRB turned out in fact to be a giant flare from a magnetar in the NGC253 galaxy, roughly 11 million light years away. A magnetar is a neutron star with extremely strong magnetic fields. The light curve of the magnetar giant flare is shown in Figure 4.7, including a magnified view showing the fine time structure of the main burst phase. As ASIM was not saturated during the main burst, we were able to identify very high frequencies in the first 3.2 ms of the burst, which gives crucial information about the processes in these first milliseconds [Castro-Tirado *et al.*, 2021]. The ASIM-team played a leading role in the study with our expertise on the ASIM instrument, spectral analysis, and timing analysis.

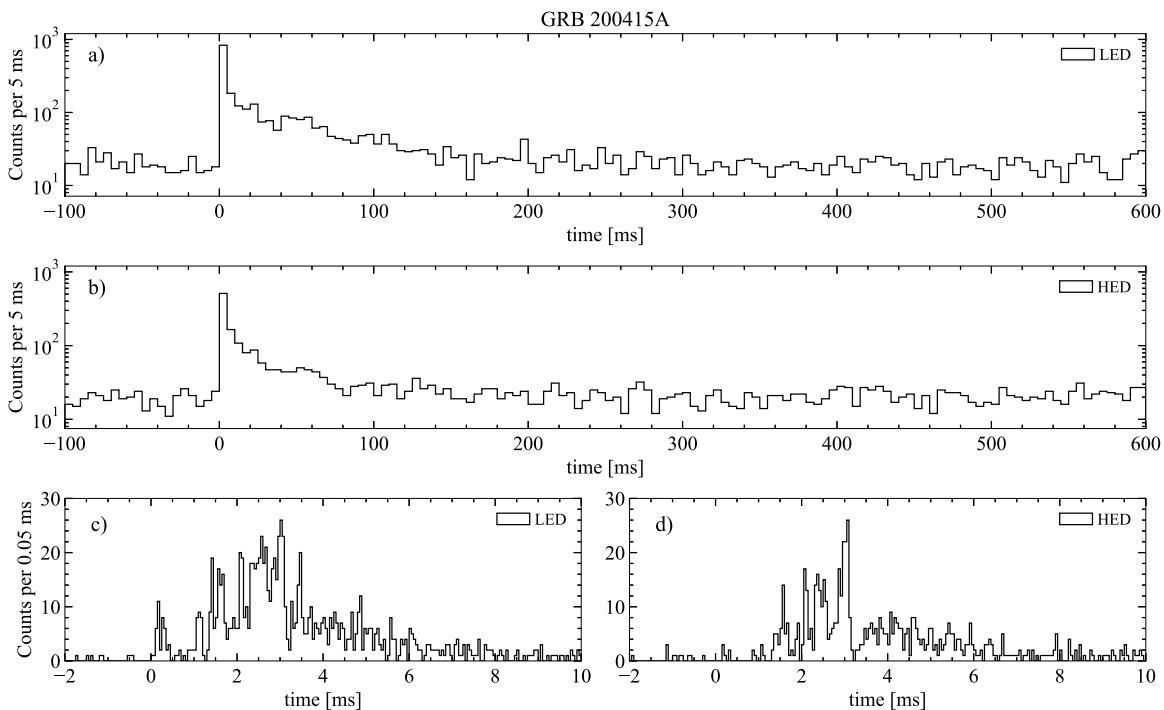


Figure 4.7: a) and b) show the light curve of the magnetar giant flare as detected by LED (50 - 400 keV) and HED (300 keV - 40 MeV) with data binned to 5 ms. c) and d) shows a magnification of the first 10 ms with the data binned to 50  $\mu$ s.

In the spectral analysis of GRB 200415 the safety time procedure, developed for TGF detection in Paper II, was applied to the measurements. The procedure removed just 53 counts out of total 2141 counts above 400 keV in HED, showing that HED did not experience significant instrumental effects during the detection of the giant flare. Time-resolved spectroscopy is shown in Figure 4.8 showing rapid spectral variability during the magnetar giant flare. Given the high flux of this event, all other instruments that observed the gamma-rays experienced strong instrumental effects and saturation, and ASIM was the only mission to fully characterize the main peak of emission.

At the time of writing, ASIM has detected three GRBs that have been notified to the astrophysics community through the Gamma-ray Coordinates Network (<https://gcn.gsfc.nasa.gov>).

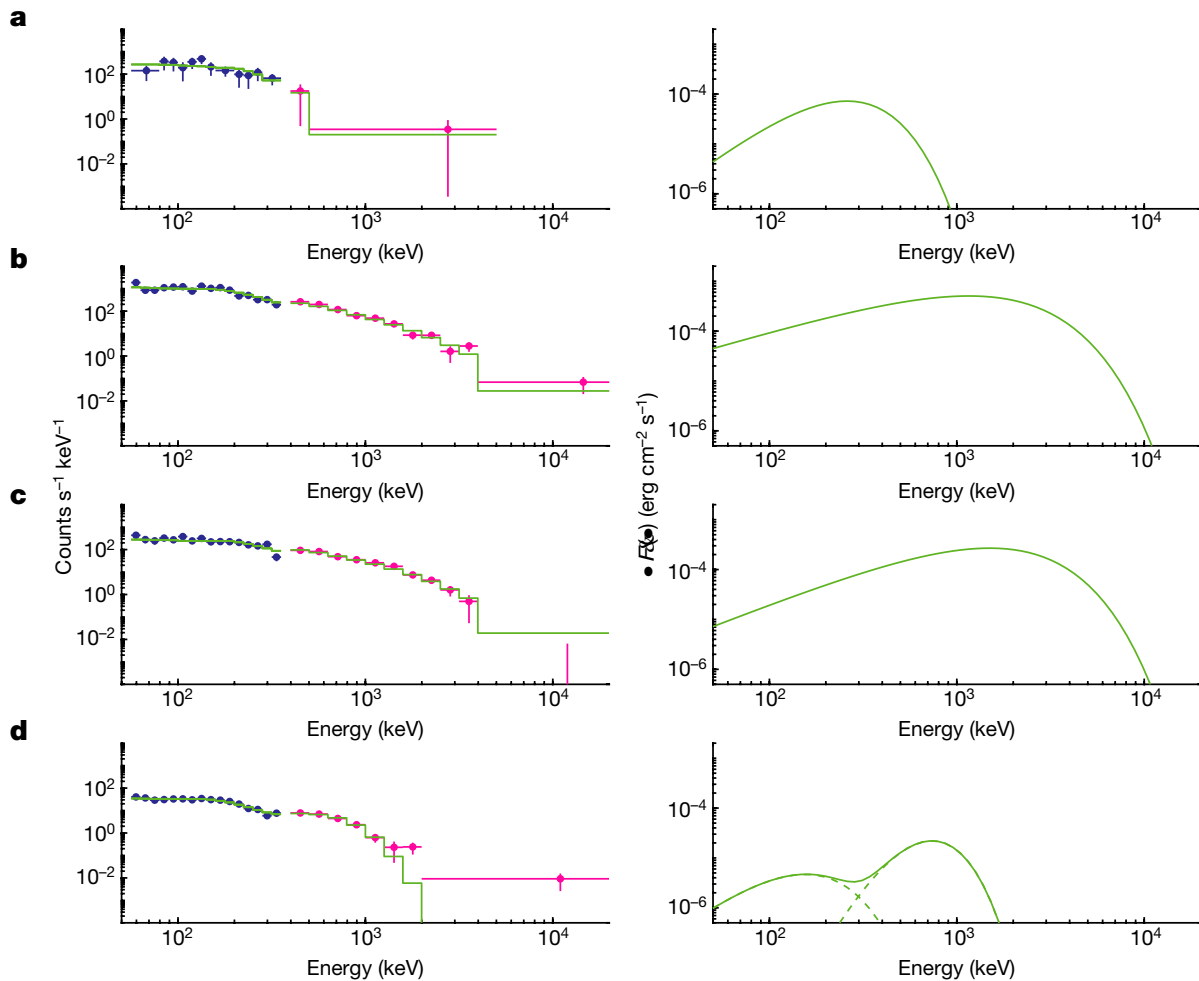


Figure 4.8: Time-resolved spectroscopy for the four time intervals during the magnetar giant flare. a) Precursor: 0.0 - 0.8 ms, b) Peak: 0.8 - 3.2 ms, c) Decay: 3.2 - 8 ms, d) Tail: 8-160 ms. The counts spectra are shown to the left, and the energy flux densities are shown to the right. Blue color is LED, red color is HED, and the green color is the best-fit model. The figure is taken from *Castro-Tirado et al. [2021]*.

#### 4.1.6 Overview of the Main Space Missions Observing TGFs

An overview over the missions is given in Table 4.1.

Table 4.1: Overview over instrumental characteristics of the main TGF-detecting missions.

Mission	Instrument	Year	Orbital Inclination [°]	Detector type	Energy range	Triggered
CGRO	BATSE	1991-2000	28.5	NaI(Tl)	20 keV - 2 MeV	Yes
RHESSI	-	2002-2018	38	HP Ge	25 keV - 17 MeV	No
Fermi	GBM	2008-	25.6	BGO	150 keV - 30 MeV	Yes*
				NaI(Tl)	8 keV - 1 MeV	Yes
AGILE	MCAL	2007-	2.5	CsI(Tl)	300 keV - 100 MeV	Yes
ASIM	MXGS	2018-	51.6	BGO	300 keV - 30 MeV	Yes
				CZT	50 keV - 400 keV	

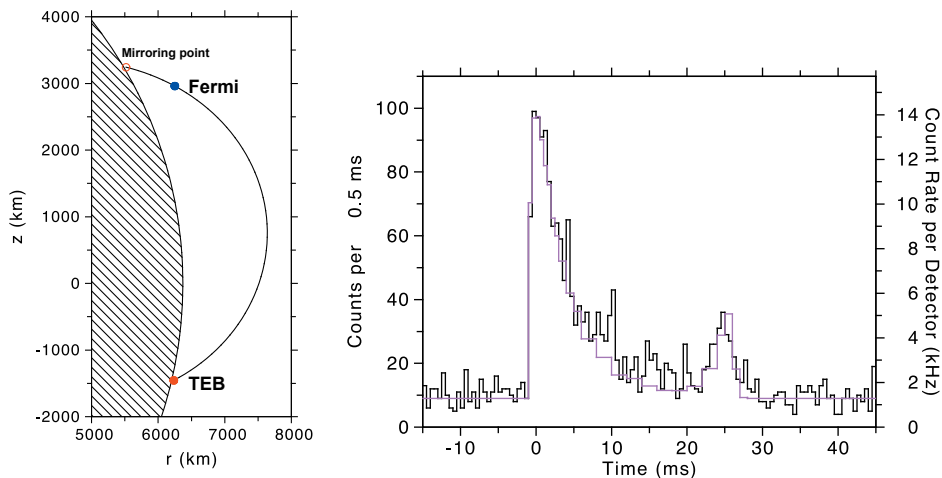
\* Changed to continuous mode in 2012.

#### 4.1.7 Terrestrial Electron Beams

The high energy photons of the TGF will interact with the atmosphere when the photons are propagating upward. These primary photons will produce secondary electrons and positrons through Compton scattering and pair production. A fraction of the secondary electrons and positrons produced above 30-40 km can reach altitudes above  $\sim$ 120 km, where they will stop interacting significantly with the atmosphere [Sarria *et al.*, 2015]. These electrons and positrons will then be guided by the geomagnetic field line, forming a Terrestrial Electron Beam (TEB). When the TEB reaches the footpoint of the geomagnetic field line, the electrons are absorbed in the atmosphere or magnetically mirrored and reflected back along the field line. TEBs were first described by Dwyer *et al.* [2008].

Figure 4.9, right panel, shows a TEB detected by Fermi-GBM [Briggs *et al.*, 2011]. The left panel illustrates the geomagnetic field line at Fermi's location, the TEB/TGF production location south for Fermi, and the mirroring point north for Fermi. The light curve shows the TEB at 0 ms and the mirrored electrons of the TEB at about 25 ms. The magenta histogram shows a Monte Carlo simulation of the TEB.

TGF-detecting spacecraft such as BATSE, RHESSI, Fermi, AGILE, BeppoSAX, and ASIM, also detects TEBs [Dwyer *et al.*, 2008; Ursi *et al.*, 2017; Roberts *et al.*, 2018; Sarria *et al.*, 2019; Lindanger *et al.*, 2020; Smith *et al.*, 2020].

Figure 4.9: A TEB detected by Fermi-GBM. Adapted from Briggs *et al.* [2011].

#### 4.1.8 Other TGF detections from Space, Aircraft and Ground

TGFs have also been detected by other space missions. BeppoSAX was a satellite designed to detect GRBs but it also detected 12 TGF candidates [Ursi *et al.*, 2017]. The RELEC space experiment on the Vernov satellite reported five TGF candidates including a TGF detected over Antarctica [Bogomolov *et al.*, 2017]. Zhao *et al.* [2020] also reported TGFs detected by the Gamma-ray Bursts Polarimeter (POLAR) onboard the Chinese space laboratory Tiangong-2.

TGFs have been detected by aircraft. The ADELE mission was an array of gamma-ray detectors onboard an airplane flying over thunderstorms in Florida in 2009. Out of 1213 lightning discharges, only one TGF was detected. This reduced the possibility that every lightning is associated with a TGF [Smith *et al.*, 2011a,b]. The ADELE mission also flew in 2015 and detected an upward TGF from behind, meaning that what they detected was the bremsstrahlung from the reverse positron beam created by the upward relativistic runaway electron avalanche (RREA) [Bowers *et al.*, 2018]. RREA is explained in section 4.3.2.

TGFs have also been detected from ground [Dwyer *et al.*, 2004b, 2012a; Hare *et al.*, 2016; Bowers *et al.*, 2017; Enoto *et al.*, 2017; Wada *et al.*, 2019; Belz *et al.*, 2020; Smith *et al.*, 2021]. These TGFs are interpreted as originated by downward directed RREA, opposite to the upward directed RREA producing the TGFs detected from space.

## 4.2 TGF Characteristics as Observed from Space

TGF characteristics have been established over several years by combining information from mainly BATSE, RHESSI, Fermi, AGILE, and ASIM. It is crucial to understand that the TGF characteristics are dependent on the instrument observing them, and the methods used to identify them in the satellite data. A clear example of this is the typical duration of TGFs. As BATSE's shortest trigger window was 64 ms, it biased the TGF detection towards long duration TGFs. BATSE single pulse TGFs had a typical duration of  $\sim 1$  ms. In the RHESSI, Fermi, and AGILE era, TGFs were reported to have a typical duration of about 100  $\mu$ s. In Østgaard *et al.* [2019c] the  $T_{50}$  duration distribution of the first ten months of ASIM observations peaks between 20 and 40  $\mu$ s. It is evident that statistical studies on TGF duration are biased by the trigger window (if the instrument is triggered), TGF search criteria, energy range, dead time, and other instrumental effects. It is also not straightforward to compare TGF duration from different instruments, as their respective teams have used different definitions and methods to estimate TGF duration.

Figure 4.10 shows global distributions of longitude, local time, duration, and number of counts for TGFs detected by AGILE. The distributions are in agreement with other missions when detections are limited to the same latitude band as AGILE. The local time and longitude distributions match the general behaviour of lightning activity.

The maximum energy of the photons produced by a TGF is reported to be  $>20$ , 38, 43, and  $>24$  MeV, according to RHESSI [Smith *et al.*, 2005], Fermi [Briggs *et al.*, 2010], AGILE [Marisaldi *et al.*, 2010], and ASIM [Lindanger *et al.*, 2021], respectively. Energies up to 100 MeV were reported by AGILE [Tavani *et al.*, 2011]. These energies are incompatible with the acknowledged production processes of TGFs, and were later

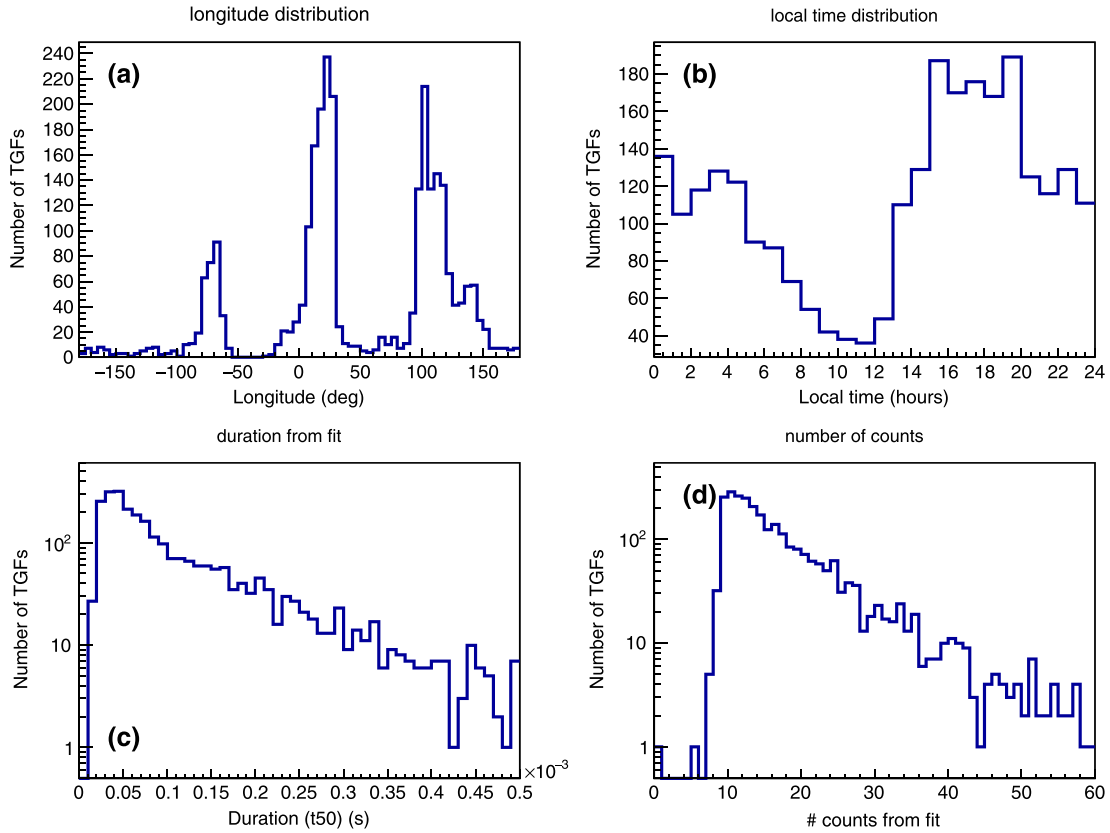


Figure 4.10: Distributions of TGFs from the 3rd AGILE catalog. a) Longitude, b) local time, c) duration ( $T_{50}$ ), and d) count distribution of the sample. Taken from *Maiorana et al.* [2020].

explained as probably caused by instrumental effects due to events with short duration and high flux [*Marisaldi et al.*, 2019].

Fluence distribution of TGFs detected by RHESSI, Fermi and AGILE can be fitted with a power law with index  $\lambda$  between  $-2.2$  and  $-2.4$  [*Østgaard et al.*, 2012; *Tierney et al.*, 2013; *Marisaldi et al.*, 2014]. The index is remarkably consistent between the instruments. As is the case with energy and duration estimates of TGFs, the fluence estimates are affected by instrumental effects and it is impossible to state the shape of the distribution outside the sensitivity range of each instrument.

A key question, still not answered, is: what is the true fraction of TGFs associated with lightning? *Albrechtsen et al.* [2019] investigated observationally weak TGFs in the RHESSI data compared with WWLLN and found that there could be approximately six times more TGFs in the RHESSI data that could not be identified individually as they are too faint. *Smith et al.* [2020] also investigated TGFs in the RHESSI data and found that the RHESSI detectors often are paralysed when detecting TGFs. Only a few counts are detected during the rising phase of the TGF before the detector is paralysed. The rest of the counts are detected in the Compton tail. This may mean that a significant portion of the high fluence TGFs are detected as low fluence TGFs or not recognized as TGFs at all.

The energy spectrum of TGFs at source is in general agreement with standard RREA photon spectrum that can be expressed with the analytical function  $1/E \cdot \exp(-E/(7.3 \text{ MeV}))$  [*Celestin and Pasko*, 2012; *Sarria et al.*, 2015; *Abbasi*

*et al.*, 2018]. This is the photon energy spectrum at source and it needs to be propagated through the atmosphere to be compared to satellite measurements. Spectral analysis of TGF spectra put an upper limit of TGF production altitude to  $\sim$ 20 km [Dwyer and Smith, 2005; Carlson *et al.*, 2007; Gjesteland *et al.*, 2010]. Performing spectral analysis of TGFs is a trade-off between enough count statistics and averaging spectral diversity. Mailyan *et al.* [2016, 2019] presented a Fermi-GBM sample of individual TGF spectra and suggest there is a significant spectral diversity among the TGF sources. Lindanger *et al.* [2021], using TGFs detected by ASIM, suggest the same.

The production altitude of TGFs was originally believed to be high in the atmosphere, typically above 40 km and up to 90 km [e.g. Nemiroff *et al.*, 1997]. This was due to the high intensity of TGFs and it was believed that it was unlikely that TGFs were produced deep in the atmosphere due to the large atmospheric absorption below 40 km. Later, spectral analysis showed production altitudes consistent with altitudes between 9 and 20 km [Dwyer and Smith, 2005; Carlson *et al.*, 2007; Hazelton *et al.*, 2009; Gjesteland *et al.*, 2010; Mailyan *et al.*, 2016, 2019; Lindanger *et al.*, 2021]. In addition to spectral analysis, low frequency radio measurements associated to TGFs, also detected from space, have provided independent estimates of production altitudes between  $\sim$ 10 and  $\sim$ 15 km [Cummer *et al.*, 2014; Pu *et al.*, 2019]. One should keep in mind that as most TGFs are detected from space, their typical production altitude will be biased towards higher altitudes due to the atmospheric absorption.

The beam morphology of TGFs at source is unknown and has been modeled as either a cone or a Gaussian beaming profile with different beaming widths. Appendix B in Lindanger *et al.* [2021] shows a comparison between cone and Gaussian beaming after the widening of the beam following scattering in the atmosphere. A cone with half angle between  $30^\circ$  and  $45^\circ$  [Gjesteland *et al.*, 2011; Mailyan *et al.*, 2016] or Gaussian beaming with  $\sigma_\theta$  between  $10^\circ$  and  $40^\circ$  [Hazelton *et al.*, 2009; Lindanger *et al.*, 2021] is consistent with TGFs detected from space.

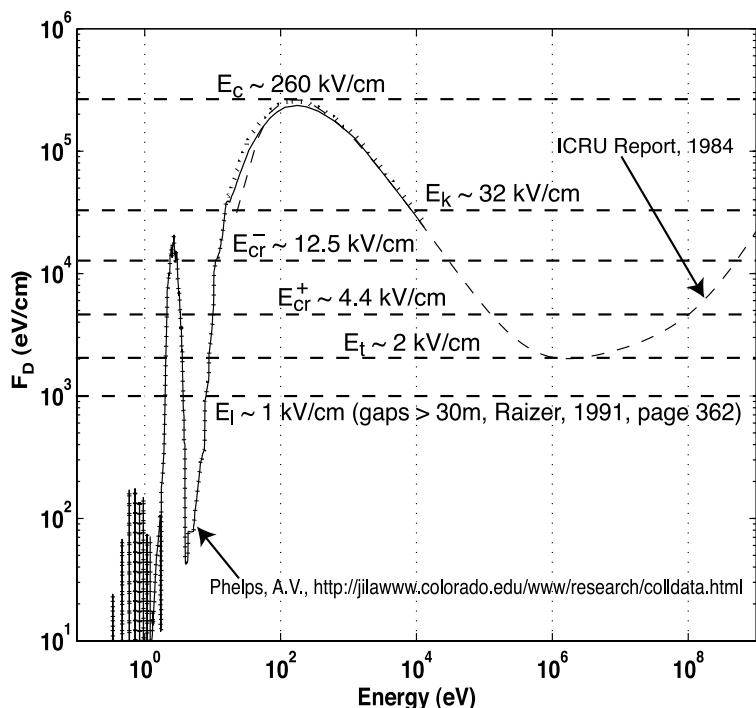
TGFs usually appear as a short pulse of gamma radiation where the light curve can be fitted with a Gaussian or log-normal function with a fast rise-time and a tail made of lower energy photons from Compton scattering [Grefenstette *et al.*, 2008; Østgaard *et al.*, 2008]. TGFs can also consist of several pulses, so-called multi-pulse, as shown for some of the TGFs in Figure 4.1, 4.4, and 4.6, or in Fishman *et al.* [1994]; Foley *et al.* [2014]; Østgaard *et al.* [2019c]; Maiorana *et al.* [2020]; Mailyan *et al.* [2021]. It has also been found that if a multi-pulse TGF has an associated sferic match, the sferic is usually associated with the last gamma-ray pulse [Mezentsev *et al.*, 2016; Lindanger *et al.*, 2020; Mailyan *et al.*, 2021]. Note that while Mezentsev *et al.* [2016]; Lindanger *et al.* [2020] only found multi-pulse TGFs with a sferic associated to the last pulse, Mailyan *et al.* [2021], using a larger sample of multi-pulse TGF, found counterexamples.

## 4.3 Production Mechanisms of TGFs

TGFs are produced when free electrons are accelerated by strong electric fields to relativistic energies and produce photons by bremsstrahlung. The accelerating electron was first described by *Wilson* [1925a] and termed “runaway electron”. This section will briefly discuss the runaway electron and the two leading processes explaining the mechanism of TGF production.

### 4.3.1 Runaway Electrons

Wilson discovered that the friction force acting on an electron in air decreases with the kinetic energy of the electron. An updated understanding of the friction force acting on an electron in air is shown in Figure 4.11. If the force from the electric field is larger than the friction force, the electron gains energy. The maximum friction force an electron can experience in air is when the energy of the electron is  $\sim 100$  eV. If the electric field is larger than  $E_c \sim 260$  kV/cm, electrons with all kinetic energies will become runaway electrons.



Thermal Runaway:	$E_c \sim 260$ kV/cm	Positive Streamer:	$E_{cr}^+ \sim 4.4$ kV/cm
Conventional:	$E_k \sim 32$ kV/cm	Relativistic Runaway:	$E_t \sim 2$ kV/cm
Negative Streamer:	$E_{cr}^- \sim 12.5$ kV/cm	Leader:	$E_l \sim 1$ kV/cm

Figure 4.11: The dynamic friction force for electrons in air at sea-level density and pressure. Taken from *Moss et al.* [2006].

### 4.3.2 Relativistic Runaway Electron Avalanches

When runaway electrons are accelerated to relativistic energies and these electrons produce new free electrons by elastic scattering with electrons initially bound in air molecules (Møller scattering) that again are accelerated to relativistic energies, we have a relativistic runaway electron avalanche (RREA) [Gurevich *et al.*, 1992]. Dwyer [2003]; Babich *et al.* [2004]; Lehtinen and Østgaard [2018] found that the minimum electric field required to sustain a RREA is  $E_{RREA} = 2.8 \text{ kV/cm}$  at sea level. This is larger than the relativistic runaway threshold  $E_t$  in Figure 4.11, as they took into consideration the misalignment between the initial momentum of the scattered electron and the electric field. It is an important point that the value of  $E_{RREA}$  is within the range of the maximum electric field measured in real thunderstorms [Rakov and Uman, 2003, p. 83]. However, the problem arises to where electrons that already have an energy of  $\sim 1 \text{ MeV}$ , that can cause a RREA, originate (the so-called “seed” electrons). One option is energetic electrons from cosmic-ray showers, or radioactive decay from radon. Another option is that somewhere in the thundercloud, for a brief moment of time, there exists an electric field large enough to accelerate electrons in that area to energies larger than 1 MeV. These electrons will then create RREAs that can be sustained by the much lower  $E_{RREA}$  electric field.

For TGF production, the number of electrons at source was estimated by Dwyer and Smith [2005] to be about  $10^{17}$  based on TGF measurements from space. Dwyer [2008] realized that RREA multiplication alone could not explain the number of electrons at source because this was estimated to be a maximum of about  $10^5$  electrons. The two following subsections will explore two mechanisms that can explain the missing  $10^{12}$  factor at source.

### 4.3.3 Relativistic Feedback Mechanism

One scenario that can produce the “missing”  $10^{12}$  multiplication factor in the number of electrons at source, is the relativistic feedback mechanism [Dwyer, 2003, 2007, 2012]. In this scenario one assumes there exists an energetic seed electron above a few MeV. This seed electron can for example be produced by cosmic rays. The energetic seed electron will runaway [Wilson, 1925a] and create a RREA [Gurevich *et al.*, 1992]. This process will produce photons by bremsstrahlung which in turn will also produce additional photons, electrons and positrons by Compton scattering and pair production. The positrons will travel in the opposite direction of the electrons in the electric field and can produce new energetic electrons through elastic scattering, creating new RREAs. Backscattered photons can also produce new electrons through pair production which will also create new RREAs if the ambient electric field is large enough. Figure 4.12 and Figure 4.13 left side, show an illustration of this process. This multiplication of RREAs, named the relativistic feedback mechanism, can account for up to  $\sim 10^{13}$  electron multiplication factor, providing a model in agreement with experimental results. The relativistic feedback mechanism is a breakdown process leading to an exponential increase in electron fluxes until the enhanced conductivity causes the ambient electric field to quench.

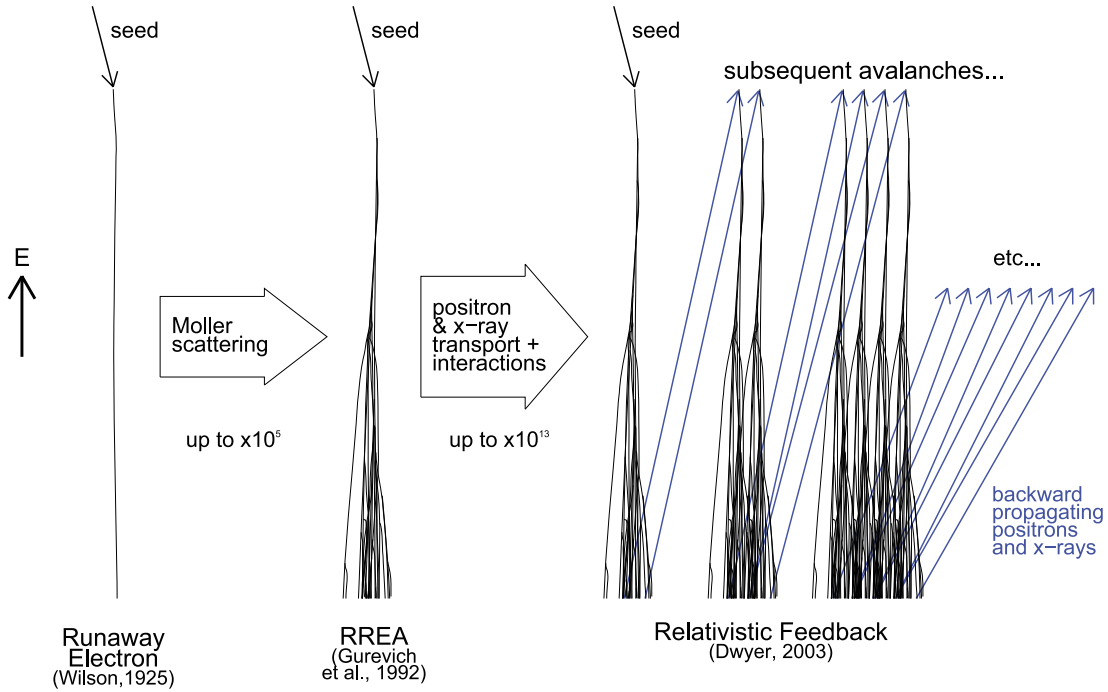


Figure 4.12: Illustration of the relativistic feedback model. Taken from Dwyer *et al.* [2012b].

#### 4.3.4 Thermal Runaway Mechanism

The thermal runaway mechanism [Celestin and Pasko, 2011; Xu *et al.*, 2012; Köhn and Ebert, 2015; Köhn *et al.*, 2017, 2020] can also provide the “missing”  $10^{12}$  multiplication factor of electrons. Instead of starting with one seed electron, the model starts with a negative streamer where thermal electrons are accelerated up to  $\sim 100$  keV (with a peak probability energy of  $\sim 60$  keV) in the very strong electric field in front of the streamer tip [Celestin and Pasko, 2011]. These electrons runaway in the strong electric field in front of the leader tip and create RREAs [Moss *et al.*, 2006; Celestin and Pasko, 2011]. This mechanism is able to generate  $\sim 10^{17}$  electrons at source, consistent with TGF production. Note that the thermal runaway mechanism does not exclude the relativistic feedback model, or opposite. The thermal runaway mechanism can provide the seed electrons for the relativistic feedback mechanism, and in the thermal runaway mechanism, backpropagation of positrons and photons can also start new RREAs if the surrounding electric field and kinetic energy of the new electrons is large enough. Figure 4.13 shows an illustrated comparison between the two mechanisms. The thermal runaway mechanism is sometimes also referred to as the streamer-leader mechanism. The thermal runaway mechanism puts the production of TGFs in the context of a propagating leader, whereas the relativistic feedback model is independent of a propagating leader.

## 4.4 Lightning Discharges and TGFs

As discussed in chapter 3, lightning discharges produce radio sferics. A lightning flash consists of several discharges where each discharge produces a radio signal, and the flash typically lasts several hundred milliseconds. The connection between lightning

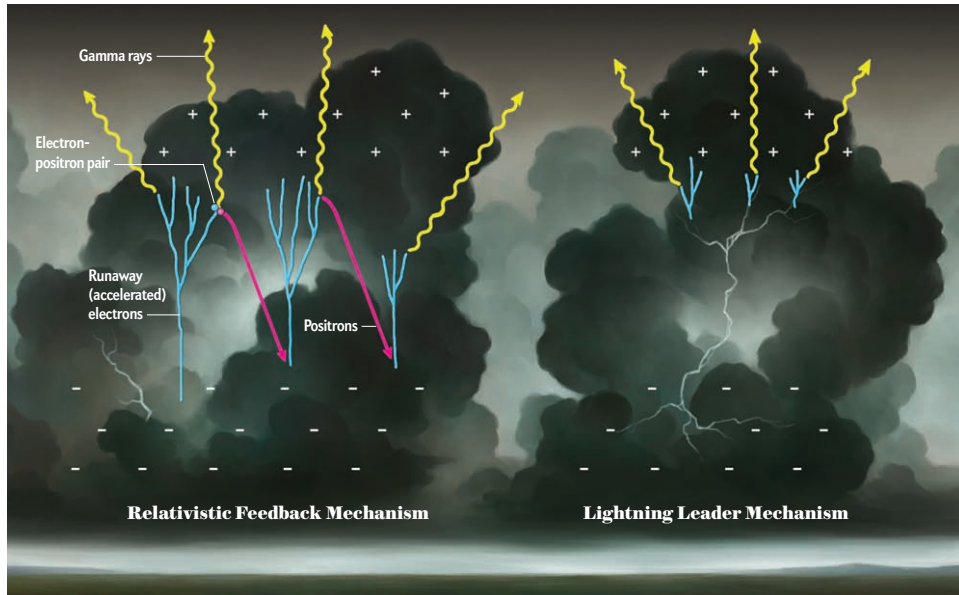


Figure 4.13: A comparison between the relativistic feedback- (left) and the streamer-leader (right) mechanisms of TGF production. Taken from *Dwyer and Smith [2012]*.

discharges and TGFs was pointed out already by *Fishman et al. [1994]* that noted that TGFs detected by BATSE were detected over thunderstorm regions. Later case studies established that TGFs can be observed in association with upward moving positive Intra-Cloud (IC+) lightning. The TGFs are typically produced in the initial phase of the lightning flash during the upward propagation of leaders [*Stanley et al., 2006; Lu et al., 2010; Shao et al., 2010; Østgaard et al., 2013; Cummer et al., 2015*]. The simultaneity of TGFs and lightning discharges was investigated by *Cummer et al. [2005]* and *Stanley et al. [2006]*, using RHESSI and sferics data, and was narrowed down to a few milliseconds. The absolute timing accuracy of RHESSI was believed to be a few milliseconds at the time, so a simultaneity between TGFs and sferics could not be ruled out. *Connaughton et al. [2010]*, using Fermi-GBM that have an absolute timing accuracy of a few microseconds, narrowed that simultaneity between TGFs and sferics down to a few tens of microseconds. This strict association has been confirmed by AGILE [*Marisaldi et al., 2015; Lindanger et al., 2020*], and the RHESSI data could be corrected down to  $\sim 100 \mu\text{s}$  absolute timing accuracy using timing corrections found by assuming simultaneity between TGFs and sferics [*Mezentsev et al., 2016*]. *Connaughton et al. [2013]* showed that the probability of having a TGF-WWLLN association increased with shorter TGF duration. This was expected from the modeling results from *Dwyer and Cummer [2013]*, and also confirmed with AGILE and WWLLN data in *Lindanger et al. [2020]*. *Smith et al. [2016]*, working with RHESSI data, found three types of sferic associations to TGFs; simultaneous association, few milliseconds after, and sferics produced few hundreds of milliseconds after the TGF. The last category was further investigated in *Lindanger et al. [2022]* (Paper III).

*Cummer et al. [2015]* and *Pu et al. [2019]* showed, for a sample of Fermi TGFs, that TGFs are simultaneous with a “slow” LF radio waveform pulse. The slow pulse has the same timescale as the duration of the associated TGF and could be a signature of the TGF itself. LF radio measurements can also provide an independent estimate of the production altitude of TGFs, by using the time delay of ionospheric reflections.

These measurements have estimated a TGF production altitude between 8 and 15 km [Lu *et al.*, 2010; Shao *et al.*, 2010; Cummer *et al.*, 2014; Pu *et al.*, 2019].

Case studies show that the TGF takes place during the upward propagation of a lightning leader, and the leader continues to propagate after the TGF. This likely places the TGF in the beginning of the lightning flash. As the previous research was based on case studies, Lindanger *et al.* [2022] investigated the TGF-flash relationship, using over 5000 TGFs with lightning data, from the TGF catalogs of RHESSI, Fermi, AGILE, and ASIM, and established that the TGF occurred in the beginning of the lightning flash. This was also supported by optical data from the MMIA instrument, part of ASIM.

## 4.5 Spectral Analysis of Terrestrial Gamma-ray Flashes

Spectral analysis of TGFs can be performed to estimate the source properties, such as production altitude, beaming width, and eventual tilting. The analysis should take into account the photon transport through the atmosphere between the source and the satellite, the energy response of the instrument, and the instrumental effects the instrument will suffer during the very high count rates of the TGF detection. One of the challenges of spectral analysis of TGFs is the limited count statistics. This was solved by Dwyer and Smith [2005] by combining the counts from several TGFs. Østgaard *et al.* [2008]; Hazelton *et al.* [2009] realized that the energy spectrum of individual TGFs also depends on the radial distance between the TGF and the satellite, where distant TGFs were much softer than TGFs closer to the subsatellite point. Hazelton *et al.* [2009] therefore grouped the cumulative energy spectra in those close to, and far away from, the satellite.

Insufficient modeling of the detector by not taking into account all instrumental effects, will affect the conclusions of the analysis. This is evident in Østgaard *et al.* [2008] that estimated TGF production altitudes up to 40 km, or in Tavani *et al.* [2011] that found a TGF spectrum up to 100 MeV, not in agreement with standard RREA production. When these works were revisited with an improved understanding of the instruments, Gjesteland *et al.* [2010] estimated TGF production altitudes below 26 km, and Marisaldi *et al.* [2019] showed that AGILE observations are compatible with the RREA model and the 100 MeV photons were likely due to energy pile-up effects in the detector during the high count rates.

Cumulative energy spectra of TGFs smear out individual spectral characteristics and do not properly take into account the radial distance between the subsatellite point and the TGF location. Mailyan *et al.* [2016, 2019] performed individual spectral analysis of TGFs detected by Fermi-GBM and found spectral diversity and production altitudes between 11 and 20 km, where the lower altitudes more frequently gave a better fit to the measured spectrum. For most of the TGFs, they could not distinguish between narrow- and wide-beam models. Lindanger *et al.* [2021] performed spectral analysis of 17 TGFs detected by ASIM that had larger count statistics per TGF than Fermi-GBM. In agreement with Mailyan *et al.* [2016, 2019], the 17 TGFs showed spectral diversity. Both Mailyan *et al.* [2016, 2019] and Lindanger *et al.* [2021] highlight the importance of a careful statistical analysis using maximum likelihood methods instead of  $\chi^2$  statistics.  $\chi^2$  statistics are unreliable for small count statistics, as the result depends on the selected energy binning. Lindanger *et al.* [2021] also highlighted that not only

the best fit model, but all accepted models, according to the maximum likelihood tests, should be considered when confining source properties of TGFs. The conclusions of *Lindanger et al.* [2021] are summarized in section 5.2 and the complete paper is found in the Paper II section.

# Chapter 5

## Summary of Papers

### 5.1 Summary of Paper I

The first paper, *Lindanger et al.* [2020], presents the 3rd AGILE TGF catalog together with its companion paper *Maiorana et al.* [2020]. The first paper developed a search for clusters (SFC) analysis identifying TGFs detected by AGILE-MCAL by comparing MCAL gamma-ray data with WWLLN data. There were several periods in the MCAL data sorted by TGF detection efficiency and absolute timing accuracy; AC-ON period with no TGF-WWLLN matches as the anti-coincidence shield suppressed TGF detection in MCAL, REF period where the anti-coincidence shield was disabled enhancing TGF sensitivity for MCAL and the instrument had  $\sim 2 \mu\text{s}$  absolute timing accuracy, DRIFT period where the absolute timing accuracy was several tens of milliseconds due to a GPS malfunctioning, and the 3D-FIX period where the absolute timing accuracy was restored to  $\sim 2 \mu\text{s}$ . An overview over the periods is shown in Table 1 in Paper I. A total of nine years of data was processed. The REF period was the starting point for *Maiorana et al.* [2020] that developed an algorithm identifying TGFs without considering ground-based lightning data from WWLLN. Paper I identified 282 TGFs with a WWLLN match in the REF and 3D-FIX period. In the DRIFT period, 1294 TGF candidates were identified. However, this data set was estimated to have at least 33% contamination due to the low absolute timing accuracy. After the DRIFT period, the AGILE onboard clock was restored to an absolute timing accuracy of  $2 \mu\text{s}$ . Here the SFC analysis continued identifying TGF-WWLLN matches providing a useful independent diagnostics tool to validate the AGILE timing accuracy. It was shown with TGF-WWLLN matches that AGILE in the 3D-FIX period had a constant time offset of 4 ms which is now accounted for in the AGILE data processing pipeline.

The geographical distribution of the TGF-WWLLN matches sample, identified in Paper I, follows the global lightning distribution and is consistent with TGFs detected by RHESSI and Fermi. The sample has a preference for coastal regions, as in the case with RHESSI and Fermi TGFs [*Roberts et al.*, 2018; *Albrechtsen et al.*, 2019], meaning that TGFs do not follow the land, coast, ocean distribution of lightning detected by WWLLN, but occur relatively more often close to the coastline. The sample also provides the first independent confirmation of *Connaughton et al.* [2013] that brief duration TGFs have a higher probability of having an associated WWLLN detection. Seven multi-pulse TGFs were identified in the sample and the WWLLN match is always associated with the last gamma-ray pulse, in agreement with RHESSI TGFs [*Mezentsev et al.*, 2016].

In the sample, the first TEB detected by AGILE was identified, although the detection of TEBs is difficult for AGILE given the screening material surrounding the detector [Sarria *et al.*, 2017].

The SFC analysis is applied to the AGILE-WWLLN data every few months, identifying more TGF-WWLLN matches and validating the AGILE absolute timing accuracy. AGILE is still operational with 2  $\mu$ s absolute timing accuracy at the time of writing. The 3rd AGILE TGF catalog is available at <https://www.ssdc.asi.it/mcal3tgfcat/> and an update including 517 TGF-WWLLN matches (October 2018 to October 2020) has been added after the publication of Paper I. An additional 171 TGFs (November 2020 to July 2021) are identified and will be published on the website at a later stage when more TGFs are detected by MCAL. Figure 5.1 shows the cumulative number of WWLLN-associated AGILE TGFs from the start of the 3D-FIX period up to July 2021.

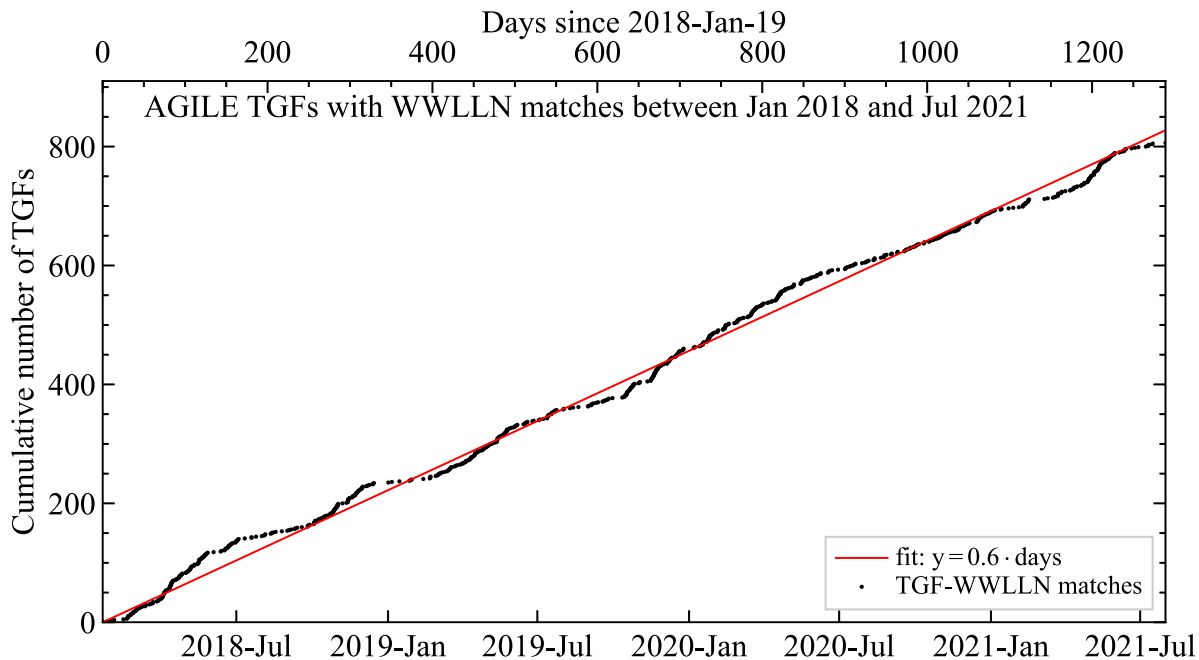


Figure 5.1: Cumulative number of TGF-WWLLN matches identified by AGILE from the start of the 3D-FIX period. AGILE detects about 0.6 TGFs with a WWLLN match per day.

## 5.2 Summary of Paper II

The second paper, Lindanger *et al.* [2021], presents spectral analysis of 17 TGFs detected by ASIM. The TGF sample is carefully selected to keep a clean sample suitable for reliable spectral analysis, meaning suitable count statistics, low instrumental effects, and reliable source locations. The Monte Carlo modeling of the TGFs takes into account photon transport through the atmosphere, the ASIM mass model, and instrumental effects. A model of the instrumental effects in HED has been developed and validated. Different assumed source altitudes and beaming geometries are modeled and compared to observed energy spectra to identify possible source properties. The paper points out that  $\chi^2$  statistics are not sufficient for evaluating if a model is accepted or not compared

with the measurement. A maximum likelihood method should be used in addition to the  $\chi^2$  test because it is more reliable for the typical count statistics we have for individual TGFs. However, the statistical tests show that we cannot well constrain the source properties (altitude and beaming geometries) of individual TGFs. Although we have a “best fit” solution, several solutions are compatible with the measurement and therefore cannot be neglected. This is important as the estimated number of photons produced by the TGF at source is highly dependent on the source altitude due to the absorption of photons in the atmosphere. Therefore, accepted solutions spanning a large range in altitudes lead to large uncertainties in the number of photons at source.

It is shown in Figure 7 in the paper by a pseudo spectral analysis, where 100 and 1000 photons were randomly sampled from a known source altitude, that even with 1000 “measured” photons there would still be several accepted solutions. It is evident that with the current generation of TGF instruments in space it is very difficult to reliably constrain the source properties of TGFs without additional measurements, for example in the radio band, that can confine the production altitude. It is shown that the radial distance between the TGF source and the subsatellite point determine how well the spectral analysis can confine the source properties of the TGF. For small radial distances the spectral analysis is more reliable confining source altitudes, but is less reliable confining beaming geometries. For larger radial distances the spectral analysis is more reliable confining beaming geometries, but not reliable confining source altitudes.

Taking into account all accepted production solutions, there is a significant variation in observed fluence independent of the distance between source and ASIM. In agreement with *Mailyan et al.* [2016], the observed energy spectra are diverse and therefore cumulative spectral analysis of TGFs should be avoided.

A lower threshold of the maximum photon energy produced by TGFs is estimated to be 24 MeV based on the 17 TGFs analyzed in the paper.

An important tool developed for the spectral analysis is the HED safety time criteria that is the minimum time between two consecutive counts that allows for a reliable energy estimate. The implementation of the safety time criteria is crucial for reliable spectral analysis of ASIM TGFs.

## 5.3 Summary of Paper III

The third paper, *Lindanger et al.* [2022], investigates the TGF time relative to the lightning flash. A lightning flash consists of several discharges, where each discharge can be detected as a radio sferic, and a typical duration of the full flash is hundreds of milliseconds.

Previous studies have focused on the sferic closest in time to the TGF [*Connaughton et al.*, 2010, 2013; *Marisaldi et al.*, 2015; *Østgaard et al.*, 2015; *Mezentsev et al.*, 2016; *Albrechtsen et al.*, 2019; *Lindanger et al.*, 2020]. Paper III takes a step back and focuses on *all* sferics close in time to the TGF. The study found that sferics and optical measurements show that TGFs are typically produced in the beginning of the flash. This conclusion is based on stacking analysis of sferics superposed at the TGF time, using the TGF catalogs of RHESSI, Fermi, AGILE, and ASIM. The optical measurements are from the MMIA module onboard ASIM. The TGFs in the sample with optical data

have a reliable location to ensure that the optical signal comes from the location of the TGF.

In agreement with *Omar et al.* [2014] and *Smith et al.* [2016] there is significant excess of sferics detected between 150 and 750 ms after the TGF. This excess of sferics is termed the second peak. The discharges producing the second peak are shown to be co-located with the production location of the TGFs within the spatial uncertainties of the lightning networks. On average 13% of the TGFs associated with a WWLLN match have sferics, detected by WWLLN, in the second peak. For GLD360 this fraction increases to 51%, showing that the detection of the sferics in the second peak is strongly dependent of the sensitivity of the lightning network. The median peak current value of the sferics closest in time to the TGF is higher than the median peak current value of the sferics in the second peak.

Finally, a blind search is performed on random lightning data to investigate if the second peak is a general property of lightning flashes. There is no evidence for a second peak in the random sample of flashes. The random sample shows a gradual decay, whereas the TGF sample shows a sharp decay of activity after the first stroke, before it again increases in activity in the second peak. This indicates that those flashes that start with a TGF, have a large initial discharge and that it takes more than 150 ms before the electric activity again is reactivated. This is different from the random selection of flashes.

# Chapter 6

## Conclusions and Future Prospects

### 6.1 Conclusions

The goal of this project has been to investigate the connection between TGFs and lightning discharges, and the source properties of TGFs by performing spectral analysis of individual TGFs.

Paper I presents the 3rd AGILE TGF catalog together with its companion paper *Maiorana et al. [2020]*. The catalog is freely available at <https://www.ssdc.asi.it/mcal3tgfcat/> and is updated at reasonable intervals. The TGF sample is consistent with what is already reported by other missions in terms of association with lightning discharges, duration, geographical distribution, and local time trends. It is confirmed that TGF production tends to prefer coastal regions, and that in multi-pulse TGF the sferic detected by WWLLN is associated with the last gamma-ray pulse. Moreover, the TGF-WWLLN matches provide an independent tool for diagnostics and correction of the absolute timing accuracy of AGILE. The search for TGF-WWLLN matches is performed every few months identifying on average 0.6 TGF-WWLLN matches per day of operation.

Paper II reports spectral analysis on TGFs observed by ASIM. The Monte Carlo modeling of the TGFs takes into account all relevant processes from TGF source to measured counts, including a newly developed model of instrumental effects in HED. The instrumental effects model includes a method to ensure reliable energy measurements during the high count rates of TGFs that is applied to both the observed data and in the forward modeling. Several combinations of beaming geometries and source altitudes are accepted by the statistical tests resulting in a large uncertainty in the estimate of the intrinsic source luminosity for the TGFs analyzed in the sample. The sample also shows variations in observed fluence independent of the distance between source and ASIM. It is found that the ability to constrain the source altitude and beaming geometries of TGFs strongly depends on the distance between source and satellite due to intrinsic limitations of the spectral analysis. It is therefore very difficult to reliably constrain the source properties without additional measurements in, for example, the radio band. A lower limit on the maximum photon energy produced by the TGFs is estimated to be 24 MeV for the TGFs in the sample.

Paper III investigates the TGF time relative to the lightning flash. The study concludes, based on a large sample of TGFs with associated lightning data, that the TGF is produced in the beginning of the lightning flash. This is also supported by a smaller sam-

ple of optical measurements by ASIM of the TGF-associated lightning flashes. Also, in agreement with previous studies, an excess of sferics is detected between 150 and 750 ms after the TGF. This excess of sferics is termed the second peak and is shown to be co-located with the production location of the TGFs within the spatial uncertainties of the lightning networks. It is also shown that the fraction of TGFs that have activity in the second peak depends on the sensitivity of the lightning networks. The second peak is only significant for stacking analysis of several TGFs and is not apparent on an event by event basis due to the stochastic nature of lightning flashes. However, for lightning flashes that start with a TGF, there is an enhanced probability of having a lightning stroke between 150 and 750 ms after the start of the flash. A blind search on random lightning data shows a different time distribution of discharges following the first stroke in the flash, and the random lightning data shows no evidence of a second peak. This indicates that the second peak is characteristic property of a significant fraction of flashes that starts with a TGF.

## 6.2 Future Prospects

This project followed three main directions: identifying and cataloging TGFs by correlation with lightning sferics, relating the time of the TGF production to lightning flashes, and spectral analysis of TGFs.

Extensive catalogs of TGF detections are essential for statistical studies and cross-correlation with other ground- or space based data as shown in Paper III. The still growing 3rd AGILE TGF catalog is not fully exploited yet and can be used for detailed exploration of seasonal and geographical characteristics. The catalog can be used to investigate the local variation of the TGF-to-lightning ratio with season and to further investigate the ratio over land, ocean and coastal regions. AGILE is particularly suitable for these studies given the large TGF detection density in a narrow region across the equator, making the statistical errors low, although on a limited geographical region. AGILE geo-located TGFs will also be the basis for further study of high-energy photons emitted by TGFs and recorded by the AGILE GRID instrument. Large TGF catalogs also form the basis for planning where and when to fly airborne missions in the future. The algorithm developed to identify TGFs by correlation of gamma-ray data with WWLLN data can easily be applied to more sensitive lightning networks to further improve the number of TGFs with a reliable location.

Regarding the TGF and associated lightning discharges there are some unanswered questions I want to point out: What is responsible, in a multi-pulse TGF, for usually having a sferic associated with the last pulse, and often not any of the previous pulses? Thinking of lightning flashes starting with a TGF, what effects created by the TGF are affecting the later electrical activity in the flash giving the enhanced lightning activity hundreds of millisecond after the TGF? What effects created by the TGF make these TGF-flashes different from lightning flashes in general?

The spectral analysis in Paper II clearly shows the need for additional measurements, in addition to detections from space, to further constrain the production properties of TGF. Simulations show that even a large increase in the effective area would not be sufficient to reliably constrain the spectral parameters. The planning of future TGF campaigns either on ground, air, or space must include additional instruments, for

example in radio, supporting the gamma-ray detectors.



# Bibliography

- Abarca, S. F., K. L. Corbosiero, and T. J. Galarneau Jr. (2010), An evaluation of the Worldwide Lightning Location Network (WWLLN) using the National Lightning Detection Network (NLDN) as ground truth, *Journal of Geophysical Research: Atmospheres*, 115(D18), doi:10.1029/2009JD013411.
- Abbasi, R. U., T. Abu-Zayyad, M. Allen, E. Barcikowski, J. W. Belz, and et al. (2018), Gamma ray showers observed at ground level in coincidence with downward lightning leaders, *Journal of Geophysical Research: Atmospheres*, 123(13), 6864–6879, doi: 10.1029/2017JD027931.
- Albrechtsen, K. H., N. Østgaard, N. Berge, and T. Gjesteland (2019), Observationally Weak TGFs in the RHESSI Data, *Journal of Geophysical Research: Atmospheres*, 124(1), 287–298, doi:10.1029/2018JD029272.
- Babich, L. P., E. N. Donskoy, R. I. Il'kaev, I. M. Kutsyk, and R. A. Roussel-Dupre (2004), Fundamental parameters of a relativistic runaway electron avalanche in air, *Plasma Physics Reports*, 30(7), 616–624, doi:10.1134/1.1778437.
- Belz, J. W., P. R. Krehbiel, J. Remington, M. A. Stanley, R. U. Abbasi, and et al. (2020), Observations of the origin of downward terrestrial gamma-ray flashes, *Journal of Geophysical Research: Atmospheres*, 125(23), e2019JD031,940, doi:10.1029/2019JD031940.
- Bogomolov, V. V., M. I. Panasyuk, S. I. Svertilov, A. V. Bogomolov, G. K. Garipov, A. F. Iyudin, P. A. Klimov, S. I. Klimov, T. M. Mishieva, P. Y. Minaev, V. S. Morozenko, O. V. Morozov, A. S. Posanenko, A. V. Prokhorov, and H. Rotkel (2017), Observation of Terrestrial gamma-ray flashes in the RELEC space experiment on the Vernov satellite, *Cosmic Research*, 55(3), 159–168, doi:10.1134/S0010952517030017.
- Bowers, G. S., D. M. Smith, G. F. Martinez-McKinney, M. Kamogawa, S. A. Cummer, J. R. Dwyer, D. Wang, M. Stock, and Z. Kawasaki (2017), Gamma ray signatures of neutrons from a terrestrial gamma ray flash, *Geophysical Research Letters*, 44(19), 10,063–10,070, doi:10.1002/2017GL075071.
- Bowers, G. S., D. M. Smith, N. A. Kelley, G. F. Martinez-McKinney, S. A. Cummer, J. R. Dwyer, S. Heckman, R. H. Holzworth, F. Marks, P. Reasor, J. Gamache, J. Dunion, T. Richards, and H. K. Rassoul (2018), A Terrestrial Gamma-Ray Flash inside the Eyewall of Hurricane Patricia, *Journal of Geophysical Research: Atmospheres*, 123(10), 4977–4987, doi:10.1029/2017JD027771.

- Briggs, M. S., G. J. Fishman, V. Connaughton, P. N. Bhat, W. S. Paciesas, R. D. Preece, C. Wilson-Hodge, V. L. Chaplin, R. M. Kippen, A. von Kienlin, C. A. Meegan, E. Bissaldi, J. R. Dwyer, D. M. Smith, R. H. Holzworth, J. E. Grove, and A. Chekhtman (2010), First results on terrestrial gamma ray flashes from the Fermi Gamma-ray Burst Monitor, *Journal of Geophysical Research: Space Physics*, 115(A7), doi:10.1029/2009JA015242.
- Briggs, M. S., V. Connaughton, C. Wilson-Hodge, R. D. Preece, G. J. Fishman, R. M. Kippen, P. N. Bhat, W. S. Paciesas, V. L. Chaplin, C. A. Meegan, A. von Kienlin, J. Greiner, J. R. Dwyer, and D. M. Smith (2011), Electron-positron beams from terrestrial lightning observed with Fermi GBM, *Geophysical Research Letters*, 38(2), doi:10.1029/2010GL046259.
- Bürgesser, R. E. (2017), Assessment of the World Wide Lightning Location Network (WWLLN) detection efficiency by comparison to the Lightning Imaging Sensor (LIS), *Quarterly Journal of the Royal Meteorological Society*, 143(708), 2809–2817, doi:10.1002/qj.3129.
- Carlson, B. E., N. G. Lehtinen, and U. S. Inan (2007), Constraints on terrestrial gamma ray flash production from satellite observation, *Geophysical Research Letters*, 34(8), doi:10.1029/2006GL029229.
- Castro-Tirado, A. J., N. Østgaard, E. Göyüş, C. Sánchez-Gil, J. Pascual-Granado, V. Reglero, A. Mezentsev, M. Gabler, M. Marisaldi, T. Neubert, C. Budtz-Jørgensen, A. Lindanger, D. Sarria, I. Kuvvetli, P. Cerdá-Durán, J. Navarro-González, J. A. Font, B. B. Zhang, N. Lund, C. A. Oxborrow, S. Brandt, M. D. Caballero-García, I. M. Carrasco-García, A. Castellón, M. A. Castro Tirado, F. Christiansen, C. J. Eyles, E. Fernández-García, G. Genov, S. Guziy, Y. D. Hu, A. Nicuesa Guelbenzu, S. B. Pandey, Z. K. Peng, C. Pérez del Pulgar, A. J. Reina Terol, E. Rodríguez, R. Sánchez-Ramírez, T. Sun, K. Ullaland, and S. Yang (2021), Very-high-frequency oscillations in the main peak of a magnetar giant flare, *Nature*, 600(7890), 621–624, doi:10.1038/s41586-021-04101-1.
- Celestin, S., and V. P. Pasko (2011), Energy and fluxes of thermal runaway electrons produced by exponential growth of streamers during the stepping of lightning leaders and in transient luminous events, *Journal of Geophysical Research: Space Physics*, 116(A3), doi:10.1029/2010JA016260.
- Celestin, S., and V. P. Pasko (2012), Compton scattering effects on the duration of terrestrial gamma-ray flashes, *Geophysical Research Letters*, 39(2), doi:10.1029/2011GL050342.
- Chanrion, O., T. Neubert, I. Lundgaard Rasmussen, C. Stoltze, D. Tcherniak, N. C. Jessen, J. Polny, P. Brauer, J. E. Balling, S. Savstrup Kristensen, S. Forchhammer, P. Hofmeyer, P. Davidsen, O. Mikkelsen, D. Bo Hansen, D. D. V. Bhanderi, C. G. Petersen, and M. Lorenzen (2019), The Modular Multispectral Imaging Array (MMIA) of the ASIM Payload on the International Space Station, *Space Science Reviews*, 215(4), 28, doi:10.1007/s11214-019-0593-y.

- Chilingarian, A., A. Daryan, K. Arakelyan, A. Hovhannisyan, B. Mailyan, L. Melkumyan, G. Hovsepyan, S. Chilingaryan, A. Reymers, and L. Vanyan (2010), Ground-based observations of thunderstorm-correlated fluxes of high-energy electrons, gamma rays, and neutrons, *Phys. Rev. D*, 82, 043,009, doi: 10.1103/PhysRevD.82.043009.
- Connaughton, V., M. S. Briggs, R. H. Holzworth, M. L. Hutchins, G. J. Fishman, C. A. Wilson-Hodge, V. L. Chaplin, P. N. Bhat, J. Greiner, A. von Kienlin, R. M. Kippen, C. A. Meegan, W. S. Paciesas, R. D. Preece, E. Cramer, J. R. Dwyer, and D. M. Smith (2010), Associations between Fermi Gamma-ray Burst Monitor terrestrial gamma ray flashes and sferics from the World Wide Lightning Location Network, *Journal of Geophysical Research: Space Physics*, 115(A12), doi:10.1029/2010JA015681.
- Connaughton, V., M. S. Briggs, S. Xiong, J. R. Dwyer, M. L. Hutchins, J. E. Grove, A. Chekhtman, D. Tierney, G. Fitzpatrick, S. Foley, S. McBreen, P. N. Bhat, V. L. Chaplin, E. Cramer, G. J. Fishman, R. H. Holzworth, M. Gibby, A. von Kienlin, C. A. Meegan, W. S. Paciesas, R. D. Preece, and C. Wilson-Hodge (2013), Radio signals from electron beams in terrestrial gamma ray flashes, *Journal of Geophysical Research: Space Physics*, 118(5), 2313–2320, doi:10.1029/2012JA018288.
- Cooray, V. (2015), *An Introduction to Lightning*, Springer, London, doi:10.1007/978-94-017-8938-7.
- Cummer, S. A., Y. Zhai, W. Hu, D. M. Smith, L. I. Lopez, and M. A. Stanley (2005), Measurements and implications of the relationship between lightning and terrestrial gamma ray flashes, *Geophysical Research Letters*, 32(8), doi: 10.1029/2005GL022778.
- Cummer, S. A., M. S. Briggs, J. R. Dwyer, S. Xiong, V. Connaughton, G. J. Fishman, G. Lu, F. Lyu, and R. Solanki (2014), The source altitude, electric current, and intrinsic brightness of terrestrial gamma ray flashes, *Geophysical Research Letters*, 41(23), 8586–8593, doi:10.1002/2014GL062196.
- Cummer, S. A., F. Lyu, M. S. Briggs, G. Fitzpatrick, O. J. Roberts, and J. R. Dwyer (2015), Lightning leader altitude progression in terrestrial gamma-ray flashes, *Geophysical Research Letters*, 42(18), 7792–7798, doi:10.1002/2015GL065228.
- Cummins, K. L., M. J. Murphy, and J. V. Tuel (2000), LIGHTNING DETECTION METHODS AND METEOROLOGICAL APPLICATIONS, in *the IV International Symposium on Military Meteorology Hydro-Meteorological Support of Allied Forces and PfP Members Tasks Realization*.
- Dowden, R. L., J. B. Brundell, and C. J. Rodger (2002), VLF lightning location by time of group arrival (TOGA) at multiple sites, *Journal of Atmospheric and Solar-Terrestrial Physics*, 64(7), 817–830, doi:10.1016/S1364-6826(02)00085-8.
- Dwyer, J. R. (2003), A fundamental limit on electric fields in air, *Geophysical Research Letters*, 30(20), doi:10.1029/2003GL017781.
- Dwyer, J. R. (2007), Relativistic breakdown in planetary atmospheres, *Physics of Plasmas*, 14(4), 042,901, doi:10.1063/1.2709652.

- Dwyer, J. R. (2008), Source mechanisms of terrestrial gamma-ray flashes, *Journal of Geophysical Research: Atmospheres*, 113(D10), doi:10.1029/2007JD009248.
- Dwyer, J. R. (2012), The relativistic feedback discharge model of terrestrial gamma ray flashes, *Journal of Geophysical Research: Space Physics*, 117(A2), doi:10.1029/2011JA017160.
- Dwyer, J. R., and S. A. Cummer (2013), Radio emissions from terrestrial gamma-ray flashes, *Journal of Geophysical Research: Space Physics*, 118(6), 3769–3790, doi:10.1002/jgra.50188.
- Dwyer, J. R., and D. Smith (2012), Deadly rays from clouds, *Scientific American*, 307(2), 54–59, doi:10.1038/scientificamerican0812-54.
- Dwyer, J. R., and D. M. Smith (2005), A comparison between monte carlo simulations of runaway breakdown and terrestrial gamma-ray flash observations, *Geophysical Research Letters*, 32(22), doi:10.1029/2005GL023848.
- Dwyer, J. R., M. A. Uman, H. K. Rassoul, M. Al-Dayeh, L. Caraway, J. Jerauld, V. A. Rakov, D. M. Jordan, K. J. Rambo, V. Corbin, and B. Wright (2003), Energetic radiation produced during rocket-triggered lightning, *Science*, 299(5607), 694–697, doi:10.1126/science.1078940.
- Dwyer, J. R., H. K. Rassoul, M. Al-Dayeh, L. Caraway, B. Wright, A. Chrest, M. A. Uman, V. A. Rakov, K. J. Rambo, D. M. Jordan, J. Jerauld, and C. Smyth (2004a), Measurements of x-ray emission from rocket-triggered lightning, *Geophysical Research Letters*, 31(5), doi:10.1029/2003GL018770.
- Dwyer, J. R., H. K. Rassoul, M. Al-Dayeh, L. Caraway, B. Wright, A. Chrest, M. A. Uman, V. A. Rakov, K. J. Rambo, D. M. Jordan, J. Jerauld, and C. Smyth (2004b), A ground level gamma-ray burst observed in association with rocket-triggered lightning, *Geophysical Research Letters*, 31(5), doi:10.1029/2003GL018771.
- Dwyer, J. R., B. W. Grefenstette, and D. M. Smith (2008), High-energy electron beams launched into space by thunderstorms, *Geophysical Research Letters*, 35(2), doi:10.1029/2007GL032430.
- Dwyer, J. R., M. M. Schaal, E. Cramer, S. Arabshahi, N. Liu, H. K. Rassoul, J. D. Hill, D. M. Jordan, and M. A. Uman (2012a), Observation of a gamma-ray flash at ground level in association with a cloud-to-ground lightning return stroke, *Journal of Geophysical Research: Space Physics*, 117(A10), doi:10.1029/2012JA017810.
- Dwyer, J. R., D. M. Smith, and S. A. Cummer (2012b), High-energy atmospheric physics: Terrestrial gamma-ray flashes and related phenomena, *Space Science Reviews*, 173(1), 133–196, doi:10.1007/s11214-012-9894-0.
- Eack, K. B., W. H. Beasley, W. D. Rust, T. C. Marshall, and M. Stolzenburg (1996), Initial results from simultaneous observation of x-rays and electric fields in a thunderstorm, *Journal of Geophysical Research: Atmospheres*, 101(D23), 29,637–29,640, doi:10.1029/96JD01705.

- Enoto, T., Y. Wada, Y. Furuta, K. Nakazawa, T. Yuasa, K. Okuda, K. Makishima, M. Sato, Y. Sato, T. Nakano, D. Umemoto, and H. Tsuchiya (2017), Photonuclear reactions triggered by lightning discharge, *Nature*, 551(7681), 481–484, doi:10.1038/nature24630.
- Fan, P., D. Zheng, Y. Zhang, S. Gu, W. Zhang, W. Yao, B. Yan, and Y. Xu (2018), A Performance Evaluation of the World Wide Lightning Location Network (WWLLN) over the Tibetan Plateau, *Journal of Atmospheric and Oceanic Technology*, 35(4), 927 – 939, doi:10.1175/JTECH-D-17-0144.1.
- Fishman, G. J., P. N. Bhat, R. Mallozzi, J. M. Horack, T. Koshut, C. Kouveliotou, G. N. Pendleton, C. A. Meegan, R. B. Wilson, W. S. Paciesas, S. J. Goodman, and H. J. Christian (1994), Discovery of intense gamma-ray flashes of atmospheric origin, *Science*, 264(5163), 1313–1316, doi:10.1126/science.264.5163.1313.
- Foley, S., G. Fitzpatrick, M. S. Briggs, V. Connaughton, D. Tierney, S. McBreen, J. R. Dwyer, V. L. Chaplin, P. N. Bhat, D. Byrne, E. Cramer, G. J. Fishman, S. Xiong, J. Greiner, R. M. Kippen, C. A. Meegan, W. S. Paciesas, R. D. Preece, A. von Kienlin, and C. Wilson-Hodge (2014), Pulse properties of terrestrial gamma-ray flashes detected by the Fermi Gamma-Ray Burst Monitor, *Journal of Geophysical Research: Space Physics*, 119(7), 5931–5942, doi:10.1002/2014JA019805.
- Gjesteland, T., N. Østgaard, P. H. Connell, J. Stadsnes, and G. J. Fishman (2010), Effects of dead time losses on terrestrial gamma ray flash measurements with the Burst and Transient Source Experiment, *Journal of Geophysical Research: Space Physics*, 115(A5), doi:10.1029/2009JA014578.
- Gjesteland, T., N. Østgaard, A. B. Collier, B. E. Carlson, M. B. Cohen, and N. G. Lehtinen (2011), Confining the angular distribution of terrestrial gamma ray flash emission, *Journal of Geophysical Research: Space Physics*, 116(A11), doi:10.1029/2011JA016716.
- Gjesteland, T., N. Østgaard, A. B. Collier, B. E. Carlson, C. Eyles, and D. M. Smith (2012), A new method reveals more TGFs in the RHESSI data, *Geophysical Research Letters*, 39(5), doi:10.1029/2012GL050899.
- Grefenstette, B. W., D. M. Smith, J. R. Dwyer, and G. J. Fishman (2008), Time evolution of terrestrial gamma ray flashes, *Geophysical Research Letters*, 35(6), doi:10.1029/2007GL032922.
- Grefenstette, B. W., D. M. Smith, B. J. Hazelton, and L. I. Lopez (2009), First RHESSI terrestrial gamma ray flash catalog, *Journal of Geophysical Research: Space Physics*, 114(A2), doi:10.1029/2008JA013721.
- Gurevich, A., G. Milikh, and R. Roussel-Dupre (1992), Runaway electron mechanism of air breakdown and preconditioning during a thunderstorm, *Physics Letters A*, 165(5), 463–468, doi:10.1016/0375-9601(92)90348-P.
- Hare, B. M., M. A. Uman, J. R. Dwyer, D. M. Jordan, M. I. Biggerstaff, J. A. Caicedo, F. L. Carvalho, R. A. Wilkes, D. A. Kotovsky, W. R. Gamerota, J. T. Pilkey, T. K.

- Ngin, R. C. Moore, H. K. Rassoul, S. A. Cummer, J. E. Grove, A. Nag, D. P. Betten, and A. Bozarth (2016), Ground-level observation of a terrestrial gamma ray flash initiated by a triggered lightning, *Journal of Geophysical Research: Atmospheres*, 121(11), 6511–6533, doi:10.1002/2015JD024426.
- Hazelton, B. J., B. W. Grefenstette, D. M. Smith, J. R. Dwyer, X.-M. Shao, S. A. Cummer, T. Chronis, E. H. Lay, and R. H. Holzworth (2009), Spectral dependence of terrestrial gamma-ray flashes on source distance, *Geophysical Research Letters*, 36(1), doi:10.1029/2008GL035906.
- Heumesser, M., O. Chanrion, T. Neubert, H. J. Christian, K. Dimitriadou, F. J. Gordillo-Vazquez, A. Luque, F. J. Pérez-Invernón, R. J. Blakeslee, N. Østgaard, V. Reglero, and C. Köhn (2021), Spectral observations of optical emissions associated with terrestrial gamma-ray flashes, *Geophysical Research Letters*, 48(4), 2020GL090,700, doi:10.1029/2020GL090700.
- Hutchins, M. L., R. H. Holzworth, J. B. Brundell, and C. J. Rodger (2012), Relative detection efficiency of the World Wide Lightning Location Network, *Radio Science*, 47(6), RS6005, doi:10.1029/2012RS005049.
- Jacobson, A. R., R. Holzworth, J. Harlin, R. Dowden, and E. Lay (2006), Performance Assessment of the World Wide Lightning Location Network (WWLLN), Using the Los Alamos Sferic Array (LASA) as Ground Truth, *Journal of Atmospheric and Oceanic Technology*, 23(8), 1082 – 1092, doi:10.1175/JTECH1902.1.
- Jayaratne, E. R., C. P. R. Saunders, and J. Hallett (1983), Laboratory studies of the charging of soft hail during ice crystal interactions, *Q. J. R. Meteorol. Soc.*, 109(461), 609–630, doi:10.1002/qj.49710946111.
- Köhn, C., and U. Ebert (2015), Calculation of beams of positrons, neutrons, and protons associated with terrestrial gamma ray flashes, *Journal of Geophysical Research: Atmospheres*, 120(4), 1620–1635, doi:10.1002/2014JD022229.
- Köhn, C., G. Diniz, and M. N. Harakeh (2017), Production mechanisms of leptons, photons, and hadrons and their possible feedback close to lightning leaders, *Journal of Geophysical Research: Atmospheres*, 122(2), 1365–1383, doi:10.1002/2016JD025445.
- Köhn, C., M. Heumesser, O. Chanrion, K. Nishikawa, V. Reglero, and T. Neubert (2020), The emission of terrestrial gamma ray flashes from encountering streamer coronae associated to the breakdown of lightning leaders, *Geophysical Research Letters*, 47(20), doi:10.1029/2020GL089749.
- Labanti, C., M. Marisaldi, F. Fuschino, M. Galli, A. Argan, A. Bulgarelli, G. D. Cocco, F. Gianotti, M. Tavani, and M. Trifoglio (2009), Design and construction of the Mini-Calorimeter of the AGILE satellite, *Nuclear Instruments and Methods in Physics Research Section A: Accelerators, Spectrometers, Detectors and Associated Equipment*, 598(2), 470 – 479, doi:10.1016/j.nima.2008.09.021.

- Lehtinen, N. G., and N. Østgaard (2018), X-ray Emissions in a Multiscale Fluid Model of a Streamer Discharge, *Journal of Geophysical Research: Atmospheres*, 123(13), 6935–6953, doi:10.1029/2018JD028646.
- Lindanger, A., M. Marisaldi, C. Maiorana, D. Sarria, K. Albrechtsen, N. Østgaard, M. Galli, A. Ursi, C. Labanti, M. Tavani, C. Pittori, and F. Verrecchia (2020), The 3rd AGILE Terrestrial Gamma Ray Flash Catalog. Part I: Association to Lightning Sferics, *Journal of Geophysical Research: Atmospheres*, 125(11), e2019JD031,985, doi:10.1029/2019JD031985.
- Lindanger, A., M. Marisaldi, D. Sarria, N. Østgaard, N. Lehtinen, C. A. Skeie, A. Mezentzev, P. Kochkin, K. Ullaland, S. Yang, G. Genov, B. E. Carlson, C. Köhn, J. Navarro-Gonzalez, P. Connell, V. Reglero, and T. Neubert (2021), Spectral Analysis of Individual Terrestrial Gamma-Ray Flashes Detected by ASIM, *Journal of Geophysical Research: Atmospheres*, 126(23), e2021JD035,347, doi: 10.1029/2021JD035347.
- Lindanger, A., C. A. Skeie, M. Marisaldi, I. Bjørge-Engeland, N. Østgaard, A. Mezentzev, D. Sarria, N. Lehtinen, V. Reglero, O. Chanrion, and T. Neubert (2022), Production of Terrestrial Gamma-ray Flashes During the Early Stages of Lightning Flashes, *under review in Journal of Geophysical Research: Atmospheres*.
- Lu, G., R. J. Blakeslee, J. Li, D. M. Smith, X.-M. Shao, E. W. McCaul, D. E. Buechler, H. J. Christian, J. M. Hall, and S. A. Cummer (2010), Lightning mapping observation of a terrestrial gamma-ray flash, *Geophysical Research Letters*, 37(11), doi:10.1029/2010GL043494.
- Mailyan, B., M. Stanbro, M. S. Briggs, S. Cummer, J. R. Dwyer, O. J. Roberts, and R. Holzworth (2021), Radio frequency emissions associated with multi-pulsed terrestrial gamma-ray flashes, *Journal of Geophysical Research: Space Physics*, 126(2), doi:10.1029/2020JA027928.
- Mailyan, B. G., M. S. Briggs, E. S. Cramer, G. Fitzpatrick, O. J. Roberts, M. Stanbro, V. Connaughton, S. McBreen, P. N. Bhat, and J. R. Dwyer (2016), The spectroscopy of individual terrestrial gamma-ray flashes: Constraining the source properties, *Journal of Geophysical Research: Space Physics*, 121(11), 11,346–11,363, doi:10.1002/2016JA022702.
- Mailyan, B. G., W. Xu, S. Celestin, M. S. Briggs, J. R. Dwyer, E. S. Cramer, O. J. Roberts, and M. Stanbro (2019), Analysis of Individual Terrestrial Gamma-Ray Flashes With Lightning Leader Models and Fermi Gamma-Ray Burst Monitor Data, *Journal of Geophysical Research: Space Physics*, 124(8), 7170–7183, doi:10.1029/2019JA026912.
- Maiorana, C., M. Marisaldi, A. Lindanger, N. Østgaard, A. Ursi, D. Sarria, M. Galli, C. Labanti, M. Tavani, C. Pittori, and F. Verrecchia (2020), The 3rd AGILE Terrestrial Gamma-ray Flashes Catalog. Part II: Optimized Selection Criteria and Characteristics of the New Sample, *Journal of Geophysical Research: Atmospheres*, 125(11), e2019JD031,986, doi:10.1029/2019JD031986, e2019JD031986 10.1029/2019JD031986.

- Maiorana, C., M. Marisaldi, M. Füllekrug, S. Soula, J. Lapierre, A. Mezentsev, C. A. Skeie, M. Heumesser, O. Chanrion, N. Østgaard, T. Neubert, and V. Reglero (2021), Observation of terrestrial gamma-ray flashes at mid latitude, *Journal of Geophysical Research: Atmospheres*, 126(18), doi:10.1029/2020JD034432.
- Mallick, S., V. A. Rakov, M. Hutchins, and R. H. Holzworth (2014), Evaluation of the WWLLN Performance Characteristics Using Rocket-Triggered Lightning Data, *Int. Conf. Grounding Earthing and 6th Int. Conf. Light. Phys. Eff.*
- Marisaldi, M., F. Fuschino, C. Labanti, M. Galli, F. Longo, E. Del Monte, G. Barbiellini, M. Tavani, A. Giuliani, E. Moretti, S. Vercellone, E. Costa, S. Cutini, I. Donnarumma, Y. Evangelista, M. Feroci, I. Lapshov, F. Lazzarotto, P. Lipari, S. Mereghetti, L. Pacciani, M. Rapisarda, P. Soffitta, M. Trifoglio, A. Argan, F. Bofelli, A. Bulgarelli, P. Caraveo, P. W. Cattaneo, A. Chen, V. Cocco, F. D'Ammando, G. De Paris, G. Di Cocco, G. Di Persio, A. Ferrari, M. Fiorini, T. Froysland, F. Gianotti, A. Morselli, A. Pellizzoni, F. Perotti, P. Picozza, G. Piano, M. Pilia, M. Prest, G. Pucella, A. Rappoldi, A. Rubini, S. Sabatini, E. Striani, A. Trois, E. Vallazza, V. Vittorini, A. Zambra, D. Zanello, L. A. Antonelli, S. Colafrancesco, D. Gasparrini, P. Giommi, C. Pittori, B. Preger, P. Santolamazza, F. Verrecchia, and L. Salotti (2010), Detection of terrestrial gamma ray flashes up to 40 MeV by the AGILE satellite, *Journal of Geophysical Research: Space Physics*, 115(A3), doi:10.1029/2009JA014502.
- Marisaldi, M., F. Fuschino, M. Tavani, S. Dietrich, C. Price, M. Galli, C. Pittori, F. Verrecchia, S. Mereghetti, P. W. Cattaneo, S. Colafrancesco, A. Argan, C. Labanti, F. Longo, E. Del Monte, G. Barbiellini, A. Giuliani, A. Bulgarelli, R. Campana, A. Chen, F. Gianotti, P. Giommi, F. Lazzarotto, A. Morselli, M. Rapisarda, A. Rappoldi, M. Trifoglio, A. Trois, and S. Vercellone (2014), Properties of terrestrial gamma ray flashes detected by AGILE MCAL below 30 MeV, *Journal of Geophysical Research: Space Physics*, 119(2), 1337–1355, doi:10.1002/2013JA019301.
- Marisaldi, M., A. Argan, A. Ursi, T. Gjesteland, F. Fuschino, C. Labanti, M. Galli, M. Tavani, C. Pittori, F. Verrecchia, F. D'Amico, N. Østgaard, S. Mereghetti, R. Campana, P. Cattaneo, A. Bulgarelli, S. Colafrancesco, S. Dietrich, F. Longo, F. Gianotti, P. Giommi, A. Rappoldi, M. Trifoglio, and A. Trois (2015), Enhanced detection of terrestrial gamma-ray flashes by AGILE, *Geophysical Research Letters*, 42(21), 9481–9487, doi:10.1002/2015GL066100.
- Marisaldi, M., M. Galli, C. Labanti, N. Østgaard, D. Sarria, S. A. Cummer, F. Lyu, A. Lindanger, R. Campana, A. Ursi, M. Tavani, F. Fuschino, A. Argan, A. Trois, C. Pittori, and F. Verrecchia (2019), On the high-energy spectral component and fine time structure of terrestrial gamma ray flashes, *Journal of Geophysical Research: Atmospheres*, 124(14), 7484–7497, doi:10.1029/2019JD030554.
- McCarthy, M., and G. K. Parks (1985), Further observations of x-rays inside thunderstorms, *Geophysical Research Letters*, 12(6), 393–396, doi:10.1029/GL012i006p00393.
- Meegan, C., G. Lichti, P. N. Bhat, E. Bissaldi, M. S. Briggs, V. Connaughton, R. Diehl, G. Fishman, J. Greiner, A. S. Hoover, A. J. van der Horst, A. von

- Kienlin, R. M. Kippen, C. Kouveliotou, S. McBreen, W. S. Paciesas, R. Preece, H. Steinle, M. S. Wallace, R. B. Wilson, and C. Wilson-Hodge (2009), THE FERMI GAMMA-RAY BURST MONITOR, *The Astrophysical Journal*, 702, 791–804, doi: 10.1088/0004-637x/702/1/791.
- Mezentsev, A., N. Østgaard, T. Gjesteland, K. Albrechtsen, N. Lehtinen, M. Marisaldi, D. Smith, and S. Cummer (2016), Radio emissions from double RHESSI TGFs, *Journal of Geophysical Research: Atmospheres*, 121(13), 8006–8022, doi:10.1002/2016JD025111.
- Moore, C. B., K. B. Eack, G. D. Aulich, and W. Rison (2001), Energetic radiation associated with lightning stepped-leaders, *Geophysical Research Letters*, 28(11), 2141–2144, doi:10.1029/2001GL013140.
- Moss, G. D., V. P. Pasko, N. Liu, and G. Veronis (2006), Monte Carlo model for analysis of thermal runaway electrons in streamer tips in transient luminous events and streamer zones of lightning leaders, *Journal of Geophysical Research: Space Physics*, 111(A2), doi:10.1029/2005JA011350.
- Nemiroff, R. J., J. T. Bonnell, and J. P. Norris (1997), Temporal and spectral characteristics of terrestrial gamma flashes, *Journal of Geophysical Research: Space Physics*, 102(A5), 9659–9665, doi:10.1029/96JA03107.
- Neubert, T., N. Østgaard, V. Reglero, E. Blanc, O. Chanrion, C. A. Oxborow, A. Orr, M. Tacconi, O. Hartnack, and D. D. V. Bhanderi (2019), The ASIM Mission on the International Space Station, *Space Science Reviews*, 215(2), 26, doi:10.1007/s11214-019-0592-z.
- Neubert, T., N. Østgaard, V. Reglero, O. Chanrion, M. Heumesser, K. Dimitriadou, F. Christiansen, C. Budtz-Jørgensen, I. Kuvvetli, I. L. Rasmussen, A. Mezentsev, M. Marisaldi, K. Ullaland, G. Genov, S. Yang, P. Kochkin, J. Navarro-Gonzalez, P. H. Connell, and C. J. Eyles (2020), A terrestrial gamma-ray flash and ionospheric ultraviolet emissions powered by lightning, *Science*, 367(6474), 183–186, doi:10.1126/science.aax3872.
- Omar, K. S., M. S. Briggs, and S. Heckman (2014), Characterizing the TGF-lightning relationship using ENTLN, in *Abstract AE31A-3388.*, AGU Fall Meeting 2014.
- Østgaard, N., T. Gjesteland, J. Stadsnes, P. H. Connell, and B. Carlson (2008), Production altitude and time delays of the terrestrial gamma flashes: Revisiting the Burst and Transient Source Experiment spectra, *Journal of Geophysical Research: Space Physics*, 113(A2), doi:10.1029/2007JA012618.
- Østgaard, N., T. Gjesteland, R. S. Hansen, A. B. Collier, and B. Carlson (2012), The true fluence distribution of terrestrial gamma flashes at satellite altitude, *Journal of Geophysical Research: Space Physics*, 117(A3), doi:10.1029/2011JA017365.
- Østgaard, N., T. Gjesteland, B. E. Carlson, A. B. Collier, S. A. Cummer, G. Lu, and H. J. Christian (2013), Simultaneous observations of optical lightning and terrestrial gamma ray flash from space, *Geophysical Research Letters*, 40(10), 2423–2426, doi:10.1002/grl.50466.

- Østgaard, N., K. H. Albrechtsen, T. Gjesteland, and A. Collier (2015), A new population of terrestrial gamma-ray flashes in the RHESSI data, *Geophysical Research Letters*, 42(24), 10,937–10,942, doi:10.1002/2015GL067064.
- Østgaard, N., H. J. Christian, J. E. Grove, D. Sarria, A. Mezentsev, P. Kochkin, N. Lehtinen, M. Quick, S. Al-Nussirat, E. Wulf, G. Genov, K. Ullaland, M. Marisaldi, S. Yang, and R. J. Blakeslee (2019a), Gamma Ray Glow Observations at 20-km Altitude, *Journal of Geophysical Research: Atmospheres*, 124(13), 7236–7254, doi:10.1029/2019JD030312.
- Østgaard, N., J. E. Balling, T. Bjørnsen, P. Brauer, C. Budtz-Jørgensen, W. Bujwan, B. Carlson, F. Christiansen, P. Connell, C. Eyles, D. Fehlker, G. Genov, P. Grudziński, P. Kochkin, A. Kohfeldt, I. Kuvvetli, P. L. Thomsen, S. M. Pedersen, J. Navarro-Gonzalez, T. Neubert, K. Njøten, P. Orleanski, B. H. Qureshi, L. R. Cenkeramaddi, V. Reglero, M. Reina, J. M. Rodrigo, M. Rostad, M. D. Sabau, S. S. Kristensen, Y. Skogseide, A. Solberg, J. Stadsnes, K. Ullaland, and S. Yang (2019b), The Modular X- and Gamma-Ray Sensor (MXGS) of the ASIM Payload on the International Space Station, *Space Science Reviews*, 215, 23, doi:10.1007/s11214-018-0573-7.
- Østgaard, N., T. Neubert, V. Reglero, K. Ullaland, S. Yang, G. Genov, M. Marisaldi, A. Mezentsev, P. Kochkin, N. Lehtinen, D. Sarria, B. H. Qureshi, A. Solberg, C. Maiorana, K. Albrechtsen, C. Budtz-Jørgensen, I. Kuvvetli, F. Christiansen, O. Chanrion, M. Heumesser, J. Navarro-Gonzalez, P. Connell, C. Eyles, H. Christian, and S. Al-nussirat (2019c), First 10 Months of TGF Observations by ASIM, *Journal of Geophysical Research: Atmospheres*, 124(24), 14,024–14,036, doi:10.1029/2019JD031214.
- Østgaard, N., S. A. Cummer, A. Mezentsev, A. Luque, J. Dwyer, T. Neubert, V. Reglero, M. Marisaldi, P. Kochkin, D. Sarria, N. Lehtinen, K. Ullaland, S. Yang, G. Genov, O. Chanrion, F. Christiansen, and Y. Pu (2021), Simultaneous Observations of EIP, TGF, Elve, and Optical Lightning, *Journal of Geophysical Research: Atmospheres*, 126(11), e2020JD033,921, doi:10.1029/2020JD033921.
- Parks, G. K., B. H. Mauk, R. Spiger, and J. Chin (1981), X-ray enhancements detected during thunderstorm and lightning activities, *Geophysical Research Letters*, 8(11), 1176–1179, doi:10.1029/GL008i011p01176.
- Pu, Y., S. A. Cummer, F. Lyu, M. Briggs, B. Mailyan, M. Stanbro, and O. Roberts (2019), Low frequency radio pulses produced by terrestrial gamma-ray flashes, *Geophysical Research Letters*, 46(12), 6990–6997, doi:10.1029/2019GL082743.
- Rakov, V. A., and M. A. Uman (2003), *Lightning: Physics and Effects*, Cambridge University Press, Cambridge, United Kingdom.
- Roberts, O. J., G. Fitzpatrick, M. Stanbro, S. McBreen, M. S. Briggs, R. H. Holzworth, J. E. Grove, A. Chekhtman, E. S. Cramer, and B. G. Mailyan (2018), The First Fermi-GBM Terrestrial Gamma Ray Flash Catalog, *Journal of Geophysical Research: Space Physics*, 123(5), 4381–4401, doi:10.1029/2017JA024837.
- Roberts, O. J., P. Veres, M. G. Baring, M. S. Briggs, C. Kouveliotou, E. Bissaldi, G. Younes, S. I. Chastain, J. J. DeLaunay, D. Huppenkothen, A. Tohuvavohu, P. N.

- Bhat, E. Göğüş, A. J. van der Horst, J. A. Kennea, D. Kocevski, J. D. Linford, S. Guiriec, R. Hamburg, C. A. Wilson-Hodge, and E. Burns (2021), Rapid spectral variability of a giant flare from a magnetar in ngc 253, *Nature*, 589(7841), 207–210, doi:10.1038/s41586-020-03077-8.
- Rodger, C. J., J. B. Brundell, and R. L. Dowden (2005), Location accuracy of VLF World-Wide Lightning Location (WWLL) network: Post-algorithm upgrade, *Annales Geophysicae*, 23(2), 277–290, doi:10.5194/angeo-23-277-2005.
- Rudlosky, S. D., and D. T. Shea (2013), Evaluating wwlln performance relative to trmm/lis, *Geophysical Research Letters*, 40(10), 2344–2348, doi:10.1002/grl.50428.
- Said, R. K., and M. J. Murphy (2016), GLD360 Upgrade: Performance Analysis and Applications, *24th International Lightning Detection Conference*.
- Said, R. K., U. S. Inan, and K. L. Cummins (2010), Long-range lightning geolocation using a VLF radio atmospheric waveform bank, *Journal of Geophysical Research: Atmospheres*, 115(D23), doi:10.1029/2010JD013863.
- Said, R. K., M. B. Cohen, and U. S. Inan (2013), Highly intense lightning over the oceans: Estimated peak currents from global GLD360 observations, *Journal of Geophysical Research: Atmospheres*, 118(13), 6905–6915, doi:10.1002/jgrd.50508.
- Sarria, D., P.-L. Blelly, and F. Forme (2015), MC-PEPTITA: A Monte Carlo model for Photon, Electron and Positron Tracking In Terrestrial Atmosphere—Application for a terrestrial gamma ray flash, *Journal of Geophysical Research: Space Physics*, 120(5), 3970–3986, doi:10.1002/2014JA020695.
- Sarria, D., F. Lebrun, P.-L. Blelly, R. Chipaux, P. Laurent, J.-A. Sauvaud, L. Prech, P. Devoto, D. Pailot, J.-P. Baronick, and M. Lindsey-Clark (2017), TARANIS XGRE and IDEE detection capability of terrestrial gamma-ray flashes and associated electron beams, *Geoscientific Instrumentation, Methods and Data Systems*, 6(2), 239–256, doi:10.5194/gi-6-239-2017.
- Sarria, D., P. Kochkin, N. Østgaard, N. Lehtinen, A. Mezentsev, M. Marisaldi, B. E. Carlson, C. Maiorana, K. Albrechtsen, T. Neubert, V. Reglero, K. Ullaland, S. Yang, G. Genov, B. H. Qureshi, C. Budtz-Jørgensen, I. Kuvvetli, F. Christiansen, O. Charnion, M. Heumesser, K. Dimitriadou, J. Navarro-González, P. Connell, and C. Eyles (2019), The First Terrestrial Electron Beam Observed by the Atmosphere-Space Interactions Monitor, *Journal of Geophysical Research: Space Physics*, 124, doi:10.1029/2019JA027071.
- Shao, X.-M., T. Hamlin, and D. M. Smith (2010), A closer examination of terrestrial gamma-ray flash-related lightning processes, *Journal of Geophysical Research: Space Physics*, 115(A6), doi:10.1029/2009JA014835.
- Smith, D., J. Trepanier, S. T. Alnussirat, M. L. Cherry, M. D. Legault, and D. J. Pleshinger (2021), Thunderstorms Producing Sferic-Geolocated Gamma-Ray Flashes Detected by TETRA-II, *Journal of Geophysical Research: Atmospheres*, 126(15), e2020JD033,765, doi:10.1029/2020JD033765.

- Smith, D. M., R. P. Lin, P. Turin, D. W. Curtis, J. H. Primbsch, R. D. Campbell, R. Abiad, P. Schroeder, C. P. Cork, E. L. Hull, D. A. Landis, N. W. Madden, D. Malone, R. H. Pehl, T. Raudorf, P. Sangsingkeow, R. Boyle, I. S. Banks, K. Shirey, and R. Schwartz (2002), The RHESSI Spectrometer, *Solar Physics*, 210(1), 33–60, doi:10.1023/A:1022400716414.
- Smith, D. M., L. I. Lopez, R. P. Lin, and C. Barrington-Leigh (2005), Terrestrial Gamma-Ray Flashes Observed up to 20 MeV, *Science (New York, N.Y.)*, 307, 1085–8, doi:10.1126/science.1107466.
- Smith, D. M., J. R. Dwyer, B. J. Hazelton, B. W. Grefenstette, G. F. M. Martinez-McKinney, Z. Y. Zhang, A. W. Lowell, N. A. Kelley, M. E. Splitt, S. M. Lazarus, W. Ulrich, M. Schaal, Z. H. Saleh, E. Cramer, H. Rassoul, S. A. Cummer, G. Lu, X.-M. Shao, C. Ho, T. Hamlin, R. J. Blakeslee, and S. Heckman (2011a), A terrestrial gamma ray flash observed from an aircraft, *Journal of Geophysical Research: Atmospheres*, 116(D20), doi:10.1029/2011JD016252.
- Smith, D. M., J. R. Dwyer, B. J. Hazelton, B. W. Grefenstette, G. F. M. Martinez-McKinney, Z. Y. Zhang, A. W. Lowell, N. A. Kelley, M. E. Splitt, S. M. Lazarus, W. Ulrich, M. Schaal, Z. H. Saleh, E. Cramer, H. K. Rassoul, S. A. Cummer, G. Lu, and R. J. Blakeslee (2011b), The rarity of terrestrial gamma-ray flashes, *Geophysical Research Letters*, 38(8), doi:10.1029/2011GL046875.
- Smith, D. M., P. Buzbee, N. A. Kelley, A. Infanger, R. H. Holzworth, and J. R. Dwyer (2016), The rarity of terrestrial gamma-ray flashes: 2. RHESSI stacking analysis, *Journal of Geophysical Research: Atmospheres*, 121(19), 11,382–11,404, doi:10.1002/2016JD025395.
- Smith, D. M., N. A. Kelley, P. Buzbee, A. Infanger, M. Splitt, R. H. Holzworth, and J. R. Dwyer (2020), Special Classes of Terrestrial Gamma Ray Flashes From RHESSI, *Journal of Geophysical Research: Atmospheres*, 125(20), e2020JD033,043, doi:10.1029/2020JD033043.
- Stanley, M. A., X.-M. Shao, D. M. Smith, L. I. Lopez, M. B. Pongratz, J. D. Harlin, M. Stock, and A. Regan (2006), A link between terrestrial gamma-ray flashes and intracloud lightning discharges, *Geophysical Research Letters*, 33(6), doi:10.1029/2005GL025537.
- Suszczynsky, D. M., R. Roussel-Dupre, and G. Shaw (1996), Ground-based search for x rays generated by thunderstorms and lightning, *Journal of Geophysical Research: Atmospheres*, 101(D18), 23,505–23,516, doi:10.1029/96JD02134.
- Svinkin, D., D. Frederiks, K. Hurley, R. Aptekar, S. Golenetskii, A. Lysenko, A. V. Ridnaia, A. Tsvetkova, M. Ulanov, T. L. Cline, I. Mitrofanov, D. Golovin, A. Kozyrev, M. Litvak, A. Sanin, A. Goldstein, M. S. Briggs, C. Wilson-Hodge, A. von Kienlin, X. L. Zhang, A. Rau, V. Savchenko, E. Bozzo, C. Ferrigno, P. Ubertini, A. Bazzano, J. C. Rodi, S. Barthelmy, J. Cummings, H. Krimm, D. M. Palmer, W. Boynton, C. W. Fellows, K. P. Harshman, H. Enos, and R. Starr (2021), A bright gamma-ray flare interpreted as a giant magnetar flare in NGC 253, *Nature*, 589(7841), 211–213, doi:10.1038/s41586-020-03076-9.

- Takahashi, T. (1978), Riming Electrification as a Charge Generation Mechanism in Thunderstorms, *J. Atmos. Sci.*, 35(8), 1536–1548, doi:10.1175/1520-0469(1978)035<1536:REAACG>2.0.CO;2.
- Tavani, M., G. Barbiellini, A. Argan, F. Boffelli, A. Bulgarelli, and et al. (2009), The AGILE Mission, *Astronomy & Astrophysics*, 502(3), 995–1013, doi:10.1051/0004-6361/200810527.
- Tavani, M., M. Marisaldi, C. Labanti, F. Fuschino, A. Argan, and et al. (2011), Terrestrial gamma-ray flashes as powerful particle accelerators, *Phys. Rev. Lett.*, 106, 018,501, doi:10.1103/PhysRevLett.106.018501.
- The Fermi-LAT Collaboration (2021), High-energy emission from a magnetar giant flare in the Sculptor galaxy, *Nature Astronomy*, 5(4), 385–391, doi:10.1038/s41550-020-01287-8.
- Tierney, D., M. S. Briggs, G. Fitzpatrick, V. L. Chaplin, S. Foley, S. McBreen, V. Connaughton, S. Xiong, D. Byrne, M. Carr, P. N. Bhat, G. J. Fishman, J. Greiner, R. M. Kippen, C. A. Meegan, W. S. Paciesas, R. D. Preece, A. von Kienlin, and C. Wilson-Hodge (2013), Fluence distribution of terrestrial gamma ray flashes observed by the Fermi Gamma-ray Burst Monitor, *Journal of Geophysical Research: Space Physics*, 118(10), 6644–6650, doi:10.1002/jgra.50580.
- Ursi, A., C. Guidorzi, M. Marisaldi, D. Sarria, and F. Frontera (2017), Terrestrial gamma-ray flashes in the BeppoSAX data archive, *Journal of Atmospheric and Solar-Terrestrial Physics*, 156, 50 – 56, doi:10.1016/j.jastp.2017.02.014.
- Wada, Y., T. Enoto, Y. Nakamura, Y. Furuta, T. Yuasa, K. Nakazawa, T. Morimoto, M. Sato, T. Matsumoto, D. Yonetoku, T. Sawano, H. Sakai, M. Kamogawa, T. Ushio, K. Makishima, and H. Tsuchiya (2019), Gamma-ray glow preceding downward terrestrial gamma-ray flash, *Communications Physics*, 2(1), 67, doi:10.1038/s42005-019-0168-y.
- Williams, E. R. (1989), The tripole structure of thunderstorms, *Journal of Geophysical Research: Atmospheres*, 94(D11), 13,151–13,167, doi:10.1029/JD094iD11p13151.
- Williams, E. R. (2010), Origin and context of C. T. R. Wilson's ideas on electron runaway in thunderclouds, *Journal of Geophysical Research: Space Physics*, 115(A8), doi:10.1029/2009JA014581.
- Wilson, C. T. R. (1925a), The Acceleration of  $\beta$ -particles in Strong Electric Fields such as those of Thunderclouds, *Proceedings of the Cambridge Philosophical Society*, 22, p. 534–538.
- Wilson, C. T. R. (1925b), The electric field of a thundercloud and some of its effects, *Proc. Phys. Soc. London*, 37, 32D–37D.
- Xu, W., S. Celestin, and V. P. Pasko (2012), Source altitudes of terrestrial gamma-ray flashes produced by lightning leaders, *Geophysical Research Letters*, 39(8), doi:10.1029/2012GL051351.

Zhao, Y., S. Xiong, J. Sun, and H. Yu (2020), Terrestrial Gamma-ray Flashes - POLAR's Observation, in *AGU Fall Meeting Abstracts*, <https://ui.adsabs.harvard.edu/abs/2020AGUFMAE005..10Z>, AE005-10.

# **Chapter 7**

## **Scientific results**



# Paper I

## The 3rd AGILE Terrestrial Gamma Ray Flash Catalog.

### Part I: Association to Lightning Sferics

A. Lindanger, M. Marisaldi, C. Maiorana, D. Sarria, K. Albrechtsen, N. Østgaard, M. Galli, A. Ursi, C. Labanti, M. Tavani, C. Pittori, and F. Verrecchia

*Journal of Geophysical Research: Atmospheres*, **125**, doi:10.1029/2019JD031985, (2020)





# JGR Atmospheres

## RESEARCH ARTICLE

10.1029/2019JD031985

This article is a companion to  
 Maiorana et al. (2020), <https://doi.org/10.1029/2019JD031986>.

### Key Points:

- A sample of 592 AGILE detected TGFs associated to lightning sferics is presented
- TGF duration, geographic dependence of the TGF/lightning ratio, and multipulse TGFs are discussed
- The first Terrestrial Electron Beam detected by AGILE is presented

### Correspondence to:

A. Lindanger,  
 Anders.Lindanger@uib.no

### Citation:

Lindanger A., Marisaldi, M., Maiorana, C., Sarria, D., Albrechtsen, K., Østgaard, N., et al. (2020). The 3rd AGILE terrestrial gamma ray flash catalog. part I: Association to lightning sferics. *Journal of Geophysical Research: Atmospheres*, 125, e2019JD031985. <https://doi.org/10.1029/2019JD031985>

Received 5 NOV 2019

Accepted 15 JAN 2020

Accepted article online 7 APR 2020

## The 3rd AGILE Terrestrial Gamma Ray Flash Catalog. Part I: Association to Lightning Sferics

**A. Lindanger<sup>1</sup> , M. Marisaldi<sup>1,2</sup> , C. Maiorana<sup>1</sup> , D. Sarria<sup>1</sup> , K. Albrechtsen<sup>1</sup> , N. Østgaard<sup>1</sup> , M. Galli<sup>3</sup> , A. Ursi<sup>4</sup>, C. Labanti<sup>2</sup>, M. Tavani<sup>4</sup>, C. Pittori<sup>5,6</sup> , and F. Verrecchia<sup>5,6</sup>**

<sup>1</sup>Birkeland Centre for Space Science, Department of Physics and Technology, University of Bergen, Bergen, Norway, <sup>2</sup>INAF-OAS Bologna, Bologna, Italy, <sup>3</sup>ENEA, via Martiri di Monte Sole 4, Bologna, Italy, <sup>4</sup>INAF-IAPS Roma, Rome, Italy, <sup>5</sup>Space Science Data Center - Agenzia Spaziale Italiana, Roma, Italy, <sup>6</sup>INAF - Osservatorio Astronomico di Roma, Monte Porzio Catone, Roma, Italy

**Abstract** We present a complete and systematic search for terrestrial gamma-ray flashes (TGFs), detected by AGILE, that are associated with radio sferics detected by the World Wide Lightning Location Network (WWLLN) in the period February 2009 to September 2018. The search algorithms and characteristics of these new TGFs will be presented and discussed. The number of WWLLN identified (WI) TGFs shows that previous TGF selection criteria needs to be reviewed as they do not identify all the WI TGFs in the data set. In this analysis we confirm with an independent data set that WI TGFs tend to have shorter time duration than TGFs without a WWLLN match. TGFs occurs more often on coastal and ocean regions compared to the distribution of lightning activity. Several multipulse TGFs were identified and their WWLLN match are always associated with the last gamma-ray pulse. We also present the first Terrestrial Electron Beam detected by AGILE. This data set together with the TGF sample identified by selection criteria (companion paper Maiorana et al., 2020) constitute the 3rd AGILE TGF catalog.

### 1. Introduction

Terrestrial gamma-ray flashes (TGFs) are sub-millisecond bursts of energetic photons produced in the Earth's atmosphere and are associated with lightning flashes (Dwyer, 2012). They were first observed by the BATSE instrument onboard the Compton Gamma-ray Observatory in 1991 and were reported by Fishman et al. (1994). Since then, TGFs have been detected by RHESSI (Albrechtsen et al., 2019; Grefenstette et al., 2009; Gjesteland et al., 2012; Østgaard et al., 2015; Smith et al., 2005), Fermi (Briggs et al., 2013; Roberts et al., 2018), AGILE (Marisaldi et al., 2010, 2014, 2015), and BeppoSAX (Ursi et al., 2017). The newest addition to space missions capable of detecting TGFs is the Atmospheric-Space Interactions Monitor (ASIM) mission, which became operational in June 2018 (Neubert et al., 2019).

In the first era of TGF detection, gamma-ray data from satellites provided the main insight into the physics of TGFs. However, to expand our knowledge supporting data from ground-based stations are necessary. As TGFs are associated with lightning flashes, the geolocation of the lightning associated to the TGF provides the source location of the TGF. To perform spectral analysis of a TGF, the production location is vital to correctly model the propagation of photons through the atmosphere reaching the satellite.

There are two main methods to identify TGFs in gamma-ray data. The gamma-ray data can be filtered by search algorithms, using some selection criteria (SC) to find the TGFs. These SC are not trivial to decide and are a trade-off between a clean sample of fewer but bright TGFs with low contamination of false TGFs, and a large sample containing more faint TGFs with risk for contamination from false TGFs. After the TGFs are identified with SC, they can be correlated with lightning flashes detected by ground stations. The other method is to start with lightning measurements and look at gamma-ray data detected by the satellite at the time of lightning. This method is able to identify weaker TGFs but is limited by the efficiency of the lightning network. The last method has previously been performed on RHESSI (Albrechtsen et al., 2019; Østgaard et al., 2015; Smith et al., 2016) and Fermi data (McTague et al., 2015), using ground-based lightning data.

In 2015, the AGILE TGF detection rate increased with one order of magnitude after the anticoincidence (AC) shield acting on the onboard mini-calorimeter (MCAL) was disabled (Marisaldi et al., 2015).

**Table 1**  
*Main Characteristics of the Different Data Sets*

Name	Date	AC shield	Timing accuracy
AC-ON	28 February 2009 to 23 March 2015	On	~2 μs
REF	23 March 2015 to 30 June 2015	Off	~2 μs
DRIFT	01 July 2015 to 31 December 2017	Off	Several tens of ms
3D-FIX	17 January 2018 to 30 September 2018	Off	~2 μs

This has led to an intensive search for TGFs in the AGILE data, to further populate the AGILE TGF catalog.

For the first time, a complete and systematic search for TGFs based on time correlation with the World Wide Lightning Location Network (WWLLN) has been applied to all available MCAL data up to September 2018. The search for TGFs based only on WWLLN data has no bias from SC, other than the WWLLN efficiency itself. As the WWLLN detection efficiency is limited (Abarca et al., 2010; Bürgesser, 2017; Rudlosky & Shea, 2013), not all TGFs can be identified in the satellite data using time correlation with WWLLN data. Therefore, a WWLLN identified (WI) TGF sample can make the basis for deciding appropriate new SC to identify TGFs without associated WWLLN detections. These new SC are discussed in the companion paper by Maiorana et al. (2020), hereafter referred to as M20.

In the following sections, we present the data sets and the methods used in this analysis, the results from the different data periods of AGILE, a discussion of the findings, and a summary and conclusions section at the end.

## 2. Data Sets

The MCAL onboard AGILE includes 30 independent self-triggering CsI(Tl) scintillator bars with an energy range ~0.35–100 MeV (Labanti et al., 2009). One should note that MCAL is triggered; for example, data are stored in the internal memory and sent to ground only if a significant excess of counts is detected in the specific time window and does not run in continuous data acquisition mode. Therefore, only a fraction of the measured data is downloaded to telemetry. Additional information on the instrument performance is included in M20.

We divide the MCAL data into four different subsets characterized by the absolute timing accuracy and if the AC shield is active on the instrument or not. A summary of the data sets is shown in Table 1.

The AC-ON data set spans from 28 February 2009 to 23 March 2015. In this period, the AC shield is active on MCAL and strongly limit the detection of brief duration events (Marisaldi et al., 2014) such as TGFs. The onboard absolute timing accuracy is on ~2 μs level.

The reference (REF) data set spans from 23 March 2015 to 30 June 2015. The AC shield is disabled for MCAL from the onset of this period, resulting in an enhanced TGF detection rate (Marisaldi et al., 2015).

The DRIFT data set spans from 1 July 2015 to 31 December 2017. An issue with the onboard GPS caused a degradation of the AGILE μs timing performance and the absolute time accuracy started “drifting”. This drift is a systematic offset in time that remains constant for periods between days and weeks, and then suddenly “jumps” to a different value. The AGILE team performed a time correction of the offset using housekeeping data, resulting in an absolute timing accuracy of several tens of milliseconds.

The 3D-FIX data set spans from 17 January 2018 to 30 September 2018. After the DRIFT period, the GPS partly recovered and the AGILE team is able to perform a time correction down to ~2 μs level, thus restoring the original timing accuracy of the instrument.

Lightning data are obtained from the WWLLN (Rodger et al., 2009) and provide time and geolocation by detecting very low frequency sferics produced by lightning flashes. Although many different sensors and lightning detection networks have been used in TGF studies (Marshall et al., 2013), WWLLN has become a standard choice and a benchmark following the work by Connaughton et al., (2010, 2013).

The timing uncertainty of WWLLN depends on the location uncertainty. Abarca et al. (2010) found an average location error of 4.03 km in the northward direction and an error of 4.98 km in the westward direction.

Hutchins et al. (2012) report that in 2011, WWLLN located 61% of the strokes within 5 km. Østgaard et al. (2013) assumed a time and location accuracy of 45  $\mu$ s and 15 km, respectively. In this work, we assume a location uncertainty of 15 km as well.

### 3. Method

In this paper, two methods are used to search for TGFs. Stacking analysis, and the so-called “search for clusters analysis.” Both methods are based on time correlation with WWLLN detections.

#### 3.1. Stacking Analysis

For every WWLLN detection within 1,000 km from the subsatellite point, a MCAL photon list is built according to equation (1), which is the time difference between the WWLLN detection and the list of counts detected by MCAL, corrected for propagation time. These photon lists are then superposed and binned. The motivation for this is to identify the few photons associated to lightning that would be indistinguishable from background without WWLLN association.

$$\delta t = \text{time}_{\text{MCAL}} - \text{time}_{\text{propagation}} - \text{time}_{\text{WWLLN}}. \quad (1)$$

The 1,000-km limit, which we will call the TGF field of view (FOV), is selected because most TGFs are detected within  $\sim$ 500 km from the subsatellite point, and very few farther away than 800 km, as it will be shown in section 4, consistent with earlier results (Collier et al., 2011; Cummer et al., 2005; Marisaldi et al., 2019). The propagation time of the photons is calculated assuming a production altitude of 15 km, which is a fair assumption based on modeling results from Dwyer and Smith (2005) and the expectation that TGFs detected from space are preferentially produced close to thunderstorm cloud tops.

#### 3.2. Search for Clusters Analysis

As stacking analysis relies on timing accuracy on few hundred of microseconds or better to be effective, a new “search for clusters analysis” (SFC) was developed and implemented due to the decreased timing accuracy in the DRIFT period. The method was then also applied to the REF and 3D-FIX periods. The idea is to look at light curves and only keep histogram bars with large counts per 100  $\mu$ s, assuming that a TGF is seen as an increased flux of counts, or a “cluster of photons” in a light curve. This is possible as the relative timing accuracy of MCAL count timestamps is still at microseconds level and the absolute timing offset is on tens of milliseconds level. The signal is defined to be a time window close to the WWLLN detection, and the background signal is defined to be some seconds before the WWLLN detection, well separated from the signal. The algorithm is described below and in Figure 1.

1. Build a light curve of MCAL photon data for each WWLLN detection for both signal and background time intervals.
2. Build the distribution of number of counts per 100  $\mu$ s bin for each light curve.
3. Superpose the distributions of counts per 100  $\mu$ s bin found in Point 2.
4. Set a threshold based on signal vs. background.
5. Define events with counts per 100  $\mu$ s bin higher than the selected threshold as TGF candidates.

Based on the distribution of counts per 100  $\mu$ s in Figure 1c, we select a threshold of  $x$  counts per 100  $\mu$ s. The fraction of false positive TGFs is estimated by taking the integral from the selected threshold to 20 for background and signal and divide the background integral by the signal integral. The threshold is a trade-off between the number of TGF candidates and the fraction of false positive TGFs. Note that a plot equivalent to Figure 1c is shown with real data in Figures 3c and 5c, while a plot equivalent to Figure 1d is shown with real data in Figure 4c.

#### 3.3. TGF Candidates Processing

After the TGF candidates are identified, each TGF is fitted by a Gaussian function on top of a constant background by means of an unbinned maximum likelihood technique. The intensity, peak time, and duration of each TGF are extracted from the parameters of the fit. The TGF duration is calculated as  $t_{50} = 1.349\sigma$ , where  $\sigma$  is the standard deviation from the Gaussian fit, and  $t_{50}$  is the central time interval including 50% of the counts. This method is described in Marisaldi et al. (2015).

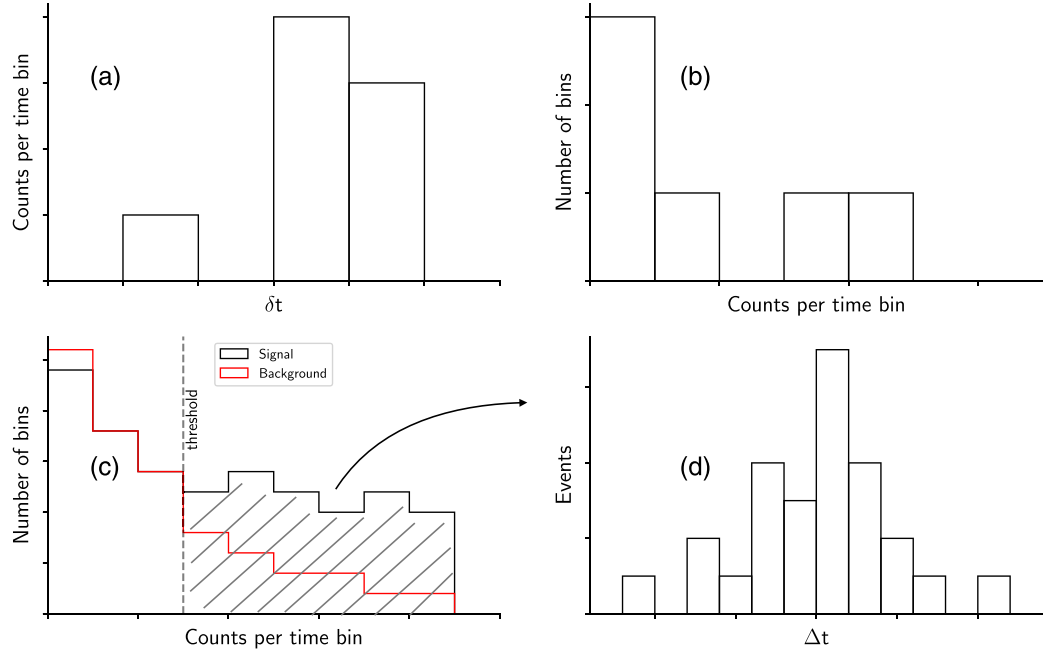


**Figure 1.** Illustration of the search for clusters analysis. (a) A single light curve associated with a WWLLN detection. (b) Distribution of number of counts per time bin for the single light curve. (c) Superposed distributions of number of counts per time bin associated to WWLLN detections in black and superposed distribution of background in red. A threshold is indicated by a dotted line. (d) The time difference between events with counts per time bin over the selected threshold, and WWLLN detections, corrected for propagation time.

If a TGF is associated with several WWLLN detections within the  $\delta t$  range of the light curve, the algorithm will report the same TGF several times, depending on the number of associated WWLLN detections. We remove the duplicates by keeping the entry corresponding to the closest WWLLN detection in time.

We also determine if the TGFs occurs over land, coast, or ocean. Like the First Fermi-GBM TGF catalog (Roberts et al., 2018), we use the pre-calculated distance to shore file (<https://www.soest.hawaii.edu/wessel/gshhg/>) that is provided from the Global Self-consistent, Hierarchical, High-resolution Geography Database (Wessel & Smith, 1996). We define the coast as  $\pm 150$  km from the shoreline.

#### 4. Results

In this section, the results of the analysis for the different data sets are presented. The number of TGF candidates and the expected fraction of spurious signal, incorrectly identified as TGFs, are shown in Table 2. The fraction of incorrectly identified TGFs is estimated by taking the integral from the selected threshold to 20 for background and signal and divide the background integral by the signal integral. The threshold is 4 for REF and 5 for 3D-FIX.

**Table 2**  
Number of TGFs Associated to WWLLN and Expected Background Contamination

Name	#TGFs	Fraction of incorrectly identified TGFs
AC-ON	0	n/a
REF	111	0.03
DRIIFT	310–1,294	n/a
3D-FIX	171	0.01

Abbreviations: TGFs, terrestrial gamma-ray flashes; WWLLN, World Wide Lightning Location Network.

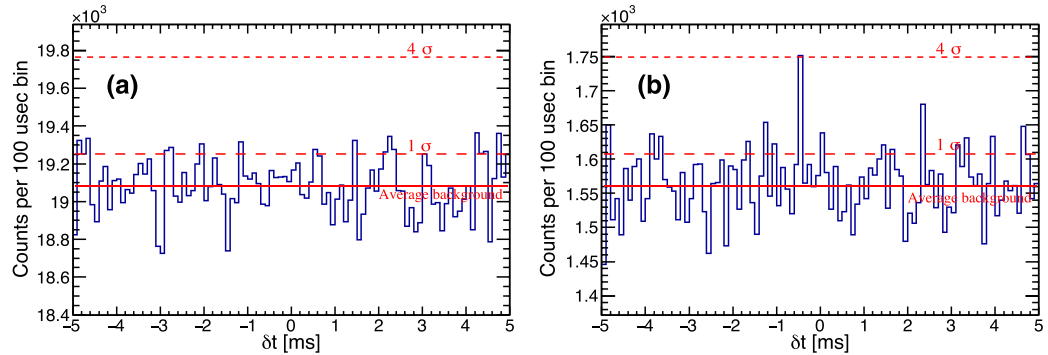


**Figure 2.** AC-ON period. (a) Stackplot of counts detected by MCAL for 440,234 WWLLN detections within 1,000 km from subsatellite point. (b) Stackplot of counts detected by MCAL for WWLLN detections within 300 km from the subsatellite point, and energies below 100 MeV.

#### 4.1. AC-ON Period

A stack plot of the MCAL data for 440,234 WWLLN detections is shown in Figure 2a. There is no significant peak visible at  $\delta t \approx 0$  confirming that the AC shield is suppressing the TGF signal as suggested in Marisaldi et al. (2014).

As most TGF-WWLLN matches occur within few hundred kilometer from the subsatellite point, a new stack plot, shown in Figure 2b, was calculated considering only WWLLN detections within 300 km from the subsatellite point and MCAL counts below 100 MeV. The distance and energy limit enhances the signal-to-noise

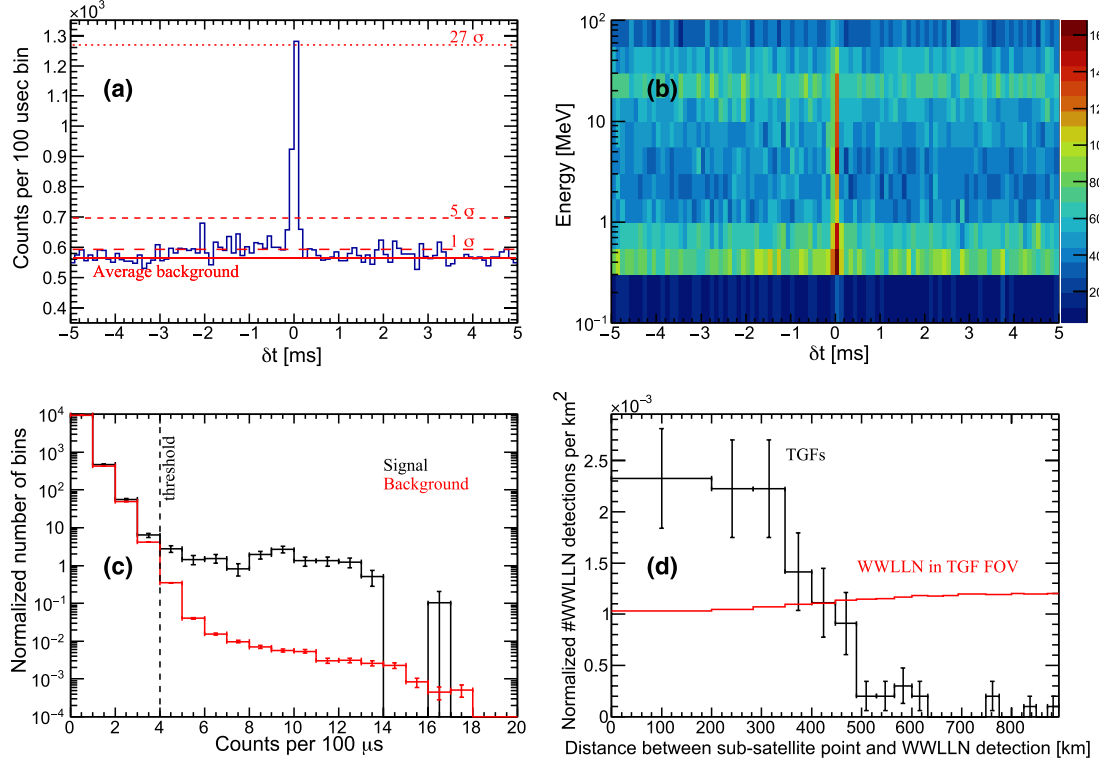


**Figure 3.** REF period. (a) Stack plot of MCAL counts for 9,754 WWLLN detections within 1,000 km from subsatellite point. (b) Energy of the counts in (a) detected by MCAL in the full energy band 0.35–100 MeV. The unit of the color scale is counts per 100  $\mu$ s per energy bin. (c) Distribution of counts per 100  $\mu$ s time bin for the REF period. The signal includes counts with  $|\delta t| \leq 500 \mu\text{s}$  and is normalized per 1 ms per 9,754 WWLLN detection. The background includes counts with  $\delta t$  between -3.5 and -2 s and is normalized per 1.5 s per 10,453 WWLLN detection. (d) WI TGFs in black, and all WWLLN detections in the TGF FOV in red, as a function of distance from the subsatellite point to WWLLN detection. Each distribution is normalized to 1.

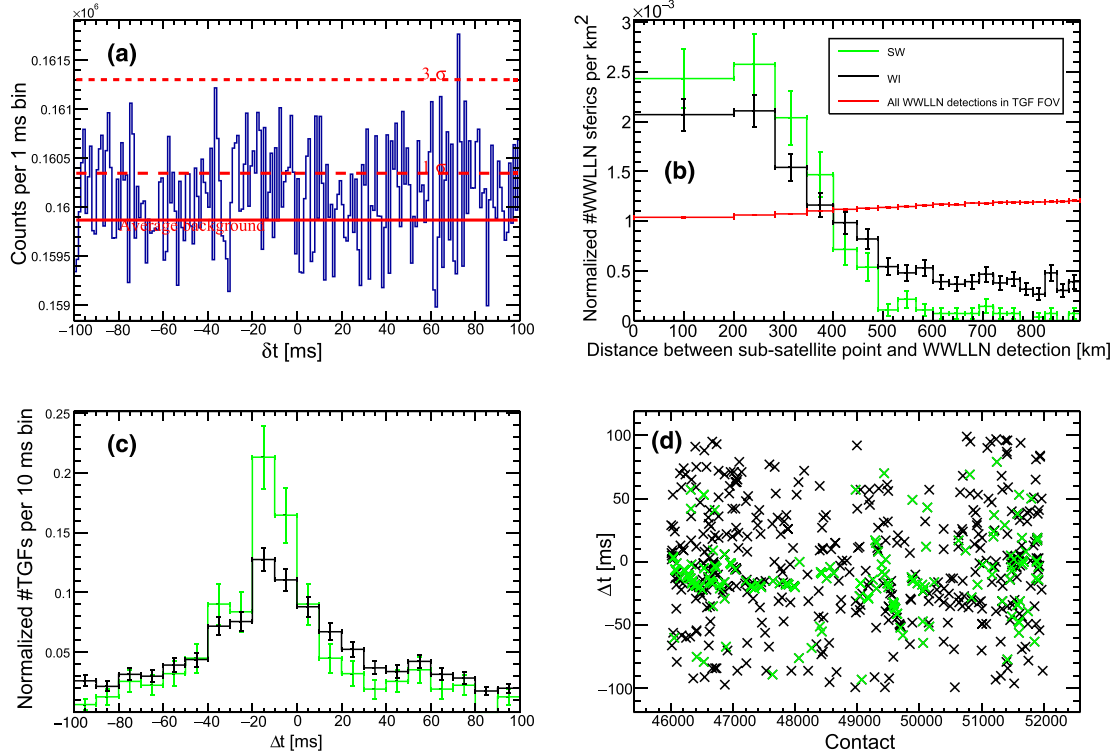


**Figure 4.** DRIFT period. Plots (b), (c), and (d) have the same color legend. (a) Stackplot of MCAL counts for 265,165 WWLLN detections within 1,000 km from subsatellite point. (b) WI TGFs in black, WI TGFs that are also identified with SC in green (SW), and all WWLLN detections in the TGF FOV in red, as a function of distance from the subsatellite point to WWLLN detection. Each distribution is normalized to 1. (c) The time difference between TGFs and WWLLN detections, corrected for propagation time, for the TGF candidates. (d) The time difference between TGFs and WWLLN detections, corrected for propagation time, as a function of contacts, which is a proxy for time as one contact is the orbit number counting from the first AGILE orbit.

ratio as TGFs far from the subsatellite point are weaker due to atmospheric attenuation, and counts above 100 MeV are expected mostly to be cosmic rays. Note that a peak of four standard deviations is obtained at  $\delta t \approx -0.5$  ms. This could be due to the detection of the first counts associated to TGFs before the AC shield suppresses the counts. However, this peak is farther from  $\delta t = 0$  than expected; therefore, we cannot draw firm conclusions on it.

The SFC analysis is not applied to the AC-ON data set, as the AC-shield suppresses any clusters associated to WWLLN detections.

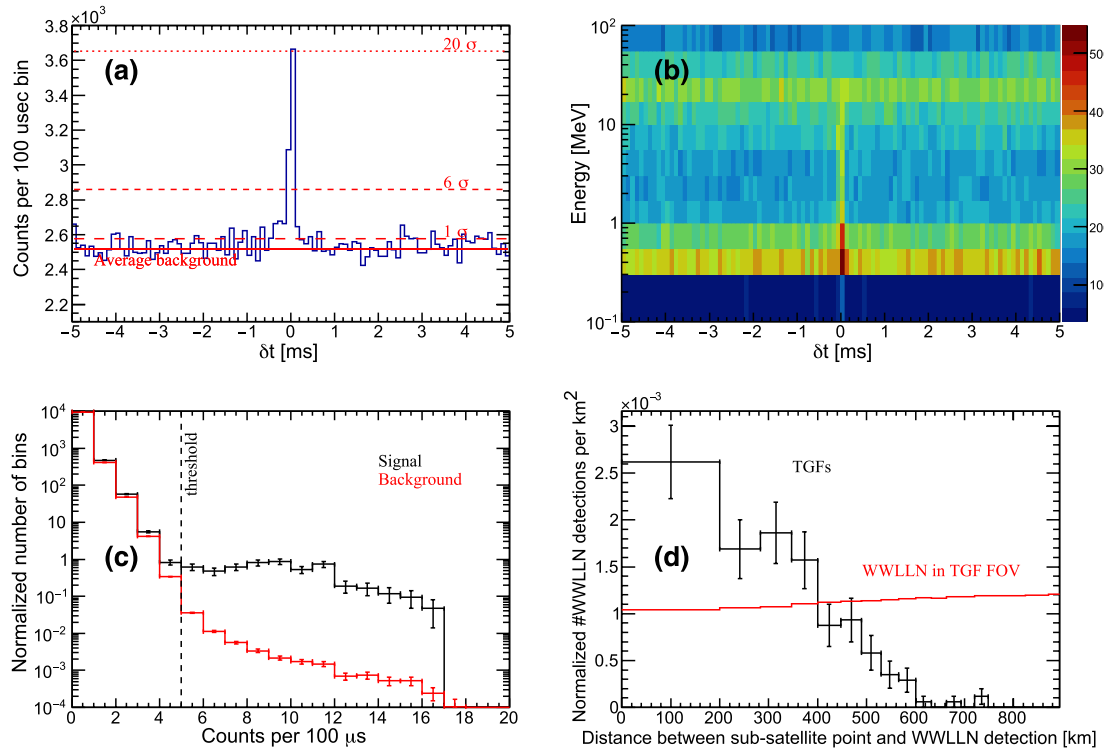
#### 4.2. REF Period

Figure 3a shows the stack plot for 9754 WWLLN detections in the REF period. The significance of the peak is  $\sim 27$  standard deviations and shows a clear time correlation between counts in MCAL and WWLLN detections. If we remove known TGFs identified by Marisaldi et al. (2015), we obtain a 16 sigma peak showing that not all TGFs-WWLLN matches are found by the SC described in Marisaldi et al. (2015).

The energy of the counts in Figure 3a is shown in Figure 3b. The peak at  $\delta t \approx 0$  indicates the energy range of the photons associated with the TGFs. Note that the energy spectrum is not corrected for background and instrumental effects.

The SFC analysis is applied to the data to identify the TGFs. Based on the distribution of counts per 100  $\mu$ s bin shown in Figure 3c, we select a threshold of 4 counts per 100  $\mu$ s. This identifies a total of 111 WI TGFs. The expected contamination of false positive TGFs is 3%. If we exclude the 111 WI TGFs from the stack plot in Figure 3a, we obtain no peak at  $\delta t \approx 0$ . Thus, the SFC analysis identifies all significant TGF-WWLLN matches in the REF period data set.

Figure 3d shows the distance between the subsatellite point and the associated WWLLN detection for the WI TGFs in black, and all WWLLN detections in the TGF FOV in red. The distance bin size is chosen so that the



**Figure 5.** 3D-FIX period. (a) Stackplot of MCAL counts for 42,243 WWLLN detections within 1,000 km from subsatellite point. (b) Energy of the counts in (a) detected by MCAL in the full energy band 0.35–100 MeV. The unit of the color scale is counts per 100  $\mu$ s per energy bin. (c) Distribution of counts per 100  $\mu$ s time bin for the 3D-FIX period. The signal includes counts with  $|\delta t| \leq 500 \mu$ s and is normalized per 1 ms per 42,243 WWLLN detection. The background includes counts with  $\delta t$  between  $-2.7$  and  $-2.1$  s and is normalized per 0.6 s per 47,966 WWLLN detection. (d) Number of TGFs, as a function of distance from the subsatellite point to WWLLN detection, and all the WWLLN detections in the TGF FOV. Each distribution is normalized to 1.

circular area, corresponding to each bin, is constant and equal to  $125,664 \text{ km}^2$ . In agreement with Cummer et al. (2005), Collier et al. (2011), and Marisaldi et al. (2019), most TGFs are detected within  $\sim 500$  km from the subsatellite point, and very few TGF are detected farther away than 800 km. The red WWLLN distribution is not flat due to the nonconstant latitude distribution of the WWLLN detections and AGILE's orbital inclination angle.

#### 4.3. DRIFT Period

Figure 4a shows the stack plot for the DRIFT period with  $\delta t$  range of  $\pm 100$  ms and bin size of 1 ms. As the absolute time accuracy is not on microsecond level, data do not show a peak at  $\delta t \approx 0$ . The SFC analysis is applied in order to improve the signal-to-noise ratio, and all events with  $\delta t$  within  $\pm 100$  ms and a threshold of 7 counts per 100  $\mu$ s is defined as TGF candidates. We choose 7 counts following the same approach as REF and 3D-FIX but the threshold needed to be higher due to the decreased absolute timing accuracy. This identifies 1,294 WI TGF candidates shown in Figures 4b, 4c, and 4d in black color. However, there is evidence of a flat component in Figure 4b in the WI TGFs. TGFs with distance longer than  $\sim 500$  km from the subsatellite point can be real TGFs, but we do not expect many of them. The flat component indicates the contamination of false events and suggests that at least 33% of the WI TGF candidates are false TGFs.

To further enhance the signal-to-noise ratio, we compared the WI TGF candidates from the SFC analysis with the TGFs identified with SC in M20. There are 310 joint TGFs (selection criteria satisfied and WWLLN identified, SW hereafter) and these are shown in green color in Figures 4b, 4c, and 4d. (See figure 2 in the companion paper M20 for a graphical overview of SC, SW, and WI TGFs.) The SW TGFs further enhance the signal-to-noise ratio as seen in Figure 4b, where the number of TGF-WWLLN matches close to the subsatellite point are relatively higher for the SW TGFs, and lower for distances far from the subsatellite point, compared to the WI TGF candidates. Also in Figure 4c, we see a higher peak and lower background component for the SW TGFs, compared to the WI TGF candidates.

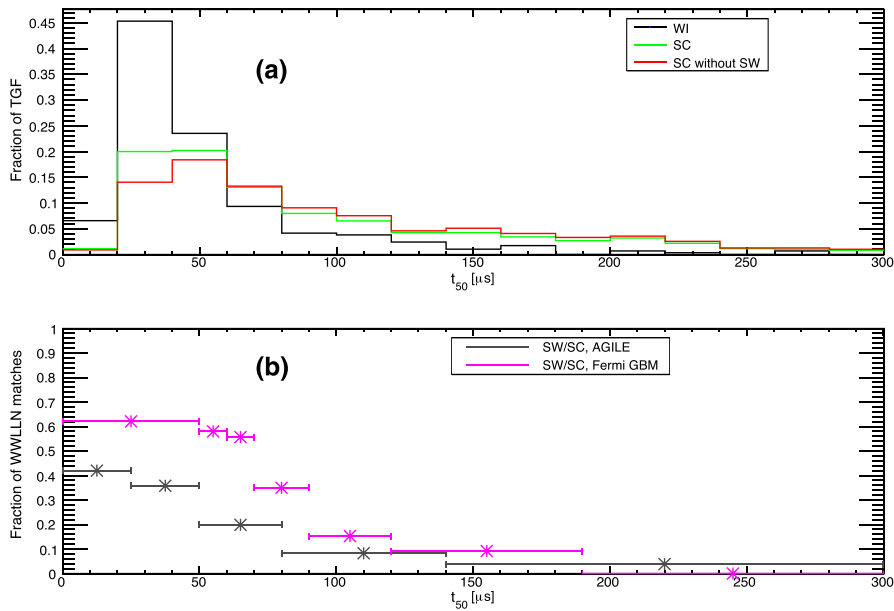


**Figure 6.** (a) Normalized  $t_{50}$  distributions for WI, SC, and SC without SW. (b) Comparison of fraction of WWLLN matches from AGILE and Fermi TGFs.

From Figure 4c, we see that the absolute timing accuracy in the DRIFT period is  $\sim 30$  ms, with an offset of approximately  $-17$  ms. However, the offset varies with time. That is evident in Figure 4d, which shows the time difference between the TGF and the WWLLN detection, corrected for propagation time, as a function of time between March 2016 and May 2017. “Contact” is the orbit number counting from the first orbit of AGILE, where one orbit is  $\sim 94$  min. Considering only the SW TGFs, we see that between contact 46,000 and 48,000, the timing uncertainty seems to be approximately  $\pm 25$  ms, and between contact 49,200 and 49,800, there seems to be a linear negative slope, indicating a constantly decreasing offset. After contact  $\sim 51,000$  the absolute timing uncertainty is approximately  $\pm 100$  ms.

#### 4.4. 3D-FIX Period

Figure 5 is the result from the same analysis as for the REF period, applied to the 3D-FIX period. These plots show the same characteristics as in Figure 3. Figure 5a has a peak of  $\sim 20$  standard deviations at  $\delta t \approx 0$ . Based on the signal-background ratio in Figure 5c, we selected a threshold of 5 counts per 100  $\mu$ s and identified a total of 171 TGFs. The expected contamination of false TGFs is 1%. If we exclude the 171 WI TGFs from the stack plot in Figure 5a, we obtain no peak at  $\delta t \approx 0$ , indicating that the SFC analysis identifies all the WI TGFs in this data set, also. The energy peak in Figure 5b is less bright compared to Figure 3b in the REF period because the noise has slightly increased. This is the reason why we cannot set the threshold to 4 as in the REF period. The differences between the REF and 3D-FIX periods in terms of significance of the TGF peak, energies, and TGF detection rate can be explained by the combination of seasonal variability (different data span) and increased instrumental noise.

## 5. Discussion

The stacking analysis for the REF period reveals that the selection criteria in Marisaldi et al. (2015) needs to be reviewed as the SC did not identify all the WI TGF found by the SFC analysis. This is discussed further in the companion paper by M20.

Due to the large timing uncertainty in the DRIFT period, we are dependent on selection criteria to identify the TGFs. Therefore, we exclude the DRIFT period from the discussion, except in section 5.1, to prevent introducing a bias due to selection criteria and to keep the sample purely based on WI TGFs. In the following sections, we discuss the absolute timing accuracy of AGILE, the duration of WI TGFs, multipulse TGFs, local time and geographical distributions, and the first Terrestrial Electron Beam (TEB) detected by AGILE.

### 5.1. Diagnostics of AGILE Timing Accuracy by TGF-WWLLN Correlation

After the issue with the onboard GPS at the start of the DRIFT period, the AGILE team performed a time correction procedure using housekeeping data. The SFC analysis provides an independent assessment of the goodness and effectiveness of this time correction. Due to the low absolute timing uncertainties of WWLLN, it is possible to use TGF-WWLLN correlations to correct the onboard satellite clock. This has previously been done on RHESSI data (Mezentsev et al., 2016). The TGF-WWLLN correlations evidenced previously unidentified trends in the DRIFT period, impossible to identify by house keeping data measurements (Figures 4c and 4d). In the 3D-FIX period, the authors of this paper identified a systematic time offset of 4 ms, constant with time. This time offset correction is already implemented in the gamma-ray data processing pipeline by the AGILE team, prior to the complete data analysis resulting in this paper. In this regard, checking AGILE data against WWLLN data provides a valuable, independent diagnostics of the AGILE timing accuracy.

### 5.2. Duration of TGFs and the Rate of Association with WWLLN

In Figure 6a, we see that the  $t_{50}$  distribution of WI TGFs peaks in the range 20–40  $\mu$ s. This is consistent with the predictions by Connaughton et al. (2013) showing that a TGF will produce a radio signal with a peak spectral energy density at 10 kHz (which is similar to lightning, and where WWLLN is optimized for), when  $t_{50} = 21.5 \mu$ s.

The  $t_{50}$  distribution of the TGFs identified with the SC in M20, and the  $t_{50}$  distribution of the TGFs in SC that are not WI are also shown. These samples are biased towards longer duration with respect to the WI sample. Figure 6b shows the fraction SW/SC for AGILE TGFs and Fermi-GBM TGFs (from figure 3 in Connaughton et al., 2013). It is hard to do a quantitative comparison of the distributions as the instruments are different, the orbital inclination are different, as well as the data span and the efficiency of WWLLN over different geographical regions. However, the trend from the two missions are compatible, where brief duration TGFs have a higher fraction of WWLLN matches.

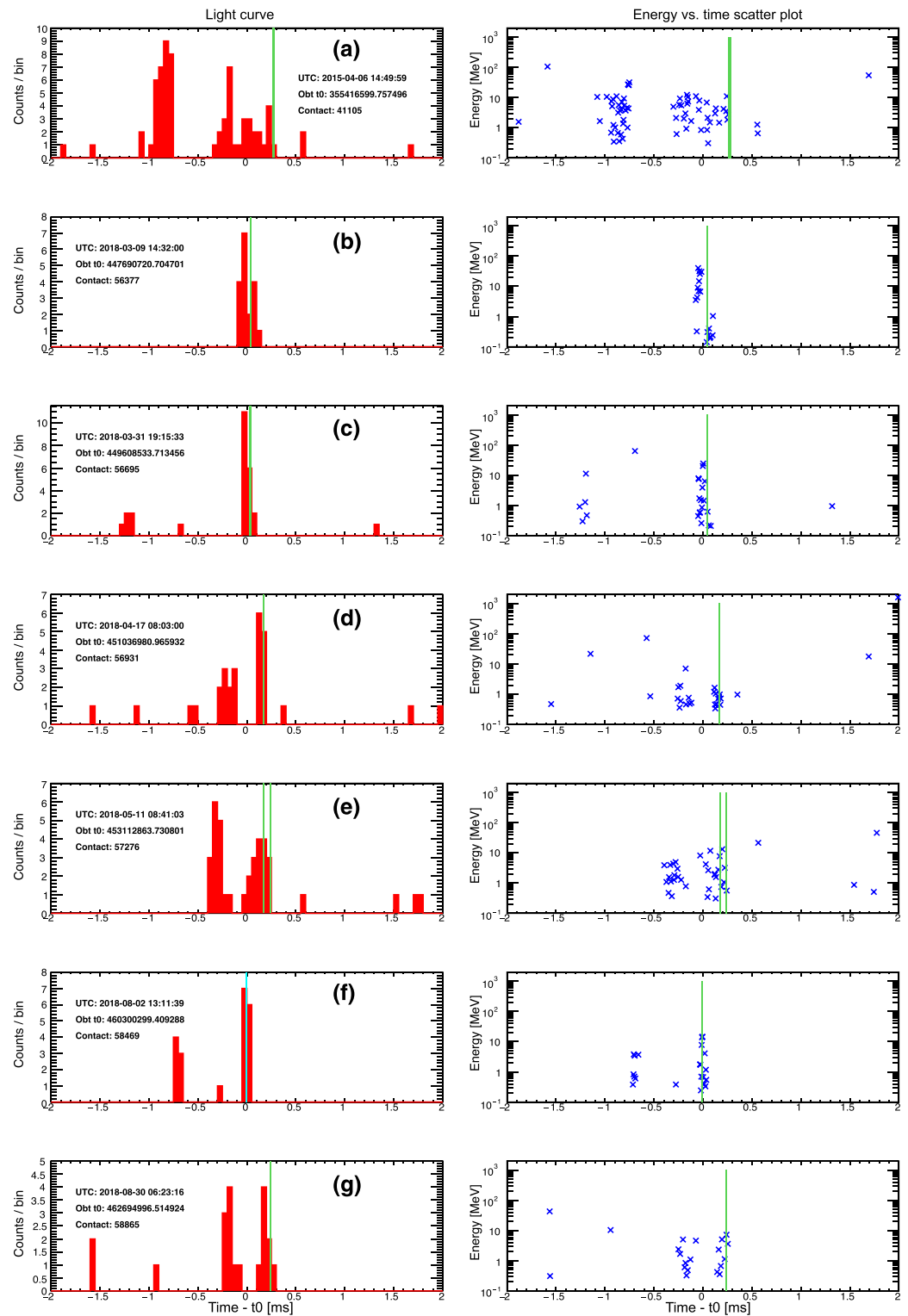
### 5.3. Multipulse TGFs

Mezentsev et al. (2016) observed 16 multipulse TGFs out of 314 TGF-WWLLN matches in RHESSI data. In these 16 multipulse TGFs, the WWLLN detection is always associated with the last TGF peak. Motivated by this finding, we manually checked the 284 TGFs in the REF- and 3D-FIX period looking for multipulse TGFs. We identified seven multipulse TGFs shown in Figures 7a to 7g. The first (a) multipulse TGF is already reported in Mezentsev et al. (2016). TGF (b) has a small time separation between pulses, suggesting that it might not be a multipulse event. However, the two candidate pulses exhibit different spectral characteristics. The second pulse is much softer than the first pulse suggesting spectral evolution with time. The third multipulse TGF (c) has a rather weak first peak. The other multipulse TGFs (d–g) are clearly multipulse TGFs with  $\sim 0.5$  ms between each peak. The multipulse TGFs observed by AGILE confirms, with an independent data set the findings of Mezentsev et al. (2016), that the WWLLN detection is always associated with the last pulse in a multipulse TGF. We found no multipulse TGFs with WWLLN associated with the first pulse. Note that sometimes WWLLN detect the same lightning flash twice, as seen in Figure 7e. The distance between the locations of the “double” lightning detections are within the uncertainties of WWLLN suggesting that the stroke responsible for the two detections is the same.

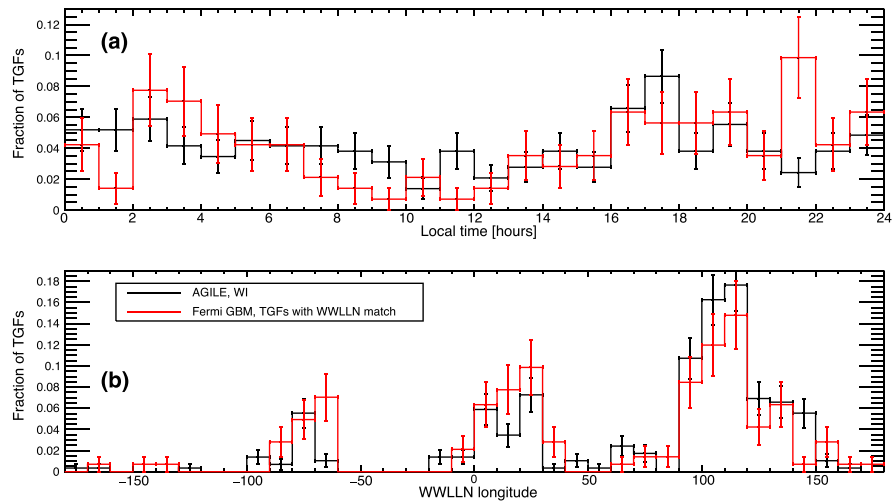
### 5.4. Local Time and Geographical Distribution

Figure 8a shows the local time distribution of AGILE WI TGFs compared with TGFs with a WWLLN association from the first Fermi-GBM TGF catalog (Roberts et al., 2018). The position of Fermi is restricted to the same latitude band as AGILE, giving a total of 142 Fermi-GBM TGFs with a WWLLN match. Figure 8b shows the longitudinal distributions of AGILE WI TGFs and Fermi-GBM TGFs with a WWLLN match. As in Figure 8a, Fermi is restricted to  $\pm 2.5^\circ$  latitude. The distributions show a consistent behavior.

Like in Albrechtsen et al. (2019), we investigated whether the TGFs are located over land, ocean, or coast. We define the coast as  $\pm 150$  km from the shoreline, and the simultaneous WWLLN matches are used to estimate the production origin of the TGFs. In Table 3, the number and percentage of TGFs detected over ocean, coast and land are shown. We also calculated the number and percentage of WWLLN detections within the TGF FOV in the REF and 3D-FIX period. This parameter basically accounts for both satellite exposure time and WWLLN efficiency over the different regions. Note that the WWLLN percentage distribution is not uniform like in Albrechtsen et al. (2019) where WWLLN detections below RHESSI is approximately



**Figure 7.** Light curve and energy vs. time scatter plot for the seven multipulse TGFs found in the REF and 3D-FIX periods. The bin size is 50  $\mu$ s. The WWLLN detections, corrected for propagation time, is indicated as a green vertical line.



**Figure 8.** (a) Local time of AGILE WI TGFs in black, and Fermi-GBM TGFs with WWLLN match in red. (b) Longitude distributions of AGILE WI TGFs in black, and Fermi-GBM TGFs with WWLLN match in red. Fermi is restricted to the same latitude band as AGILE ( $\pm 2.5^\circ$ ).

one third each over ocean, coast, and land. This may be explained by the much large orbital inclination of RHESSI compared to AGILE. It is evident that TGFs detected by AGILE, like both Fermi-GBM and RHESSI (Albrechtsen et al., 2019; Roberts et al., 2018), are mostly detected over coastal regions. If TGFs follow exactly the lightning distribution, the probability of having a TGF at the coast would be 0.51. If we consider whether a TGF is produced at the coast or not as a binomial process with probability of success 0.51, the probability of having 184 successes out of 282 trials is in the order of  $10^{-7}$ . Doing the same calculation for land and ocean gives a probability of  $\sim 10^{-5}$  and 0.02, respectively. This shows that the ocean, land, coast distribution of TGFs does not follow the ocean, land, coast distribution of lightning detected by WWLLN. TGF production occurs relatively more often  $\pm 150$  km from the coastline. This is also evident in Figure 9, where the AGILE WI TGFs, and TGFs with WWLLN matches from Fermi-GBM, are plotted together with the LIS 0.1 Degree Very High Resolution Gridded Lightning Full Climatology (VHRFC) dataset. The VHRFC dataset is gridded lightning rate density from the Lightning Imaging Sensor (LIS) from 1998 to 2013 (Albrecht et al., 2016). The color bar indicates flash rate density with unit flashes per square km per year. Fermi-GBM is not restricted to  $\pm 2.5^\circ$  latitude in this figure. The three maps corresponds to each of the three lightning chimneys in Figure 8b. Figure 9a shows mainly Colombia and Ecuador, Figure 9b shows West and Central Africa, and Figure 9c shows the Borneo Sumatra regions. The lack of TGFs south of Colombia is due to the South Atlantic Anomaly. We see that the TGFs follow the lightning activity, but clusters more on the coast than over ocean and land. Where there is high lightning activity on land, like in the Congo basin, more TGFs are observed. These results contribute to the discussion of the geographical asymmetry in the TGF/lightning ratio, already addressed in Smith et al. (2010), Fuschino et al. (2011), Briggs et al. (2013), and recently discussed in Fabrò et al. (2019) specially concerning the physical characteristics of thunderstorms over Africa.

**Table 3**  
*Land, Ocean, Coast Distributions for WI TGFs Detected by AGILE, and Land, Ocean, Coast Distributions of WWLLN Detections Within the TGF FOV in the Same Period the TGFs was Detected*

	#TGFs	%TGFs	#WWLLN	%WWLLN
Ocean	49	17.4%	483 498	21%
Coast	184	65.2%	1 155 716	51%
Land	49	17.4%	634 793	28%
Total	282	100%	2 274 007	100%

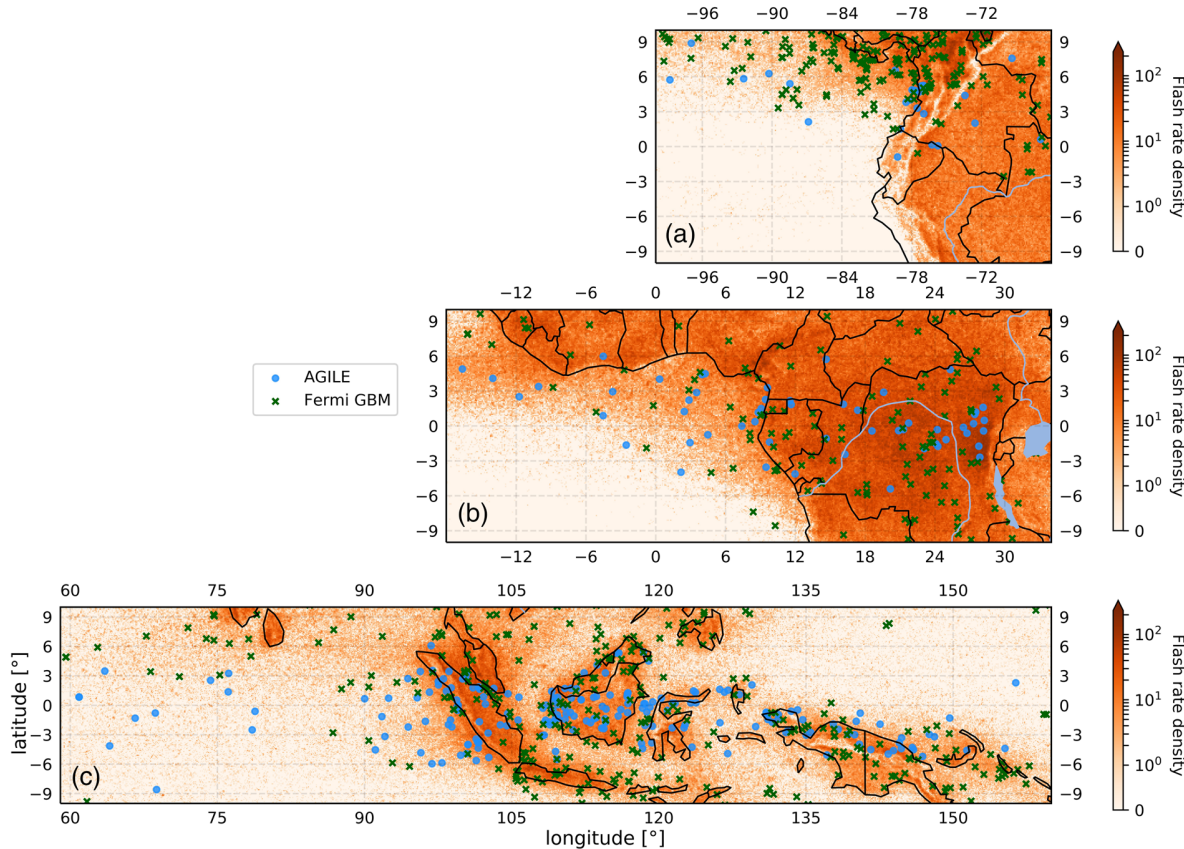


**Figure 9.** The position WWLLN matches associated to TGFs detected by AGILE and Fermi-GBM. The color scale shows flash rate density with unit flashes per square kilometer per year from the LIS 0.1 Degree VHIRFC dataset.

### 5.5. Terrestrial Electron Beam

High-energy photons of the TGF will interact with the atmosphere and produce secondary electrons and positrons. A fraction of the secondary electrons and positrons produced above 30–40 km can reach high enough altitudes (above  $\sim$ 120 km) where they stop interacting significantly with the atmosphere (Sarria et al., 2015). The geomagnetic field will then guide the motion of the electrons and positrons so that they stay together, forming a TEB. The TEBs were first described in Dwyer et al. (2008). Spacecraft detecting TGFs, such as BATSE, RHESSI, Fermi, BeppoSAX and ASIM, also detect TEBs (Dwyer et al., 2008; Roberts et al., 2018; Sarria et al., 2019; Ursi et al., 2017).

Here we present the first high confidence TEB identified in AGILE data. The TEB took place over the Indian ocean on 6 April 2018 20:51:50.404601 UTC. There is no lightning activity detected by WWLLN within 1 s of the TEB in a radius of 1,000 km from the subsatellite point, except two WWLLN matches close to the southern footpoint of the magnetic field line that intercepts AGILE at the moment of observation,  $\sim$ 733 km from the subsatellite point. We pick the closest WWLLN match to the magnetic footpoint as the most likely sferic associated with the TGF producing the TEB.

In Figure 10, lightning activity  $\pm$ 1 minute around the time of the TEB, the location of AGILE's subsatellite point, and the magnetic field line and footpoints are shown. The southern magnetic footpoint is located at  $-8.60^\circ$  latitude and  $68.80^\circ$  longitude. The subsatellite point of AGILE is located at  $-2.04^\circ$  latitude and  $68.08^\circ$  longitude and AGILE has an altitude of 462.6 km. In Figure 10a, it is evident that there is no WWLLN detections directly below AGILE, but there is a cluster of WWLLN detections at the southern magnetic footpoint. The WWLLN match associated with the TEB are found in this cluster. The WWLLN match occurs 0.087 ms before the start of TEB, corrected for propagation time, assuming a straight line.

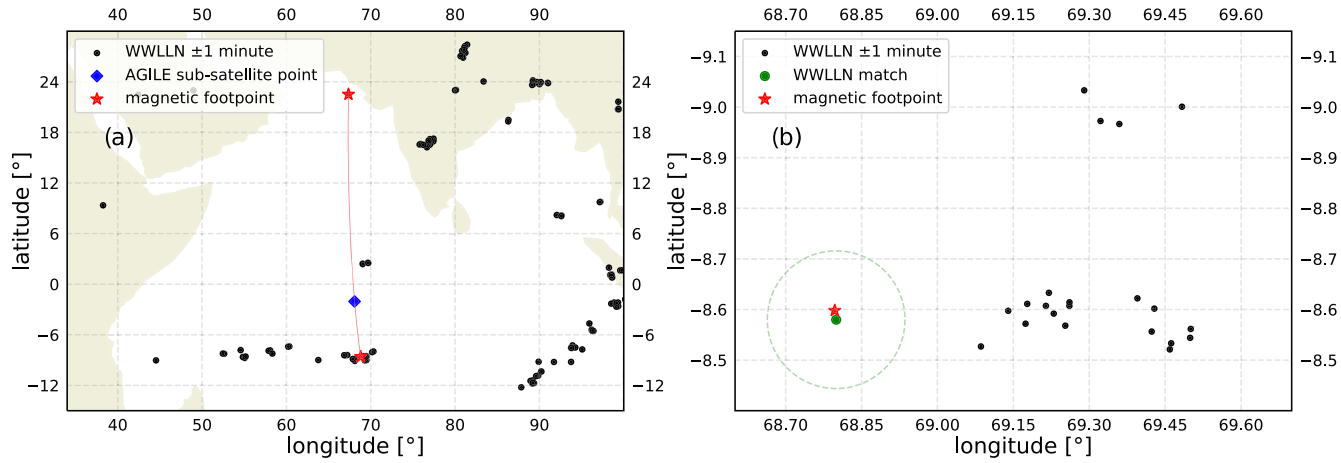


**Figure 10.** Two maps of the TEB event. (a) Map of WWLLN detections  $\pm 1$  minute around the TEB, AGILE's subsatellite point, and the magnetic field line and footpoints. (b) Zoomed version of the southern magnetic footpoint. The 15-km uncertainty of the WWLLN match is indicated as a green circle.

Figure 11 shows the detected energy spectra and time histogram of the TEB, together with a simulation of the TEB. The TEB is simulated with a Geant4 based code assuming a TGF with a RREA energy spectrum proportional to  $1/E \cdot \exp(-E/7.3 \text{ MeV})$ , up to 40 MeV. The Geant4 code is the same as in Sarria et al. (2019). The source TGF is initiated at the WWLLN match with an assumed production altitude of 15 km. The photons are beamed upward with a Gaussian distribution with  $\sigma_\theta = 30^\circ$ . The Earth's magnetic field is obtained using the IGRF-12 model (Thébault et al., 2015) and the atmosphere composition is obtained using the NRLMSISE-00 model (Picone et al., 2002). Geant4 includes all the relevant processes physical processes of photon, electron and positron transportation (Compton scattering, pair production, Rayleigh scattering, photoelectric absorption electrons inelastic and elastic scatterings, bremsstrahlung, position annihilation). The photons, electrons, and positrons reaching satellite altitude are saved including their energy and momentum information. The output from this simulation is used as input to the AGILE mass model, which simulates

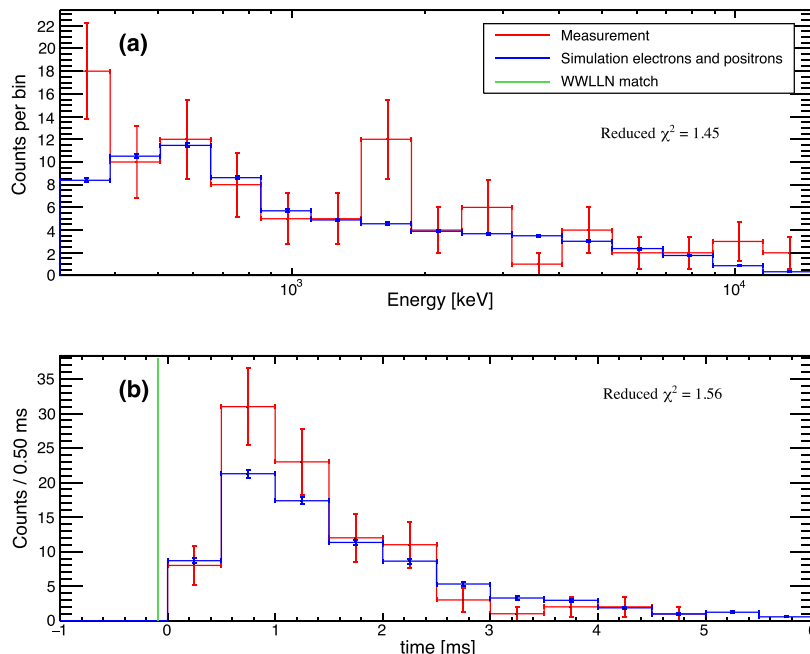


**Figure 11.** (a) Energy spectra of the detected TEB. (b) Time histogram of the TEB. The measurement by AGILE is in red color. The simulation of the TEB in blue color. The WWLLN match corrected for propagation time is shown in green color.

AGILE's detector response to the particles, in terms of energy spectrum and arrival time. The energy spectrum accounts for energy resolution of the instrument. The proper attitude of the satellite at the TEB time is accounted for. This is shown in blue color in Figure 11. To evaluate the compatibility between the simulation and the measurement, we performed a  $\chi^2$  test. The reduced  $\chi^2$  value is 1.45 for the energy spectrum and the critical value for compatibility is 1.69 (14 degrees of freedom). The reduced  $\chi^2$  value is 1.56 for the time histogram and the critical value for compatibility is 1.94 (8 degrees of freedom and the start of the TEB is a free parameter.). Figure 11 shows the resulting energy spectrum (a) and light curves (b), and the results of the  $\chi^2$  tests. In both cases, the simulation is compatible with the measurement.

Given the observed WWLLN detection and the magnetic field line configuration, as well as consistency of simulated and measured spectra and time profile, we conclude that the event on 6 April 2018 20:51:50.404601 UTC is the first observation of a TEB detected by AGILE. The detection of TEBs is difficult for AGILE given the amount of screening material surrounding the detector, as pointed out in the comparative study by Sarria et al. (2017).

## 6. Summary and Conclusions

In this paper, we analyzed more than 9 years of AGILE gamma-ray data, searching for TGFs correlating with lightning strokes detected by WWLLN. We confirm that the AC shield suppresses the TGF signal in the AC-ON period, as suggested in Marisaldi et al. (2014). We have also selected a total of 282 WWLLN identified (WI) TGFs with high absolute timing accuracy (REF and 3D-FIX period), and 310 WI TGFs with low absolute timing accuracy, which also is satisfied by selection criteria (DRIFT period).

The search for clusters (SFC) method proved successful in identifying all significant TGFs with a WWLLN match where the absolute timing accuracy of AGILE is high. These WI TGFs provided a basis for improvements in selection criteria discussed in the companion paper M20. In the DRIFT period, when AGILE experienced absolute timing issues, the SFC method together with the selection criteria provided a very useful TGF-WWLLN data set capable of independent diagnostics of the AGILE timing accuracy. In the 3D-FIX period, the authors also identified a constant systematic offset of 4 ms.

The analysis of the WI TGF sample can be summarized as follows:

1. The duration of TGFs and the rate of association with WWLLN is assessed and shows, in agreement with Connaughton et al. (2013), that brief duration TGFs have a higher fraction of WWLLN matches than longer duration TGFs.
2. Seven multipulse TGFs detected by AGILE confirms the findings of Mezentsev et al. (2016) that a WWLLN detection associated with a multipulse TGF is always associated with the last pulse. No counterexamples were found.
3. The local time and geographical longitude distributions of WI TGFs, detected by AGILE, is consistent with TGFs with a WWLLN match detected by Fermi GBM.
4. The ocean, land, coast distribution of TGFs does not follow the ocean, land, coast distribution of lightning detected by WWLLN. TGF production occurs relatively more often  $\pm 150$  km from the coastline.
5. The first TEB detected by AGILE is identified with a WWLLN detection close to the magnetic footprint of the satellite. Measured and simulated energy spectra and time profiles are consistent.

A catalog of the TGFs, including the TEB, from the REF, DRIFT, and 3D-FIX period are available online for the scientific community ([www.ssdc.asi.it/mcal3tgfcat](http://ssdc.asi.it/mcal3tgfcat)).

## References

- Abarca, S. F., Corbosiero, K. L., & Galarneau Jr., T. J. (2010). An evaluation of the Worldwide Lightning Location Network (WWLLN) using the national lightning detection network (NLDN) as ground truth. *Journal of Geophysical Research*, 115, D18206. <https://doi.org/10.1029/2009JD013411>
- Albrecht, Rachel, I., Goodman, S., Buechler, D., Blakeslee, R. J., & Christian, H. (2016). Lis 0.1 degree very high resolution gridded lightning full climatology [vhrfc\_lis\_frd]. dataset available online from the NASA Global Hydrology Center DAAC, Huntsville, Alabama, U.S.A. <https://ghrc.nsstc.nasa.gov/hydro/details/lisvhrfc>
- Albrechtsen, K. H., Østgaard, N., Berge, N., & Gjesteland, T. (2019). Observationally weak TGFs in the RHESSI data. *Journal of Geophysical Research: Atmospheres*, 124, 287–298. <https://doi.org/10.1029/2018JD029272>
- Briggs, M. S., Xiong, S., Connaughton, V., Tierney, D., Fitzpatrick, G., Foley, S., et al. (2013). Terrestrial gamma-ray flashes in the fermi era: Improved observations and analysis methods. *Journal of Geophysical Research: Space Physics*, 118, 3805–3830. <https://doi.org/10.1002/jgra.50205>

## Acknowledgments

AGILE is a mission of the Italian Space Agency (ASI), with co-participation of INAF (Istituto Nazionale di Astrofisica) and INFN (Istituto Nazionale di Fisica Nucleare). This study was supported by the Research Council of Norway under contracts 208028/F50 and 223252/F50 (CoE). This project has received funding from the European Union's Horizon 2020 research and innovation program under the Marie Skłodowska-Curie grant agreement 722337. Some part of the simulations were performed on resources provided by UNINETT Sigma2—the National Infrastructure for High Performance Computing and Data Storage in Norway, under project no. NN9526K. The authors wish to thank the World Wide Lightning Location Network (<http://wwln.net>), a collaboration among over 50 universities and institutions, for providing the lightning location data used in this paper. WWLLN data are available upon subscription. In the online catalog we provide information (timing and location) on the sferic simultaneous to the TGF only. The properties of the TGF sample presented in this work are publicly available at the ASI Space Science Data Center (SSDC) website ([www.ssdc.asi.it/mcal3tgfcat](http://ssdc.asi.it/mcal3tgfcat)).

- Bürgesser, R. E. (2017). Assessment of the World Wide Lightning Location Network (WWLLN) detection efficiency by comparison to the lightning imaging sensor (lis). *Quarterly Journal of the Royal Meteorological Society*, 143(708), 2809–2817. <https://doi.org/10.1002/qj.3129>
- Collier, A. B., Gjesteland, T., & Østgaard, N. (2011). Assessing the power law distribution of TGFs. *Journal of Geophysical Research*, 116, A10320. <https://doi.org/10.1029/2011JA016612>
- Connaughton, V., Briggs, M. S., Holzworth, R. H., Hutchins, M. L., Fishman, G. J., Wilson-Hodge, C. A., et al. (2010). Associations between fermi gamma-ray burst monitor terrestrial gamma ray flashes and sferics from the World Wide Lightning Location Network. *Journal of Geophysical Research*, 115, A12307. <https://doi.org/10.1029/2010JA015681>
- Connaughton, V., Briggs, M. S., Xiong, S., Dwyer, J. R., Hutchins, M. L., Grove, J. E., et al. (2013). Radio signals from electron beams in terrestrial gamma ray flashes. *Journal of Geophysical Research: Space Physics*, 118, 2313–2320. <https://doi.org/10.1029/2012JA018288>
- Cummer, S. A., Zhai, Y., Hu, W., Smith, D. M., Lopez, L. I., & Stanley, M. A. (2005). Measurements and implications of the relationship between lightning and terrestrial gamma ray flashes. *Geophysical Research Letters*, 32, L08811. <https://doi.org/10.1029/2005GL022778>
- Dwyer, J. R. (2012). The relativistic feedback discharge model of terrestrial gamma ray flashes. *Journal of Geophysical Research*, 117, A02308. <https://doi.org/10.1029/2011JA017160>
- Dwyer, J. R., Grefenstette, B. W., & Smith, D. M. (2008). High-energy electron beams launched into space by thunderstorms. *Geophysical Research Letters*, 35, L02815. <https://doi.org/10.1029/2007GL032430>
- Dwyer, J. R., & Smith, D. M. (2005). A comparison between monte carlo simulations of runaway breakdown and terrestrial gamma-ray flash observations. *Geophysical Research Letters*, 32, L22804. <https://doi.org/10.1029/2005GL023848>
- Fabró, F., Montanyà, J., van der Velde, O. A., Pineda, N., & Williams, E. R. (2019). On the TGF/lightning ratio asymmetry. *Journal of Geophysical Research: Atmospheres*, 124, 6518–6531. <https://doi.org/10.1029/2018JD030075>
- Fishman, G. J., Bhat, P. N., Mallozzi, R., Horack, J. M., Koschut, T., Kouveliotou, C., et al. (1994). Discovery of intense gamma-ray flashes of atmospheric origin. *Science*, 264(5163), 1313–1316. <https://doi.org/10.1126/science.264.5163.1313>
- Fuschino, F., Marisaldi, M., Labanti, C., Barbiellini, G., Del Monte, E., Bulgarelli, A., et al. (2011). High spatial resolution correlation of AGILE TGFs and global lightning activity above the equatorial belt. *Geophysical Research Letters*, 38, L14806. <https://doi.org/10.1029/2011GL047817>
- Gjesteland, T., Østgaard, N., Collier, A. B., Carlson, B. E., Eyles, C., & Smith, D. M. (2012). A new method reveals more TGFs in the RHESSI data. *Geophysical Research Letters*, 39, L05102. <https://doi.org/10.1029/2012GL050899>
- Grefenstette, B. W., Smith, D. M., Hazelton, B. J., & Lopez, L. I. (2009). First RHESSI terrestrial gamma ray flash catalog. *Journal of Geophysical Research*, 114, A02314. <https://doi.org/10.1029/2008JA013721>
- Hutchins, M. L., Holzworth, R. H., Brundell, J. B., & Rodger, C. J. (2012). Relative detection efficiency of the World Wide Lightning Location Network. *Radio Science*, 47, RS6005. <https://doi.org/10.1029/2012RS005049>
- Labanti, C., Marisaldi, M., Fuschino, F., Galli, M., Argan, A., Bulgarelli, A., et al. (2009). Design and construction of the mini-calorimeter of the AGILE satellite. *Nuclear Instruments and Methods in Physics Research Section A: Accelerators, Spectrometers, Detectors and Associated Equipment*, 598(2), 470–479. <https://doi.org/10.1016/j.nima.2008.09.021>
- Maiorana, C., Marisaldi, M., Lindanger, A., Østgaard, N., Ursi, A., Sarria, D., et al. (2020). The 3rd AGILE terrestrial gamma-ray flashes catalog. part ii: Optimized selection criteria and characteristics of the new sample to be submitted. *Journal of Geophysical Research: Atmospheres*.
- Marisaldi, M., Argan, A., Ursi, A., Gjesteland, T., Fuschino, F., Labanti, C., et al. (2015). Enhanced detection of terrestrial gamma-ray flashes by AGILE. *Geophysical Research Letters*, 42, 9481–9487. <https://doi.org/10.1002/2015GL066100>
- Marisaldi, M., Fuschino, F., Labanti, C., Galli, M., Longo, F., Del Monte, E., et al. (2010). Detection of terrestrial gamma ray flashes up to 40 MeV by the AGILE satellite. *Journal of Geophysical Research*, 115, A00E13. <https://doi.org/10.1029/2009JA014502>
- Marisaldi, M., Fuschino, F., Tavani, M., Dietrich, S., Price, C., Galli, M., et al. (2014). Properties of terrestrial gamma ray flashes detected by AGILE mcal below 30 MeV. *Journal of Geophysical Research: Space Physics*, 119, 1337–1355. <https://doi.org/10.1002/2013JA019301>
- Marisaldi, M., Galli, M., Labanti, C., Østgaard, N., Sarria, D., Cummer, S. A., et al. (2019). On the high-energy spectral component and fine time structure of terrestrial gamma ray flashes. *Journal of Geophysical Research: Atmospheres*, 124, 7484–7497. <https://doi.org/10.1029/2019JD030554>
- Marshall, T., Stolzenburg, M., Karunarathne, S., Cummer, S., Lu, G., Betz, H.-D., et al. (2013). Initial breakdown pulses in intracloud lightning flashes and their relation to terrestrial gamma ray flashes. *Journal of Geophysical Research: Atmospheres*, 118, 10,907–10,925. <https://doi.org/10.1002/jgrd.50866>
- McTague, L. E., Cummer, S. A., Briggs, M. S., Connaughton, V., Stanbro, M., & Fitzpatrick, G. (2015). A lightning-based search for nearby observationally dim terrestrial gamma ray flashes. *Journal of Geophysical Research: Atmospheres*, 120, 12,003–12,017. <https://doi.org/10.1002/2015JD023475>
- Mezentsev, A., Østgaard, N., Gjesteland, T., Albrechtsen, K., Lehtinen, N., Marisaldi, M., et al. (2016). Radio emissions from double RHESSI TGFs. *Journal of Geophysical Research: Atmospheres*, 121, 8006–8022. <https://doi.org/10.1002/2016JD025111>
- Neubert, T., Østgaard, N., Reglero, V., Blanc, E., Chanrion, O., Oxborow, C. A., et al. (2019). The ASIM mission on the international space station. *Space Science Reviews*, 215(2), 26. <https://doi.org/10.1007/s11214-019-0592-z>
- Østgaard, N., Albrechtsen, K. H., Gjesteland, T., & Collier, A. (2015). A new population of terrestrial gamma-ray flashes in the RHESSI data. *Geophysical Research Letters*, 42, 10,937–10,942. <https://doi.org/10.1002/2015GL067064>
- Østgaard, N., Gjesteland, T., Carlson, B. E., Collier, A. B., Cummer, S. A., Lu, G., & Christian, H. J. (2013). Simultaneous observations of optical lightning and terrestrial gamma ray flash from space. *Geophysical Research Letters*, 40, 2423–2426. <https://doi.org/10.1029/2013GL05466>
- Picone, J. M., Hedin, A. E., Drob, D. P., & Aikin, A. C. (2002). Nrlmsise-00 empirical model of the atmosphere: Statistical comparisons and scientific issues. *Journal of Geophysical Research*, 107(A12), SIA 15–1–SIA 15–16. <https://doi.org/10.1029/2002JA009430>
- Roberts, O. J., Fitzpatrick, G., Stanbro, M., McBreen, S., Briggs, M. S., Holzworth, R. H., et al. (2018). The first Fermi-GBM terrestrial gamma ray flash catalog. *Journal of Geophysical Research: Space Physics*, 123, 4381–4401. <https://doi.org/10.1029/2017JA024837>
- Rodger, C. J., Brundell, J. B., Holzworth, R. H., & Lay, E. H. (2009). Growing detection efficiency of the world wide lightning location network. *AIP Conference Proceedings*, 1118(1), 15–20. <https://doi.org/10.1063/1.3137706>
- Rudlosky, S. D., & Shea, D. T. (2013). Evaluating WWLLN performance relative to TRMM/LIS. *Geophysical Research Letters*, 40, 2344–2348. <https://doi.org/10.1002/grl.50428>
- Sarria, D., Blelly, P.-L., & Forme, F. (2015). Mc-peptita: A Monte Carlo model for photon, electron and positron tracking in terrestrial atmosphere—Application for a terrestrial gamma ray flash. *Journal of Geophysical Research: Space Physics*, 120, 3970–3986. <https://doi.org/10.1002/2014JA020695>



- Sarria, D., Kochkin, P., Østgaard, N., Lehtinen, N., Mezentsev, A., Marisaldi, M., et al. (2019). The first terrestrial electron beam observed by the atmosphere-space interactions monitor. *Journal of Geophysical Research: Space Physics*, *124*, 10,497–10,511. <https://doi.org/10.1029/2019JA027071>
- Sarria, D., Lebrun, F., Blelly, P.-L., Chipaux, R., Laurent, P., Sauvaud, J.-A., et al. (2017). Taranis XGRE and IDEE detection capability of terrestrial gamma-ray flashes and associated electron beams. *Geoscientific Instrumentation, Methods and Data Systems*, *6*(2), 239–256. <https://doi.org/10.5194/gi-6-239-2017>
- Smith, D. M., Buzbee, P., Kelley, N. A., Infanger, A., Holzworth, R. H., & Dwyer, J. R. (2016). The rarity of terrestrial gamma-ray flashes: 2. RHESSI stacking analysis. *Journal of Geophysical Research: Atmospheres*, *121*, 11,382–11,404. <https://doi.org/10.1002/2016JD025395>
- Smith, D. M., Hazelton, B. J., Grefenstette, B. W., Dwyer, J. R., Holzworth, R. H., & Lay, E. H. (2010). Terrestrial gamma ray flashes correlated to storm phase and tropopause height. *Journal of Geophysical Research*, *115*, A00E49. <https://doi.org/10.1029/2009JA014853>
- Smith, D. M., Lopez, L. I., Lin, R. P., & Barrington-Leigh, C. (2005). Terrestrial gamma-ray flashes observed up to 20 MeV. *Science*, *307*, 1085–1088. <https://doi.org/10.1126/science.1107466>
- Thébault, E., Finlay, C. C., Beggan, C. D., Alken, P., Aubert, J., Barrois, O., et al. (2015). International geomagnetic reference field: The 12th generation. *Earth, Planets and Space*, *67*(1), 79. <https://doi.org/10.1186/s40623-015-0228-9>
- Ursi, A., Guidorzi, C., Marisaldi, M., Sarria, D., & Frontera, F. (2017). Terrestrial gamma-ray flashes in the BeppoSAX data archive. *Journal of Atmospheric and Solar-Terrestrial Physics*, *156*, 50–56. <https://doi.org/10.1016/j.jastp.2017.02.014>
- Wessel, P., & Smith, WalterH. F. (1996). A global, self-consistent, hierarchical, high-resolution shoreline database. *Journal of Geophysical Research*, *101*(B4), 8741–8743. <https://doi.org/10.1029/96JB00104>

## Paper II

### **Spectral Analysis of Individual Terrestrial Gamma-ray Flashes Detected by ASIM**

A. Lindanger, M. Marisaldi, D. Sarria, N. Østgaard, N. Lehtinen, C. A. Skeie, A. Mezentzev, P. Kochkin, K. Ullaland, S. Yang, G. Genov, B. E. Carlson, C. Köhn, J. Navarro-Gonzalez, P. Connell, V. Reglero, T. Neubert

*Journal of Geophysical Research: Atmospheres*, **126**, doi:10.1029/2021JD035347, (2021)



**Key Points:**

- Spectral analysis of individual terrestrial gamma-ray flashes (TGFs) detected by the Atmosphere-Space Interactions Monitor is performed
- Source properties such as altitude, beam size and intensity are explored, showing it is difficult to constrain the source parameter space
- Limitations on TGF spectral analysis due to count statistics are investigated

**Supporting Information:**

Supporting Information may be found in the online version of this article.

**Correspondence to:**

A. Lindanger,  
Anders.Lindanger@uib.no

**Citation:**

Lindanger, A., Marisaldi, M., Sarria, D., Østgaard, N., Lehtinen, N., Skeie, C. A., et al. (2021). Spectral analysis of individual terrestrial gamma-ray flashes detected by ASIM. *Journal of Geophysical Research: Atmospheres*, 126, e2021JD035347. <https://doi.org/10.1029/2021JD035347>

Received 1 JUN 2021

Accepted 5 NOV 2021

## Spectral Analysis of Individual Terrestrial Gamma-Ray Flashes Detected by ASIM

A. Lindanger<sup>1</sup> , M. Marisaldi<sup>1,2</sup> , D. Sarria<sup>1</sup> , N. Østgaard<sup>1</sup> , N. Lehtinen<sup>1</sup>, C. A. Skeie<sup>1</sup> , A. Mezentzev<sup>1</sup> , P. Kochkin<sup>1</sup> , K. Ullaland<sup>1</sup> , S. Yang<sup>1</sup>, G. Genov<sup>1</sup> , B. E. Carlson<sup>1,3</sup> , C. Köhn<sup>4</sup> , J. Navarro-Gonzalez<sup>5</sup>, P. Connell<sup>5</sup>, V. Reglero<sup>5</sup>, and T. Neubert<sup>4</sup>

<sup>1</sup>Department of Physics and Technology, Birkeland Centre for Space Science, University of Bergen, Bergen, Norway, <sup>2</sup>INAF-OAS Bologna, Bologna, Italy, <sup>3</sup>Carthage College, Kenosha, WI, USA, <sup>4</sup>National Space Institute, Technical University of Denmark, Copenhagen, Denmark, <sup>5</sup>University of Valencia, Valencia, Spain

**Abstract** The Atmosphere-Space Interactions Monitor (ASIM) is the first instrument in space specifically designed to observe terrestrial gamma-ray flashes (TGFs). TGFs are high energy photons associated with lightning flashes and we perform the spectral analysis of 17 TGFs detected by ASIM. The TGF sample is carefully selected by rigorous selection criteria to keep a clean sample suitable for spectral analysis, that is, suitable count statistics, low instrumental effects, and reliable source location. Monte Carlo modeling of individual TGFs has been compared to the observed energy spectra to study the possible source altitudes and beaming geometries. A careful model of the instrumental effects has been developed and validated. Several combinations of source altitudes and beaming geometries are accepted by the statistical tests for all the TGFs in the sample resulting in a large uncertainty in the estimate of the intrinsic source luminosity. The analyzed TGFs show significant variations in observed fluence independent of the distance between source and ASIM. A lower limit on the maximum photon energy produced by TGFs is estimated to be 24 MeV for the analyzed TGFs. The intrinsic limitations of TGF spectral analysis from space are also investigated and it is found that the ability to constrain the source altitude and beaming geometries of TGFs strongly depends on the distance between source and satellite. With the current generation of instruments with effective areas in the range of few hundreds cm<sup>2</sup>, it is very difficult to constrain reliably the source properties without the help of simultaneous measurements in the radio band.

### 1. Introduction

Terrestrial gamma-ray flashes (TGFs) originate from Earth and are associated with lightning flashes. They are observed by satellites as sub-millisecond bursts of energetic photons and were first reported by Fishman et al. (1994) using data from the BATSE experiment onboard the Compton Gamma-Ray Observatory. TGFs have also been detected by RHESSI (Smith et al., 2005), AGILE (Marisaldi et al., 2010), the Fermi Gamma-ray Burst Monitor (GBM) (Briggs et al., 2010), and BeppoSAX (Ursi et al., 2017). The first space mission specifically designed to detect TGFs is the Atmosphere-Space Interactions Monitor (ASIM) operational since June 2018 (Neubert et al., 2019).

TGFs are explained as bremsstrahlung photons produced by a population of relativistic electrons accelerated within a thundercloud electric field. Wilson (1924) was the first to realize that electrons could be accelerated to relativistic energies in electric fields in thunderclouds. Gurevich et al. (1992) further developed the idea that these runaway electrons could undergo a multiplication process through Møller scattering and form an avalanche in the opposite direction to the electric field. This process is termed relativistic runaway electron avalanche (RREA). Dwyer and Smith (2005) estimated that there must be about  $10^{17}$  electrons at source based on TGF observations from space assuming a source altitude of 15 km. Dwyer (2008) realized that RREA multiplication alone could not explain the number of electrons at source and two leading hypotheses have been proposed to overcome this problem: the relativistic feedback mechanism (Dwyer, 2003, 2007, 2012) and the thermal runaway mechanism (Celestin & Pasko, 2011; Köhn & Ebert, 2015; Köhn et al., 2017, 2020; Xu et al., 2012). Both models are able to produce the required number of electrons at source. In the relativistic feedback mechanism runaway electrons produce energetic bremsstrahlung photons and some of these photons' backscatter or produce electron-positron pairs. These positrons or backscattered photons produce new REAs, hence multiplying the number of electrons at source. In the thermal runaway mechanism sufficiently many runaway electrons are produced in the high

© 2021. The Authors.

This is an open access article under the terms of the Creative Commons Attribution License, which permits use, distribution and reproduction in any medium, provided the original work is properly cited.

electric field in front of streamers in the vicinity of a lightning leader tip, and further accelerated by the electric field in front of the lightning leader tip. The relativistic feedback mechanism and the thermal runaway mechanism can be active at the same time.

The TGF source has mostly been characterized by three observables: fluence, source altitude, and beam opening angle (sometimes referred as angular distribution). As most satellites detecting TGFs were not designed to handle the very high count rate of TGFs, a large fraction of the photons are not detected due to dead-time effects. To increase count statistics Dwyer and Smith (2005) combined data from RHESSI TGFs to build a cumulative spectrum that they compared to Monte Carlo models. They estimated the production source altitude of TGFs to be 15–21 km. Hazelton et al. (2009) used RHESSI TGFs and took into account the radial distance using lightning sferics detected by the World Wide Lightning Location Network (WWLLN) to estimate the geolocation of the TGFs. The radial distance is the distance following the surface of the Earth between the TGF foot-point and the sub-satellite point. For the cumulative spectrum of TGFs within 300 km from the subsatellite point, their most likely model had a wide-beam geometry and a source altitude of 15 km. For TGFs produced with a radial distance larger than 300 km they showed that a narrow-beam model at  $\geq 20$  km altitude was unlikely to reproduce the observed data. Gjesteland et al. (2011), also using RHESSI data, concluded that an isotropic emission cone with a half angle between 30° and 40° was the best fit to the data.

Spectral analysis of individual TGFs is complicated due to the photon transport through the atmosphere and high count rates. Østgaard et al. (2008) estimated a production altitude up to 40 km using BATSE data and Monte Carlo modeling, however Grefenstette et al. (2009) realized that the measured brightness of TGFs, observed by RHESSI and BATSE, were underestimated due to dead-time effects. When Gjesteland et al. (2010) revised the analysis on the BATSE data, taking dead-time into account, the new production altitude estimates were below 26 km. Mailyan et al. (2016) performed spectral analysis on 46 individual TGFs, detected by Fermi-GBM, finding spectral diversity. This implies that cumulative TGF spectra miss important information as spectral diversity gets smeared out. The observed data were compared to Monte Carlo simulations of a large scale RREA model, including the propagation through the atmosphere. They tested production altitudes of 11.6, 13.4, 16, and 20.2 km, with narrow- and wide-beam models. The narrow beam model is modeling the intrinsic angular distribution of bremsstrahlung photons in the RREA region. In the wide-beam model the photons are emitted isotropically in a cone with half angle 45°. For most of the TGFs they could not distinguish between narrow- and wide-beam models. Models produced at 11.6 km gave frequently a better fit than higher altitude models, however 13.6 km could not be rejected in those cases. There are also events where 20.2 km models gave the best fit, but lower altitude models could not be rejected. Of the 46 TGFs 6 had poor fits, but it is speculated that this is due to instrumental effects. Their TGF sample had between 21 and 53 counts per TGF in one BGO detector. A follow-up study by Mailyan et al. (2019) compared also lightning leader models to TGFs detected by Fermi-GBM. They found that for most of the TGFs one mechanism was not favored over the other.

In addition to spectral analysis from space, low frequency (LF) radio measurements can provide an independent estimate of the production altitude. These independent LF measurements estimate TGF production altitudes between 10 and 15 km (Cummer et al., 2014; Pu et al., 2019). Very low frequency radio measurements of sferics produced by lightning can be used to geolocate TGFs. TGFs and sferics are simultaneous within few hundred microseconds (Connaughton et al., 2010, 2013; Lindanger et al., 2020).

In this work we present the individual spectral analysis of 17 TGFs detected by ASIM with a number of counts between 82 and 254 in the High Energy Detector (HED). 11 of the TGFs also have data in the Low Energy Detector (LED) down to 60 keV. We will present the ASIM instrument and discuss instrumental effects and its impact on the energy measurements during TGF detection. The forward modeling from the source to the detection of the photons in ASIM is explained in detail, and we will show normalized energy spectra of the different models observed at different radial distances. The results of the spectral analysis are presented in detail for one TGF, while the results of the other TGFs are presented in table format with further documentation in Supporting Information S1. We will then discuss the source properties of TGFs and we will also address the intrinsic limitations of the spectral analysis approach.

## 2. The ASIM Instrument

ASIM was launched in April 2018 to the International Space Station (ISS). ASIM is designed to observe TGFs, Transient Luminous Events (TLEs), and lightning. Chanrion et al. (2019); Neubert et al. (2019); Østgaard, Balling, et al. (2019) give a thorough description of the ASIM mission and the instruments onboard.

### 2.1. The MXGS and MMIA Instruments Onboard ASIM

The scientific payload onboard ASIM consists of the Modular X- and Gamma-ray Sensor (MXGS) and the Modular Multispectral Imaging Assembly (MMIA). MMIA includes two cameras and three high-speed photometers used for lightning and TLE detection. The main instrument for this analysis is the MXGS, which consists of two detectors: HED and LED. HED consists of 12 Bismuth-Germanium-Oxide (BGO) scintillators, each connected to a photomultiplier tube (PMT). Each BGO is sensitive to photons between 300 keV and >30 MeV. The time resolution of HED is 27.8 ns and each BGO-PMT detector has a dead-time of ~550 ns.

LED consists of pixelated Cadmium-Zink-Telluride (CZT) detector crystals that are sensitive to photons with energies from 20 to 400 keV. The time resolution of LED is ~1 μs. A total of 16,384 pixels together with a coded mask in front of the detector makes LED capable of imaging the incident TGFs by using a deconvolution technique. TGFs detected in LED are routinely analyzed in search for source location using the imaging techniques. The pixels are divided into 16 independent readout chains, and each chain is arranged into 8 Application Specific Integrated Circuits (ASIC) with a dead-time of 1.4 μs. If two hits occur in different ASICs in the same chain within 1.4 μs the two hits will be distinguishable, however their energies will be added together. These multi-hit events are flagged. The LED energy calibration was performed for each individual pixel, as described in Østgaard, Balling, et al. (2019), by the pre-launch calibration and the onboard energy calibration system, and has been found to be stable. The energy resolution of LED is <10% at 60 keV. LED and MMIA are only operative during nighttime.

The absolute timing accuracy of MXGS is between ~0 and ~30 ms due to a non-optimal timing interface between the ASIM payload and the ISS. The relative timing uncertainty between MMIA and MXGS was ±80 μs prior to April 2019. A software update in April 2019 reduced the relative timing uncertainty to ±5 μs (Østgaard, Neubert, et al., 2019). When MMIA is active and there is lightning activity in its field of view, it is possible to align MMIA photometer data with several ground detected sferics to correct the absolute timing of MMIA down to less than 2 ms. We can then correct the absolute timing of MXGS accordingly.

### 2.2. Measurements and Instrumental Effects in HED

The energy resolution of HED is <20% at 511 keV (Østgaard, Balling, et al., 2019). The energy channels are converted to keV by a quadratic fit to the 511 keV, 1,275 keV, and 31 MeV peaks in the background energy spectrum. 511 and 1,275 keV are produced by the onboard  $^{22}\text{Na}$  calibration source, and 31 MeV is the most probable value of the energy deposition produced by cosmic protons. The energy deposit of the cosmic protons was estimated by the Geant4 ASIM mass model (Agostinelli et al., 2003; Østgaard, Balling, et al., 2019). The dead-time of each individual HED detector is 550 ns and if there is more than one hit within this dead-time, only one count will be recorded and the energy measurement will result from a combination of the two pulses. This is called pulse-pile-up. If we have a new count in HED after the 550 ns dead-time, the recorded energy will be the sum of the energy of the new count and the tail of the previous count. This is called tail-pile-up and is well illustrated in Figure 6c in Østgaard, Balling, et al. (2019). The HED data acquisition system is keeping track of tail-pile-up. The counts are labeled as either a *normal*-, *valley*- or *fast* events. The *fast* events are tail-pile-up events. *Normal* events are events that are not sitting on the tail of a previous pulse. The *valley* event is the local minimum between the *fast* event pulse and the previous pulse and is only associated with *fast* events. *Valley* events are not physical counts, but can be used to reconstruct the signal amplitude of *fast* events. For *fast* events, a lower energy threshold is implemented. This threshold has been adjusted a few times during the mission.

In the HED PMTs we have a voltage drop over the PMT dynode chain after high energy counts are detected. The time before the high voltage restores itself depends on the energy of the previous count and can be up to ~30 μs for counts above 30 MeV, and ~0 μs for counts less than 400 keV when there is no voltage drop. As the voltage is not constant over the dynode chain, the gain varies. Therefore, the channel to keV energy calibrations is not valid during the voltage drop as the pulse-heights of the following counts are measured incorrectly.

We account for this by implementing an energy dependent “safety time”, which is the time the high voltage in the dynode chains needs for recovering to a level where the energy is within 20% accuracy. Counts that do not meet this criterion are not used for spectral analysis, but are still valid counts for light curves and fluence. The safety time does not bias the energy spectrum if we assume a constant source spectrum during the production of the TGF. The safety time and the voltage drop are further discussed in Appendix A. As HED consists of 12 independent BGO-PMT detectors, a voltage drop introduced by a high energy count in one of the detectors does not affect the other 11 detectors. Dead-time, energy resolution, *fast* events, pulse-pile-up and safety time are taken into account in the instrument model discussed in Section 3.2.

### 3. Spectral Analysis

#### 3.1. TGF Sample Selection

Three criteria have to be fulfilled in spectral analysis of individual TGFs: (a) a bright TGF with good count statistics, (b) the geolocation of the TGF is known, (c) minimal instrumental effects. The first criterion is due to that we need good count statistics of the TGF so that the statistical testing is not limited by low count statistics in the detectors. We set this criterion to a minimum of 80 counts in HED.

The second criterion is necessary as we need to know the TGF production location in order to have the correct propagation path from source to MXGS. This is done by correlating lightning data, detected by ground based lightning location networks, to the time of the TGF. Lightning data are obtained from WWLLN (Rodger et al., 2009), and GLD360 provided by Vaisala Inc (Said & Murphy, 2016). Both networks provide time and geolocation by detecting sferics produced by lightning flashes. For each TGF that satisfies the criterion of minimum count statistics we inspect the ground-based lightning data. We inspect the full map of lightning activity in a time interval around the TGF, to see whether there are multiple active lightning cells at different locations. If there is one sferic correlated with the TGF within the absolute timing uncertainty, we assume it is the sferic associated with the TGF. If there are sferics from different locations within the uncertainty, we cannot perform spectral analysis on the TGF as we do not know its geolocation. If an independent source location is provided by LED imaging, this will be considered as an independent check of the lightning location.

The third and last criterion is to avoid pile-up and saturation for very high flux levels, which is a common challenge for all gamma-ray instruments. For HED such pile-up and saturation will manifest itself as a large number of *fast* events, which will be removed according to the safety time criteria. For LED they will be labeled as multi-hits, which cannot be used for spectral analysis. To assure that the accepted counts from HED and LED used for spectral analysis are representative for the event, we claim that a fraction of *fast* to *normal* events should not exceed 20% for HED, and the multi-hits in LED should not be more than 30% of the total. This criterion will bias the TGF sample toward low intensity and longer duration TGFs.

#### 3.2. Forward Modeling

To be able to compare modeled TGFs with ASIM measurements, we need to model the TGF source, the photon propagation through the atmosphere, the deposition of counts in LED and HED, and instrumental effects in the detectors. We model TGFs at different altitudes and different source beam opening angles to check which models fit the measured energy spectrum.

The forward modeling is computed in several steps. For a particular TGF produced at an altitude with a certain beaming the following steps are performed:

1. Source assumptions.
2. Photon propagation through the atmosphere from source to satellite altitude.
3. The time-energy distribution from step 2 is used as an input distribution to the ASIM mass model.
4. The output time-energy distribution from step 3 is used as an input distribution to simulate duration and instrumental effects.
5. The energy distribution from step 4 is compared to the measured data.

In step 1 the TGF source is modeled assuming a RREA photon spectrum proportional to the analytical function  $1/E \exp(-E/(7.3 \text{ MeV}))$ , with a maximum energy of 40 MeV. This is the only TGF source model spectrum we

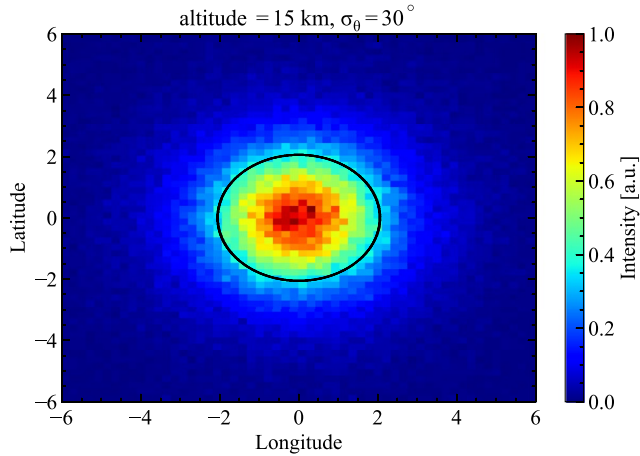


**Figure 1.** Photons produced by a modeled terrestrial gamma-ray flash (TGF) at latitude =  $0^\circ$  and longitude =  $0^\circ$ , reaching the satellite plane at an altitude of 408 km. The TGF is beamed upward with a Gaussian profile with  $\sigma_\theta = 30^\circ$  from a source altitude of 15 km. The black ellipse marks the  $30^\circ$  off-nadir angle from the source.

assume and we will explore beam width, production altitude, and fluence. In the following, we will refer to the term model as any tested combination of beam width and altitude. We do not consider tilting of the TGF beam to prevent overfitting. After generating TGF photons with a RREA energy spectrum, we perform step 2 where the photons are beamed upward with a Gaussian profile with a  $\sigma_\theta$  that defines the beaming profile. Figure 1 illustrates a Gaussian beaming profile and shows a simulated TGF in the satellite altitude plane at 408 km with  $\sigma_\theta = 30^\circ$ . At source this is a two dimensional Gaussian, meaning that 39% of the photons are within one  $\sigma_\theta$  before they are further scattered in the atmosphere. We elaborate more on how to compare isotropic and Gaussian beaming models in Appendix B. The time profile at source is instantaneous, and the time profile at satellite altitude is due to the transport through the atmosphere in addition to the source duration that will be implemented in step 4.

In step 2, we use the Geant4 Monte Carlo code presented in Sarria et al. (2019) to model the photon propagation through the atmosphere. The atmospheric composition is obtained using the NRLMSIS-00 model (Picone et al., 2002). Geant4 takes into account all the relevant physical processes of photon, electron and positron transportation (Compton scattering, Rayleigh scattering, photo-electric absorption, electrons inelastic and elastic scattering, bremsstrahlung, and positron annihilation). The magnetic gyration of elec-

trons and positrons produced by the gammas are not taken into account as this enhance computation time and are only relevant for Terrestrial Electron Beams (Ebert et al., 2010; Köhn & Ebert, 2015; Sarria et al., 2019, 2021). The energy, position, momentum and timing information of photons reaching satellite altitude are saved. Note that the energy distribution of the photons from an instantaneous source is dependent on time after propagation through the atmosphere as shown in Figure 6 in Marisaldi et al. (2019). Step 2 is simulated for TGFs produced at 9, 11, 13, 15, 17, and 19 km altitude, for  $\sigma_\theta = 5^\circ, 10^\circ, 15^\circ, 22^\circ$  and  $30^\circ$ . In total, this gives 30 time-energy spectra matrices dependent on production altitude and  $\sigma_\theta$ . For the 30 time-energy spectra (from an instantaneous source) we calculate different distributions depending on the radial distance. Figure 2 shows a TGF produced at an altitude of 13 km and  $\sigma_\theta = 30^\circ$  observed at different radial distances. We see that the energy spectra get softer at larger radial distances due to a larger fraction of Compton scattering compared to the energy spectra at smaller radial distances. Figures 3a–3c compares two models with  $\sigma_\theta = 15^\circ$  produced at an altitude of 9 and 19 km,

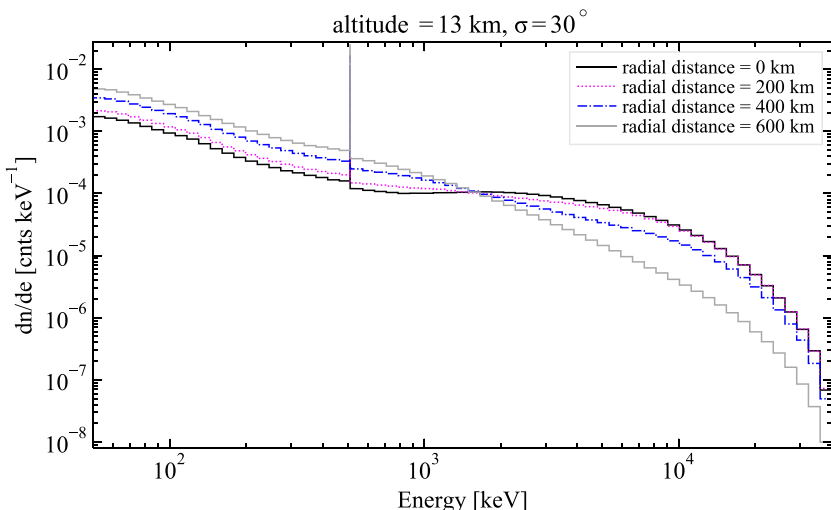


**Figure 2.** Normalized energy spectra of a terrestrial gamma-ray flash produced at an altitude of 13 km and  $\sigma_\theta = 30^\circ$  propagated through the atmosphere and observed at an altitude of 408 km at different radial distances. The spectra are normalized to one.

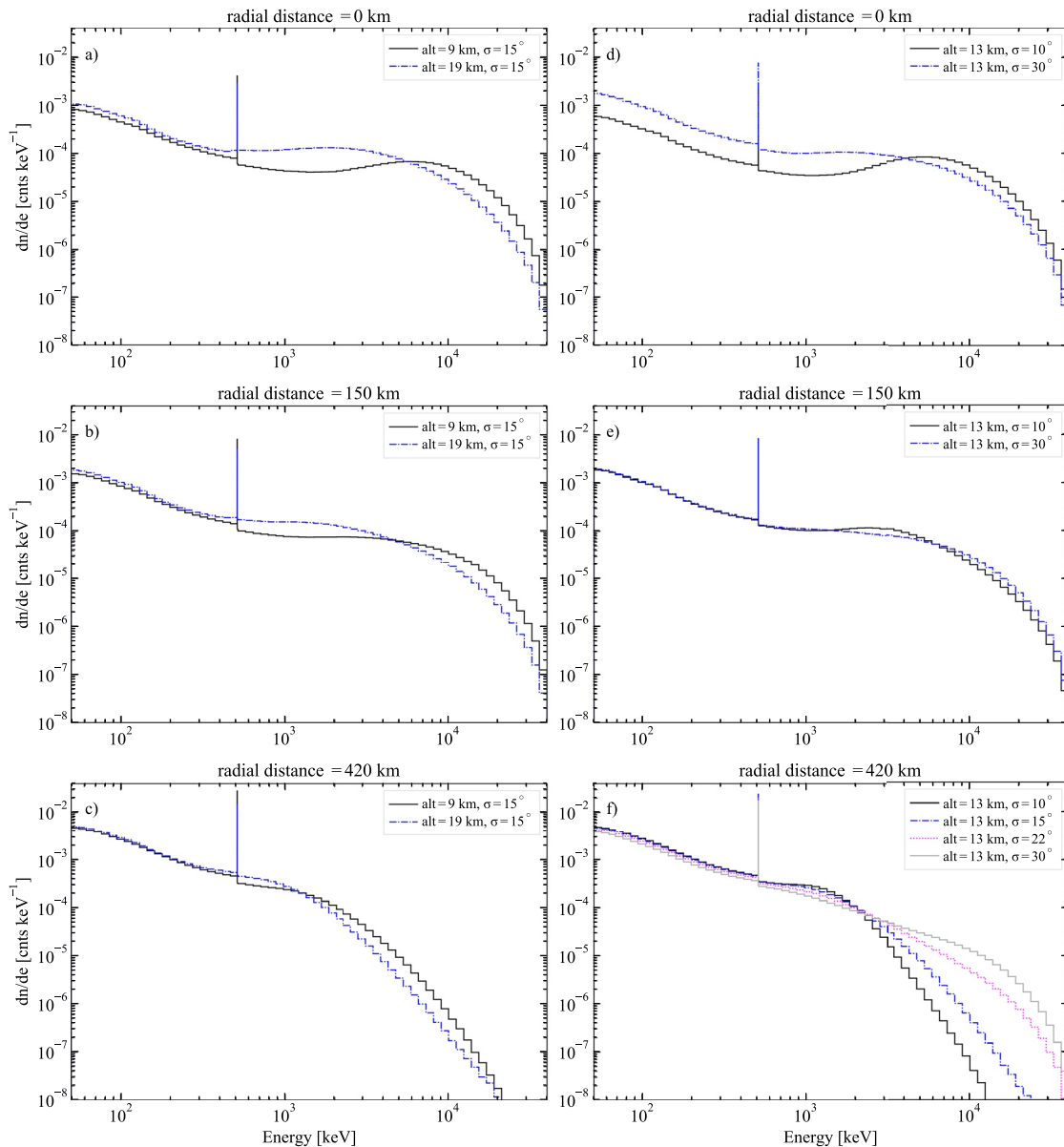


**Figure 3.** Comparison of terrestrial gamma-ray flash models produced at different altitudes and different  $\sigma_\theta$ , observed at different radial distances at an altitude of 408 km. The spectra are normalized to one.

observed at radial distance 0, 150, and 420 km. Figures 3d–3f compares two models produced at an altitude of 13 km with  $\sigma_\theta = 10^\circ$  and  $30^\circ$ . These plots are further discussed in Section 5.1.

In step 3 the ASIM mass model uses the time-energy spectra from step 2 as input to model the detection of counts. The radial distance is fixed based on the TGF source position obtained by lightning detection data. This produces 60 (HED and LED) new time-energy spectra for the given radial distance. The ASIM mass model is a full scale Geant4 model of the ASIM instrument mounted on the Columbus module on the ISS (Østgaard, Balling, et al., 2019). Note that we removed from the Monte Carlo code the ACES instrument from Figure 11 in Østgaard, Balling, et al. (2019) as it is not present on ISS together with ASIM.

In step 4 the output spectra from step 3 are used to simulate TGF duration and instrumental effects in HED. We generate a very large photon list sampled from the time-energy output spectra from step 3. In order to account for the physical duration at source we add a random number, sampled from a Gaussian time distribution, to each

simulated time tag. The standard deviation of the Gaussian time distribution is fitted such that the modeled time profile matches the duration of the measured TGF. This duration and the time profile after propagation through the atmosphere does not bias the analysis as the safety time criteria are implemented both in the forward modeling and on the observed data. The energy spectrum after step 4 consists of a large number of separate TGFs simulated under the same conditions, including instrumental effects, cumulated to obtain a sample spectrum with large count statistics. We take into account the individual energy range of each of the 12 HED detectors, energy resolution, pulse-pileup, lower energy threshold for *fast* events and the previously discussed safety criteria in Section 2.2. This gives a modeled spectra that we can compare to the measured spectra. For LED we only apply the energy resolution to the output from the mass model.

### 3.3. Statistical Tests

The output from step 4, which is given for a range of altitudes and beaming angles can be compared with the measured spectra when we know the geolocation of the TGF and therefore the incident angle of photons. To find the most likely altitude and beaming angle we use maximum likelihood estimation (MLE) and  $\chi^2$  statistics to compare and quantify the goodness of fit. MLE based on Poisson statistic is the best approach to estimate parameters in counting experiments, especially if we have small total numbers of counts (Hauschild & Jentschel, 2001). We estimate the best fit model using MLE by minimizing  $-2\log \mathcal{L}$  (Briggs et al., 2010; Mailyan et al., 2016) with

$$\log \mathcal{L} = \sum_i [O_i \ln(M_i) - M_i - \ln(O_i!)] \quad (1)$$

where  $O_i$  and  $M_i$  are the observed and modeled number of counts in each energy bin  $i$ . We will refer to  $-2\log \mathcal{L}$  as the negative log likelihood (NLL). The modeled energy spectra are fitted to the measured energy spectrum by minimizing NLL. When the difference in NLL between two models is greater than five, the best fit model is preferred above the other model with greater than 99% confidence level (Mailyan et al., 2016; Sarria et al., 2021). This method does not state if the best model is any good in an absolute term, but only states the relative goodness. Therefore we also use the Pearson  $\chi_P^2$  statistic to quantify the goodness of fit.

$$\chi_P^2 = \sum_i \frac{(O_i - M_i)^2}{M_i} \quad (2)$$

The reduced  $\chi^2$  is given by

$$\chi_v^2 = \frac{\chi_P^2}{v} \quad (3)$$

where  $v$  is the number of degrees of freedom and is given by  $v = \text{"number of bins"} - \text{"number of free parameters"} - 1$ , where the free parameters are production altitude, beaming angle, intensity of HED, and intensity of LED. That gives three free parameters using only HED data and four free parameters if LED data are available. If the  $\chi_v^2$  statistic is close to one it is a good fit. If it is below the critical value given by the  $\chi^2$ -distribution, the model is considered compatible with the measurement with a 95% significance level. If it is above, the model is rejected. The energy bins in both MLE and  $\chi^2$  statistics are chosen by the following criteria: (a) At least five measured counts in each bin, (b) every bin has the same number of counts according to the model, (c) as many bins as possible (James, 2008).

A third statistical test is also implemented to assess the absolute goodness of fit using MLE. This is done by generating a NLL distribution by calculating the NLL for each individual simulated TGF in step 4 to the full energy spectrum of all the simulated TGFs after step 4. The NLL for the observed spectrum compared to the full simulated energy spectrum is compared to the NLL distribution (Lyons, 1986). We chose a 90% confidence level to reject the model, that is, the model is rejected if 90% or more of the NLL distribution have a lower NLL than the observed data. There is a generally good compatibility between the three statistical tests. Therefore, this third method is not discussed further in this study but a comparison between the three statistical tests is shown in Figure S1 in Supporting Information S1.

When we have data from both HED and LED, multi-hits in LED are removed and we scale both simulations to the HED and LED data independently. We do not model the multi-hit counts in LED because they do not take part

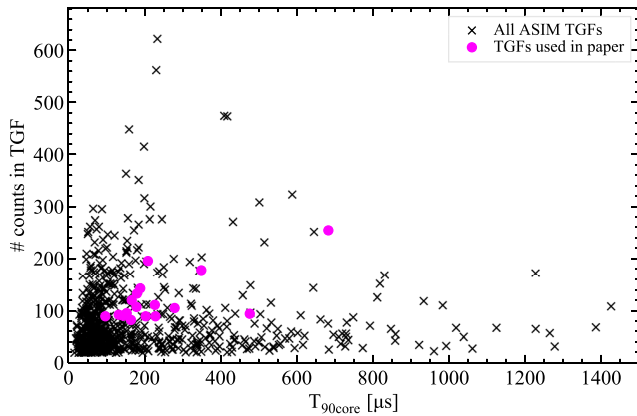


**Figure 4.** Total number of raw counts in a TGF versus  $T_{90\text{core}}$  duration scatter plot. The duration and number of counts are calculated for HED data.

in the spectral analysis. This is the reason why we keep the normalization between HED and LED independent. The energy range considered for HED is 400 keV to 40 MeV, and the energy range considered for LED is 60–350 keV.

#### 4. Results

The total number of TGFs detected by ASIM is about 900 TGFs between June 2018 and December 2020. Of these, 17 TGFs meet the TGF sample selection where we have good count statistics, known production geolocation, and minimal instrumental effects. The TGFs are shown in Figure 4 where we plot the number of counts per TGF versus duration.  $T_{90\text{core}}$  is defined as the minimum duration where 90% of the counts in the TGF are included.

Table 1 shows the observed properties of the TGFs included in the analysis. The TGFs are ordered in increasing radial distance from the ISS footpoint. The datetimes marked with an asterisk are time corrected down to less than 2 ms by correlating MMIA photometer data with ground based lightning detections. The total number of counts per TGF in HED and LED are shown,

and we also show the number of counts used in the spectral analysis. The counts used for spectral analysis are counts inside the suitable energy range and not removed by safety time criteria (HED) or multi-hits (LED). If there are no LED data for the event the number of counts is marked with a dash. The radial distance between the subsatellite point and the source geolocation of the TGF foot-point are given together with the latitude and longitude of the source geolocation. The TGF geolocation is estimated from lightning detections associated with the TGF and independently checked with imaging results from LED when available. The duration of each TGF in HED is presented as both  $T_{50\text{core}}$  and  $T_{90\text{core}}$ . These are the minimum durations where 50% and 90% of the counts in the TGF are included. The standard  $T_{50}$  and  $T_{90}$  are calculated by taking the cumulative count distribution of

**Table 1**  
*Observed Parameters of the TGFs*

TGF ID	Datetime	All counts (HED/LED)	Counts used in spectral analysis (HED/LED)	$T_{50\text{core}}$ (μs)	$T_{90\text{core}}$ (μs)	Radial distance (km)	Lat/Lon (degrees)
1	2019-Sep-03 18:51:57.091569*	254/102	200/66	226	683	39	20.89/83.77
2	2018-Jul-26 09:23:21.381379	177/66	130/38	147	349	92	14.48/−93.82
3	2019-Feb-19 00:51:47.519043*	107/37	78/19	83	179	168	−21.18/48.79
4	2019-May-28 07:00:03.420724*	89/55	61/37	36	97	170	11.47/−79.75
5	2018-Jul-03 23:37:55.256759	82/27	62/13	71	164	179	6.37/21.63
6	2019-Jan-06 13:10:45.987044*	111/46	86/30	92	227	187	−12.80/133.30
7	2020-Mar-22 17:51:17.439568	143/64	103/36	90	189	190	−12.96/157.04
8	2019-Nov-20 22:38:22.732144*	120/53	83/31	64	166	193	12.53/73.24
9	2019-Sep-17 03:03:36.202750	89/-	79/-	78	229	193	17.00/−124.16
10	2020-Nov-14 10:45:19.803592	195/-	133/-	81	209	194	3.49/114.37
11	2019-Jan-30 03:46:56.982759	105/-	81/-	105	279	196	−10.96/131.05
12	2018-Jul-27 19:24:05.069539*	95/60	72/31	52	153	222	4.03/116.90
13	2018-Dec-04 05:46:39.269203	92/-	68/-	38	132	234	6.25/96.61
14	2020-Jun-14 17:29:34.476529	90/-	67/-	49	144	239	6.13/7.27
15	2019-Sep-17 03:04:28.380704	94/-	77/-	159	477	266	16.98/−124.29
16	2018-Jun-05 04:55:55.390864	89/48	64/32	73	203	312	10.12/−80.19
17	2018-Oct-11 13:43:25.048869	133/90	105/62	74	180	326	3.46/113.17

*Note.* The durations  $T_{50\text{core}}$  and  $T_{90\text{core}}$  are calculated for HED data. The latitude and longitude are the geolocation of the sferic associated with the TGF, and the radial distance is the distance between the subsatellite point and the geolocation of the associated sferic. The datetimes marked with an asterisk are time corrected down to less than 2 ms absolute timing accuracy.

**Table 2**Results of the Spectral Analysis Showing the Accepted Models by MLE and  $\chi^2$  Statistical Tests

TGF ID	5°(MLE)	5°( $\chi^2$ )	10°(MLE)	10°( $\chi^2$ )	15°(MLE)	15°( $\chi^2$ )	22°(MLE)	22°( $\chi^2$ )	30°(MLE)	30°( $\chi^2$ )	Best fit (km, degrees)
1	—	17–19	—	15–17	13–15	11–17	9–15	9–15	9–13	9–15	11,30
2	—	—	19	—	15–19	15–17	13–19	13–17	9–17	9–15	13,30
3	—	—	9–11	9–13	9–15	9–17	9–15	9–17	9–15	9–17	9,30
4	—	—	9–17	9–17	9–19	9–19	9–19	9–19	9–19	9–19	17,30
5	—	—	9–19	9–19	11–19	9–19	13–19	9–19	11–19	9–19	19,30
6	—	—	—	—	9–15	9–17	9–17	9–19	9–17	9–17	9,15
7	—	—	—	—	9–15	9–17	9–17	9–17	9–17	9–17	9,15
8	—	—	—	—	9–15	9–13	9–17	9–15	9–17	9–15	11,30
9	—	—	9–19	11–15	13–19	15–19	15–19	17–19	15–19	15–19	19,15
10	—	—	—	—	9–17	9–17	9–17	9–19	11–19	9–19	15,22
11	—	—	—	—	9–15	9–15	9–17	9–17	9–15	9–17	11,22
12	—	—	—	—	9–15	9–19	9–19	9–19	9–19	9–19	13,22
13	—	—	9	9	9–19	9–19	15–19	13–19	15–19	13–19	19,15
14	—	—	—	—	9–17	9–19	9–19	9–19	9–19	9–19	15,22
15	—	—	—	—	9–13	9–15	9–19	9–19	9–19	9–19	13,22
16	—	—	—	—	—	—	9–19	9–19	9–19	9–19	19,30
17	—	—	—	—	9–15	9–17	—	9,17–19	—	—	9,15

Note. The table shows the accepted production altitudes in km for different  $\sigma_\theta$ .

the signal and calculate the duration between 25% and 75% (5% and 95%) of the count distribution. However, this method is more sensitive than the core method to where the start and the end of the signal is defined. As it is not always straight forward to define the exact starting- and ending point of a TGF, the core method is preferred.

We present the results of the spectral analysis in Table 2. For each individual TGF the accepted altitude range according to MLE- and  $\chi^2$  statistics is presented for different beaming angles  $\sigma_\theta$ . We also have a column for the best fit model. If LED data are available they are included in the spectral analysis, however the results using only HED are not very different from the results using both HED and LED. Note that TGF 9 and TGF 15 are originating from the same thunderstorm with  $\sim 1$  min separation.

For clarity we will present the analysis results of TGF 2 in detail. Figure 5a) shows WWLLN and GLD360 detections within  $\pm 5$  min of the TGF, and within  $\pm 30$  s of the TGF. We also show the lightning detection that is closest in time to the TGF within 0–30 ms and within a radial distance of 1,000 km as a triangle. This lightning detection is assumed to be the lightning associated to the TGF. In the center of the map we plot the subsatellite point surrounded by a circle with a radius of 500 km. Figure 5b) shows a time-energy scatter plot of the TGF detected in HED and LED. Only the counts with correctly measured energies are shown. Figure 5c) shows the light curve of all the counts detected in HED and LED, and the light curve using only counts used in the spectral analysis. Figure 5d) shows the results of the MLE statistical test. As only the relative difference in NLL is used to decide which models are a better fit we plot  $NLL - \min(NLL)$ , where  $\min(NLL)$  is the minimum NLL value, that is, the best fit model. If the model has a value below the critical value of 5, the model is considered accepted by the MLE, for example, for  $\theta_\sigma = 22^\circ$ , the accepted altitudes are 13–19 km. Figure 5e) shows the results of the reduced  $\chi^2$  test. If a model has a value below the critical value shown with the dashed line, the model is considered accepted. In general there is a good agreement between the MLE- and  $\chi^2$ -tests except for models that are close to the critical values of both tests. Figures 5f and 5g) shows the measured energy spectrum together with the best fit model. Figure 5f) shows the energy spectrum with counts on the y-axis. As discussed in Section 3.3 the energy bins are selected to have a flat model spectrum. The uncertainty of the data points is  $\pm 1$  standard deviation assuming Poisson statistics. Figure 5g) shows the differential energy spectrum. Figures with the same format as Figure 5 are found in Supporting Information S1 for each TGF analyzed in this study. For four of the TGFs the

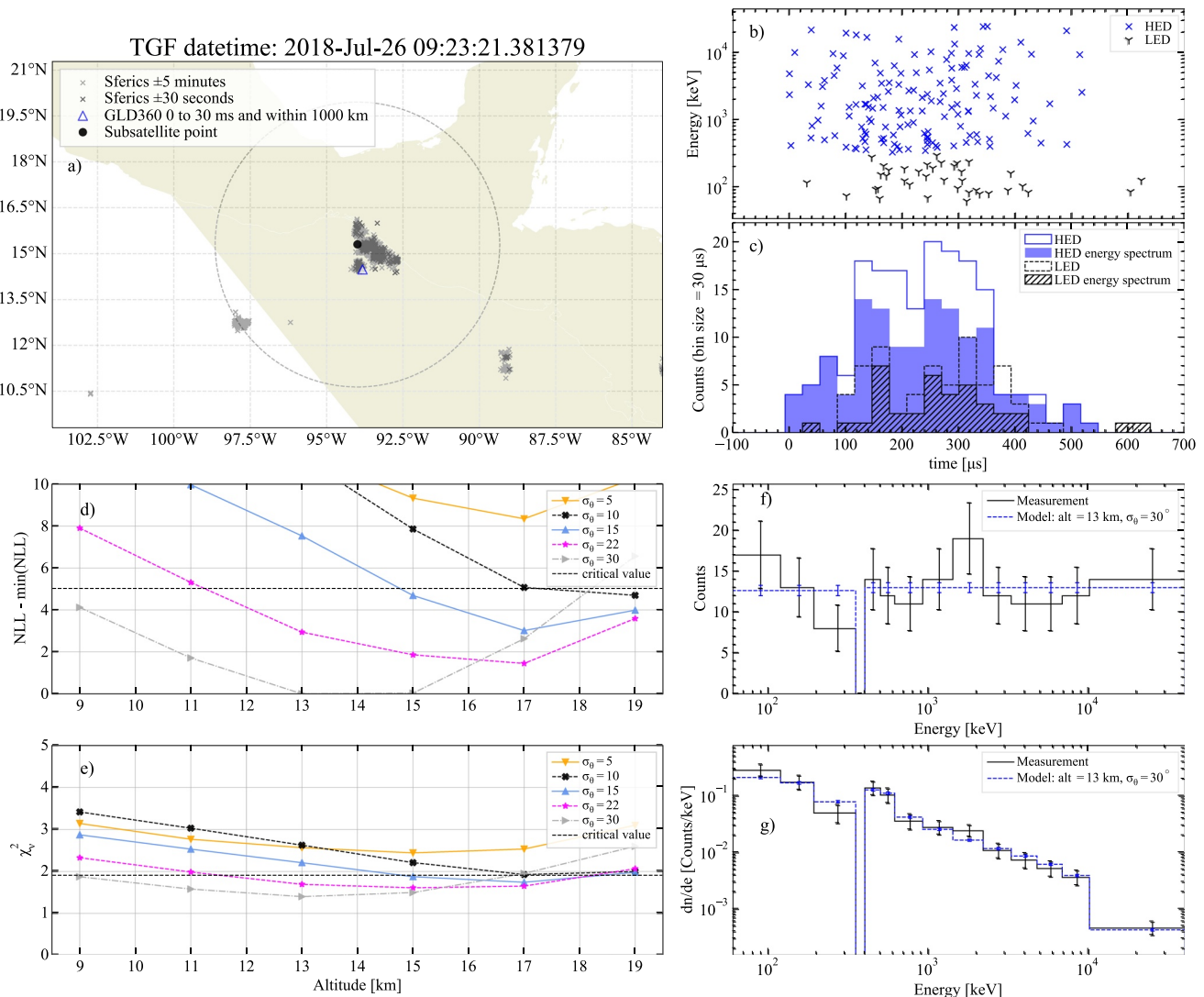


**Figure 5.** Plots summarizing the spectral analysis of TGF 2. (a) Map giving an overview of the lightning activity at the time and location of the TGF. The circle around the subsatellite point has a radius of 500 km. (b) Time-energy scatter plot of the counts used in the spectral analysis for HED and LED. (c) Light curve showing all the counts detected in HED and LED and the counts used for spectral analysis. (d) The results of the spectral analysis using MLE statistical test. If  $NLL - \min(NLL) < 5$  the model is considered accepted by the MLE. (e) Results of the  $\chi^2$  statistical test showing the reduced  $\chi^2$  value. If the model has value below a critical value the model is considered accepted by the  $\chi^2$  test. (f) Count energy spectrum of the observed TGF compared to the best fit model. (g) Differential energy spectrum of the observed TGF compared to the best fit model.

source geolocation could be estimated by the imaging capabilities of LED. For these TGFs the geolocation and 1 sigma uncertainty provided by the LED imaging are plotted.

Figure 6a shows the observed fluence,  $f_o$ , given by the number of counts in HED divided by the effective area of HED. The number of counts in HED are corrected for instrumental effects and the effective area of HED varies with the simulated models. The effective area is calculated using the simulated models as input spectrum to the mass model. Figure 6b shows the estimated number of photons with energies larger than 1 MeV at source for all the accepted models. The values are calculated by

$$\# \text{photons at source} = \frac{f_o}{f_m} \times 10^{17} \quad (4)$$

where  $f_o$  is the observed fluence and  $f_m$  is the modeled fluence for the given production altitude, beaming, and radial distance, assuming  $10^{17}$  photons above 1 MeV at source.

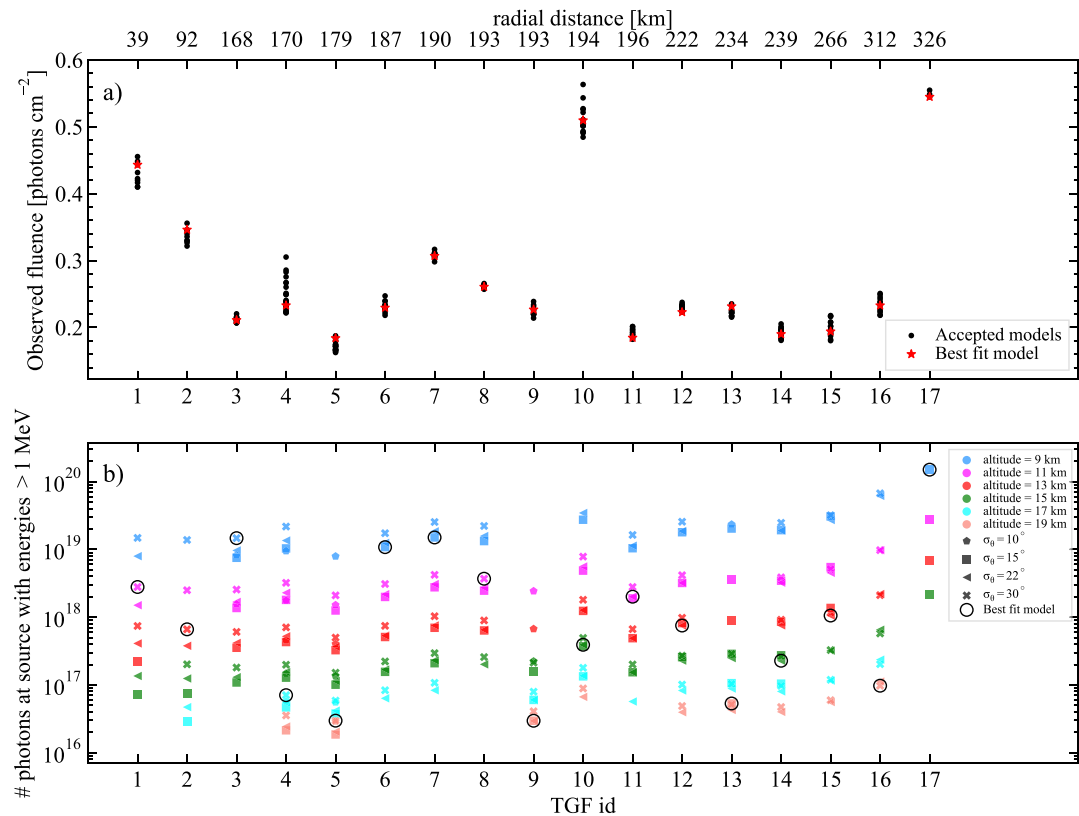


**Figure 6.** (a) Observed fluence for all the models accepted by maximum likelihood estimation (MLE). (b) Estimated number of photons at source with energy  $> 1 \text{ MeV}$  for all models accepted by MLE. The terrestrial gamma-ray flashes are sorted in increasing radial distance. Note the linear scale in (a) and the logarithmic scale in (b).

## 5. Discussion

As this is the first spectral analysis of TGFs detected by ASIM, we keep the TGF sample as clean as possible selecting only 17 of  $\sim 900$  TGFs. The number of suitable TGFs is low because of strict requirements on the reliability of the energy estimate, good count statistics, and on the availability of a reliable geolocation. The sample size would increase if we relaxed the minimum number of counts or the maximum allowed fraction of counts affected by instrumental effects. However, it would not result in a better quality of the scientific interpretation as the uncertainty in the results would increase. In this study, we cannot claim any generalization of the properties of TGFs as we analyze a small sub-sample that is biased by the TGF sample selection discussed in Section 3.1.

All of the 17 TGFs analyzed in this work have a GLD360 lightning match. The two briefest duration TGFs, TGF 4 and 13, also have a WWLLN match at a position compatible with GLD360 within location uncertainties. This is in agreement with Connaughton et al. (2013); Lindanger et al. (2020) that show that brief duration TGFs are more likely to have a WWLLN match.

### 5.1. Source Properties of TGFs

ASIM TGFs are compared to models with source altitude of 9–19 km and Gaussian beaming angle  $\sigma_\theta$  from  $5^\circ$  to  $30^\circ$ . A larger beaming angle,  $\sigma_\theta = 40^\circ$ , was simulated but not included in the study as it gave very similar results to  $\sigma_\theta = 30^\circ$ . There were no cases where all altitudes for  $\sigma_\theta = 30^\circ$  were accepted while all altitudes for  $\sigma_\theta = 40^\circ$  were rejected, or opposite. As no TGFs have an accepted model by MLE with  $\sigma_\theta = 5^\circ$  we may reject  $\sigma_\theta = 5^\circ$  as a plausible TGF beaming based on the 17 TGFs in this sample. This is consistent with the minimum beam width expected from bremsstrahlung produced by RREA in a perfectly uniform electric field (Hazelton et al., 2009). Figure 2a in Hazelton et al. (2009) shows approximately a Gaussian distribution with FWHM =  $18^\circ$ , which

corresponds to  $\sigma_\theta = 7.6^\circ$ . Therefore, the lack of good fits with  $\sigma_\theta = 5^\circ$  is a consistency check, because the model, if accepted, would be incompatible with the basic physics of photon scattering in air.

Cummer et al. (2014); Pu et al. (2019) estimate TGF production altitudes between 10 and 15 km using LF radio measurements. Heumesser et al. (2021) get similar results by modeling light propagation through clouds assuming typical values of size and density of cloud particles. Mailyan et al. (2016) analyzed Fermi-GBM TGFs and found that 11.6 km models gave frequently a better fit than higher altitude models, but 13.6 km could not be rejected for those cases. Sometimes also TGFs had a best fit at 20.2 km, but lower altitude models could not be rejected. Table 1 in Mailyan et al. (2016) shows which models are accepted and even though the best fit model is highlighted, most of the other models are also accepted for most of the TGFs. This is in agreement with our results, see Table 2, where only a few models are rejected per TGF. The MLE and  $\chi^2$  tests state that if a model is below or above a critical value it is accepted or rejected. If a model is accepted it could explain the observation even though there exists a better fit. Therefore the “best fit model” should be handled with caution and not used to draw general conclusions on the source spectrum. Figures 3a–3c show that it is increasingly harder to distinguish 9 and 19 km production altitude with increasing radial distance. Remember that we only have  $\sim 100$  counts per TGF and the number of counts at high energies are few. Figures 3d–3f shows that it is very hard to distinguish beaming angles  $\sigma_\theta$  at a radial distance of 150 km. For a radial distance of 420 km it is easier to distinguish the beaming angle as the observation point is then outside the direct photon beam for small  $\sigma_\theta$  relative to large  $\sigma_\theta$ , seeing a larger fraction of Compton scattered photons softening the energy spectrum for small  $\sigma_\theta$ . These properties of TGF modeling are reflected in the results in Table 2. It is easier to distinguish altitudes for TGFs observed at smaller radial distances, and it is easier to distinguish  $\sigma_\theta$  at larger radial distances.

The TGF id's are sorted in increasing radial distance. At distances larger than TGF 9 (193 km) only one TGF has an accepted model with  $\sigma_\theta = 10^\circ$ . As it is easier to distinguish  $\sigma_\theta$  at larger radial distances, this may indicate that in general the beaming of TGFs has  $\sigma_\theta \geq 15^\circ$ . As discussed in the beginning of this subsection, the intrinsic beam width of bremsstrahlung photons from RREA in a perfectly uniform field correspond to  $\sigma_\theta \approx 7.6^\circ$ . It is not unreasonable to expect further widening due to non-perfectly uniform electric field in a thundercloud that leads to  $\sigma_\theta > 10^\circ$ . However, based on the 17 TGFs analyzed we cannot state, based on observations, that in general  $\sigma_\theta \geq 15^\circ$ . Also to distinguish  $\sigma_\theta$  we need to observe TGFs at large radial distances. If we assume that TGFs with smaller  $\sigma_\theta$  exist, they would not have been included in this analysis due to few observed counts at large radial distances, that is, our TGF sample is biased according to our selection criteria.

Figure 6a shows the observed fluence of the detected TGFs for all accepted models according to the MLE test. If all TGFs had the same brightness at source the observed fluence would decrease with increasing radial distance. This is not evident in Figure 6a as TGF 10 and 17 are observed at large radial distances with high observed fluence. This supports the idea that TGFs have a wide range of brightness at source or significant tilting with respect to the vertical axis. Figure 6b shows the estimated number of photons at source with energies above 1 MeV. All the accepted models are shown with different colors representing altitudes, and markers representing  $\sigma_\theta$ . It is clear from the plot that the uncertainty of the number of photons at source is three orders of magnitude. This is due to high photon absorption in the atmosphere from 9 km to space, compared to 19 km to space. A wide range of altitudes is accepted for each TGF. The best fit models are indicated with a black circle and range from  $1.9 \times 10^{16}$  to  $1.5 \times 10^{20}$  photons at source as both 9 and 19 km altitude are best fit models dependent on the TGF. This is roughly in agreement with Figure 8, top panel, in Mailyan et al. (2016) that shows the number of relativistic electrons above 1 MeV at source. The number of electrons in Mailyan et al. (2016) varies from  $4 \times 10^{16}$  to  $3 \times 10^{19}$ . Conversion from relativistic electrons to bremsstrahlung photons is done using Equations 5 and 9 in Dwyer et al. (2017) resulting in a bremsstrahlung photons to relativistic electrons ratio of 0.33 for an electric field strength at sea-level of 400 kV/m. This is the electric field assumed in Mailyan et al. (2016). In order to compare the results in Mailyan et al. (2016) with ours, we convert from electrons to photons and get a range of  $1.3 \times 10^{16}$  to  $10^{19}$  photons. The one order of magnitude difference for the maximum number of photons at source can well be explained by that the lowest production altitude modeled in this study is 9 km, while in Mailyan et al. (2016) the lowest altitude modeled was 11.6 km. The uncertainties in Figure 6b would be reduced by several orders of magnitude if the source altitude of TGFs were estimated by for example LF radio measurement (Cummer et al., 2014; Pu et al., 2019), lightning mapping arrays (LMA) (Lu et al., 2010), radar measurements (Mailyan et al., 2018), or the electric field antenna part of the TARANIS mission (Lefevre et al., 2008). Given the accepted idea that a TGF is produced inside a cloud it is not likely that production altitudes above the tropopause are physical. Even

if production altitudes of 17 and 19 km are accepted solutions of the spectral analysis, they may not be realistic as the tropopause height is on average  $\sim 16.5$  km in the tropical latitude band of the TGFs analyzed (Seidel et al., 2001). One would need a significant overshooting top and TGF production close to the top for a TGF source to be located at 17–19 km altitude. Production altitudes above the tropopause are also not in agreement with typical values from Cummer et al. (2014); Pu et al. (2019), and Heumesser et al. (2021).

The maximum energy count per TGF of the 17 individual TGFs analyzed in this study is in the range 16–28 MeV. The median of the maximum energies is 21 MeV. There is a total of 8 counts with energies above 24 MeV during the 17 TGFs. Note that this is not the photon energy, but the energy of the count in the detector. A larger photon energy is expected, as a partial energy deposit in the detector is likely at these energies. To assess if these 8 counts above 24 MeV originates from the TGFs and not background radiation we use data between  $-900$  ms and  $-100$  ms prior to the TGF detection as background. The average background rate was found to be 482 counts above 24 MeV per second. Given this background rate, the Poisson probability of having 8 counts or more above 24 MeV during the 17 TGFs (4060  $\mu$ s) is 0.001. Therefore we can conclude that the maximum energy produced by the TGFs is larger than 24 MeV. For comparison RHESSI (Smith et al., 2005), AGILE (Marisaldi et al., 2010), and Fermi (Briggs et al., 2010) teams reported TGF single photon energies of  $>= 20$ , 43, and 38 MeV, respectively. Tavani et al. (2011) reported higher energies detected by AGILE, however, Marisaldi et al. (2019) questioned this after an improved understanding of instrumental effects under high-flux conditions.

## 5.2. Limitations on Spectral Analysis From Space

This study emphasize that the spectral analysis does not constrain well the parameter space of the source models. Therefore we want to investigate what the intrinsic limitations of this method are. To assess the limitations on the spectral analysis of TGFs detected from space, we performed a pseudo spectral analysis by randomly sampling 100 and 1,000 photons from the energy distribution of photons after atmospheric propagation from a production altitude of 11 km and  $\sigma_\theta = 22^\circ$ . We performed the spectral analysis on these pseudo observations assuming a perfect instrument without taking into account a mass model or instrumental effects. The radial distances considered are 0, 150, and 420 km. The results are shown in Figure 7 where the pseudo observation consist of 100 photon energies on the left side, and 1,000 photon energies on the right side. Note that the results can be slightly different selecting a different random seed for the random sampling. The correct model corresponding to the pseudo observation is always accepted, but it is not always the best fit. Several models can be accepted and in agreement with Hauschild and Jentschel (2001), MLE performs better than  $\chi^2$  estimating the correct model. The  $\chi^2$  test is unreliable for low count statistics and it should be avoided in such cases, however it can be used as an additional test to give a measure of absolute goodness of fit, not provided by MLE method, if count statistics is large enough. For a radial distance of 420 km, the altitude is nearly impossible to constrain as MLE accepts altitudes between 9 and 17 km even for a pseudo observation of 1,000 photons. It is clear from Figure 7 that for 100 photons the correct model is accompanied by other accepted models. Therefore all accepted models should be taken into account when trying to confine the source properties of TGFs. If independent measurements of the production altitude were provided, the beaming properties may be confined by the spectral analysis, depending on the radial distance between the source and the satellite. This conclusion is only valid assuming no or negligible tilting of the TGF beam. Tilting of the TGF beam is expected both in leader models and models dominated by large-scale electric fields. However, no observations have shown evidence of TGF tilting yet, as several spacecraft need to be observing the same TGF from different locations in order to resolve the degeneracy between tilt and beam opening angle. The results of these simulations provide valuable recommendations for the design phase of future TGF detecting missions: a large effective area, that is, large count statistics, is not enough for the purpose of spectral analysis of individual TGFs, and complementary observations to constrain the production altitude should be planned.

## 6. Summary

This study provides the first spectral analysis of TGFs detected by ASIM, comparing individual TGFs to modeling. A sample of 17 TGFs is selected by rigorous selection criteria to keep a clean sample. In agreement with Mailyan et al. (2016) the observed energy spectra are diverse meaning the cumulative spectral analysis of TGFs should be avoided. Monte Carlo modeling of individual TGFs have been compared to observations allowing us to study the possible source altitudes and beaming geometries of TGFs. A careful statistical method using both

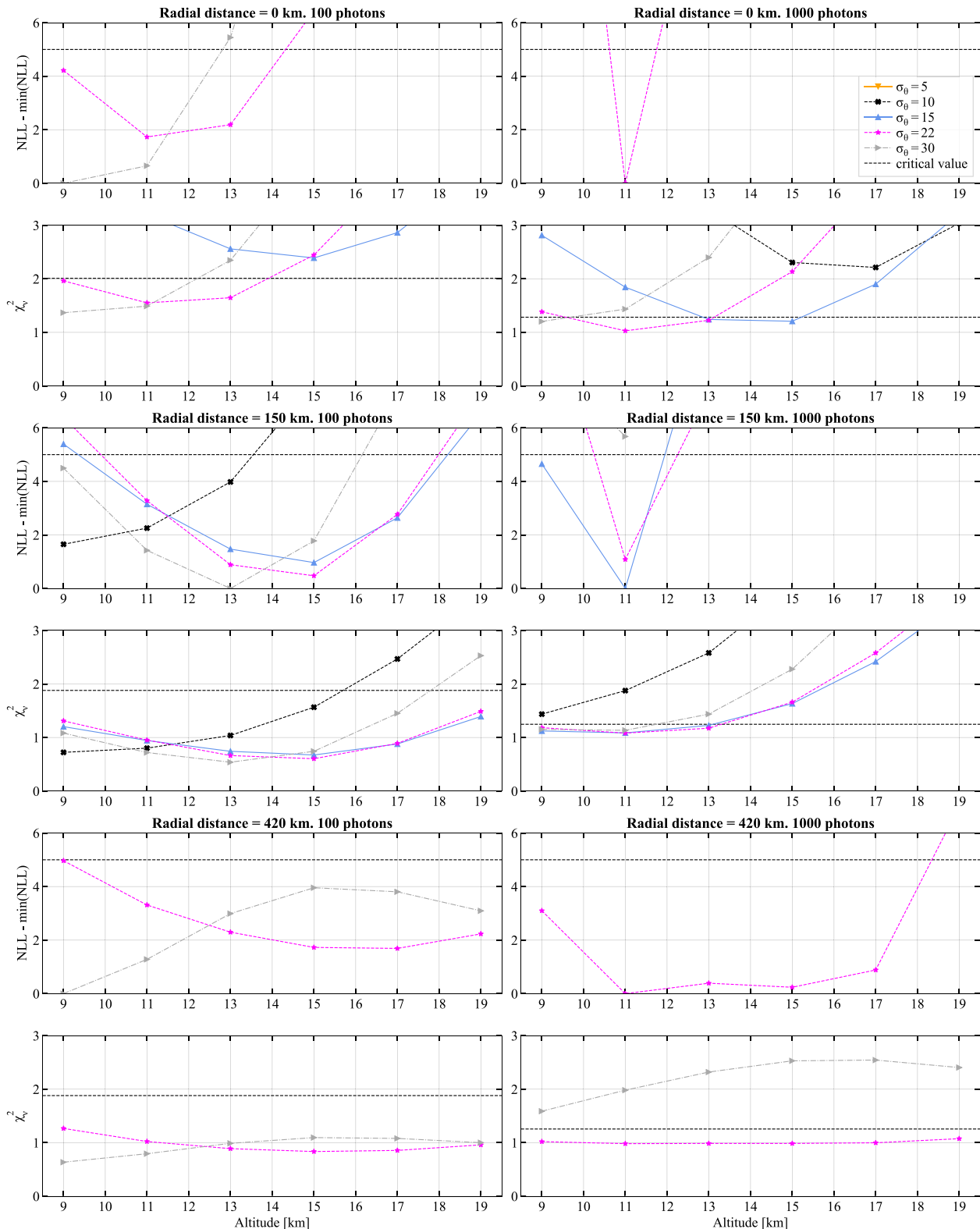


**Figure 7.** Pseudo spectral analysis by randomly selecting 100 and 1,000 photons from the model corresponding to an altitude of 11 km and  $\sigma_\theta = 22^\circ$ . The results from MLE and  $\chi^2$  are shown for different radial distances with a pseudo observation of 100 photons on the left side, and 1,000 photons on the right side.

$\chi^2$  and maximum likelihood estimation is implemented to assess which models fit the observations. A large effort has also been made to properly account for instrumental effects in the high energy detector. For all the TGFs in the sample, several combinations of source altitudes and beaming geometries are accepted by the statistical tests. Tilting of the TGF beam has not been considered in this analysis as adding another free parameter to the statistical tests would lead to overfitting. TGFs may not be centered perfectly in the upward direction, however, only simultaneous TGF observation from a constellation of satellites could solve the degeneracy between beaming angle and tilt.

This work also highlights the limitations of spectral analysis of TGFs from space if no additional measurement can be used to narrow the parameter space, for example by setting a smaller altitude range by radio measurements. The ability to confine source altitude and beaming angle depends on the radial distance in addition to count statistics. All accepted models, according to maximum likelihood estimation, should be considered when trying to confine the source properties of TGFs, not only the best fit. The  $\chi^2$  test is unreliable for low count statistics and maximum likelihood estimation should be used instead (Hauschild & Jentschel, 2001).

The analyzed TGFs show diverse observed fluence independent of the distance between the source and ASIM supporting the idea that TGFs have a wide range of brightness at source. The number of photons at source with energies larger than 1 MeV ranges from  $10^{16}$  to  $10^{20}$  and an independent measure of the altitude, for example by LF-radio (Cummer et al., 2014; Pu et al., 2019) or LMA (Lu et al., 2010; Mailyan et al., 2018), is needed to further constrain the number of photons at source. Based on the 17 analyzed TGFs a lower threshold of the maximum photon energy produced by TGFs is estimated to be 24 MeV.

## Appendix A: The HED Safety Time Criteria

For high fluxes and high energy photons the HED instrument suffers from high voltage drops in the PMTs which have to be handled carefully. This high voltage drop is shown in Figure S19 in Supporting Information S1 where flight data from one of the 12 detectors in HED are shown. Figure S19a in Supporting Information S1 shows the first count following a count with energy  $E_0 = 500 \text{ keV} \pm 10\%$ . The *fast* events are shown in orange color and *normal* events are shown in blue color. Figure S19b in Supporting Information S1 shows the same data displayed as a 2D histogram. Figure S19c in Supporting Information S1 shows the first count following an energetic count with energy  $E_0 = 25,000 \text{ keV} \pm 10\%$ . Figure S19d in Supporting Information S1 shows the same data displayed as a 2D histogram. The proton peak, which should be at  $\sim 31 \text{ MeV}$ , is clearly decreasing toward lower energy channels for smaller  $dt$  after an energetic count. This effect is less substantial when the energy of the first count,  $E_0$ , is lower. The white gap for *fast* events when  $dt < 10 \mu\text{s}$  in Figure S19c and S19d in Supporting Information S1 is due to a higher threshold for *fast* events to be recorded in the data, than for *normal* events. Note that HED consists of 12 independent BGO-PMT detectors and a voltage drop introduced by an energetic pulse in one of the detectors does not affect the other 11 detectors.

The voltage drop effect was investigated further at ground using a spare BGO-PMT detector used in HED. In the laboratory, three natural radioactive background energy peaks were used together with a weak  $^{60}\text{Co}$  source. The  $^{60}\text{Co}$  source emits gamma-rays with energies 1.17 MeV and 1.33 MeV. From the radioactive background in the laboratory we had 1.46 MeV from  $^{40}\text{K}$ , 2.6 MeV from  $^{208}\text{Tl}$ , and  $\sim 32 \text{ MeV}$  from cosmic muons. The energy deposit of muons on the BGO was calculated using the ASIM mass model. A diode, emitting light through the BGO, was used to mimic the energy deposits corresponding to muons sending a new light pulse every 100  $\mu\text{s}$ . Figure S20 in Supporting Information S1 shows the first count after an energetic pulse created by the diode or a muon. We clearly see the muon/diode peak decreasing to a lower energy channel as the time after the energetic pulse gets smaller. Note also that the effect in the lower energy counts in channels 200 and 400 is less significant, but at  $dt \approx 5 \mu\text{s}$  and  $dt \approx 7 \mu\text{s}$  the counts are measured in higher energy channels. The voltage drop in the PMT following an energetic count leads to underestimated pulse heights for high energies and overestimated pulse heights for low energies. We do not know the behavior for counts with energies between 2.6 and 30 MeV. In principle, a correction function dependent on  $E_0$ ,  $dt$ , and the energy of the count following the count with energy  $E_0$ , could be defined. However, Figure S19c and S19d in Supporting Information S1 show that an energy band of 30 MeV is compressed to an energy band of  $\sim 1 \text{ MeV}$  at  $dt \approx 2 \mu\text{s}$ . A correction function going from an energy band of 1–30 MeV must be very accurate to be trusted to restore the original pulse height. We do not have enough

data points and calibration lines in the energy band between 1,275 keV and 30 MeV to make such a correction function reliable.

Instead of a correction function we account for this instrumental effect by implementing an energy dependent “safety time”. We define the safety time as the time we have to wait after an energetic pulse for the proton peak to be above 24.8 MeV (within 20% of 31 MeV), see dashed magenta line in Figure S19 in Supporting Information S1. As the on-ground experiment (Figure S20 in Supporting Information S1) showed that the high energy counts at 32 MeV are most affected by the voltage drop, we know that the energy measurement accuracy at the safety time is  $\leq 20\%$ . A plot of the safety time is shown in Figure S21 in Supporting Information S1.

The safety time presumably does not bias the spectral analysis as it is part of the forward modeling of instrumental effects, as well as implemented on the observed TGF data. We do not remove counts dependent on their energy, but we do remove counts dependent on the energy of the previous count in the same detector. If there exists an unknown significant correlation between the energy of consecutive counts in TGFs at source, then the safety time criteria may bias our spectral analysis as the only time dependence we model is the time profile caused by the transport through the atmosphere added to a Gaussian time distribution that is fitted to each individual TGF. The alternative to the safety time criteria is a fixed dead time of  $\sim 30 \mu\text{s}$  which would remove too many counts during TGF detection.

## Appendix B: TGF Beaming Type Modeling

In the literature (Dwyer & Smith, 2005; Gjesteland et al., 2010, 2011; Hazelton et al., 2009; Mailyan et al., 2016, 2019; Østgaard et al., 2008), the angular distribution of the TGF beam at the source is usually modeled using two possibilities:

1. An isotropic distribution within a given angle range, that is parameterized as a cone half angle  $\theta_{\text{cone}}$ .
2. A Gaussian distribution that is parameterized with  $\sigma_\theta$ .

In the Gaussian beaming the direction of the photons are given by  $x, y, z$ , where  $z$  is upwards and equal to one, and  $x$  and  $y$  are independently sampled from a Gaussian distribution. Even if the Gaussian beaming could be considered more realistic (see e.g., Hazelton et al., 2009), the half angle is easier to understand (visualize) and leads to quite close results after propagation through the atmosphere, due to the angular scattering of the photons. For any  $\theta_{\text{cone}}$ , there is an equivalent  $\sigma_\theta$  for which the fluence distribution after atmospheric propagation is quite close. In Figure B1, we present the equivalence between  $\sigma_\theta$  and  $\theta_{\text{cone}}$ . To produce this plot, the TGF propagation code was

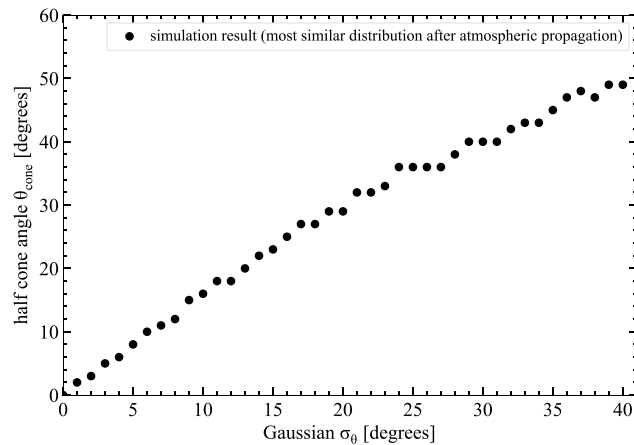


**Figure B1.** Plot showing the equivalence between half cone angle  $\theta_{\text{cone}}$  and Gaussian beaming  $\sigma_\theta$  of terrestrial gamma-ray flashes (TGFs).

run for a series of  $\sigma_\theta$  and  $\theta_{cone}$ , and we calculated for which values the resulting fluence (photons/cm<sup>2</sup>) profile, as a function of radial distance, is as close as possible (using a maximum likelihood evaluation).

## Data Availability Statement

ASIM data are available at the ASIM Science Data Center (<https://asdc.space.dtu.dk>). Additional data for this paper are available at <https://doi.org/10.5281/zenodo.4882745>. The library of simulated TGFs are available as time-energy matrices and fluence estimations for different altitudes, beaming and radial distances at <https://doi.org/10.5281/zenodo.5493579>. The TGF propagation code is available at <https://doi.org/10.5281/zenodo.5493589>. The TGF simulations were performed on resources provided by UNINETT Sigma2—the National Infrastructure for High Performance Computing and Data Storage in Norway, under project no. NN9526K.

## Acknowledgments

The authors thank three anonymous reviewers, whose comments helped us improve the paper. This study was supported by the Research Council of Norway under contracts 208028/F50 and 223252/F50 (CoE). The authors wish to thank the World Wide Lightning Location Network (<http://wwlln.net>), a collaboration among over 50 universities and institutions, for providing the lightning location data used in this study. The authors also wish to thank Vaisala (<https://www.vaisala.com/en>) for providing lightning data. A. Lindanger thanks Michael Briggs, University of Alabama, Huntsville, for a useful discussion on statistical methods.

## References

- Agostinelli, S., Allison, J., Amako, K., Apostolakis, J., Araujo, H., Arce, P., et al. (2003). Geant4—A simulation toolkit. *Nuclear Instruments and Methods in Physics Research Section A: Accelerators, Spectrometers, Detectors and Associated Equipment*, 506(3), 250–303. [https://doi.org/10.1016/S0168-9002\(03\)01368-8](https://doi.org/10.1016/S0168-9002(03)01368-8)
- Briggs, M. S., Fishman, G. J., Connaughton, V., Bhat, P. N., Paciesas, W. S., Preece, R. D., et al. (2010). First results on terrestrial gamma ray flashes from the Fermi Gamma-ray Burst Monitor. *Journal of Geophysical Research*, 115(A7). <https://doi.org/10.1029/2009JA015242>
- Celestin, S., & Pasko, V. P. (2011). Energy and fluxes of thermal runaway electrons produced by exponential growth of streamers during the stepping of lightning leaders and in transient luminous events. *Journal of Geophysical Research*, 116(A3). <https://doi.org/10.1029/2010JA016260>
- Chanrion, O., Neubert, T., Lundgaard Rasmussen, I., Stoltze, C., Tcherniak, D., Jessen, N. C., et al. (2019). The Modular Multispectral Imaging Array (MMIA) of the ASIM payload on the International Space Station. *Space Science Reviews*, 215(4). <https://doi.org/10.1007/s11214-019-0593-y>
- Connaughton, V., Briggs, M. S., Holzworth, R. H., Hutchins, M. L., Fishman, G. J., Wilson-Hodge, C. A., et al. (2010). Associations between Fermi Gamma-ray Burst Monitor terrestrial gamma ray flashes and sferics from the World Wide Lightning Location Network. *Journal of Geophysical Research*, 115(A12). <https://doi.org/10.1029/2010JA015681>
- Connaughton, V., Briggs, M. S., Xiong, S., Dwyer, J. R., Hutchins, M. L., Grove, J. E., et al. (2013). Radio signals from electron beams in terrestrial gamma ray flashes. *Journal of Geophysical Research: Space Physics*, 118(5), 2313–2320. <https://doi.org/10.1029/2012JA018288>
- Cummer, S. A., Briggs, M. S., Dwyer, J. R., Xiong, S., Connaughton, V., Fishman, G. J., et al. (2014). The source altitude, electric current, and intrinsic brightness of terrestrial gamma ray flashes. *Geophysical Research Letters*, 41(23), 8586–8593. <https://doi.org/10.1002/2014GL062196>
- Dwyer, J. R., Liu, N., Eric Grove, J., Rassoul, H., & Smith, D. M. (2017). Characterizing the source properties of terrestrial gamma ray flashes. *Journal of Geophysical Research: Space Physics*, 122(8), 8915–8932. <https://doi.org/10.1002/2017JA024141>
- Dwyer, J. R. (2003). A fundamental limit on electric fields in air. *Geophysical Research Letters*, 30(20). <https://doi.org/10.1029/2003GL017781>
- Dwyer, J. R. (2007). Relativistic breakdown in planetary atmospheres. *Physics of Plasmas*, 14(4), 042901. <https://doi.org/10.1063/1.2709652>
- Dwyer, J. R. (2008). Source mechanisms of terrestrial gamma-ray flashes. *Journal of Geophysical Research*, 113(D10). <https://doi.org/10.1029/2007JD009248>
- Dwyer, J. R. (2012). The relativistic feedback discharge model of terrestrial gamma ray flashes. *Journal of Geophysical Research*, 117(A2). <https://doi.org/10.1029/2011JA017160>
- Dwyer, J. R., & Smith, D. M. (2005). A comparison between monte carlo simulations of runaway breakdown and terrestrial gamma-ray flash observations. *Geophysical Research Letters*, 32(22). <https://doi.org/10.1029/2005GL023848>
- Ebert, U., Nijdam, S., Li, C., Luque, A., Briels, T., & van Veldhuizen, E. (2010). Review of recent results on streamer discharges and discussion of their relevance for sprites and lightning. *Journal of Geophysical Research*, 115(A7). <https://doi.org/10.1029/2009JA014867>
- Fishman, G. J., Bhat, P. N., Mallozzi, R., Horack, J. M., Koshut, T., Kouveliotou, C., et al. (1994). Discovery of intense gamma-ray flashes of atmospheric origin. *Science*, 264(5163), 1313–1316. <https://doi.org/10.1126/science.264.5163.1313>
- Gjesteland, T., Østgaard, N., Collier, A. B., Carlson, B. E., Cohen, M. B., & Lehtinen, N. G. (2011). Confining the angular distribution of terrestrial gamma ray flash emission. *Journal of Geophysical Research*, 116(A11). <https://doi.org/10.1029/2011JA016716>
- Gjesteland, T., Østgaard, N., Connell, P. H., Stadsnes, J., & Fishman, G. J. (2010). Effects of dead time losses on terrestrial gamma ray flash measurements with the Burst and Transient Source Experiment. *Journal of Geophysical Research*, 115(A5). <https://doi.org/10.1029/2009JA014578>
- Grefenstette, B. W., Smith, D. M., Hazelton, B. J., & Lopez, L. I. (2009). First RHESSI terrestrial gamma ray flash catalog. *Journal of Geophysical Research*, 114(A2). <https://doi.org/10.1029/2008JA013721>
- Gurevich, A. V., Milikh, G. M., & Roussel-Dupre, R. (1992). Runaway electron mechanism of air breakdown and preconditioning during a thunderstorm. *Physics Letters A*, 165(5–6), 463–468. [https://doi.org/10.1016/0375-9601\(92\)90348-p](https://doi.org/10.1016/0375-9601(92)90348-p)
- Hauschild, T., & Jentschel, M. (2001). Comparison of maximum likelihood estimation and chi-square statistics applied to counting experiments. *Nuclear Instruments and Methods in Physics Research Section A: Accelerators, Spectrometers, Detectors and Associated Equipment*, 457(1–2), 384–401. [https://doi.org/10.1016/s0168-9002\(00\)00756-7](https://doi.org/10.1016/s0168-9002(00)00756-7)
- Hazelton, B. J., Grefenstette, B. W., Smith, D. M., Dwyer, J. R., Shao, X.-M., Cummer, S. A., et al. (2009). Spectral dependence of terrestrial gamma-ray flashes on source distance. *Geophysical Research Letters*, 36(1). <https://doi.org/10.1029/2008GL035906>
- Heumesser, M., Chanrion, O., Neubert, T., Christian, H. J., Dimitriadou, K., Gordillo-Vazquez, F. J., et al. (2021). Spectral observations of optical emissions associated with terrestrial gamma-ray flashes. *Geophysical Research Letters*, 48(4), 2020GL090700. <https://doi.org/10.1029/2020GL090700>
- James, F. (2008). *Statistical methods in experimental physics* (2nd ed.). World Scientific Publishing Co. Pte. Ltd.
- Köhn, C., Diniz, G., & Harakeh, M. N. (2017). Production mechanisms of leptons, photons, and hadrons and their possible feedback close to lightning leaders. *Journal of Geophysical Research: Atmospheres*, 122(2), 1365–1383. <https://doi.org/10.1002/2016JD025445>
- Köhn, C., & Ebert, U. (2015). Calculation of beams of positrons, neutrons, and protons associated with terrestrial gamma ray flashes. *Journal of Geophysical Research: Atmospheres*, 120(4), 1620–1635. <https://doi.org/10.1002/2014JD022229>

- Köhn, C., Heumesser, M., Chanrion, O., Nishikawa, K., Reglero, V., & Neubert, T. (2020). The emission of terrestrial gamma ray flashes from encountering streamer coronae associated to the breakdown of lightning leaders. *Geophysical Research Letters*, 47(20). <https://doi.org/10.1029/2020GL089749>
- Lefèuvre, F., Blanc, E., Pinçon, J.-L., Roussel-Dupré, R., Lawrence, D., Sauvaud, J.-A., et al. (2008). TARANIS—A satellite project dedicated to the physics of TLEs and TGFs. *Space Science Reviews*, 137(1–4), 301–315. <https://doi.org/10.1007/s11214-008-9414-4>
- Lindanger, A., Marisaldi, M., Maiorana, C., Sarria, D., Albrechtsen, K., Østgaard, N., et al. (2020). The 3rd AGILE terrestrial gamma ray flash catalog. Part I: Association to lightning sferics. *Journal of Geophysical Research: Atmospheres*, 125(11), e2019JD031985. <https://doi.org/10.1029/2019JD031985>
- Lu, G., Blakeslee, R. J., Li, J., Smith, D. M., Shao, X.-M., McCaul, E. W., et al. (2010). Lightning mapping observation of a terrestrial gamma-ray flash. *Geophysical Research Letters*, 37(11). <https://doi.org/10.1029/2010GL043494>
- Lyons, L. (1986). *Statistics for nuclear and particle physics*. Cambridge University Press.
- Mailyan, B. G., Briggs, M. S., Cramer, E. S., Fitzpatrick, G., Roberts, O. J., Stanbro, M., et al. (2016). The spectroscopy of individual terrestrial gamma-ray flashes: Constraining the source properties. *Journal of Geophysical Research: Space Physics*, 121(11), 11346–11363. <https://doi.org/10.1002/2016JA022702>
- Mailyan, B. G., Nag, A., Murphy, M. J., Briggs, M. S., Dwyer, J. R., Rison, W., et al. (2018). Characteristics of radio emissions associated with terrestrial gamma-ray flashes. *Journal of Geophysical Research: Space Physics*, 123(7), 5933–5948. <https://doi.org/10.1029/2018JA025450>
- Mailyan, B. G., Xu, W., Celestin, S., Briggs, M. S., Dwyer, J. R., Cramer, E. S., et al. (2019). Analysis of individual terrestrial gamma-ray flashes with lightning leader models and Fermi Gamma-ray Burst Monitor data. *Journal of Geophysical Research: Space Physics*, 124(8), 7170–7183. <https://doi.org/10.1029/2019JA026912>
- Marisaldi, M., Fuschino, F., Labanti, C., Galli, M., Longo, F., Del Monte, E., et al. (2010). Detection of terrestrial gamma ray flashes up to 40 MeV by the AGILE satellite. *Journal of Geophysical Research*, 115(A3). <https://doi.org/10.1029/2009JA014502>
- Marisaldi, M., Galli, M., Labanti, C., Østgaard, N., Sarria, D., Cummer, S. A., et al. (2019). On the high-energy spectral component and fine time structure of terrestrial gamma ray flashes. *Journal of Geophysical Research: Atmospheres*, 124(14), 7484–7497. <https://doi.org/10.1029/2019JD030554>
- Neubert, T., Østgaard, N., Reglero, V., Blanc, E., Chanrion, O., Oxborrow, C. A., et al. (2019). The ASIM mission on the international space station. *Space Science Reviews*, 215(2). <https://doi.org/10.1007/s11214-019-0592-z>
- Østgaard, N., Balling, J. E., Bjørnsen, T., Brauer, P., Budtz-Jørgensen, C., Bujwan, W., et al. (2019). The Modular X- and Gamma-Ray Sensor (MXGS) of the ASIM payload on the International Space Station. *Space Science Reviews*, 215(2). <https://doi.org/10.1007/s11214-018-0573-7>
- Østgaard, N., Gjesteland, T., Stadsnes, J., Connell, P. H., & Carlson, B. (2008). Production altitude and time delays of the terrestrial gamma flashes: Revisiting the Burst and Transient Source Experiment spectra. *Journal of Geophysical Research*, 113(A2). <https://doi.org/10.1029/2007JA012618>
- Østgaard, N., Neubert, T., Reglero, V., Ullaland, K., Yang, S., Genov, G., et al. (2019). First 10 months of TGF observations by ASIM. *Journal of Geophysical Research: Atmospheres*, 124(24), 14024–14036. <https://doi.org/10.1029/2019JD031214>
- Picone, J. M., Hedin, A. E., Drob, D. P., & Akin, A. C. (2002). NRLMSISE-00 empirical model of the atmosphere: Statistical comparisons and scientific issues. *Journal of Geophysical Research*, 107(A12), SIA 15–1–SIA 15–16. <https://doi.org/10.1029/2002JA009430>
- Pu, Y., Cummer, S. A., Lyu, F., Briggs, M., Mailyan, B., Stanbro, M., & Roberts, O. (2019). Low frequency radio pulses produced by terrestrial gamma-ray flashes. *Geophysical Research Letters*, 46(12), 6990–6997. <https://doi.org/10.1029/2019GL082743>
- Rodger, C. J., Brundell, J. B., Holzworth, R. H., & Lay, E. H. (2009). Growing detection efficiency of the World Wide Lightning Location Network. *AIP Conference Proceedings*, 1118(1), 15–20. <https://doi.org/10.1063/1.3137706>
- Said, R. K., & Murphy, M. J. (2016). GLD360 upgrade: Performance analysis and applications. *24th International Lightning Detection Conference (Ic)*.
- Sarria, D., Kochkin, P., Østgaard, N., Lehtinen, N., Mezentsev, A., Marisaldi, M., et al. (2019). The first terrestrial electron beam observed by the Atmosphere-Space Interactions Monitor. *Journal of Geophysical Research: Space Physics*, 124. <https://doi.org/10.1029/2019JA027071>
- Sarria, D., Østgaard, N., Kochkin, P., Lehtinen, N., Mezentsev, A., Marisaldi, M., et al. (2021). Constraining spectral models of a terrestrial gamma-ray flash from a terrestrial electron beam observation by the Atmosphere-Space Interactions Monitor. *Geophysical Research Letters*, 48(9), e2021GL093152. <https://doi.org/10.1029/2021GL093152>
- Seidel, D. J., Ross, R. J., Angell, J. K., & Reid, G. C. (2001). Climatological characteristics of the tropical tropopause as revealed by radiosondes. *Journal of Geophysical Research*, 106(D8), 7857–7878. <https://doi.org/10.1029/2000JD900837>
- Smith, D. M., Lopez, L. I., Lin, R. P., & Barrington-Leigh, C. (2005). Terrestrial gamma-ray flashes observed up to 20 MeV. *Science*, 307, 1085–1088. <https://doi.org/10.1126/science.1107466>
- Tavani, M., Marisaldi, M., Labanti, C., Fuschino, F., Argan, A., Trois, A., et al. (2011). Terrestrial gamma-ray flashes as powerful particle accelerators. *Physical Review Letters*, 106, 018501. <https://doi.org/10.1103/PhysRevLett.106.018501>
- Ursi, A., Guidorzi, C., Marisaldi, M., Sarria, D., & Frontera, F. (2017). Terrestrial gamma-ray flashes in the bepposax data archive. *Journal of Atmospheric and Solar-Terrestrial Physics*, 156, 50–56. <https://doi.org/10.1016/j.jastp.2017.02.014>
- Wilson, C. T. R. (1924). The electric field of a thundercloud and some of its effects. *Proceedings of the Physical Society of London*, 37(1), 32D–37D. <https://doi.org/10.1088/1478-7814/37/1/314>
- Xu, W., Celestin, S., & Pasko, V. P. (2012). Source altitudes of terrestrial gamma-ray flashes produced by lightning leaders. *Geophysical Research Letters*, 39(8). <https://doi.org/10.1029/2012GL051351>

# Supporting Information for Spectral Analysis of Individual Terrestrial Gamma-ray Flashes Detected by ASIM

A. Lindanger<sup>1</sup>, M. Marisaldi<sup>1,2</sup>, D. Sarria<sup>1</sup>, N. Østgaard<sup>1</sup>, N. Lehtinen<sup>1</sup>, C. A.

Skeie<sup>1</sup>, A. Mezentzev<sup>1</sup>, P. Kochkin<sup>1</sup>, K. Ullaland<sup>1</sup>, S. Yang<sup>1</sup>, G. Genov<sup>1</sup>, B.

E. Carlson<sup>3,1</sup>, C. Köhn<sup>4</sup>, J. Navarro-Gonzalez<sup>5</sup>, P. Connell<sup>5</sup>, V. Reglero<sup>5</sup>, T.

Neubert<sup>4</sup>

<sup>1</sup>Birkeland Centre for Space Science, Department of Physics and Technology, University of Bergen, Bergen, Norway

<sup>2</sup>INAF-OAS Bologna, Bologna, Italy

<sup>3</sup>Carthage College, Kenosha, WI, USA

<sup>4</sup>National Space Institute, Technical University of Denmark, Denmark

<sup>5</sup>University of Valencia, Spain

## Contents of this file

1. Figures S1 to S21

**Introduction** This document contains a comparison between the three statistical tests applied to the TGF spectra (Figure S1). It also contains additional plots for each of the 17 TGF analyzed in the main paper (Figure S2 to S18). Figure S3 is explained in detail in Section 4 in the main paper and Figure S2 to S18 follows the same structure.

---

## **96 Spectral Analysis of Individual Terrestrial Gamma-ray Flashes Detected by ASIM**

---

X - 2

:

Figure S19 and S20 shows the voltage drop in the photomultiplier tubes used in the ASIM high energy detector. Figure S21 shows the safety time criteria. The voltage drop and safety time criteria are discussed in Appendix A in the main paper.

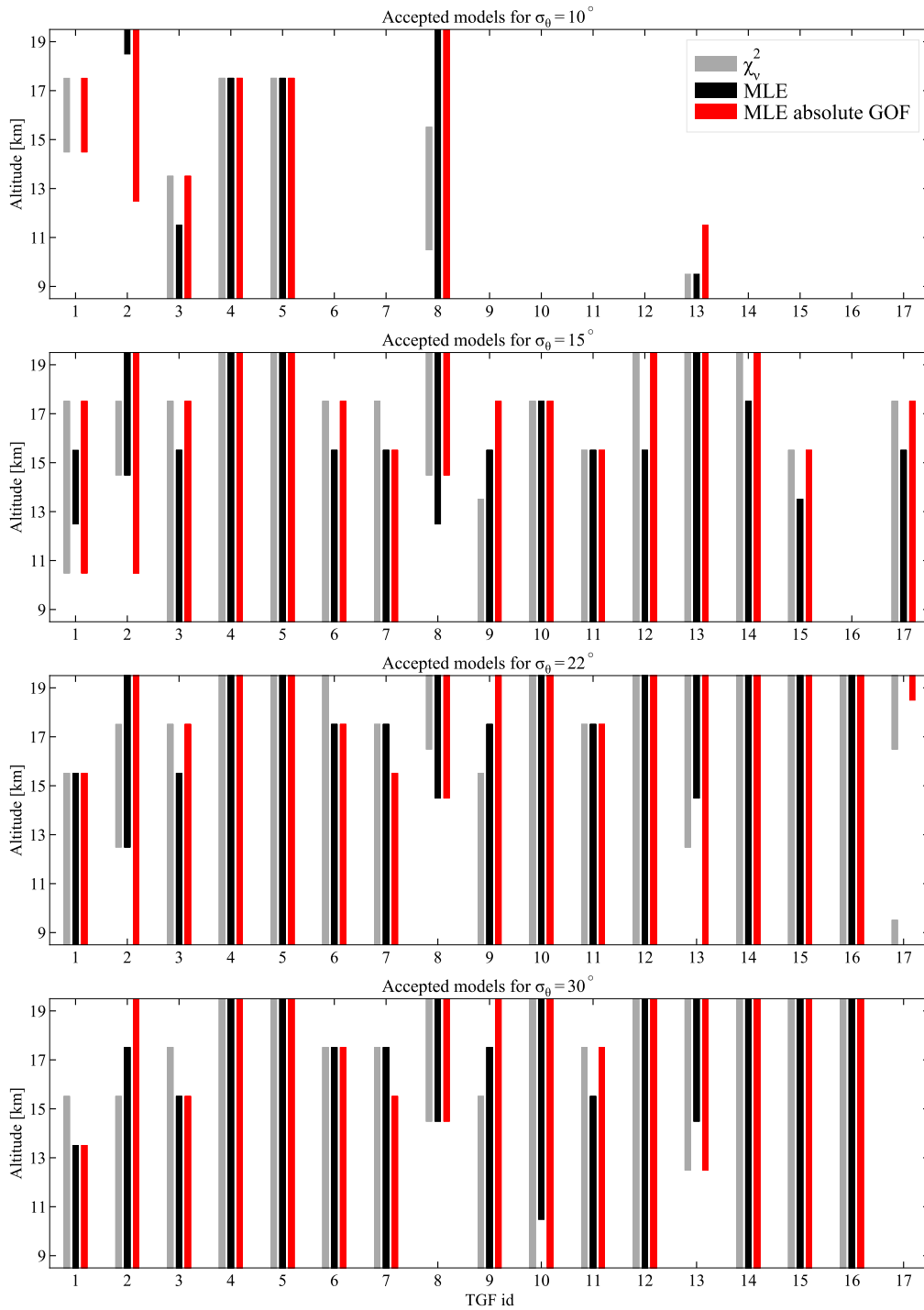


**Figure S1.** A comparison between  $\chi^2$ , MLE, and MLE absolute goodness of fit (GOF)

described in Section 3.3 in the main paper. There is generally a good agreement between the three statistical tests.

X - 4

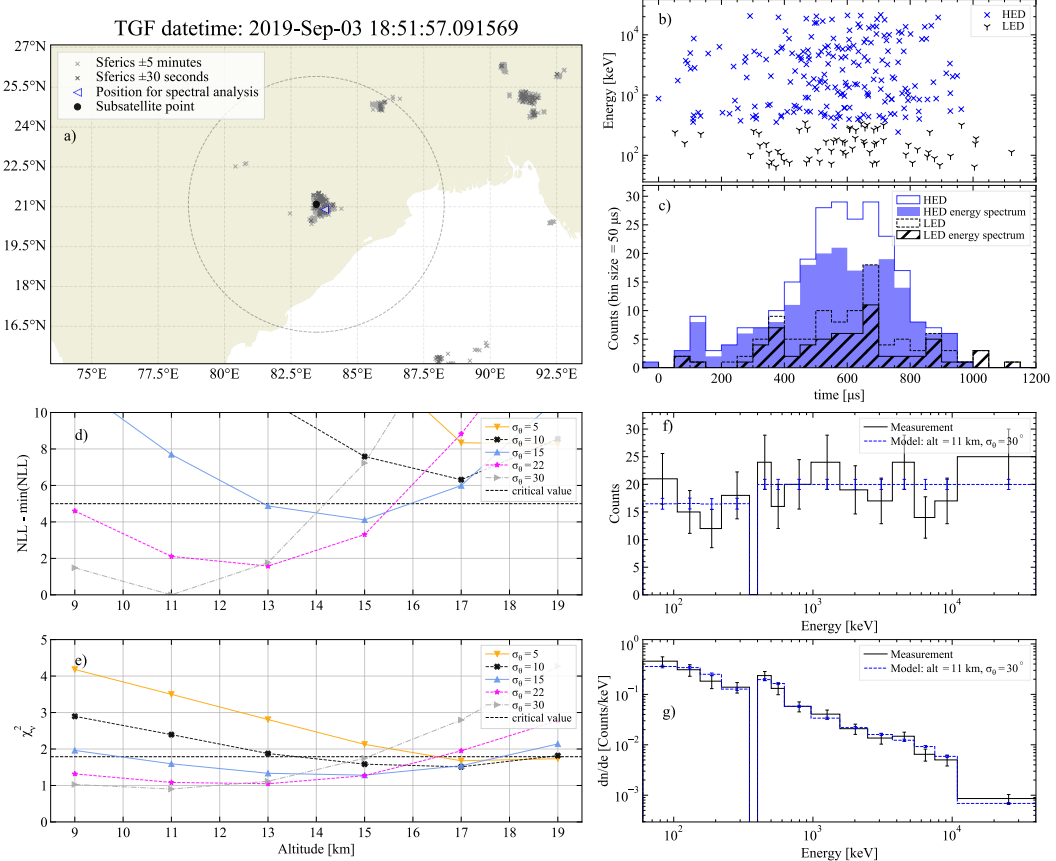


**Figure S2.** TGF 1. For TGF 1 there are two active lightning clusters. The first cluster is directly under ISS and the second cluster is at a radial distance of 450 km. As the first cluster is most active closest to the time of the TGF, and the TGF has the most counts in HED in the TGF sub-sample, we assume this is the production location of the TGF. The geolocation selected for this event is a lightning detection inside the first cluster.

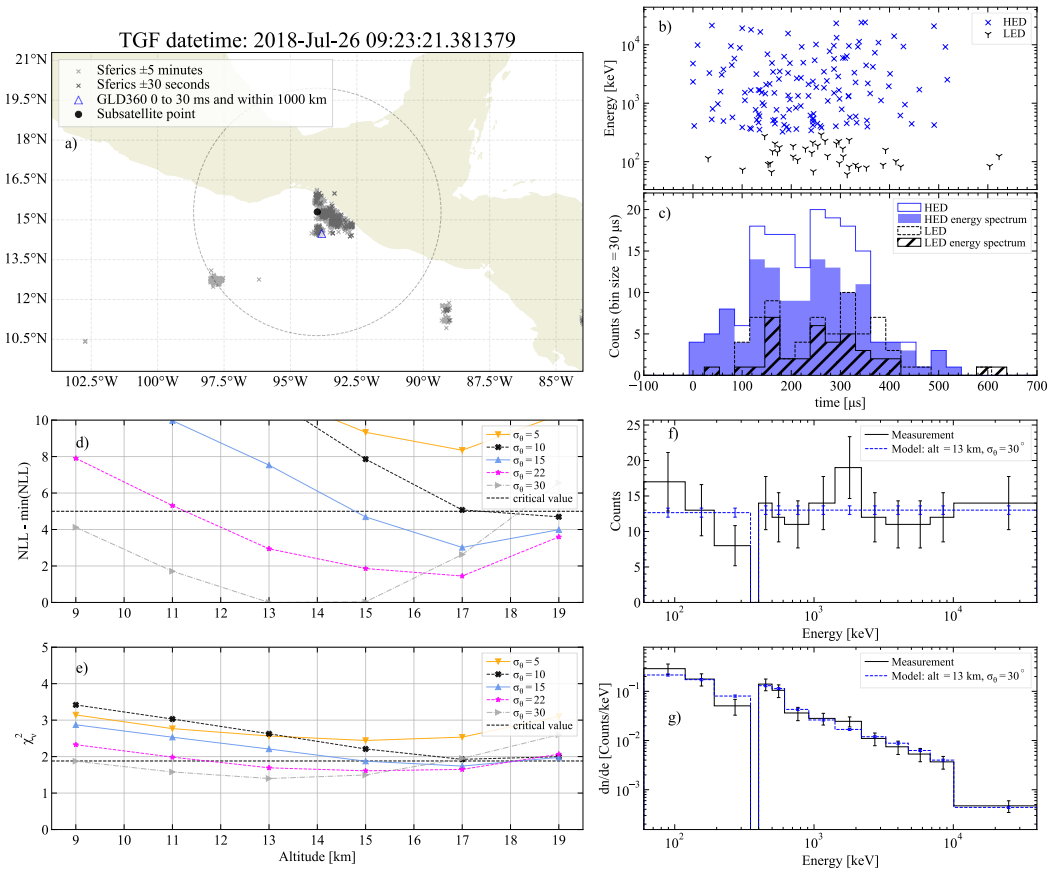


Figure S3. TGF 2

X - 6

:

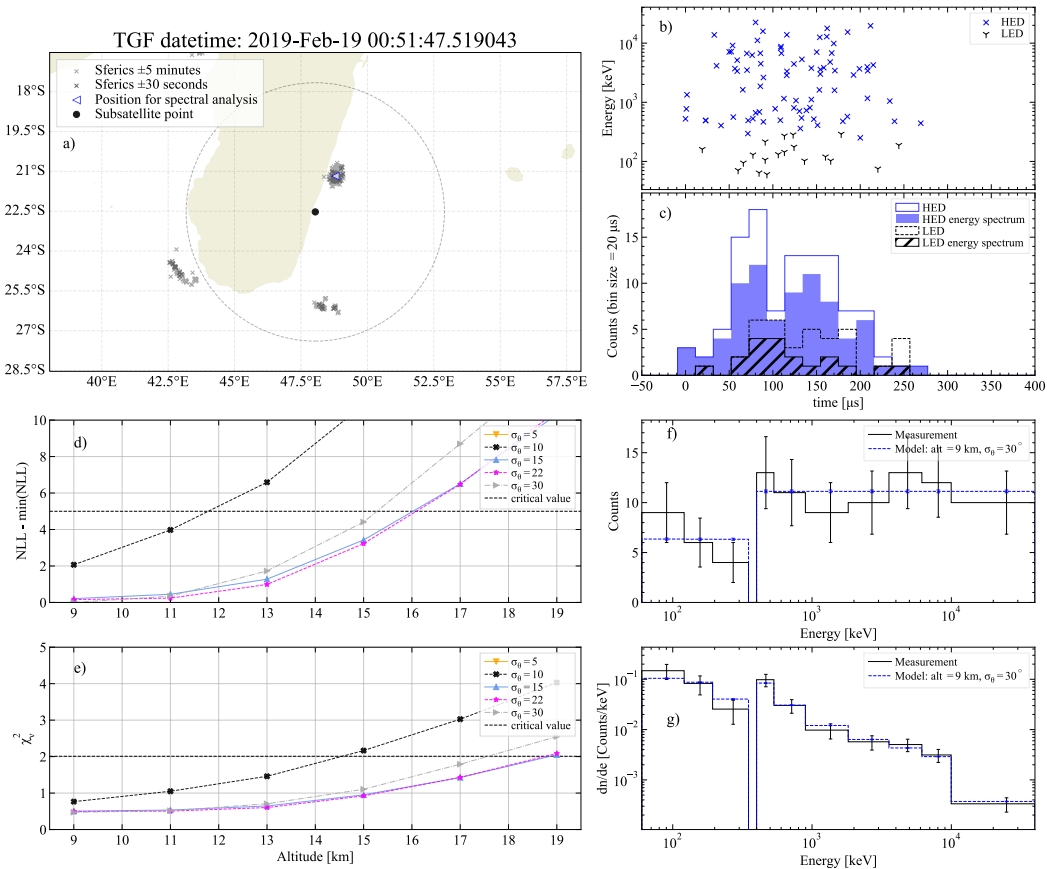
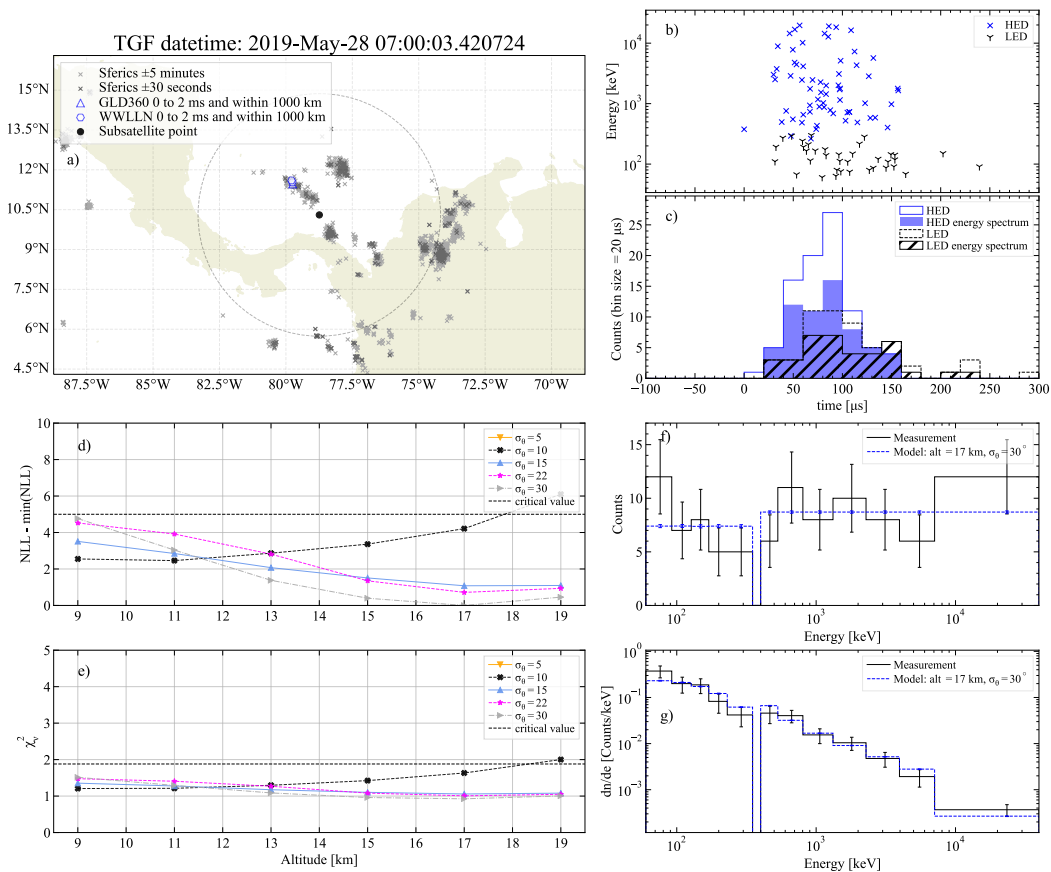


Figure S4. TGF 3



**Figure S5.** TGF 4

X - 8

:

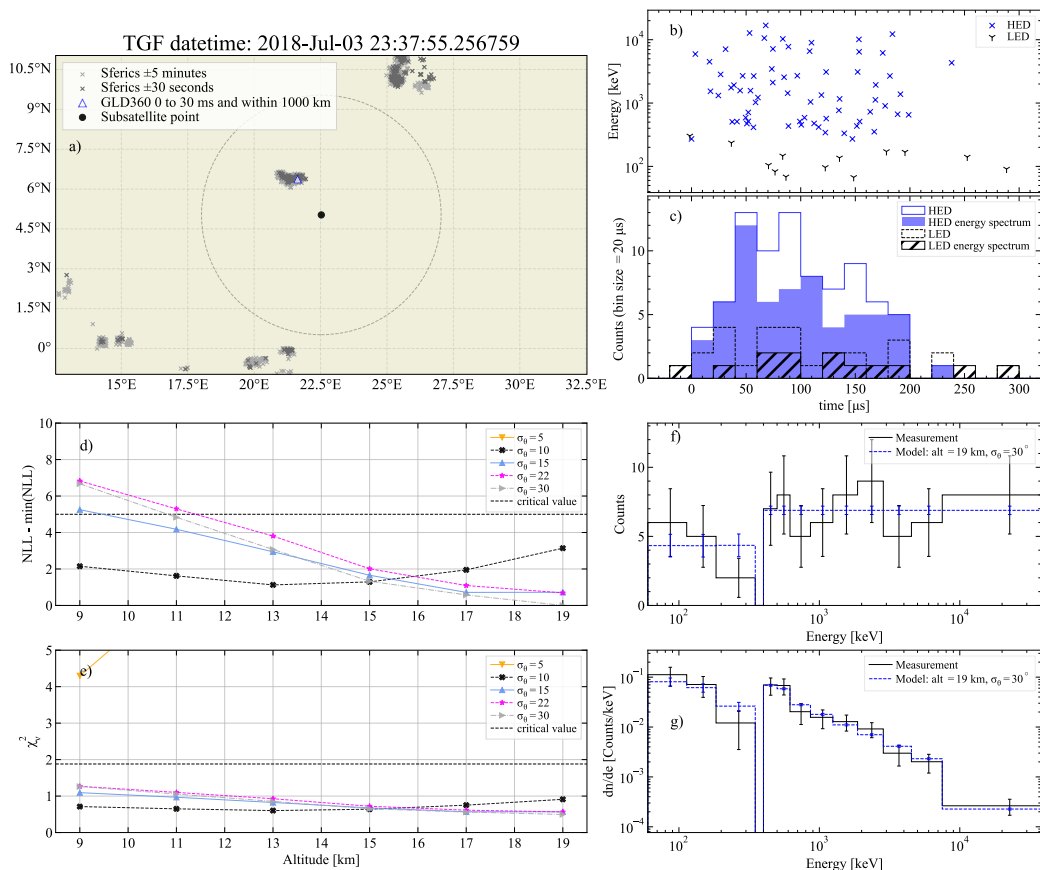


Figure S6. TGF 5

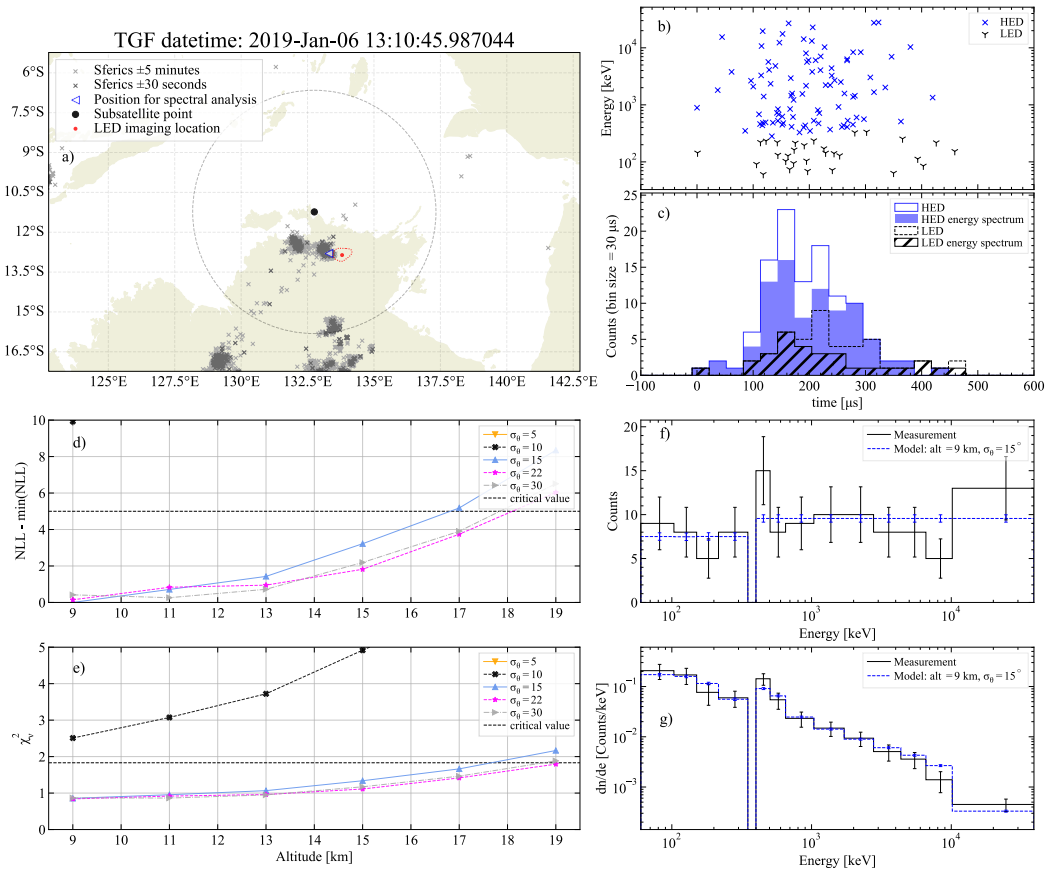


Figure S7. TGF 6

X - 10

:

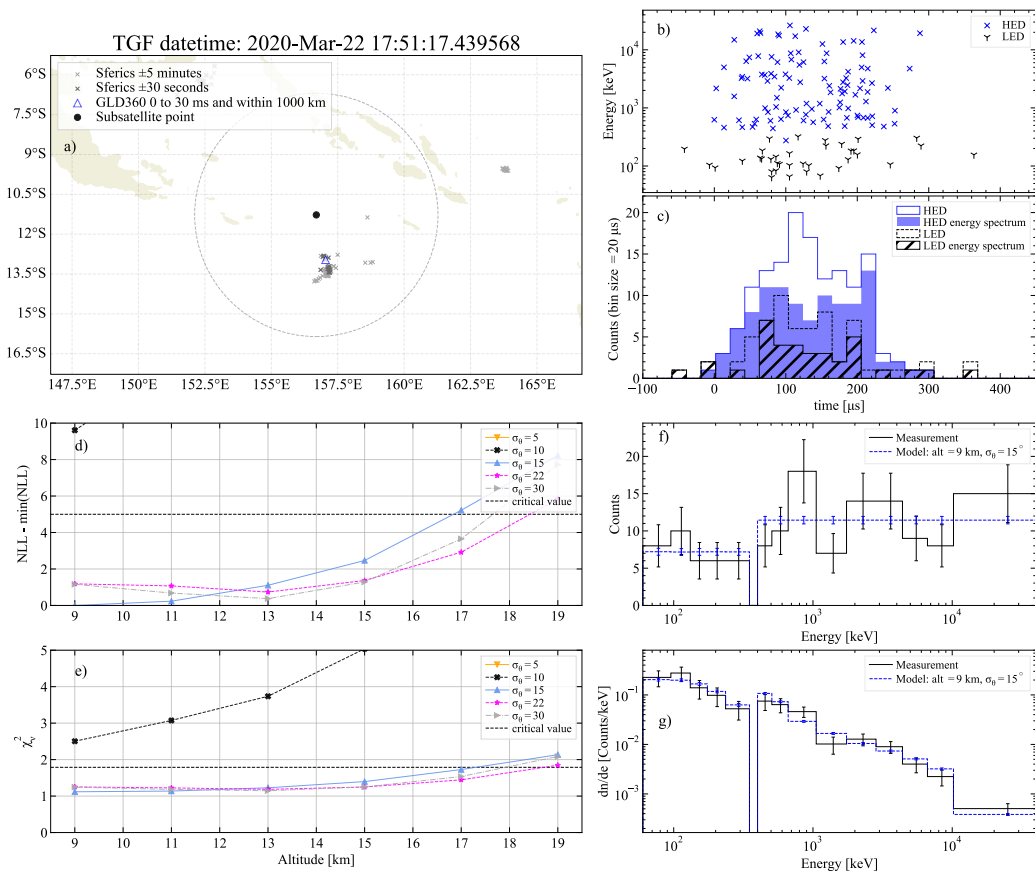


Figure S8. TGF 7

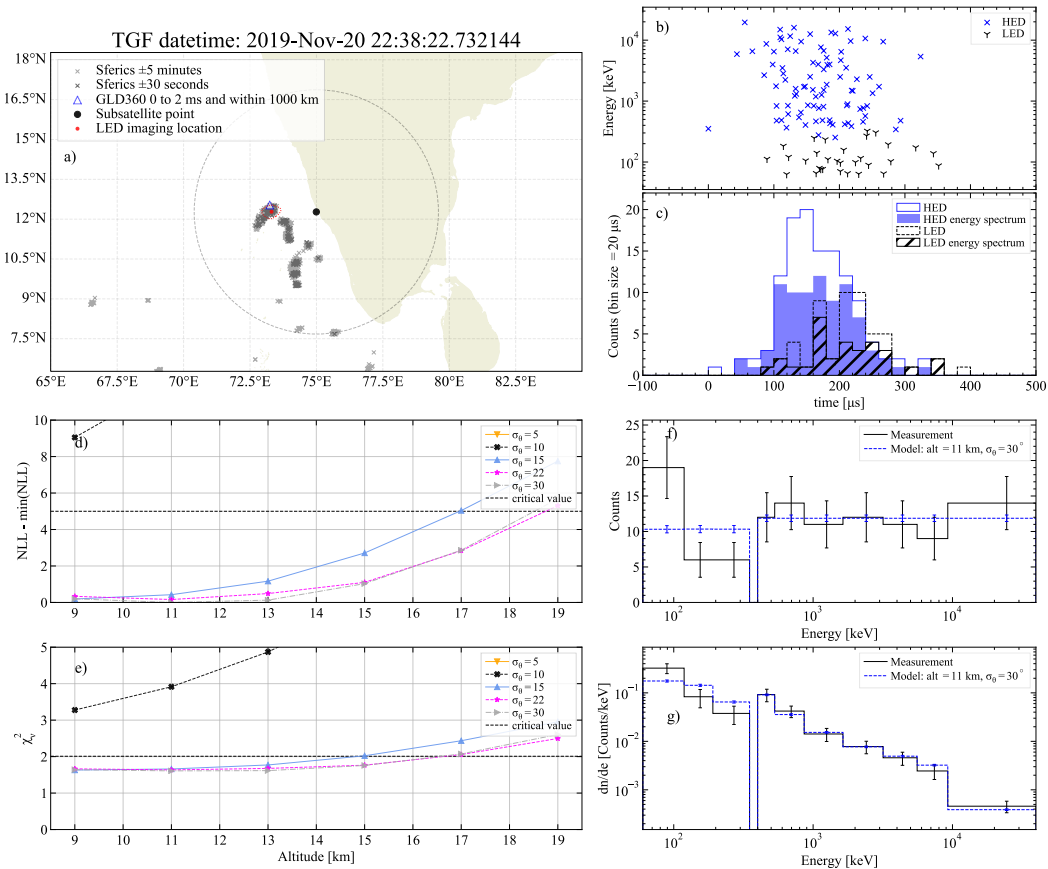


Figure S9. TGF 8

X - 12

:

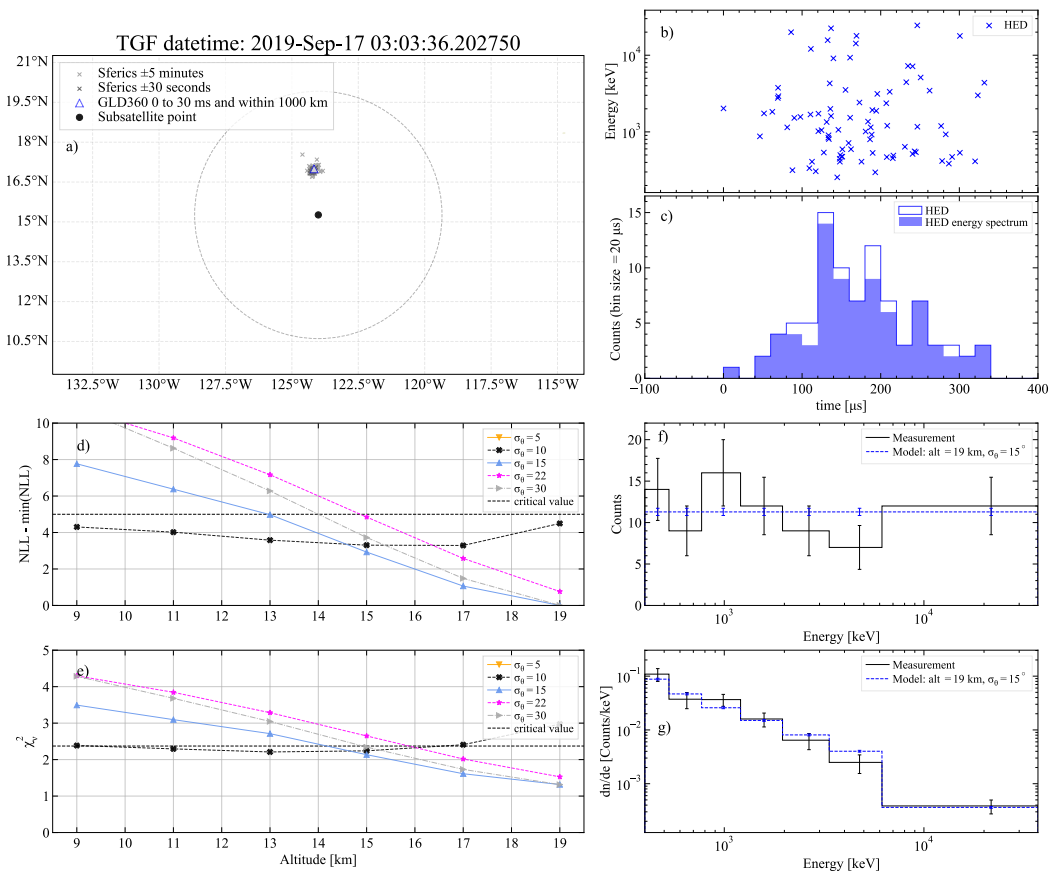


Figure S10. TGF 9

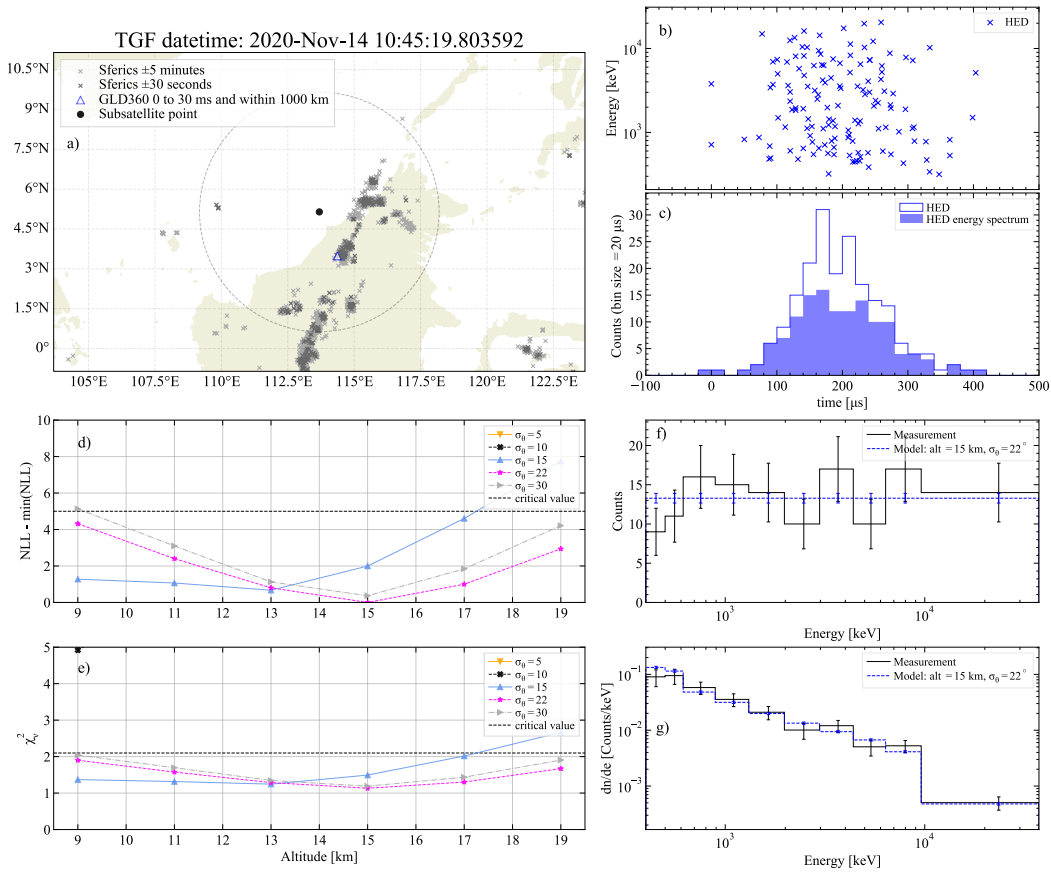


Figure S11. TGF 10

X - 14

:

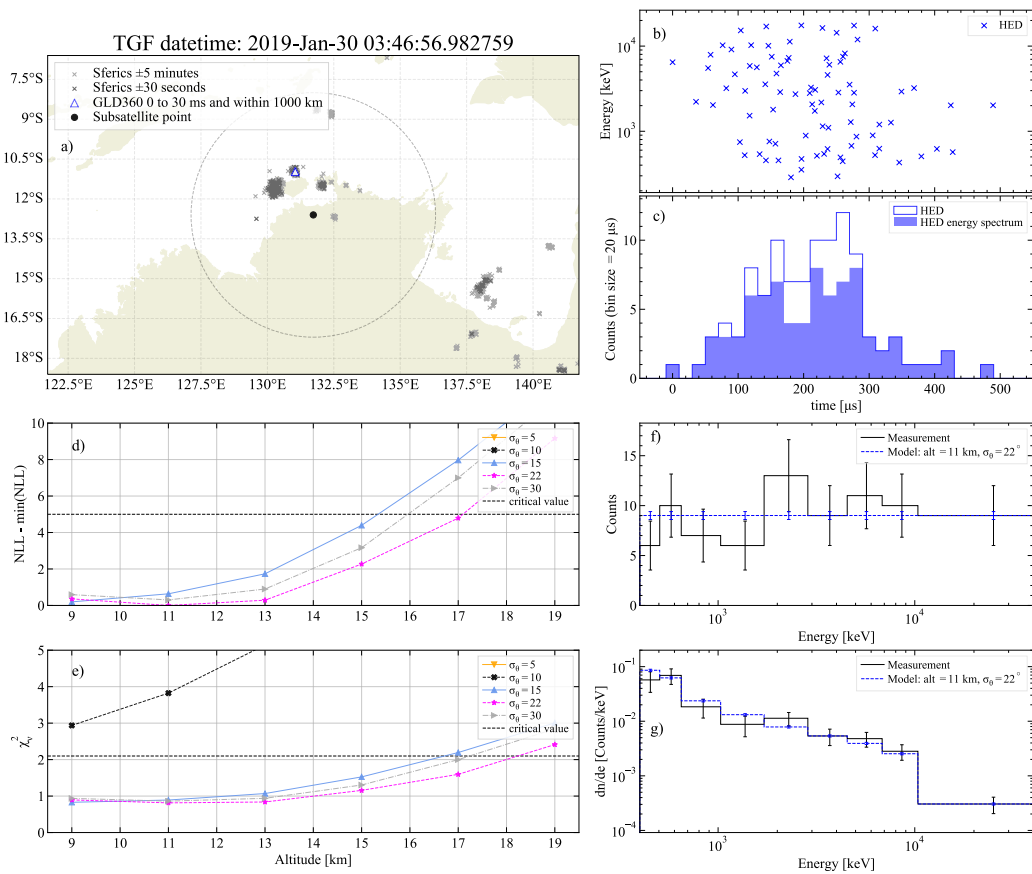


Figure S12. TGF 11

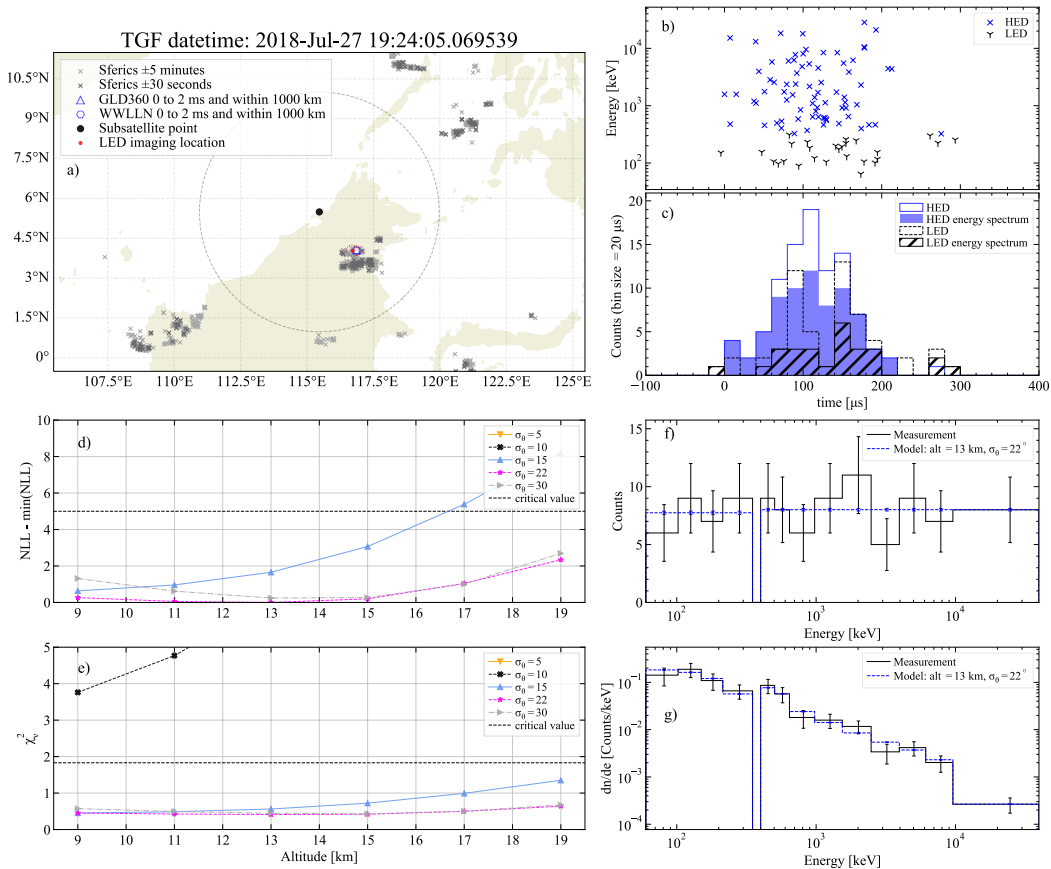


Figure S13. TGF 12

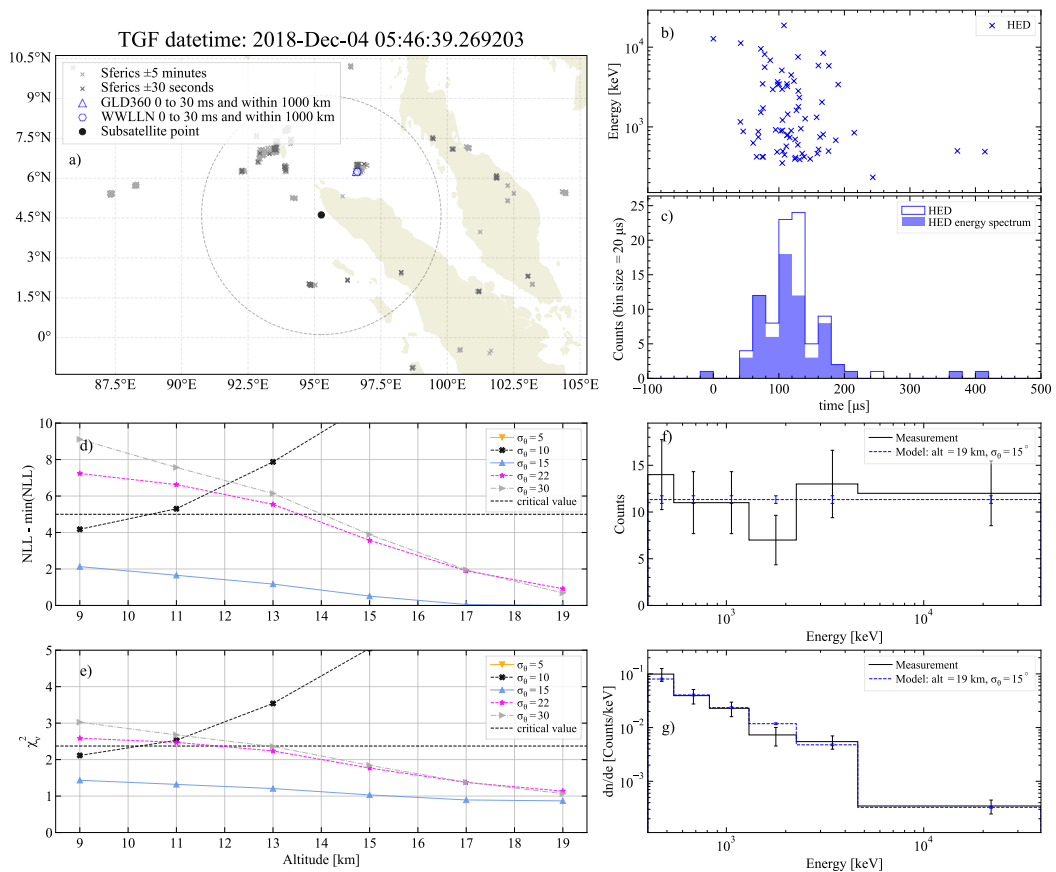


Figure S14. TGF 13

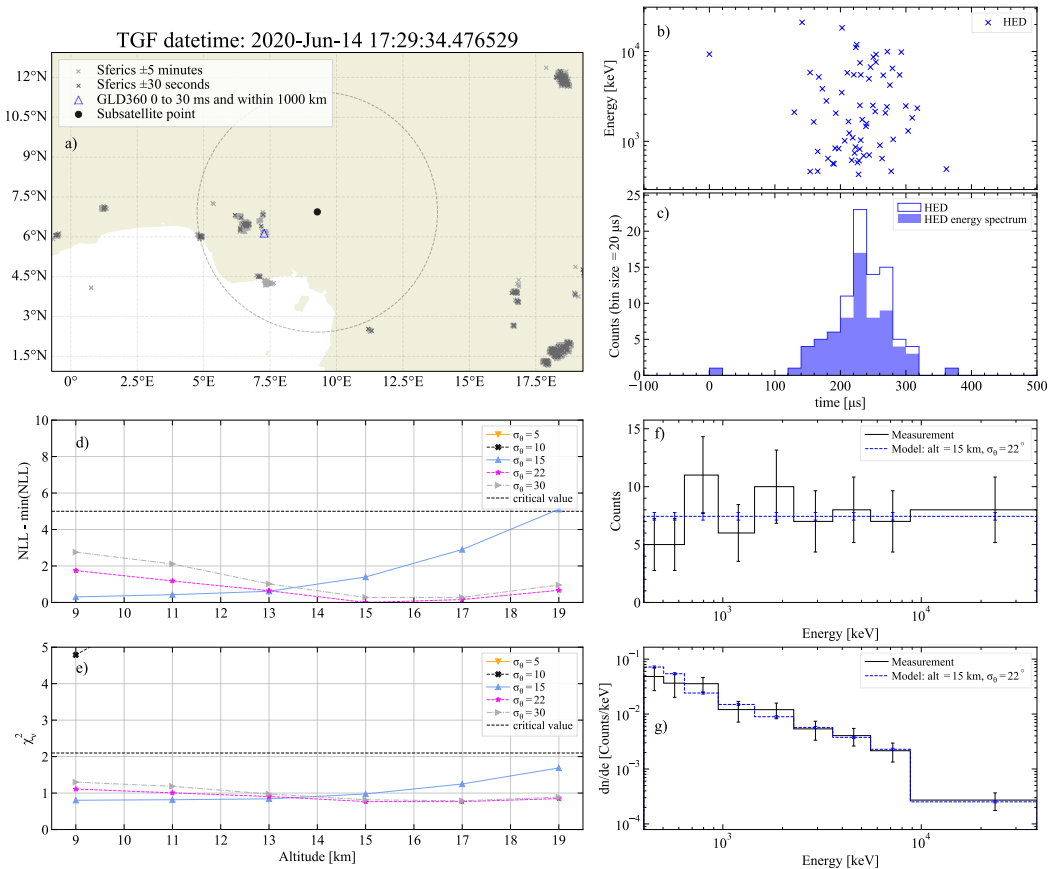


Figure S15. TGF 14

X - 18

:

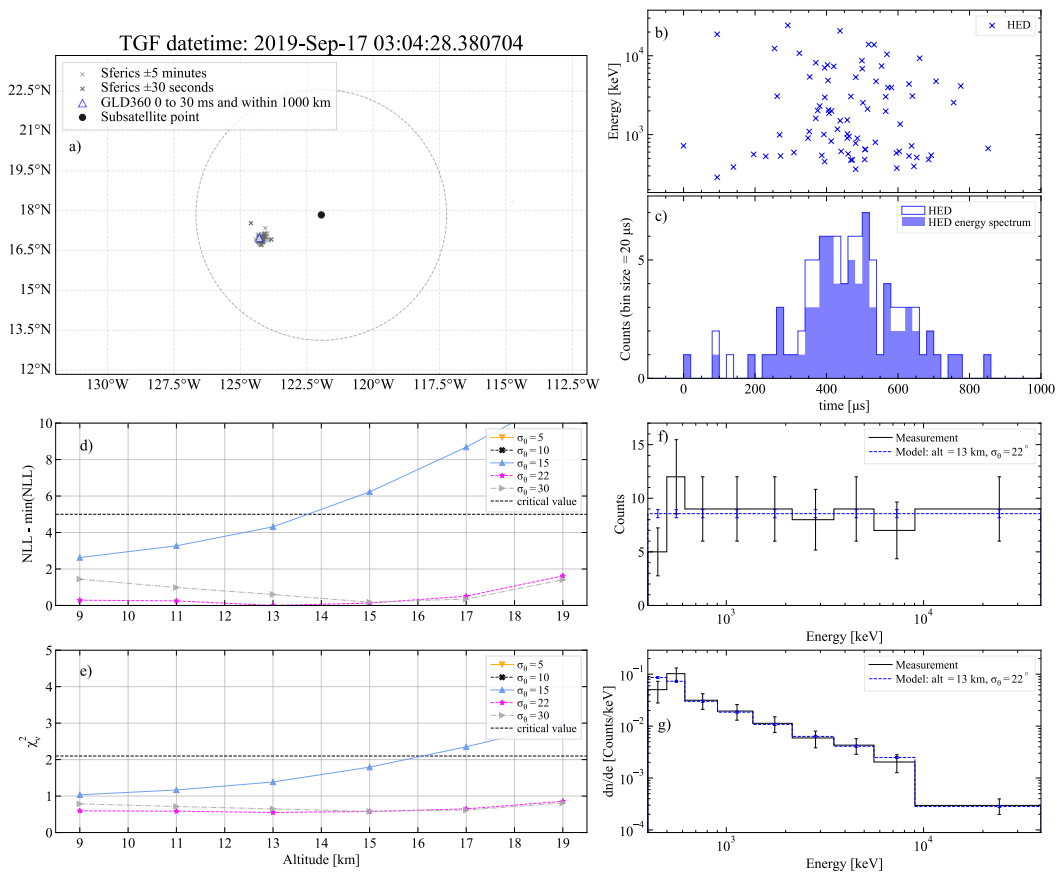


Figure S16. TGF 15

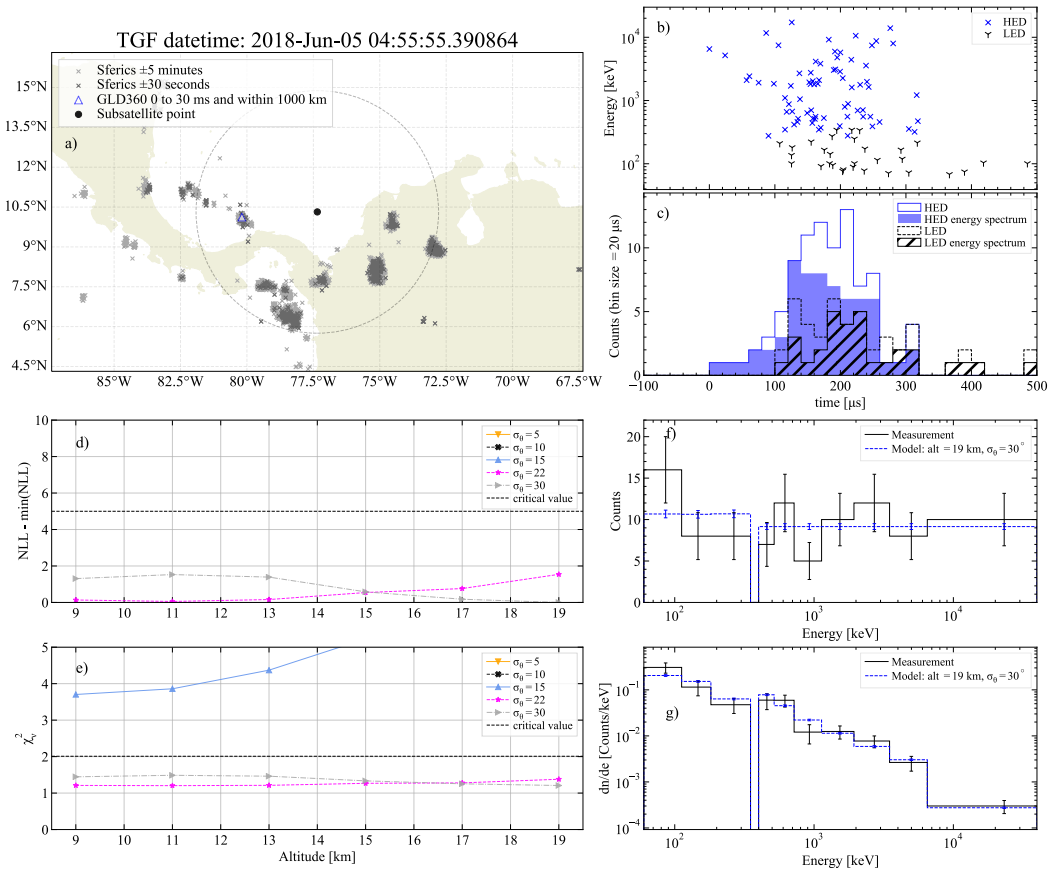


Figure S17. TGF 16

X - 20

:

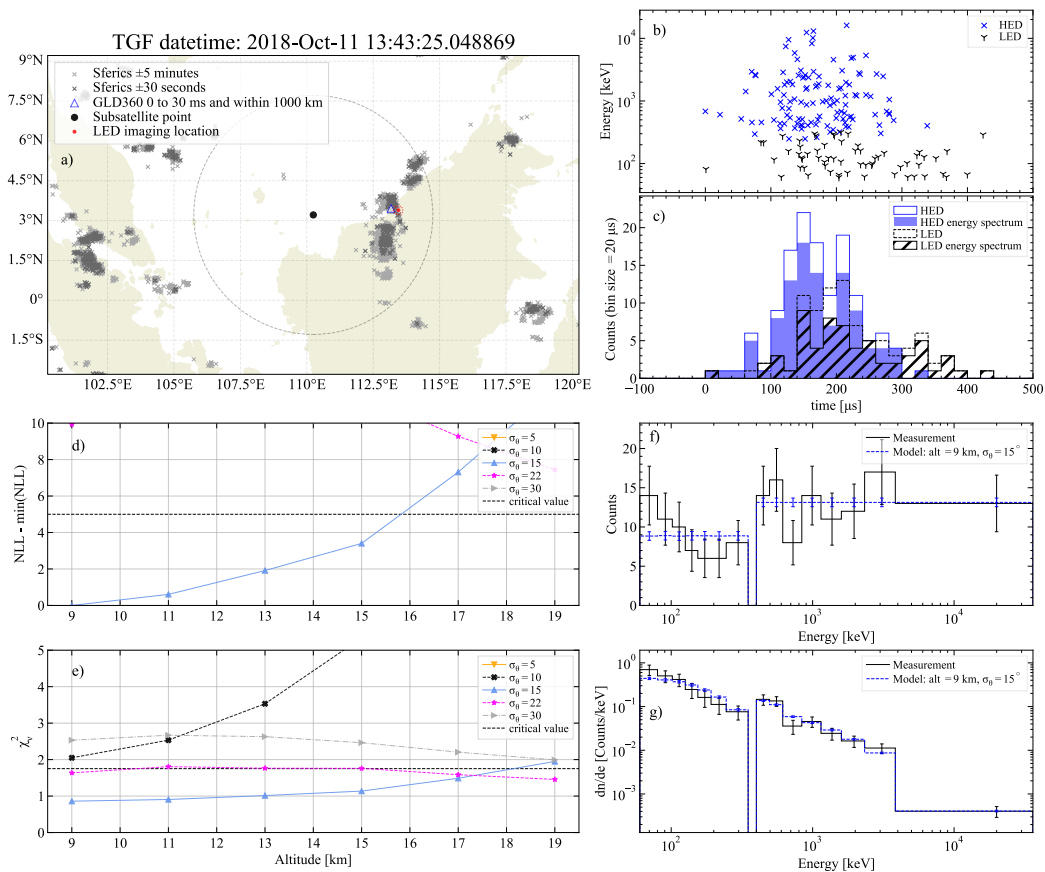
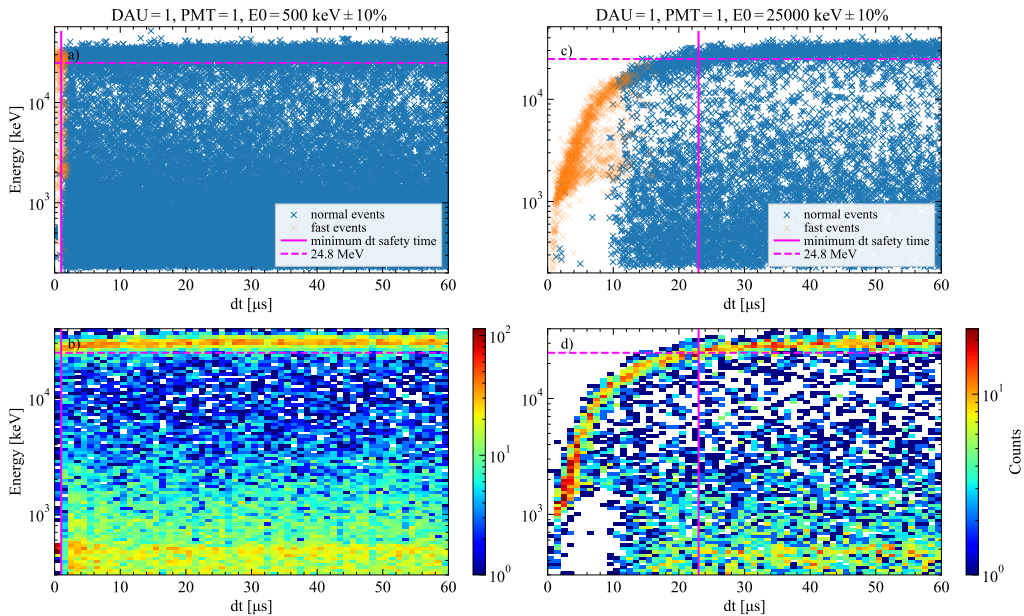


Figure S18. TGF 17



**Figure S19.** Accumulated ASIM data from one of the 12 detectors in HED.  $dt$  is the time between the count with energy  $E_0$  and the following count. a) Accumulated scatter plot showing the first count after a count with energy  $E_0 = 500\text{keV} \pm 10\%$ . b) Same data as in a) plotted as a 2D histogram. The proton peak is visible at  $\sim 31$  MeV. c) Accumulated scatter plot showing the first count after a count with energy  $E_0 = 25\text{MeV} \pm 10\%$ . d) Same data as in c) plotted as a 2D histogram. The dashed magenta line shows the 24.8 MeV which is 20% of 31 MeV.

X - 22

:

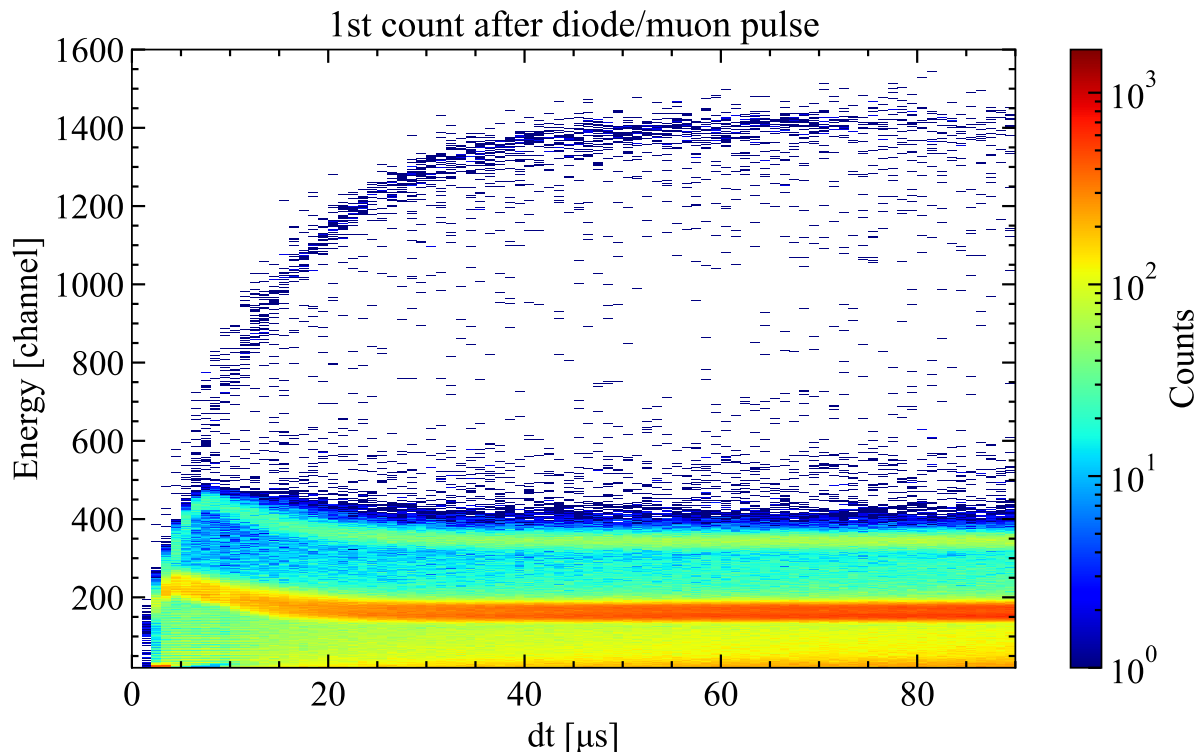


**Figure S20.** Accumulated data from the on-ground experiment showing the voltage drop after diode/muon pulse.  $dt$  is the time between the diode/muon pulse and the following count. We see 1.17 MeV, 1.46 MeV and 1.33 MeV in channel 200. 2.6 MeV in channel 400, and muons (31.7 MeV) in channel 1400.

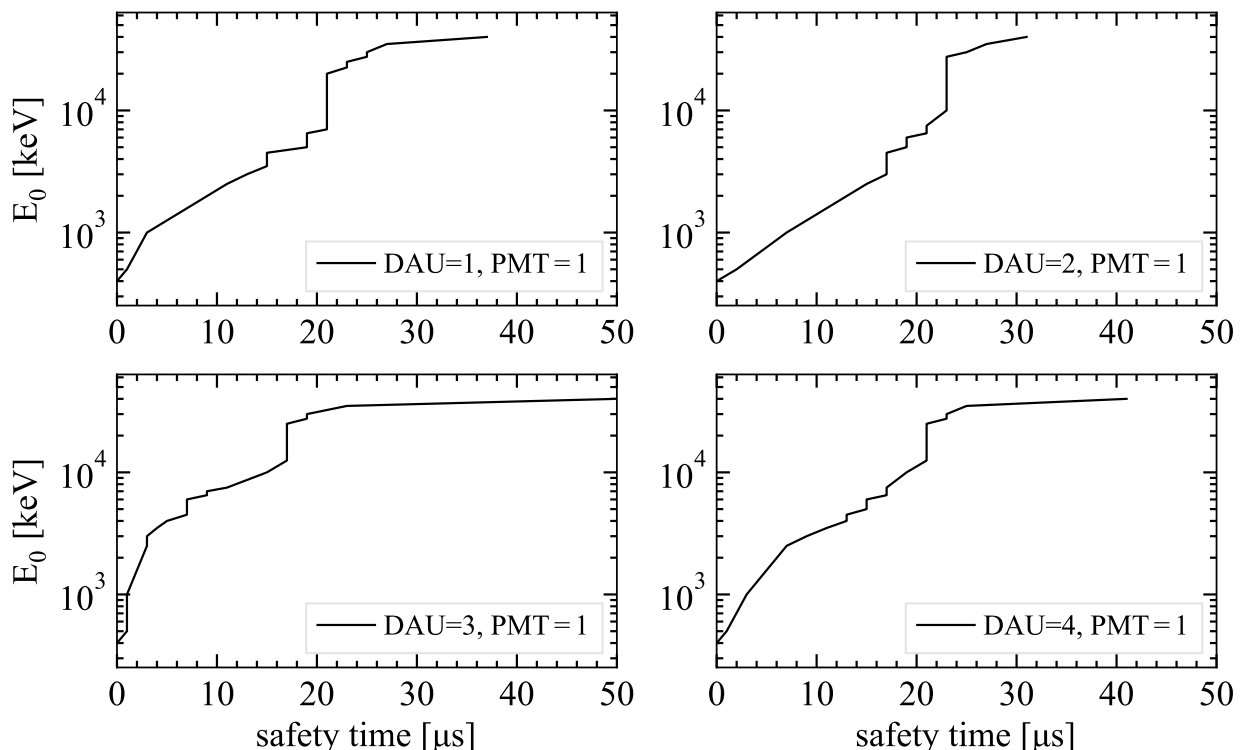


**Figure S21.** Safety time criteria for 4 of the 12 detectors in the high energy detector in ASIM.

The other 8 detectors have a similar behaviour.



## Paper III

### **Production of Terrestrial Gamma-ray Flashes During the Early Stages of Lightning Flashes**

A. Lindanger, C. A. Skeie, M. Marisaldi, I. Bjørge-Engeland, N. Østgaard, A. Mezentsev, D. Sarria, N. Lehtinen, V. Reglero, O. Chanrion, T. Neubert

*Journal of Geophysical Research: Atmospheres*, **127**, doi:10.1029/2021JD036305, (2022)





## RESEARCH ARTICLE

10.1029/2021JD036305

### Key Points:

- VLF radio and optical measurements show that upward TGFs are typically produced in the beginning of a lightning flash
- Stacking analysis confirms an excess of lightning activity 150–750 ms after the TGFs
- When a TGF is simultaneous to a lightning stroke, the enhanced activity after is usually co-located with the first lightning stroke

### Supporting Information:

Supporting Information may be found in the online version of this article.

### Correspondence to:

A. Lindanger,  
anders511@protonmail.com

### Citation:

Lindanger, A., Skeie, C. A., Marisaldi, M., Bjørge-Engeland, I., Østgaard, N., Mezentsev, A., et al. (2022). Production of terrestrial gamma-ray flashes during the early stages of lightning flashes.

*Journal of Geophysical Research: Atmospheres*, 127, e2021JD036305.  
<https://doi.org/10.1029/2021JD036305>

Received 3 DEC 2021

Accepted 31 MAR 2022

## Production of Terrestrial Gamma-Ray Flashes During the Early Stages of Lightning Flashes

A. Lindanger<sup>1</sup> , C. A. Skeie<sup>1</sup> , M. Marisaldi<sup>1,2</sup> , I. Bjørge-Engeland<sup>1</sup> , N. Østgaard<sup>1</sup> , A. Mezentsev<sup>1</sup> , D. Sarria<sup>1</sup> , N. Lehtinen<sup>1</sup> , V. Reglero<sup>3</sup>, O. Chanrion<sup>4</sup> , and T. Neubert<sup>4</sup> 

<sup>1</sup>Department of Physics and Technology, Birkeland Centre for Space Science, University of Bergen, Bergen, Norway, <sup>2</sup>INAF-OAS Bologna, Bologna, Italy, <sup>3</sup>University of Valencia, Paterna, Spain, <sup>4</sup>National Space Institute, Technical University of Denmark, Kgs. Lyngby, Denmark

**Abstract** Terrestrial Gamma-ray Flashes (TGFs) are short emissions of high energy photons associated with thunderstorms. It has been known since the discovery of TGFs that they are associated with lightning, and several case studies have shown that the TGFs are produced at the initial phase of the lightning flash. However, it has not been tested whether this is true in general. By using the largest TGF sample up to date, combined with ground-based radio lightning detection data, we perform a statistical study to test this. One of the TGF missions is the Atmosphere-Space Interactions Monitor (ASIM) consisting of the innovative combination of X- and gamma-ray detectors, optical photometers and cameras. This allows us to investigate the temporal relation between gamma-rays produced by TGFs and the optical signal produced by lightning discharges. Based on stacking analysis of the TGF sample and ground-based measurements of associated lightning activity, together with the high temporal resolution of the optical signal from the ASIM photometers, it is shown that TGFs are produced in the beginning of the lightning flashes. In addition, for a significant fraction of the TGFs, the lightning activity detected in radio is enhanced in an interval between 150 and 750 ms following the TGFs, and is co-located with the lightning associated with the TGFs. The enhanced lightning activity is not evident in a randomly selected sample of flashes. This indicates that the activity between 150 and 750 ms is a characteristic property of a significant fraction of flashes that start with a TGF.

### 1. Introduction

Terrestrial gamma-ray flashes (TGFs) are sub-millisecond bursts of energetic photons up to several tens of MeV produced in the atmosphere. The energy spectra of TGFs are compatible with the Relativistic Runaway Electron Avalanche (RREA) process followed by bremsstrahlung emissions (Dwyer, 2003; Dwyer & Smith, 2005; Gurevich et al., 1992; Lindanger et al., 2021; Mailyan et al., 2016). The connection between TGFs and thunderstorm regions has been suggested since the first TGFs were detected by the BATSE instrument onboard the Compton Gamma-ray Observatory (Fishman et al., 1994). TGFs have since been detected from space by RHESSI (Smith et al., 2005), Fermi (Briggs et al., 2013), AGILE (Marisaldi et al., 2010), BeppoSAX (Ursi et al., 2017), the RELEC space experiment on the Vernov satellite (Bogomolov et al., 2017), and ASIM (Østgaard, Neubert, et al., 2019).

Case studies have shown that TGFs can be observed in association with positive Intra-Cloud (IC+) lightning, and several case studies have shown that TGFs are typically produced in the initial phase of lightning flashes during the upward propagation of leaders (Cummer et al., 2015; Lu et al., 2010; Shao et al., 2010; Stanley et al., 2006; Østgaard et al., 2013). Connaughton et al. (2010, 2013) used very low frequency (VLF) radio atmospherics, so-called sferics, produced by lightning and detected by the World Wide Lightning Location Network (WWLLN) together with TGFs detected by Fermi to show that a significant fraction of TGFs is simultaneous with a sferic detection within a few hundred microseconds. This strict association has been confirmed by RHESSI (Mezentsev et al., 2016) and AGILE (Lindanger et al., 2020; Marisaldi et al., 2015). Connaughton et al. (2013) inferred that the radio signal simultaneous with the TGF is produced by the TGF-current itself, and Dwyer and Cummer (2013) modeled this. Østgaard et al. (2021), using a combination of ASIM gamma-ray data, optical data and LF-radio measurements concluded that the TGF-associated radio signal was produced by either the hot-leader lightning channel or the TGF, or a combination of the two. Smith et al. (2016) identified three types of associations between TGFs and sferics; simultaneous association, few milliseconds difference, and those where the radio signals are hundreds of milliseconds after the TGF. The last category will be further investigated in this study.

© 2022. The Authors.

This is an open access article under the terms of the [Creative Commons Attribution License](#), which permits use, distribution and reproduction in any medium, provided the original work is properly cited.

This likely places the TGF at the beginning of a lightning flash, during the upward propagation of a leader that continues propagating after the TGF. However, this is only based on case studies and has not been shown for a large sample of TGFs. As recent scientific efforts have been focused on the “simultaneity” of TGFs and the temporally closest radio measurement (Connaughton et al., 2010, 2013; Cummer et al., 2011; Lindanger et al., 2020; Mailyan et al., 2020; Marisaldi et al., 2015; Mezentsev et al., 2016), this work will take a step back and focus on TGFs and *all* lightning detections associated to the TGF on 100’s ms scale. This will follow up the enhanced lightning activity detected hundreds milliseconds after the TGFs reported by Omar et al. (2014); Smith et al. (2016). Using a large data set of TGF catalogs together with ground-based lightning radio data and optical data from ASIM, we will answer the question: when does the TGF occur in the sequence of discharges constituting a lightning flash and are there any special characteristics with those flashes?

## 2. Data and Method

This study uses four TGF catalogs from different instruments, lightning data from WWLLN and GLD360, and optical data from the Modular Multispectral Imaging Array (MMIA) instrument onboard ASIM. The TGF catalogs are obtained from the TGF detecting space missions RHESSI, Fermi, AGILE, and ASIM. There are 2824 TGFs (August 2004 to November 2013) from the RHESSI TGF catalog (Smith et al., 2020), 4774 TGFs (August 2008 to July 2016) from the first Fermi-GBM TGF catalog (Roberts et al., 2018), 3473 TGFs (March 2015 to October 2020) from the 3rd AGILE TGF catalog (Lindanger et al., 2020; Maiorana et al., 2020), and 729 ASIM TGFs (June 2018 to September 2020) available from <https://asdc.space.dtu.dk>. The ASIM instrument is described in detail in Chanrion et al. (2019); Neubert et al. (2019); Østgaard, Balling, et al. (2019). TGFs detected by the same instrument occurring within 5 ms of the previous TGF are removed so that multi-pulse TGFs are counted as a single entry, corresponding to the first TGF. The timing resolution provided by the RHESSI TGF catalog is 1 ms and the absolute timing accuracy is corrected to ~1 ms by the timing correction provided by Mezentsev et al. (2016). The 3rd AGILE TGF catalog is updated including WWLLN-identified TGFs up to October 2020. We also remove TGFs detected by AGILE between July 2015 and December 2017 because AGILE experienced a degradation of the absolute timing accuracy during that period (Lindanger et al., 2020).

Lightning data are obtained from WWLLN (Rodger et al., 2009) and GLD360 provided by Vaisala Inc. (Said & Murphy, 2016). Both lightning networks detect sferics produced by lightning discharges and provides geolocation and timestamps of the sferics. GLD360 also provides peak current values for their detections. WWLLN data from August 2004 and onward are compared to the RHESSI, Fermi, AGILE, and ASIM TGF catalogs. Abarca et al. (2010) and Hutchins et al. (2012) found the location accuracy of WWLLN to be ~5 km for the continental United States, and Østgaard et al. (2013) assumed a global WWLLN location accuracy of 15 km. Comparing WWLLN with Lightning Imaging Sensor (LIS), Bürgesser (2017) estimated a detection efficiency between 1% and 10% for continental regions, and 20% for oceanic regions worldwide. Through the ASIM Science Data Center, GLD360 data are only available for the ASIM mission, therefore it will be used only in association with ASIM data. Using one month of NLDN data over the United States, Said and Murphy (2016) reported the median location accuracy of GLD360 to be ~2 km and the 90th percentile is ~6 km. The detection efficiency was estimated to be ~80% for CG flashes and ~45% for IC flashes.

The time difference between the TGF and the sferic is defined by Equation 1. The time of the sferic is the time of lightning discharge. The propagation time of photons traveling from the lightning location to the satellite is calculated assuming a TGF production altitude of 12 km. Moving three km down or up is only a maximum time difference of 10  $\mu$ s.

$$\delta t = \text{time}_{\text{sferic}} + \text{time}_{\text{propagation}} - \text{time}_{\text{TGF}} \quad (1)$$

For all the TGFs we keep track of: TGF time and its associated lightning information including the radial distance between the subsatellite point and the location of the sferic source lightning discharge,  $\delta t$  of all sferics,  $\delta t$  of the temporally closest sferic match, and the radial distance between the temporally closest sferic match and the other surrounding sferics. The radial distance is the distance along the surface of the Earth between two coordinates.

Due to instrument sensitivity and efficiency of the various instruments most TGFs are detected within ~500 km from the subsatellite point (Collier et al., 2011; Cummer et al., 2005; Lindanger et al., 2020; Marisaldi et al., 2019; Smith et al., 2016). Therefore, we only consider sferics within 500 km from the subsatellite point to ensure a

**Table 1**

*Overview of the Data Sets and the Sferic Match Criteria Corresponding to Each Space Mission*

Instrument	Lightning network	Sferic match criteria	Number of TGFs with sferic match
RHESSI	WWLLN	$ \delta t  < 1$ ms	441
Fermi	WWLLN	$ \delta t  < 0.2$ ms	948
AGILE	WWLLN	$ \delta t  < 0.2$ ms	619
ASIM	WWLLN	$0 \text{ ms} < \delta t < 30 \text{ ms}$	230
ASIM	GLD360	$0 \text{ ms} < \delta t < 30 \text{ ms}$	477

*Note.* We require the sferic match to be within 500 km from the subsatellite point.

high signal-to-noise ratio in the stacking analysis. We define a sferic match as the sferic with the smallest  $|\delta t|$  value but not larger than the following sferic match criteria. The sferic match criteria depend on the absolute timing accuracy of the instrument we consider. For RHESSI we require  $\delta t$  to be within  $\pm 1$  ms, and for Fermi and AGILE we use a sferic match criteria of  $\pm 0.2$  ms as their onboard clocks are on microsecond level. The absolute timing accuracy of ASIM varies stochastically between 0 and 30 ms and we chose this as the sferic match criterion. The location of the sferic match is assumed to be the production location of the TGF. An overview of the datasets and their sferic match criteria is shown in Table 1.

This analysis also includes optical data from the MMIA instrument onboard ASIM. MMIA consists of two cameras providing 12 images per second, and three high-speed photometers with a 100 kHz sampling rate. The instrument is described in detail in Chanrion et al. (2019). The two cameras are sensitive in 337.0 and 777.4 nm bands, and the photometers are sensitive in 337.0 nm,

180–240 nm (UV), and 777.4 nm bands. The bandwidths of 337 and 777.4 nm cameras are 5 and 3 nm, respectively. The bandwidths of 337 and 777.4 nm photometers are 4 and 5 nm, respectively. The 777 nm emission is due to atomic oxygen in hot lightning channels and is weakly absorbed in the atmosphere. The UV is strongly absorbed in the atmosphere and is therefore most sensitive to high altitude phenomena such as Elves and other Transient Luminous Events (TLEs). The 337 nm is most sensitive to lightning but will also see some signal from TLEs as it is close to the UV band. The 337 nm is more absorbed in the atmosphere compared to 777 nm. MMIA data acquisition is triggered, and a trigger is generated if the signal is larger than a threshold over a dynamically calculated background. There is also a cross-trigger system that stores MMIA data if the companion instrument, the Modular X- and Gamma-ray Sensor (MXGS), onboard ASIM triggers independently of the MMIA signal. MMIA is only active during nighttime, meaning that we only have optical data for TGFs detected during nighttime. The cameras and the photometers field of view (FOV) is a square 80° diagonal, except the UV photometer that has a circular 80° full cone angle. The relative timing accuracy between MXGS and MMIA was  $\pm 80$  μs before March 2019 and  $\pm 5$  μs after.

In this study we investigate 71 ASIM detected TGF events with MMIA optical data. These 71 events have been found by Skeie et al., manuscript in preparation, to have optical data associated with the detected TGFs, that is, a clean sample with the TGF produced well inside MMIA FOV and photometer data associated to the TGF. This sample was determined using the photometers, cameras, the high and low energy detector data, as well as lightning sferic activity and TGFs characteristics. For 45 of the TGF events it was also possible to use the GLD360-detected sferics to correct the absolute timing of ASIM down to a few milliseconds, by aligning several photometer pulses with the sferics, similar to what was done in Heumesser et al. (2021); Østgaard et al. (2021); Maiorana et al. (2021).

### 3. Results

#### 3.1. Stacking Analysis of Lightning Data

To determine whether the TGFs are in the beginning of the lightning flash we did a stacking analysis of sferics. Figure 1 shows a stacking plot of sferics relative to the time of the TGFs, as detected by RHESSI, Fermi, AGILE, and ASIM. The right panels are a close-up version of the left panels. The black histograms shows all sferics without applying the sferic match criteria of Table 1. The first peak at  $\delta t \approx 0$  consists mostly of sferics associated with the TGFs. We emphasize that we include *all* sferics within 500 km from the subsatellite point in the stacking analysis, not just the temporally closest sferic. Using a 50 ms bin size means that sferics 25 ms before and after the TGF will be included in the central bin. This implies that the bin will also include some sferics that are not directly associated to the TGF. Note also that the lightning networks sometimes detect the same sferic several times. Therefore, the central bin has more counts than the number of TGFs stacked. Note the enhanced signal from sferics between  $\sim 150$  and  $\sim 750$  ms, evident for all instruments. We will call this enhanced signal the “second peak” hereafter. The blue histograms are a sub-selection of events that have a sferic match (Table 1) within 500 km of the subsatellite point, and where only sferics within 20 km radius of the sferic match are included. A schematic of the selection of the two histograms is shown in Figure 2 and the 20 km limit will

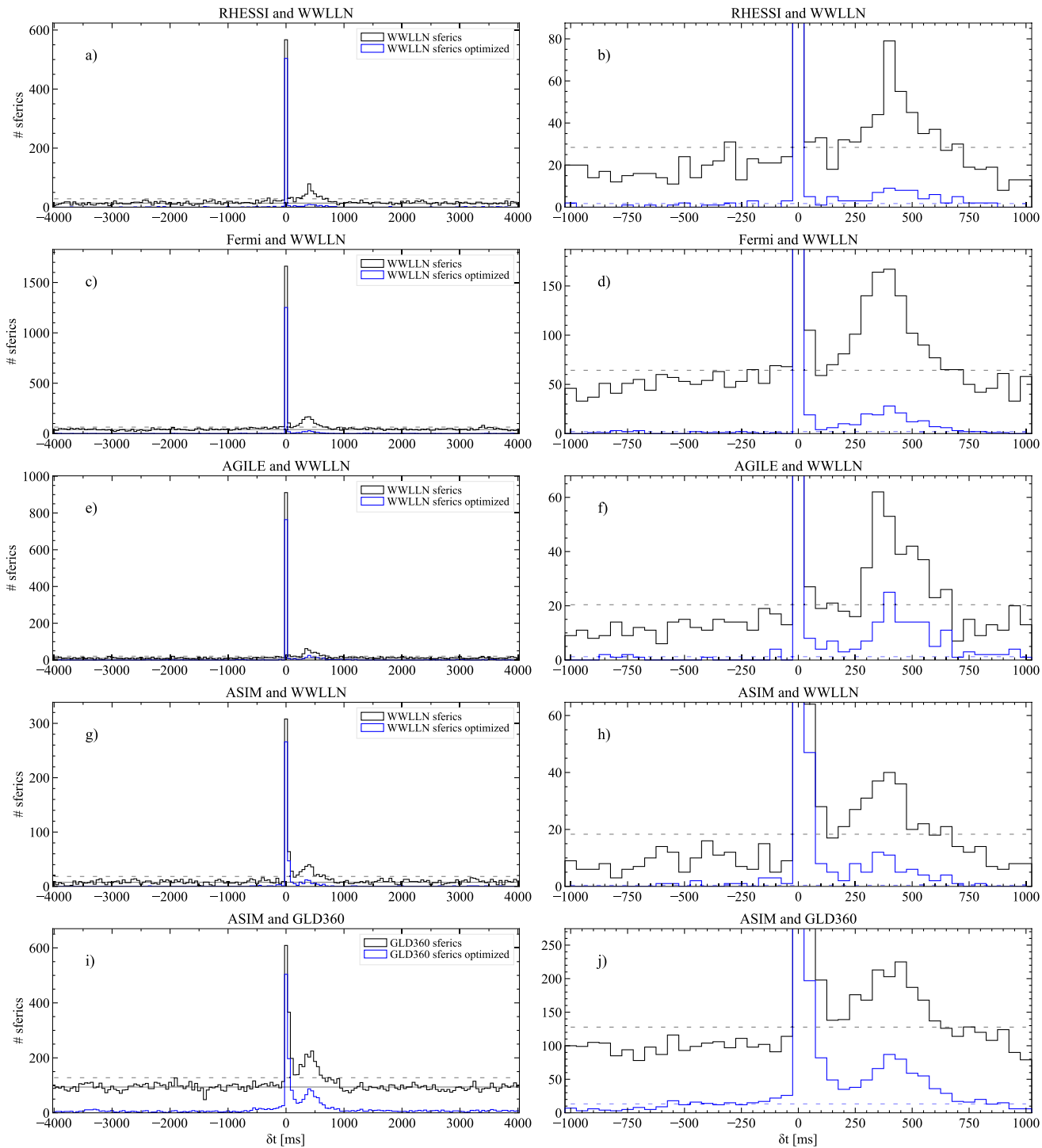


**Figure 1.** Stacking analysis of sferics as a function of time.  $\delta t = 0$  is the TGF time (Equation 1). The right panels are a close-up version of the left panels. The black histograms show *all* sferics within 500 km and the blue histograms show the sferics within 20 km of the TGF-sferic match (Table 1). The selection is illustrated in Figure 2. The solid black line in the left panels is the average background during  $\delta t$  between  $-4$  to  $-1$  s and the black dashed line marks the  $3\sigma$  level above background assuming Poisson distribution in counts per bin. The dashed blue line in the right panels is  $3\sigma$  above the background for the blue histograms. Note that the dashed blue line is very close to the  $x$ -axis for (b, d, f, and h). The bin size is 50 ms.

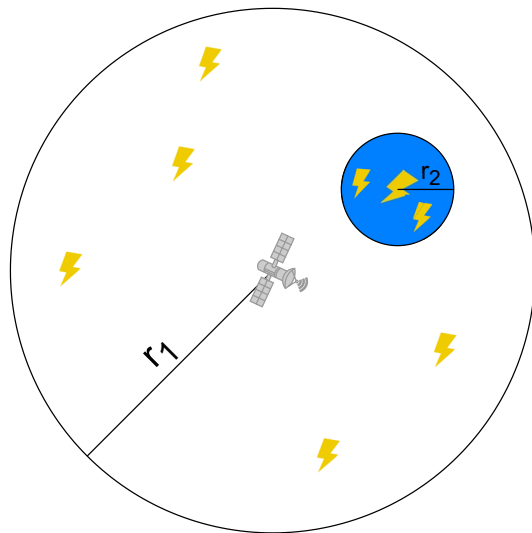


**Figure 2.** Figure illustrating the selection of sferics for the black and blue histograms in Figure 1. The black histograms consist of all sferics within  $r_1 = 500$  km of the subsatellite point. The blue histograms consist of sferics within  $r_2 = 20$  km of the sferic match in the middle of the blue circle in the illustration. The illustration is not to scale.

measurements by the photometers. One example is shown in Figure S2 in Supporting Information S1. The 13 events are removed from the analysis and we are left with 58 TGF events.

The TGF precedes the large MMIA optical pulse associated with the TGF in 57 cases. Some of the TGFs have a weak optical signal a few milliseconds before the large optical pulse associated with the TGF. This is compatible with lightning leader propagation (Cummer et al., 2015) and has been termed preactivity in earlier studies (Heumesser et al., 2021; Neubert et al., 2020; Østgaard, Neubert, et al., 2019; Østgaard et al., 2021). For the 57 TGFs there are either only one large optical pulse following the TGF (42 events), or there are several optical pulses (15 events) following the pulse associated with the TGF. An example of these is shown in Figure 4. In Figures 4a–4d it is clear that there are no signals detected by MMIA up to  $\sim 100$  ms before the TGF. The TGF is indicated in (a and b) as a magenta vertical line at time = 0. There is a clear 337 and 777 nm peak associated with the TGF, and following optical pulses are evident in both photometers up to  $\sim 400$  ms after the TGF. The cropped camera (CHU1 and CHU2) images in Figures 4f and 4g show only one active area that corresponds well with the position of the sferic associated with the TGF in Figure 4e).

In Figure 5, photometer data for 777 nm are shown for 8 (out of 15) TGF events with several pulses following the first pulse associated with the TGF. The TGF time is centered at time = 0, and it is evident that there is no lightning activity before the TGF.

In one of the 58 TGF events, the TGF seems to be in the middle of the flash where we have three optical pulses between 70 and 50 ms before the TGF, not placing the TGF in the beginning of the flash. This TGF event is shown in Figure S3 in Supporting Information S1, and will be discussed later.

## 4. Discussion

### 4.1. The TGF Time Relative to the Lightning Flash

Considering first the results of Fermi and AGILE that have the best absolute timing accuracy of  $\sim 2$   $\mu$ s, it is clear from Figure 1 that the TGF is produced in the beginning of the flash as there is no signal from sferics before the TGF.

be justified in the next paragraph. The blue histograms show a higher signal-to-noise ratio for the second peak than the black histogram. The  $3\sigma$  significance level is shown as a dashed line for the black and the blue histograms. Figure S1 in Supporting Information S1, shows a zoomed view of the same data as in Figures 1c and 1e with a bin size of 50  $\mu$ s instead of a bin size of 50 ms as in Figure 1.

Figure 3 shows the radial distance between the sferic match and the sferics in the second peak, where the second peak is defined to be  $\delta t$  between 150 and 750 ms. The bin size is chosen so that the area corresponding to each bin is constant, meaning that  $A_1 = \pi r_1^2 = A_n = \pi(r_n^2 - r_{(n-1)}^2) = \text{constant}$ , where  $n$  is the bin index. We see that there is an excess of sferics, within 5–10 km of the location of the sferic match, showing that most activity related to the lightning flash starting with a TGF occur within a radial distance of 20 km. This result is the reason for the 20 km limit to enhance the signal-to-noise ratio in the second peak for the blue histograms in Figure 1.

### 3.2. Analysis of Optical Data

A sample of 71 ASIM detected TGF events with associated optical data is used to investigate the lightning activity at times close to the TGFs. The TGF production locations are inside the FOV of MMIA. For 13 of the events, several cells were active at the same time of the TGF, which made it impossible to determine at what time they occur in the progression of a flash from

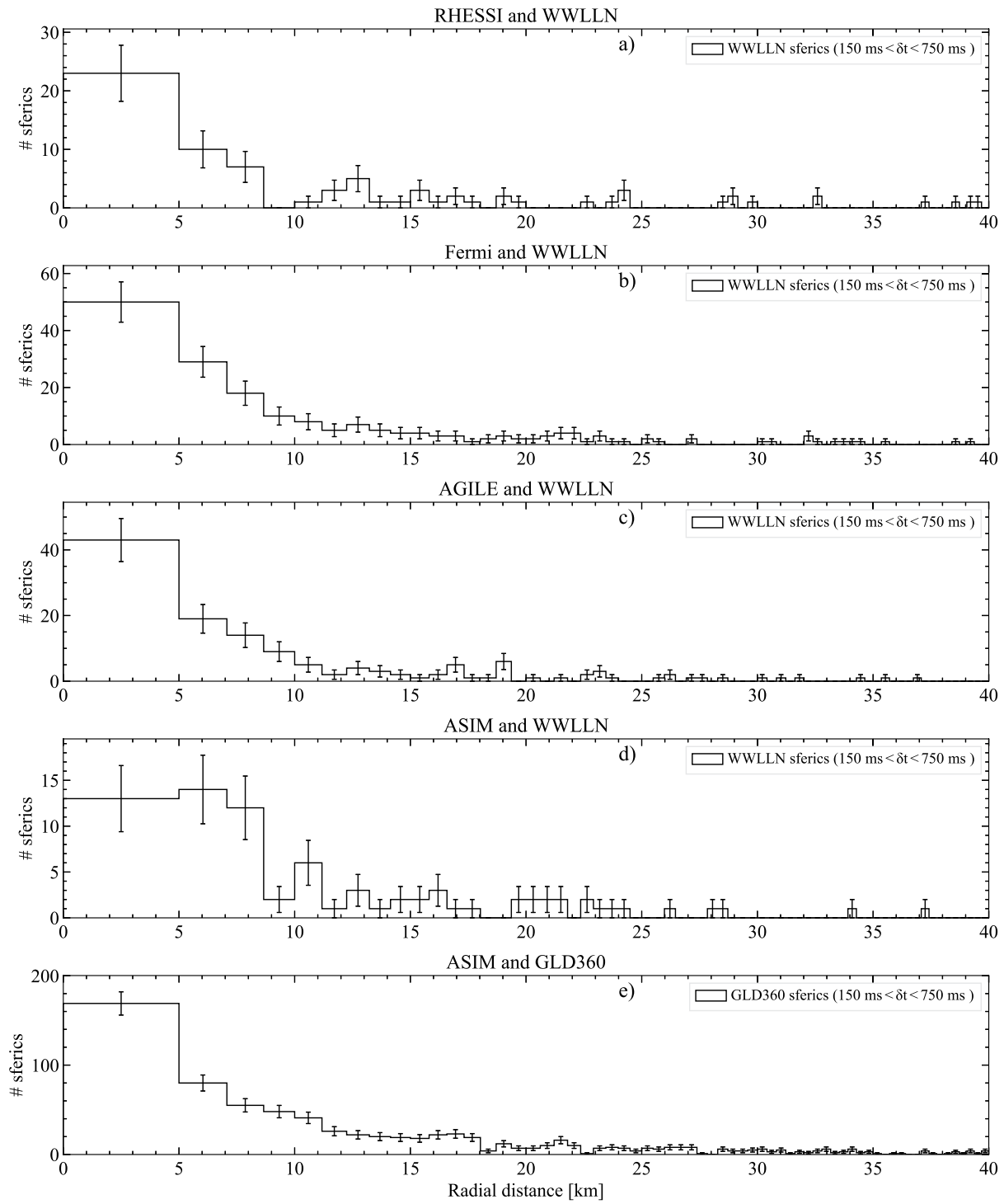


**Figure 3.** Stack plot showing the radial distance between the sferic matches associated to the TGFs and the sferics in the second peak. The plot shows that most activity related to the lightning flash that starts with a TGF, occur within a radial distance of 20 km. Only TGFs with a sferic match within 500 km of the subsatellite point are stacked. The bin size is chosen so that the area corresponding to each bin is constant. The uncertainty of the data points is  $\pm 1$  standard deviation assuming Poisson statistics.

The TGFs of ASIM precede the optical pulses for 57 of 58 events left in the analysis. Out of these, 42 are followed by several optical pulses. For these cases it is clear that the TGF is produced in the beginning of the lightning flash. Figure 5 shows examples of 8 of these events. For 15 of the 57 TGFs there are no additional pulses

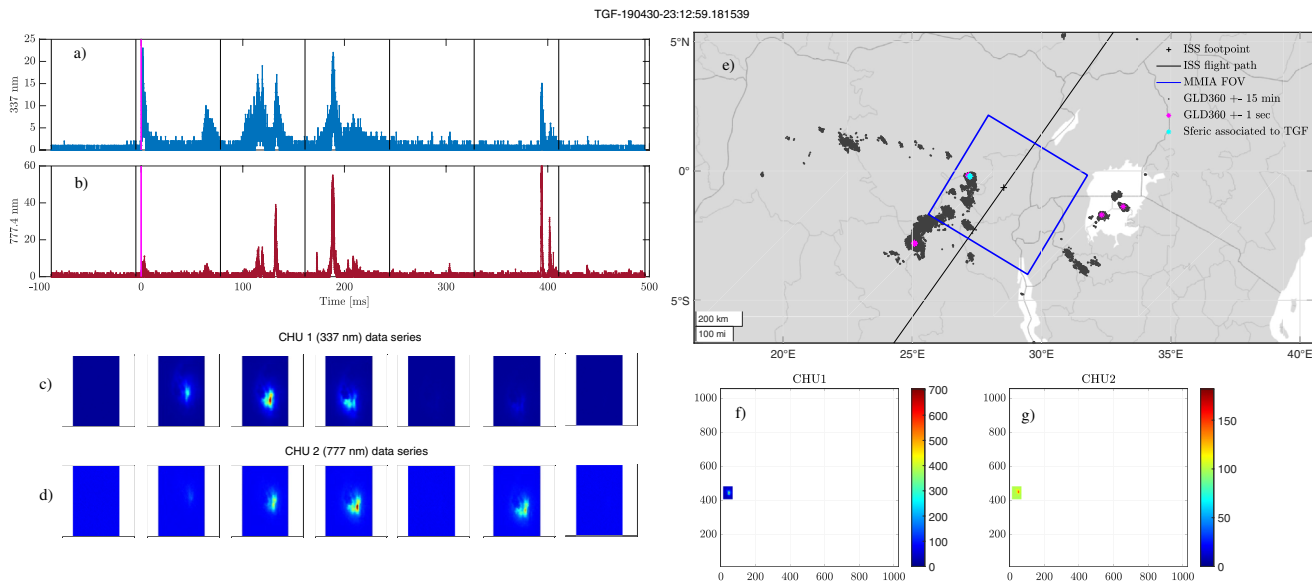


**Figure 4.** Overview over MMIA data at the time of a TGF that is in the beginning of a lightning flash. Panels (a and b) show the 337 and 777 nm photometer data with ADC units on the y-axis. The vertical black lines indicate the camera frames. The first peak in the 6th frame ( $\sim 400$  ms) in 777 nm peaks at ADC unit 100. The start of the TGF is indicated as a magenta vertical line at time = 0. Panels (c and d) show the corresponding CHU 1 and CHU 2 close-up camera frames. Panel (e) shows a map with MMIA FOV (blue square), ISS position and flight path, and sferics detected by GLD360. The velocity direction of ISS is to the right. Panels (f and g) show the CHU1 and CHU 2 camera frames at the time of the TGF. The full plot is the MMIA FOV and the velocity direction of ISS is in the positive vertical axes.

following the first optical pulse after the TGF. For one event we have optical pulses tens of milliseconds before and after the TGF and its large optical pulse. The time delay between the TGF and the optical pulse is  $\sim 1.4$  ms. However, we cannot exclude the possibility that the TGF is produced outside MMIA FOV, as there exist active lightning cells outside MMIA FOV as well. This would mean that the detected flash in the photometer data is not correlated with the TGF and it is a chance coincidence. As there is only 1 of the 58 TGFs in the sample with lightning activity before the TGF, it does not change the conclusion that the TGF is produced in the beginning of the lightning flash, especially if we consider that this event may be a timing chance coincidence given the  $\sim 1.4$  ms delay of the optical pulse relative to the TGF, the active lightning cells outside MMIA FOV, and the rarity of these events in the sample.

Based on the two different, but complementary approaches, where one approach makes use of a large TGF data set with associated sferics, and the other approach makes use of a selected TGF data set with high resolution optical measurements, we conclude that the TGF is produced in the beginning of a lightning flash.

#### 4.2. Increased Lightning Activity After the TGF

It is evident in Figure 1 that we have a second peak of sferics between 150 and 750 ms after the TGF for all TGF catalogs. This is much later than expected for sferics counted twice by lightning detection networks as this happens on less than 100  $\mu$ s scale, thus it must be a real physical feature of the flashes. After the first peak, at the time of the TGF, the lightning activity decreases almost to background level before it increases again to a local maximum around 400 ms, before it decreases again to the background level. We see that the second peak is significant above  $3\sigma$  for both black and blue histograms for all space missions. This second peak was first presented by Omar et al. (2014) and discussed in Smith et al. (2016) where it is speculated that the second peak involves cases associated to a subsequent process in the IC flash where horizontal breakdowns occur coupling new charge regions into the already established channel, so-called K-changes. To enhance the signal-to-noise ratio of the second peak, the blue histograms in Figure 1 consist of only TGFs with a sferic match according to Table 1, keeping only sferics within 20 km from the sferic match. Because we require a TGF-sferic match for the blue histogram, the second peak is smaller because we remove TGFs without a sferic match that may have sferics in the second peak. We must remember that a large fraction of TGFs does not have a detectable sferic match (Connaughton et al., 2010, 2013; Lindanger et al., 2020). We can see from Figure 1 that this selection

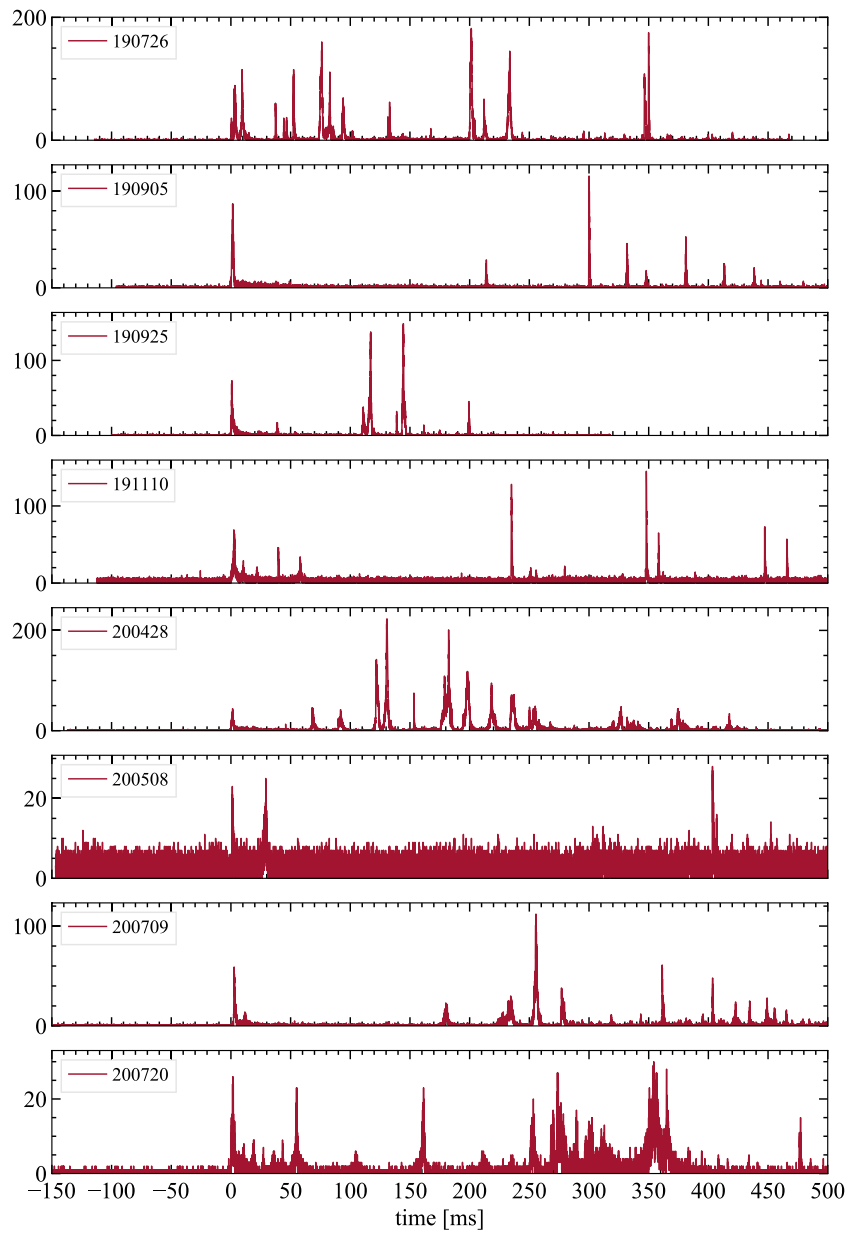


**Figure 5.** Optical data from the 777 nm photometer for 8 TGFs with lightning activity following the TGF. The TGF time is at time = 0, and the y-axis is in ADC units.

strategy removes almost all the background therefore enhancing the signal-to-noise ratio of the second peak. This is because most of the sferics producing the second peak are not located farther than 20 km from the sferic match. At a resolution of less than 20 km we approach the global location accuracy of WWLLN and GLD360, and from Figure 3 we can see that the 20 km radial distance from the TGF-sferic match is a conservative upper limit. Thus, we conclude that the second peak is co-located with the first peak within the localization uncertainties of the lightning detection networks meaning that the lightning discharges producing the second peak are co-located with the production location of the TGF. Note that Figure 5 shows a wide variability of the lightning activity, as observed in the optical bands, following the TGF, and that a second peak can only be seen on a larger sample of TGFs as shown in Figure 1.

To investigate if all TGFs with a sferic match (blue histograms in Figure 1) also have a sferic contributing to the second peak, we calculate the fraction of TGFs that also has one or more sferics in the second peak, between 150

**Table 2***Overview Over the Fraction of TGFs With a Sferic Match That Also Have Sferic Detections in the Second Peak*

Instrument-network	# TGFs with a sferic match and activity in 2nd peak	Fraction relative to 1st peak
RHESSI-WWLLN	44	0.10
Fermi-WWLLN	118	0.12
AGILE-WWLLN	83	0.13
ASIM-WWLLN	41	0.18
ASIM-GLD360	243	0.51

*Note.* The fraction is calculated by dividing the second column by the last column in Table 1.

and 750 ms. The results are shown in Table 2 and reveal that on average 13% of the TGFs with a WWLLN-sferic match also have sferic activity in the second peak. The fraction of TGFs with activity in second peak increases from RHESSI to ASIM. This can be explained by the improvement of the detection efficiency of WWLLN over time as the instruments are sorted from the oldest to newest time span of TGF detections. It is interesting to note that comparing ASIM-WWLLN with ASIM-GLD360, 18% of the TGFs with WWLLN-sferic matches have WWLLN detected sferics in the second peak, while 51% of the TGFs with GLD360-sferic matches have GLD360-detected sferics in the second peak. This can be explained by the difference in detection efficiency and sensitivity for the lightning detection networks. The median absolute peak current value, provided for GLD360 detections, for the first peak is 30 kA, and the median value for the second peak is 12 kA. As the strokes in the second peak in general have smaller peak currents than the first peak, the strokes in the second peak are harder to detect by lightning detection networks. This means that the detection of strokes in the second peak is strongly dependent on the sensitivity of the detection network, that is, in the threshold peak current. This is a further confirmation that when TGFs are compared to lightning data provided by lightning detection networks, the results are heavily affected by the networks' detection efficiency and sensitivity.

Mailyan et al. (2020) report a median peak current of 82 kA for sferics simultaneous with the TGFs within  $\pm 200 \mu\text{s}$ , and a median peak current of 26 kA for sferics associated with the TGFs from 200  $\mu\text{s}$  to 3.5 ms, before and after the TGF. The median value of 30 kA in the first peak in Figure 1i consists of sferics  $\pm 25$  ms relative to the TGF, therefore including non-simultaneous sferics, biasing the median value toward lower values. Due to the timing uncertainty of ASIM, this study cannot reproduce the median peak current values from Mailyan et al. (2020).

To check if the second peak is unique for TGF production, or just a common feature of lightning flashes, we did a blind search in the GLD360 data for the first stroke in a lightning flash. The blind search data were downloaded independent of ASIM TGF triggers. We defined the first stroke in a flash as the first sferic that had no other detected sferics up to 2 s before within a radial distance of 800 km. This is done for randomly selected GLD360 data between  $\pm 23^\circ$  latitude identifying 167 300 flashes with a total of 515 399 detected strokes/sferics. We did the same stacking analysis as we did for TGFs, stacking all sferics superposed at the time of the first lightning stroke. The results are shown in Figure 6 where we plot the sferics within 20 km following the first stroke, not including the first stroke itself, with the same time bin of 50 ms as used for Figure 1. The 20 km limit is applied to enhance a possible second peak between 150 and 750 ms as evidenced in the analysis of the TGF sample. The four panels have different thresholds on peak currents for the first stroke. The same analysis was also performed, with similar results as GLD360, for WWLLN data without any selection on polarity and peak current, because these variables are not available for WWLLN data. If the second peak is a general characteristic of +IC flashes, selection based on polarity and peak current of the flash as reported by GLD360 are not adequate enough to identify the second peak univocally in this sample.

As we could not identify a general second peak in the lightning data it seems that the second peak is not evident for flashes in general, thus suggesting that the second peak is a characteristic feature of a significant fraction of flashes that start with a TGF. Contrary to the blind search lightning flash sample (Figure 6), the TGF flashes (Figure 1) show a sharp decay after the first stroke which is not evident in the blind search sample. This suggests that those strokes with a TGF represent a large discharge and that it takes more than 150 ms before the electric activity is reactivated.

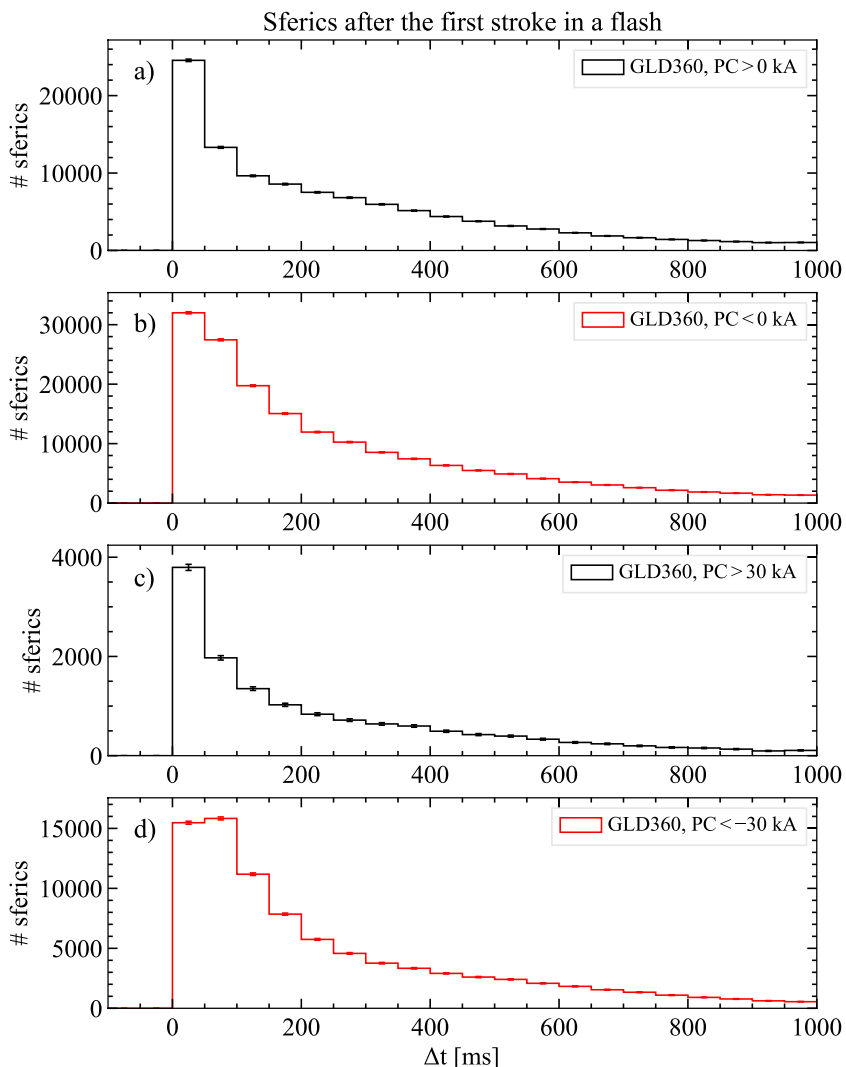


**Figure 6.** Histograms showing sferics within 20 km of the first stroke in a lightning flash. The first stroke is defined as the first sferic within a radius of 800 km with no detected sferics up to 2 s before. The first stroke itself is not included in the plot. The bin size is 50 ms. Each panel has a criterion, shown in the legend, on the peak current of the first stroke in the flash. The uncertainty of the data points is  $\pm 1$  standard deviation assuming Poisson statistics.

## 5. Summary

The TGF catalogs of RHESSI, Fermi, AGILE, and ASIM, a total of over 5,000 TGFs with sferic data  $\pm 4$  s within 500 km from the subsatellite point, are used to investigate the correlation between TGFs and sferics. The temporally closest sferic to the TGF has been studied in detail before (Albrechtsen et al., 2019; Connaughton et al., 2010, 2013; Lindanger et al., 2020; Marisaldi et al., 2015; Mezentsev et al., 2016; Østgaard et al., 2015), but the focus in these previous works was to find the *temporally closest* sferic associated to the TGF. In this study we have taken into account *all* sferics temporally close to the TGF. The study supports the idea that the TGFs are produced in the beginning of the lightning flash.

The conclusion is also supported by data from the ASIM instrumental suite, that provide a detailed high resolution data set combining TGF gamma-ray detection and optical lightning measurements. 98% (57 events out of 58) of the TGFs, where we only have optical data from the TGF location, show no lightning activity before the TGF. In the 98% sample, 26% have only one measured optical pulse and 74% have several optical pulses following the TGF. For one event of the 58 TGF events there is flash activity prior to the TGF. However, we cannot rule out that this event is a time coincidence and that the TGF is not associated with the optical signal.

There is an excess of sferics detected 150–750 ms after the TGFs in agreement with Omar et al. (2014); Smith et al. (2016). We term this excess of sferics the second peak. This study shows that in general the second peak is co-located with the first peak within <20 km, meaning that the discharges producing the second peak are co-located with the production location of the TGFs within the spatial uncertainties of the lightning detection networks. For TGFs associated with WWLLN, on average 13% of the TGFs with a WWLLN-sferic match have sferics in the second peak. For GLD360 and ASIM TGFs this fraction grows to 51%, showing that the presence or not of sferics in the second peak is strongly dependent on the sensitivity of the lightning network. A blind search in the lightning data, investigating if the second peak is a general property of lightning flashes, shows no evidence of a second peak for various selections on peak current. This suggests that the second peak is a characteristic feature for some lightning flashes that start with a TGF.

## Data Availability Statement

WWLLN and VAISALA data are available upon subscription. ASIM is a mission of the European Space Agency (ESA) and is funded by ESA and by national grants of Denmark, Norway and Spain. ASIM data used for this study are available from the authors upon reasonable request or can be downloaded from the ASIM Science Data Center (<https://asdc.space.dtu.dk>). The RHESSI, Fermi, and AGILE TGF catalogs are available from the following links: <https://scipp.pbsci.ucsc.edu/rhessi/>, <https://fermi.gsfc.nasa.gov/ssc/data/access/gbm/tgf/>, and <https://www.ssdc.asi.it/mcal3tgfeat/>. Additional data for this paper are available at <https://doi.org/10.5281/zenodo.5493848>.

## Acknowledgments

This study was supported by the Research Council of Norway under contract 223252/F50 (CoE). The authors thank the International Space Science Institute, Bern, Switzerland, for providing financial support and meeting facilities in the frame of the International Team no. 471: Understanding the Properties of the Terrestrial Gamma-Ray Flash Population. The authors also wish to thank the World Wide Lightning Location Network (<http://wwlln.net>), a collaboration among over 50 universities and institutions, for providing the lightning location data used in this paper. The authors also wish to thank VAISALA for the GLD360 lightning data.

## References

- Abarca, S. F., Corbosiero, K. L., & Galarneau, Jr., T. J. (2010). An evaluation of the Worldwide Lightning Location Network (WWLLN) using the National Lightning Detection Network (NLDN) as ground truth. *Journal of Geophysical Research*, 115(D18). <https://doi.org/10.1029/2009JD013411>
- Albrechtsen, K. H., Østgaard, N., Berge, N., & Gjesteland, T. (2019). Observationally weak TGFs in the RHESSI data. *Journal of Geophysical Research: Atmospheres*, 124(1), 287–298. <https://doi.org/10.1029/2018JD029272>
- Bogomolov, V. V., Panasyuk, M. I., Svertilov, S. I., Bogomolov, A. V., Garipov, G. K., Iyudin, A. F., et al. (2017). Observation of terrestrial gamma-ray flashes in the RELEC space experiment on the Vernov satellite. *Cosmic Research*, 55(3), 159–168. <https://doi.org/10.1134/S0010952517030017>
- Briggs, M. S., Xiong, S., Connaughton, V., Tierney, D., Fitzpatrick, G., Foley, S., et al. (2013). Terrestrial gamma-ray flashes in the Fermi era: Improved observations and analysis methods. *Journal of Geophysical Research: Space Physics*, 118(6), 3805–3830. <https://doi.org/10.1002/jgra.50205>
- Bürgesser, R. E. (2017). Assessment of the world wide lightning location network (WWLLN) detection efficiency by comparison to the Lightning Imaging Sensor (LIS). *Quarterly Journal of the Royal Meteorological Society*, 143(708), 2809–2817. <https://doi.org/10.1002/qj.3129>
- Chamrion, O., Neubert, T., Lundgaard Rasmussen, I., Stoltze, C., Tcherniak, D., Jessen, N. C., et al. (2019). The Modular Multispectral Imaging Array (MMIA) of the ASIM payload on the International Space Station. *Space Science Reviews*, 215(4), 28. <https://doi.org/10.1007/s11214-019-0593-y>
- Collier, A. B., Gjesteland, T., & Østgaard, N. (2011). Assessing the power law distribution of TGFs. *Journal of Geophysical Research*, 116(A10). <https://doi.org/10.1029/2011JA016612>
- Connaughton, V., Briggs, M. S., Holzworth, R. H., Hutchins, M. L., Fishman, G. J., Wilson-Hodge, C. A., et al. (2010). Associations between Fermi gamma-ray burst Monitor terrestrial gamma ray flashes and sferics from the world wide lightning location network. *Journal of Geophysical Research*, 115(A12). <https://doi.org/10.1029/2010JA015681>
- Connaughton, V., Briggs, M. S., Xiong, S., Dwyer, J. R., Hutchins, M. L., Grove, J. E., et al. (2013). Radio signals from electron beams in terrestrial gamma ray flashes. *Journal of Geophysical Research: Space Physics*, 118(5), 2313–2320. <https://doi.org/10.1029/2012JA018288>
- Cummer, S. A., Lu, G., Briggs, M. S., Connaughton, V., Xiong, S., Fishman, G. J., & Dwyer, J. R. (2011). The lightning-TGF relationship on microsecond timescales. *Geophysical Research Letters*, 38(14). <https://doi.org/10.1029/2011GL048099>
- Cummer, S. A., Lyu, F., Briggs, M. S., Fitzpatrick, G., Roberts, O. J., & Dwyer, J. R. (2015). Lightning leader altitude progression in terrestrial gamma-ray flashes. *Geophysical Research Letters*, 42(18), 7792–7798. <https://doi.org/10.1002/2015GL065228>
- Cummer, S. A., Zhai, Y., Hu, W., Smith, D. M., Lopez, L. I., & Stanley, M. A. (2005). Measurements and implications of the relationship between lightning and terrestrial gamma ray flashes. *Geophysical Research Letters*, 32(8). <https://doi.org/10.1029/2005GL022778>
- Dwyer, J. R. (2003). A fundamental limit on electric fields in air. *Geophysical Research Letters*, 30(20). <https://doi.org/10.1029/2003gl017781>
- Dwyer, J. R., & Cummer, S. A. (2013). Radio emissions from terrestrial gamma-ray flashes. *Journal of Geophysical Research: Space Physics*, 118(6), 3769–3790. <https://doi.org/10.1002/jgra.50188>
- Dwyer, J. R., & Smith, D. M. (2005). A comparison between Monte Carlo simulations of runaway breakdown and terrestrial gamma-ray flash observations. *Geophysical Research Letters*, 32(22). <https://doi.org/10.1029/2005GL023848>
- Fishman, G. J., Bhat, P. N., Mallozzi, R., Horack, J. M., Koshut, T., Kouveliotou, C., et al. (1994). Discovery of Intense gamma-ray flashes of atmospheric Origin. *Science*, 264(5163), 1313–1316. <https://doi.org/10.1126/science.264.5163.1313>
- Gurevich, A., Milikh, G., & Roussel-Dupre, R. (1992). Runaway electron mechanism of air breakdown and preconditioning during a thunderstorm. *Physics Letters A*, 165(5), 463–468. [https://doi.org/10.1016/0375-9601\(92\)90348-p](https://doi.org/10.1016/0375-9601(92)90348-p)
- Heumesser, M., Chamrion, O., Neubert, T., Christian, H. J., Dimitriadou, K., Gordillo-Vazquez, F. J., et al. (2021). Spectral observations of optical emissions associated with terrestrial gamma-ray flashes. *Geophysical Research Letters*, 48(4), 2020GL090700. <https://doi.org/10.1029/2020GL090700>
- Hutchins, M. L., Holzworth, R. H., Brundell, J. B., & Rodger, C. J. (2012). Relative detection efficiency of the world wide lightning location network. *Radio Science*, 47(6), RS6005. <https://doi.org/10.1029/2012rs005049>

- Lindanger, A., Marisaldi, M., Maiorana, C., Sarria, D., Albrechtsen, K., Østgaard, N., et al. (2020). The 3rd AGILE terrestrial gamma ray flash catalog. Part I: Association to lightning sferics. *Journal of Geophysical Research: Atmospheres*, 125(11). <https://doi.org/10.1029/2019JD031985>
- Lindanger, A., Marisaldi, M., Sarria, D., Østgaard, N., Lehtinen, N., Skeie, C. A., et al. (2021). Spectral analysis of individual terrestrial gamma-ray flashes detected by ASIM. *Journal of Geophysical Research: Atmospheres*, 126(23), e2021JD035347. <https://doi.org/10.1029/2021JD035347>
- Lu, G., Blakeslee, R. J., Li, J., Smith, D. M., Shao, X.-M., McCaul, E. W., et al. (2010). Lightning mapping observation of a terrestrial gamma-ray flash. *Geophysical Research Letters*, 37(11). <https://doi.org/10.1029/2010GL043494>
- Mailyan, B. G., Briggs, M. S., Cramer, E. S., Fitzpatrick, G., Roberts, O. J., Stanbro, M., & Dwyer, J. R. (2016). The spectroscopy of individual terrestrial gamma-ray flashes: Constraining the source properties. *Journal of Geophysical Research: Space Physics*, 121, 11–346. <https://doi.org/10.1002/2016ja022702>
- Mailyan, B. G., Nag, A., Dwyer, J. R., Said, R. K., Briggs, M. S., Roberts, O. J., et al. (2020). Gamma-ray and radio-frequency Radiation from thunderstorms observed from space and ground. *Scientific Reports*, 10(1), 7286. <https://doi.org/10.1038/s41598-020-63437-2>
- Maiorana, C., Marisaldi, M., Füllekrug, M., Soula, S., Lapierre, J., Mezentsev, A., et al. (2021). Observation of terrestrial gamma-ray flashes at mid latitude. *Journal of Geophysical Research: Atmospheres*, 126(18). <https://doi.org/10.1029/2020JD034432>
- Maiorana, C., Marisaldi, M., Lindanger, A., Østgaard, N., Ursi, A., Sarria, D., et al. (2020). The 3rd AGILE terrestrial gamma-ray flashes catalog. Part II: Optimized selection criteria and characteristics of the new sample. *Journal of Geophysical Research: Atmospheres*, 125(11). <https://doi.org/10.1029/2019JD031986>
- Marisaldi, M., Argan, A., Ursi, A., Gjesteland, T., Fuschino, F., Labanti, C., et al. (2015). Enhanced detection of terrestrial gamma-ray flashes by AGILE. *Geophysical Research Letters*, 42(21), 9481–9487. <https://doi.org/10.1002/2015GL066100>
- Marisaldi, M., Fuschino, F., Labanti, C., Galli, M., Longo, F., Del Monte, E., et al. (2010). Detection of terrestrial gamma ray flashes up to 40 MeV by the AGILE satellite. *Journal of Geophysical Research*, 115(A3). <https://doi.org/10.1029/2009JA014502>
- Marisaldi, M., Galli, M., Labanti, C., Østgaard, N., Sarria, D., Cummer, S. A., et al. (2019). On the high-energy spectral Component and fine time Structure of terrestrial gamma ray flashes. *Journal of Geophysical Research: Atmospheres*, 124(14), 7484–7497. <https://doi.org/10.1029/2019JD030554>
- Mezentsev, A., Østgaard, N., Gjesteland, T., Albrechtsen, K., Lehtinen, N., Marisaldi, M., et al. (2016). Radio emissions from double RHESSI TGFs. *Journal of Geophysical Research: Atmospheres*, 121(13), 8006–8022. <https://doi.org/10.1002/2016JD025111>
- Neubert, T., Østgaard, N., Reglero, V., Blanc, E., Chanrion, O., Oxborow, C. A., et al. (2019). The ASIM mission on the International space station. *Space Science Reviews*, 215(2), 26. <https://doi.org/10.1007/s11214-019-0592-z>
- Neubert, T., Østgaard, N., Reglero, V., Chanrion, O., Heumesser, M., Dimitriadou, K., et al. (2020). A terrestrial gamma-ray flash and ionospheric ultraviolet emissions powered by lightning. *Science*, 367(6474), 183–186. <https://doi.org/10.1126/science.aax3872>
- Omar, K. S., Briggs, M. S., & Heckman, S. (2014). Characterizing the TGF-lightning relationship using ENTLN. AGU Fall Meeting.
- Østgaard, N., Albrechtsen, K. H., Gjesteland, T., & Collier, A. (2015). A new population of terrestrial gamma-ray flashes in the RHESSI data. *Geophysical Research Letters*, 42(24), 10–937. <https://doi.org/10.1002/2015GL067064>
- Østgaard, N., Balling, J. E., Bjørnsen, T., Brauer, P., Budtz-Jørgensen, C., Bujwan, W., et al. (2019). The Modular X- and Gamma-Ray Sensor (MXGS) of the ASIM Payload on the International Space Station. *Space Science Reviews*, 215, 23. <https://doi.org/10.1007/s11214-018-0573-7>
- Østgaard, N., Cummer, S. A., Mezentsev, A., Luque, A., Dwyer, J., Neubert, T., et al. (2021). Simultaneous observations of EIP, TGF, Elve, and optical lightning. *Journal of Geophysical Research: Atmospheres*, 126(11), e2020JD033921. <https://doi.org/10.1029/2020JD033921>
- Østgaard, N., Gjesteland, T., Carlson, B. E., Collier, A. B., Cummer, S. A., Lu, G., & Christian, H. J. (2013). Simultaneous observations of optical lightning and terrestrial gamma ray flash from space. *Geophysical Research Letters*, 40(10), 2423–2426. <https://doi.org/10.1002/grl.50466>
- Østgaard, N., Neubert, T., Reglero, V., Ullaland, K., Yang, S., Genov, G., et al. (2019). First 10 Months of TGF observations by ASIM. *Journal of Geophysical Research: Atmospheres*, 124(24), 14024–14036. <https://doi.org/10.1029/2019JD031214>
- Roberts, O. J., Fitzpatrick, G., Stanbro, M., McBreen, S., Briggs, M. S., Holzworth, R. H., et al. (2018). The first Fermi-GBM terrestrial gamma ray flash catalog. *Journal of Geophysical Research: Space Physics*, 123(5), 4381–4401. <https://doi.org/10.1029/2017JA024837>
- Rodger, C. J., Brundell, J. B., Holzworth, R. H., Lay, E. H., Crosby, N. B., Huang, T.-Y., & Rycroft, M. J. (2009). Growing detection efficiency of the world wide lightning location network. *AIP Conference Proceedings*, 1118(1), 15–20. <https://doi.org/10.1063/1.3137706>
- Said, R. K., & Murphy, M. J. (2016). GLD360 Upgrade: Performance analysis and applications. In *24th International Lightning Detection Conference (IC)*.
- Shao, X.-M., Hamlin, T., & Smith, D. M. (2010). A closer examination of terrestrial gamma-ray flash-related lightning processes. *Journal of Geophysical Research*, 115(A6). <https://doi.org/10.1029/2009JA014835>
- Smith, D. M., Buzbee, P., Kelley, N. A., Infanger, A., Holzworth, R. H., & Dwyer, J. R. (2016). The rarity of terrestrial gamma-ray flashes: 2. RHESSI stacking analysis. *Journal of Geophysical Research: Atmospheres*, 121(19), 11–382. <https://doi.org/10.1002/2016JD025395>
- Smith, D. M., Kelley, N. A., Buzbee, P., Infanger, A., Splitt, M., Holzworth, R. H., & Dwyer, J. R. (2020). Special Classes of terrestrial gamma ray flashes from RHESSI. *Journal of Geophysical Research: Atmospheres*, 125(20), e2020JD033043. <https://doi.org/10.1029/2020JD033043>
- Smith, D. M., Lopez, L. I., Lin, R. P., & Barrington-Leigh, C. (2005). Terrestrial gamma-ray flashes observed up to 20 MeV. *Science (New York, N.Y.)*, 307, 1085–1088. <https://doi.org/10.1126/science.1107466>
- Stanley, M. A., Shao, X. M., Smith, D. M., Lopez, L. I., Pongratz, M. B., Harlin, J. D., et al. (2006). A link between terrestrial gamma-ray flashes and intracloud lightning discharges. *Geophysical Research Letters*, 33(6). <https://doi.org/10.1029/2005GL025537>
- Ursi, A., Guidorzi, C., Marisaldi, M., Sarria, D., & Frontera, F. (2017). Terrestrial gamma-ray flashes in the BeppoSAX data archive. *Journal of Atmospheric and Solar-Terrestrial Physics*, 156, 50–56. <https://doi.org/10.1016/j.jastp.2017.02.014>

# Supporting Information for “Production of Terrestrial Gamma-ray Flashes During the Early Stages of Lightning Flashes”

A. Lindanger<sup>1</sup>, C. A. Skeie<sup>1</sup>, M. Marisaldi<sup>1,2</sup>, I. Bjørge-Engeland<sup>1</sup>, N.

Østgaard<sup>1</sup>, A. Mezentsev<sup>1</sup>, D. Sarria<sup>1</sup>, N. Lehtinen<sup>1</sup>, V. Reglero<sup>3</sup>, O.

Chanrion<sup>4</sup>, T. Neubert<sup>4</sup>

<sup>1</sup>Birkeland Centre for Space Science, Department of Physics and Technology, University of Bergen, Bergen, Norway.

<sup>2</sup>INAF-OAS Bologna, Bologna, Italy

<sup>3</sup>University of Valencia, Spain

<sup>4</sup>National Space Institute, Technical University of Denmark, Denmark

## Contents of this file

1. Figures S1 to S3

## Introduction

This document contains three figures with supplementary material for the paper “Production of Terrestrial Gamma-ray Flashes During the Early Stages of Lightning Flashes”.

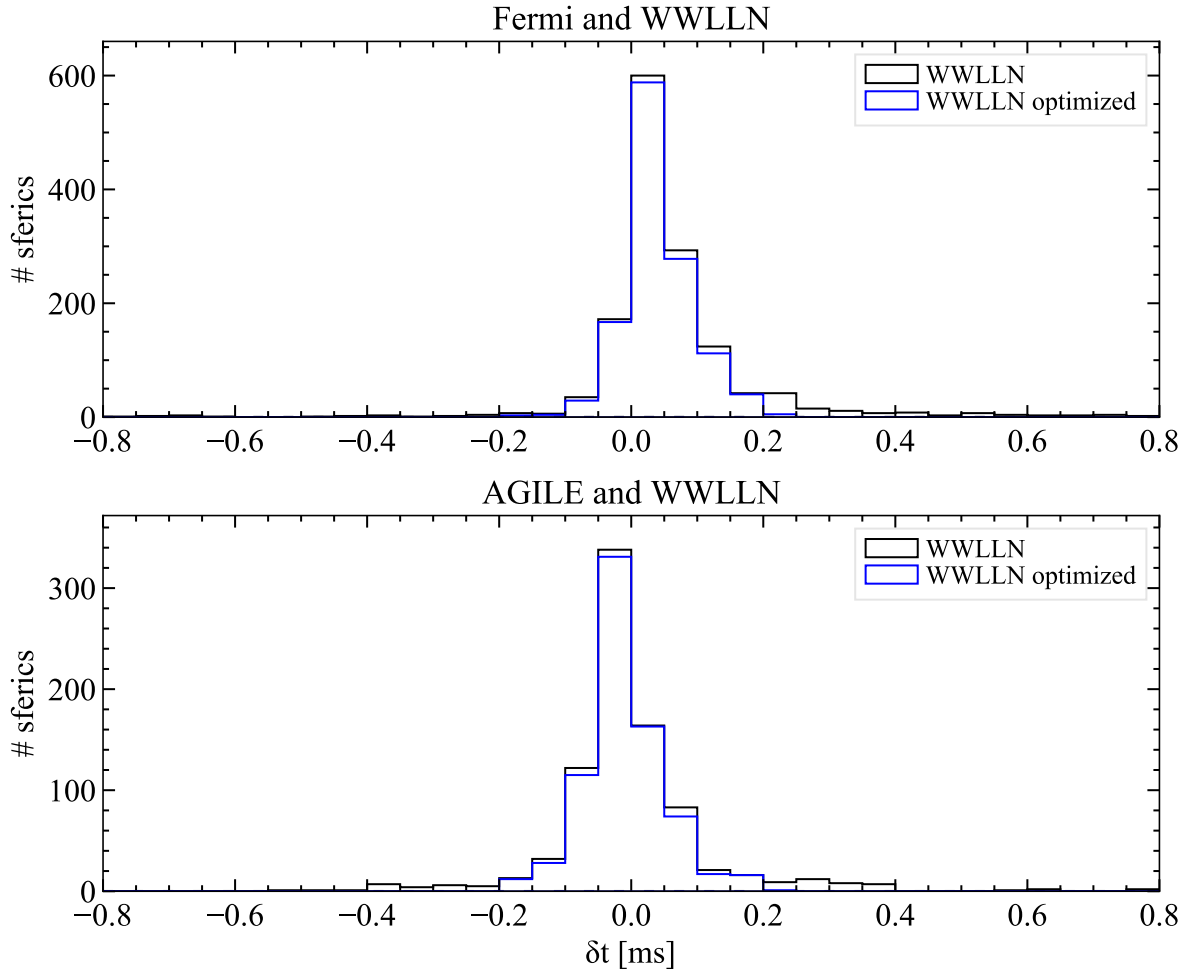


**Figure S1.** Close-up view of the same data as in Figure 1 c) and e) in the main paper. There is no visible structure for  $\delta t$  larger than  $\pm 0.8$  ms with this bin size. The bin size is 50  $\mu$ s.

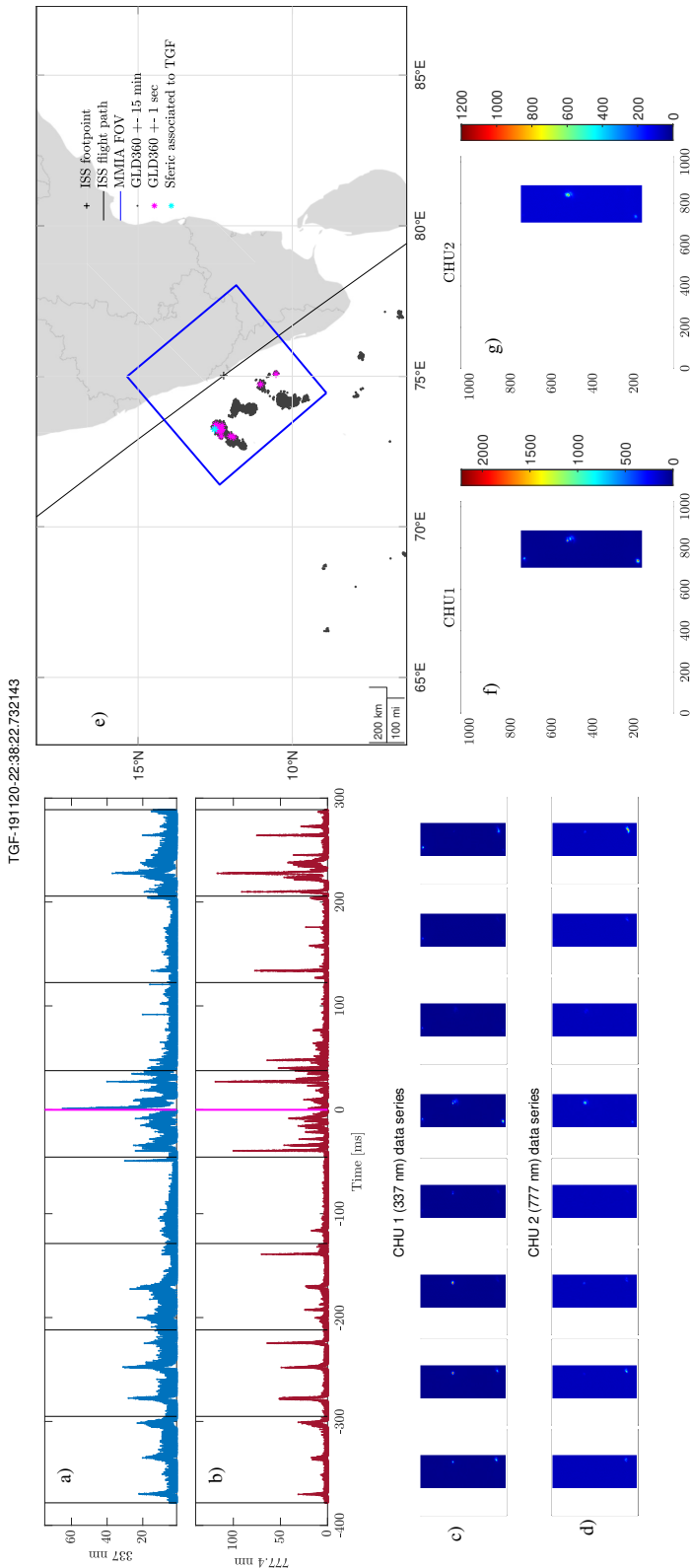


**Figure S2.** Overview over MMIA data at the time of a TGF where we cannot state if the TGF is in the start of the lightning flash or not. Panels a) and b) show the 337 nm and 777 nm photometer data with ADC units on the y-axis. The start of the TGF is indicated as a magenta vertical line at time = 0. The vertical black lines indicate the camera frames. Panels c) and d) show the corresponding CHU 1 and CHU 2 close-up camera frames. Panel e) shows a map with MMIA FOV, ISS position and flight path, and sferics detected by GLD360. The velocity direction of ISS is to the right. Panels f) and g) show the CHU1 and CHU 2 camera frames at the time of the TGF. The full plot is the MMIA FOV and the velocity direction of ISS is in the positive vertical axes. It is clear that the cropped camera images correspond to the lightning activity detected by GLD360. It is evident that there is several active regions, hence it is impossible to state the origin of the photometer signal in the corresponding frame.

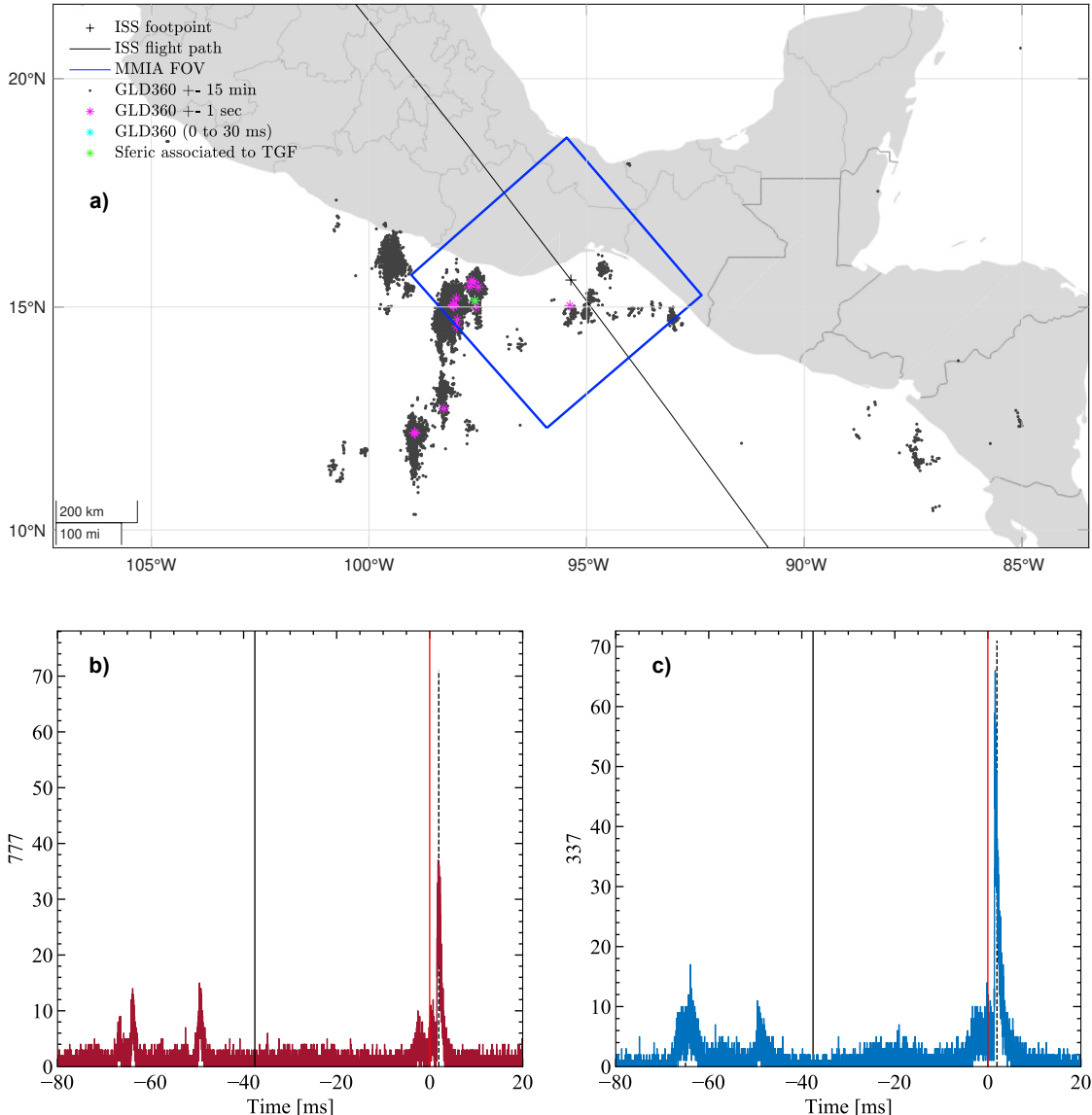


**Figure S3.** A TGF (190921-09:46:58) with lightning activity before the TGF. Figure b) and c) are zoomed to the beginning of the flash. The lightning flash ends after  $\sim 400$  ms. The black dashed line in b) and c) is the TGF associated sferic marked in green in a). The black solid line marks the start of a new camera frame in the cameras (not shown). Both camera frames only show lightning activity compatible with the sferic associated to the TGF. Thus, this TGF is not produced in the beginning of the lightning flash if we assume the TGF is associated to the optical data. The time delay between the optical data and the TGF is  $\sim 1.4$  ms. However, note that there is lightning activity outside MMIA FOV and that the TGF might have been produced there. The y-axis unit in b) and c) is in ADC units.

March 8, 2022, 1:00pm

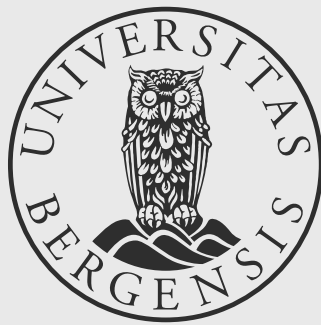




# List of abbreviations

AGILE	Astrorivelatore Gamma a Immagini Leggero
ASIM	Atmosphere-Space Interaction Monitor
BATSE	Burst and Transient Source Experiment
BGO	Bismuth-Germanium Oxide
CG	Cloud-to-Ground (lightning flash)
CGRO	Compton Gamma-Ray Observatory
CZT	Cadmium-Zinc Telluride
GBM	Gamma-Ray Burst Monitor
GLD360	Global Lightning Dataset
GRB	Gamma-Ray Burst
HED	High Energy Detector
IC	Intra-Cloud (lightning flash)
ISS	International Space Station
LED	Low Energy Detector
LF	Low Frequency (radio)
MCAL	Mini Calorimeter
MDF	Magnetic Direction Finding
MMIA	Modular Multi-spectral Imaging Array
MXGS	Modular X- and Gamma-ray Sensor
NLDN	National Lightning Detection Network
PMT	Photomultiplier tube
RHESSI	Reuven-Ramaty High Energy Solar Spectroscopic Imager
RREA	Relativistic Runaway Electron Avalanche
TEB	Terrestrial Electron Beam
TGF	Terrestrial Gamma-ray Flash
TLE	Transient Luminous Event
TOA	Time of arrival
TOGA	Time of group arrival
VLF	Very Low Frequency (radio)
WWLLN	World Wide Lightning Location Network





uib.no

ISBN: 9788230855539 (print)  
9788230866085 (PDF)